

**Designing Treatment Individualization
in Photodynamic Therapy to
Compensate for Pharmacokinetic
Variability**

A PH.D. THESIS

SUBMITTED BY XIAODONG R. ZHOU

THAYER SCHOOL OF ENGINEERING, DARTMOUTH COLLEGE

HANOVER, NH 03755

Abstract

The main theme of this thesis is to investigate the origins of photosensitizer pharmacokinetic variability, how this pharmacokinetic variation affects photodynamic therapy (PDT), and to search for innovative strategies to reduce the inter-individual pharmacokinetic variability and variability in treatment response. PDT involves photosensitizer administration and light irradiation to the tissue to be destroyed. With this inherent dual selectivity, PDT can have high inter-individual variability in response to treatment, due to the variation in photosensitizer uptake, delivered light dose, and tumor oxygenation. Although light irradiation dosimetry can be achieved to improve the treatment in clinical practice, inter-individual photosensitizer pharmacokinetic variability has not been optimized as extensively. The ability to individualize PDT treatment according individual photosensitizer pharmacokinetics has not yet been investigated. To address this issue in a mechanistic way this study focuses on the microscopic transport pathways of the drug. Both transvascular and interstitial transport processes have been characterized in the Dunning prostate MAT-LyLu tumor model using the drug verteporfin. The dominant factors determining

macroscopic tumor uptake at two time points after drug administration have been identified. Correlation between verteporfin pharmacokinetics and PDT treatment efficacy has also been studied in this thesis such that a cause-effect relationship can be established connecting the photosensitizer microscopic transport process with its pharmacokinetics and treatment efficacy. Two strategies to reduce the inter-individual variability in response to PDT are then proposed. The first approach addresses the photosensitizer microscopic transport processes by modulating photosensitizer transport parameters such that an enhanced photosensitizer delivery can be achieved. The second approach utilizes photosensitizer dosimetry techniques to control the PDT light treatment. In both approaches, the inter-individual variability in response to PDT was reduced. Thus, the study illustrates that a focused quantification of mechanisms of drug delivery combined with subject-specific changes can have a significant impact upon how to optimize therapy.

Table of Contents

Table of Contents	vi
List of Figures	xvi
List of Tables	xxi
List of Acronyms	xxiii
I Preliminaries	1
1 Introduction to Photodynamic Therapy	2
1.1 Photochemical Physics of Photodynamic Therapy	3
1.2 Photosensitizers	5
1.2.1 Porphyrin-related Photosensitizers	5
1.2.2 Non-porphyrin Photosensitizers	13

1.3	Biology of Photodynamic Therapy	13
1.3.1	Cellular Targeting Mechanism	13
1.3.2	Vascular Targeting Mechanism	15
1.3.3	Immune Effects	17
2	Motivation, Specific Aims and Thesis Overview	20
2.1	Motivation and Specific Aims	20
2.1.1	Patient Variation in Response to PDT	20
2.1.2	Photon Distribution	23
2.1.3	Photosensitizer Pharmacokinetics	23
2.1.4	Specific Aims	24
2.2	Thesis Overview	26
II	Quantification of Photosensitizer Pharmacokinetic Variability	29
3	Origins of Photosensitizer Pharmacokinetic Variability	30
3.1	Photosensitizer Delivery with Liposomes	31
3.1.1	Conventional Liposomes	33
3.1.2	Passive Targeting Liposomes	35
3.1.3	Active Targeting Liposomes	37

3.2	Photosensitizer Administration and Systemic Distribution	38
3.3	Photosensitizer Distribution in Tumor	40
3.3.1	Photosensitizer Distribution through the Tumor Vascular Network	42
3.3.2	Transport of Photosensitizers across Microvascular Walls	44
3.3.3	Transport of Photosensitizers through Tumor Interstitium	52
3.3.4	Summary of Barriers to Photosensitizer Distribution in Tumor	58
3.3.5	Photosensitizer Photobleaching	59
3.4	Photosensitizer Metabolism and Excretion	60
3.4.1	Metabolism	60
3.4.2	Excretion	60
3.4.3	Photosensitizer Clearance and Half-life	61
4	Effects of Tumor Host-site on Verteporfin Pharmacokinetics and PDT Treatment	62
4.1	Introduction	63
4.2	Materials and Methods	65
4.2.1	Photosensitizer	65
4.2.2	Animals and Tumor Models	66
4.2.3	Analysis of Tumor Host-site Effects on Tumor Microenvironment	67

4.2.4	Analysis of Tumor Host-site Effects on Verteporfin Tumor Uptake	70
4.2.5	Analysis of Tumor Host-site Effects on Transport Parameters	71
4.2.6	Analysis of Tumor Host-site Effects on PDT Treatment	73
4.2.7	Statistical Analysis	74
4.3	Results	75
4.3.1	Effect of Tumor Host-site on MAT-LyLu Tumor Growth and His- tology	75
4.3.2	Effect of Tumor Host-sites on MAT-LyLu Tumor Vasculature Mor- phology	75
4.3.3	Effect of Tumor Host-site on Tumor VEGF level	77
4.3.4	Effect of Tumor Host-site on Tumor Oxygenation	77
4.3.5	Effect of Tumor Host-sites on Macroscopic Permeability	80
4.3.6	Effect of Tumor Host-site on Microscopic Permeability	80
4.3.7	Effect of Tumor Host-sites on Interstitial Diffusion Coefficient	81
4.3.8	Effect of Tumor Host Micro-environment on Verteporfin Uptake	81
4.3.9	Tumor response to PDT	84
4.4	Discussion	87
4.5	Conclusions	92

5	Correlation between Transport Parameters and Pharmacokinetics	94
5.1	Introduction	95
5.2	Materials and Methods	99
5.2.1	Photosensitizer	99
5.2.2	Animals and Tumor Models	99
5.2.3	Verteporfin Plasma Pharmacokinetics	100
5.2.4	Microscopy and Image Analysis	101
5.2.5	Verteporfin Transvascular Transport	102
5.2.6	Verteporfin Interstitial Transport	104
5.3	Results	110
5.3.1	Verteporfin Plasma Pharmacokinetics	110
5.3.2	BPD localization changes over time	111
5.3.3	BPD fluorescence intravascular and extravascular distribution	113
5.3.4	Microscopic Permeability	118
5.3.5	Interstitial Diffusion	120
5.3.6	Correlation between Transport Parameters and Verteporfin Pharmacokinetics	124
5.4	Discussion	126
5.5	Conclusion	137

6	Photosensitizer Dosimetry: Effects of sampling volume	139
6.1	Introduction	141
6.2	Materials and Methods	146
6.2.1	Photosensitizer	146
6.2.2	Tumor and Animal Models	146
6.2.3	Flow Cytometry	147
6.2.4	Fluorescence Microscopy	148
6.2.5	<i>In vivo</i> Fluorescence Quantification	148
6.2.6	Image Analysis and Statistical Analysis	149
6.3	Results	150
6.3.1	Flow Cytometry Analysis of Cellular Fluorescence	150
6.3.2	Fluorescence Microscopy of Frozen Tumor Sections	152
6.3.3	Histogram Analysis of Fluorescence Microscopy	156
6.3.4	<i>In vivo</i> Fluorescence Measurements	159
6.4	Discussion	162
6.5	Conclusions	167

III Strategies for PDT Treatment Individualization	169
7 Correlation between PS Pharmacokinetics and PDT Outcome	170
7.1 Introduction	171
7.2 Material and Methods	172
7.2.1 Animals and Tumor Model	172
7.2.2 Cellular and Vascular Targeting Photodynamic Therapy	173
7.2.3 Tumor Regrowth Assay	173
7.2.4 Photosensitizer Pharmacokinetics Quantification	174
7.3 Results	177
7.3.1 Intra-tumor and Inter-tumor Variation in Verteporfin Pharmacokinetics	177
7.3.2 Growth Dynamics post Cellular and Vascular Targeting PDT	185
7.3.3 Correlation between Verteporfin Pharmacokinetics and PDT Treatment Outcome	187
7.4 Discussion	190
7.5 Conclusion	200
8 Photosensitizer Pharmacokinetic Modulation	201
8.1 Introduction	203

8.2	Materials and Methods	205
8.2.1	Tumor and Animal Model	205
8.2.2	Photosensitizer and Inflammatory Mediator	206
8.2.3	Laser Doppler Blood Flow Monitoring	206
8.2.4	Transvascular Permeability Coefficient Evaluation	206
8.2.5	Verteporfin Plasma Pharmacokinetics	208
8.2.6	Verteporfin Tumor Pharmacokinetics	209
8.2.7	PDT Treatment and Tumor Regrowth Assay	210
8.3	Results	211
8.3.1	Verteporfin Plasma Pharmacokinetics	211
8.3.2	Tumor Vasculature Morphology	213
8.3.3	Change of Tumor Vascular Permeability to Evans Blue	214
8.3.4	Change of Tumor Microscopic Vascular Permeability	215
8.3.5	Change of Verteporfin Tumor Pharmacokinetics	216
8.3.6	Change of Tumor Blood Flow	217
8.3.7	Enhancement of PDT Treatment Efficacy	217
8.4	Discussion	222
8.5	Conclusions	227

9	Photosensitizer Dosimetry Controlled PDT Treatment Planning	229
9.1	Introduction	229
9.2	Materials and Methods	232
9.2.1	Animals and tumor model	232
9.2.2	Photosensitizer	232
9.2.3	Photosensitizer dosimetry	233
9.2.4	Photodynamic dose calculation and Photodynamic therapy treatment	234
9.2.5	Tumor Regrowth Assay and Model Based Interpretation	236
9.3	Results	237
9.3.1	Inter-tumor and intra-tumor variation in photosensitizer uptake . . .	237
9.3.2	Inter-tumor variation in treatment response	238
9.3.3	Compensated PDT reduces the inter-tumor variation in treatment response	241
9.3.4	Comparison of treatment efficacy of PDT treatments	242
9.4	Discussion	245
9.5	Conclusions	252
IV	Conclusions	253
10	Conclusions	254

Bibliography

261

List of Figures

1.1	Jablonski Diagram.	4
1.2	Type I and Type II photo reactions.	5
1.3	Hematoporphyrin.	6
1.4	ALA and PpIX.	7
1.5	Phthalocyanines.	8
1.6	Chlorin e6 and Chlorin e ₆ derivative.	9
1.7	Verteporfin.	10
1.8	SnET ₂	10
1.9	<i>m</i> THPC.	11
1.10	HPPH.	12
1.11	Lutex	12
1.12	Methylene Blue and Nile Blue.	13

3.1	Three categories of liposomes.	34
3.2	<i>In vivo</i> behavior of three types of liposome delivery systems.	39
4.1	Histology images of orthotopic and subcutaneous tumors.	76
4.2	Comparison of tumor vasculature at two host-sites.	78
4.3	VEGF expression in two tumor host-sites.	79
4.4	Tumor oxygenation profile at two host-sites.	79
4.5	Orthotopic and subcutaneous tumor vascular permeability to Evans Blue. . .	81
4.6	Averaged effective permeability coefficients of two tumor types	82
4.7	Averaged effective interstitial diffusion coefficient of two tumor types . . .	83
4.8	Fluorescence images of verteporfin in orthotopic and subcutaneous MAT- LyLu tumors at 15 minutes or 3 hours after injection.	85
4.9	Effect of tumor host environment on verteporfin uptake.	86
5.1	Example finite element mesh.	108
5.2	BPD plasma pharmacokinetics.	112
5.3	Fluorescence images of subcutaneous and orthotopic tumors.	114
5.4	Intravascular and extravascular compartment segmentation.	115
5.5	Histogram of mean BPD fluorescence intensity in intravascular and ex- travascular spaces.	116

5.6	Averaged BPD fluorescence radial profile.	117
5.7	BPD fluorescence radial distribution for individual animals.	118
5.8	Histogram of regional effective permeability coefficient.	119
5.9	Simulation of BPD interstitial transport in orthotopic tumor.	121
5.10	Simulation of BPD interstitial transport in subcutaneous tumor.	122
5.11	Histogram of regional effective interstitial diffusion coefficients.	123
5.12	Correlation between intra-individual variability in transport parameters and mean fluorescence intensity.	125
5.13	Correlation between inter-individual variability in transport parameters and mean fluorescence intensity as measured by fluorescence microscopy. . . .	127
6.1	Flow cytometry histograms of BPD cellular uptake	151
6.2	Fluorescence images of BPD distribution at different time after administration	153
6.3	Co-registration of perfusion and diffusion images	155
6.4	Histogram of BPD fluorescence intensity and radial distribution profile . . .	156
6.5	Histograms of BPD fluorescence intensity analyzed from microscopy data. .	157
6.6	Histogram of BPD fluorescence intensity evaluated with fluorescence mi- croscopy.	160
7.1	Verteporfin plasma pharmacokinetics	178

7.2	Verteporfin tumor uptake evaluated by fluorescence microscopy.	180
7.3	Correlation between verteporfin uptake intra-tumor variability and inter-tumor variability analyzed from fluorescence microscopy	182
7.4	Verteporfin tumor uptake evaluated by the Aurora fluorometer.	184
7.5	Correlation between verteporfin intra-tumor variability and inter-tumor variability analyzed from the Aurora Fluorometer.	186
7.6	MAT-LyLu tumor growth dynamics and cPDT, vPDT control of tumor regrowth.	188
7.7	Correlation between normalized verteporfin plasma concentration and vPDT treatment response.	189
7.8	Correlation between verteporfin level and cellular targeting PDT treatment responses	190
7.9	Comparison of verteporfin concentration intra-tumor variation and inter-tumor variation.	197
8.1	BPD plasma pharmacokinetics.	212
8.2	Tumor vasculature geometry analysis.	213
8.3	Effects of SP on vascular permeability to Evans blue.	214
8.4	Average effective permeability coefficients before and after SP application. .	215
8.5	Verteporfin tumor uptake evaluated by the fluorescence microscopy.	218

8.6	Verteporfin tumor uptake evaluated by the Aurora fluorometer.	219
8.7	Blood flow changes after SP application recorded in MAT-LyLu tumors using a laser Doppler blood flow system.	220
8.8	Tumor volume changes in response to PDT treatments.	221
8.9	Individual growth dynamics for SP+PDT and PDT group.	228
9.1	BPD intra-tumor and inter-tumor variation.	239
9.2	MAT-LyLu tumor growth dynamics and NC-PDT control of tumor regrowth.	240
9.3	Intra-tumor and inter-tumor variation observed in treatment groups.	243
9.4	Tumor growth dynamics after compensated PDT treatments.	244
9.5	Coefficient of variation for tumor growth dynamics.	245
9.6	Treatment efficacy comparisons among different treatment groups.	246

List of Tables

1.1	Lists of photosensitizers.	14
2.1	Variability factors in cancer chemotherapy, radiation therapy and photodynamic therapy.	22
2.2	Variation in response to PDT.	22
3.1	Summary of photosensitizer-protein conjugates.	41
4.1	Role of tumor host microenvironment in pathophysiological and physical functions of tumor.	64
4.2	Comparison of tumor oxygenation at two host-sites.	80
4.3	Comparison of PDT efficacy at two host-sites.	87
5.1	Two-compartment model parameter estimations for individual animals . . .	111
6.1	Statistics analysis of histograms shown in Figure 6.5.	158

6.2	Statistics analysis of histograms shown in Figure 6.6	161
7.1	One compartment model parameter estimations.	178
7.2	Statistical analysis for histograms shown in Figure 7.2.	181
7.3	Statistics for histograms shown in Figure 7.4.	183
7.4	Tumor doubling time, growth delay and surviving fraction for CTRL, cPDT and vPDT groups.	187
8.1	Two-compartment model parameter estimations for SP treated animals and control animals.	212
9.1	Tumor doubling time, growth delay and surviving fraction.	241
9.2	Statistics analysis of tumor growth dynamics.	244

List of Acronyms

PDT	Photodynamic Therapy
PS	Photosensitizer
FDA	Food and Drug Administration
VFI	Verteporfin For Injection
BPD-MA	Benzoporphyrin Derivatives
AMD	Age-related Macular Degeneration
HpD	Hematoporphyrin Derivatives
ALA	5-Aminolevulinic Acid
PpIX	Protoporphyrin IX
Pc	Phthalocyanine
SnET2	Tin etiopupurin
<i>m</i> THPC	5,10,15,20-tetra(3-hydroxyphenyl)-2,3-dihydroporphyrin
CR	Complete Response
PR	Partial Response

NR	No Response
BCC	Basal-cell Carcinoma
SCC	Squamous-cell Carcinoma
ADME	Administration Distribution Metabolism Excretion
BSA	Bovine Serum Albumin
HSA	Human Serum Albumin
LDL	Low Density Lipoprotein
HDL	High Density Lipoprotein
VEGF	Endothelial Growth Factors
PDGF	Platelet-derived Growth Factors
TNF	Tumor Necrosis Factors
ECM	Extracellular Matrix
CT	Computed Tomography
MRI	Magnetic Resonance Imaging
FEM	Finite Element Method
LAPACK	Linear Algebra PACKage
SGEMM	Single precision GEneral Matrix Multiplication
SGBSV	Single precision General Band Simple driVer
PDE	Partial Differential Equation
ECM	Extracellular Matrix

SDS	Sodium Dodecyl Sulfate
PBS	Phosphate Buffered Saline
MAT-LyLu	Metastatic AT-Lymph Node and Lung
RIF-1	Radiation-Induced Fibrocarcinoma

Part I

Preliminaries

Chapter 1

Introduction to Photodynamic Therapy

Photodynamic therapy (PDT) is a new technique for treating cancer and other malignancies. After drug administration, photosensitizer molecules are preferentially accumulated in tumor cells and are retained by the tumor cells. Then ideally after a time, there is an optimal light treatment time when there is more photosensitizer in the tumor tissue than in the normal tissue. Photosensitizers are used because they absorb the electromagnetic energy, and eventually produce active free radicals that are toxic to cells [1–3]. If there is less photosensitizer in the normal tissue, then less reaction will occur in the normal adjacent tissue, and biological function of the adjacent tissue will be preserved because of a reduced photosensitization as compared to the diseased tissue.

1.1 Photochemical Physics of Photodynamic Therapy

The photochemical reaction that occurs in PDT can be depicted by a Jablonski diagram (Figure 1.1) [4]. Upon illumination, a photosensitizer molecule is excited from ground state S_0 to the first excited singlet state S_1 (Figure 1.1a). The photosensitizer can then relax back to the ground state by emitting a fluorescent photon (Figure 1.1b) or through non-radiative relaxation quenching processes (Figure 1.1c), or to an excited triplet state T_1 via intersystem crossing (Figure 1.1d). From the triplet excited state, the photosensitizer molecules can relax back to the ground state by emitting a phosphorescent photon (Figure 1.1e) or transferring energy to another molecule via collisional radiationless transition (1.1f). Additionally, excited photosensitizers can also lose energy through internal conversion.

In an oxygenated environment, the photosensitizers transfer their energy to ground-state oxygen molecules (3O_2) to produce singlet oxygen (1O_2). Photodynamic reaction of this kind is referred to as a Type II photo reaction, and it is characterized by a transfer of the triplet state photosensitizer energy to oxygen (Figure 1.2).

In an anoxic environment, the excited triplet photosensitizer ($^3PS^*$) can react directly with organic substrate (S) by electron exchange producing an oxidized substrate (S^+) and reduced photosensitizer (PS^-). In a hypoxic environment, the reduced photosensitizer (PS^-) can react with oxygen to produce superoxide anions (O_2^-), which can then form highly reactive hydroxyl radicals ($OH\cdot$). The excited photosensitizer ($^3PS^*$) can also react with super-oxidized radicals (O_2^*) to produce superoxide anion (O_2^-). These reactions

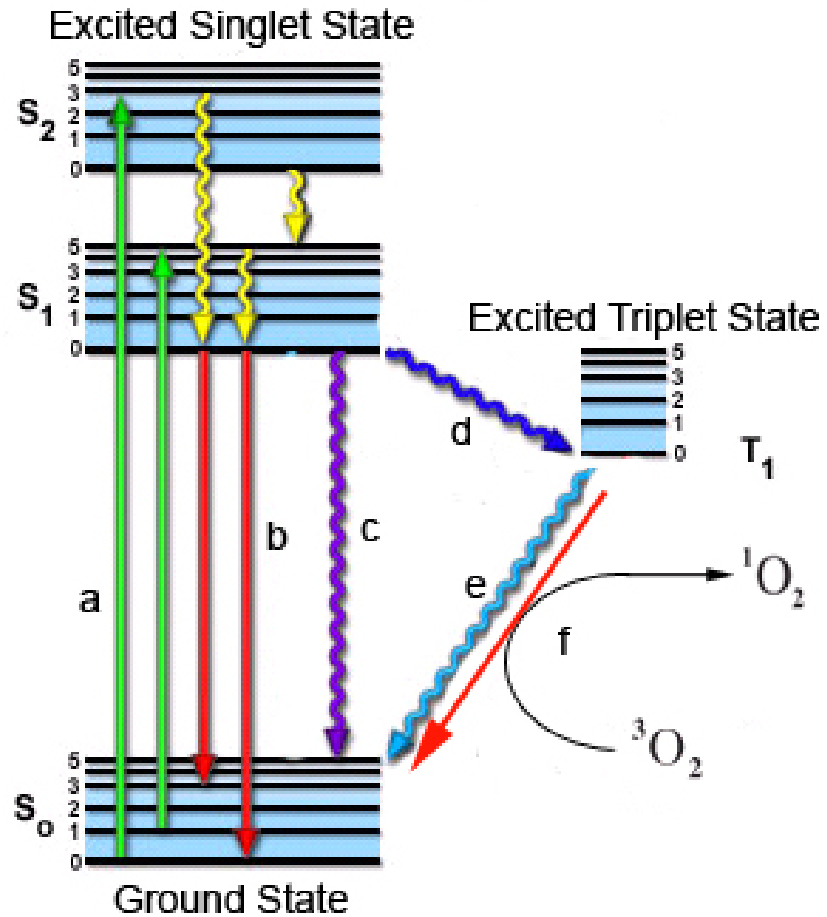


Figure 1.1: Jablonski Diagram showing the various models of excitation and relaxation in a chromophore: (a) Excitation; (b) fluorescence; (c) non-radioactive relaxation quenching process; (d) inter-system crossing; (e) phosphorescence; (f) collisional radiationless transition. Modified from <http://www.olympusmicro.com/primer/java/jablonski/jabintro/>.

are classified as Type I photo reactions and are characterized by a dependence on the target substrate concentration and no dependence upon oxygen (Figure 1.2) [2].

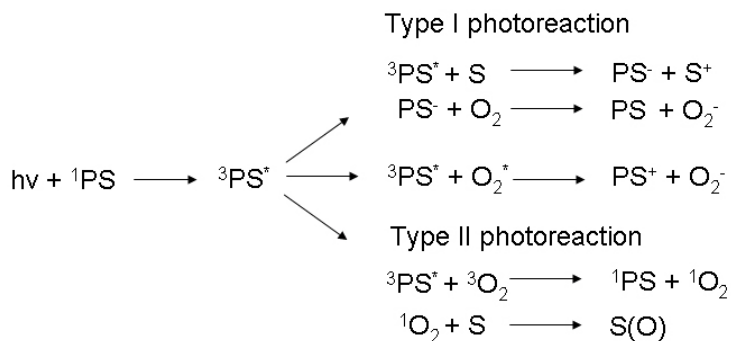


Figure 1.2: Type I and Type II photo reactions, where ${}^1\text{PS}$ is a photosensitizer in a singlet ground state, ${}^3\text{PS}^*$ is a photosensitizer in a triplet states, S is a substrate molecule, PS^- is reduced photosensitizer molecule, S^+ is an oxidized substrate molecule, O_2 is molecular oxygen, O_2^- is the superoxide anion, O_2^* is the superoxide radical, PS^+ is the oxidized photosensitizer, ${}^3\text{O}_2$ is triplet ground-state oxygen, ${}^1\text{O}_2$ is oxygen in a singlet excited state, and $\text{S}(\text{O})$ is an oxygen adduct of a substrate [2].

1.2 Photosensitizers

1.2.1 Porphyrin-related Photosensitizers

Porphyrin photosensitizers

The first generation photosensitizer was hematoporphyrin derivative (HpD), which was purified and commercialized as Photofrin. This is the most commonly used and studied photosensitizer to date. Photofrin is a mixture of compounds including hematoporphyrin monomers, dimers, and oligomers. Photofrin (Axcan Pharma, Montreal, Canada) is the

partial purification of the mixture. Photofrin received regulatory approval in Canada in 1993 and subsequently in U.S., Europe and Japan for a number of indications, such as cervical cancer, endobronchial cancer, esophageal cancer, bladder cancer and gastric cancer. Photofrin has a weak absorbance in the red region of the spectrum, with a relatively low extinction coefficient $\epsilon \approx 1,170 \text{ M}^{-1}\text{cm}^{-1}$ at 630 nm [5–7].

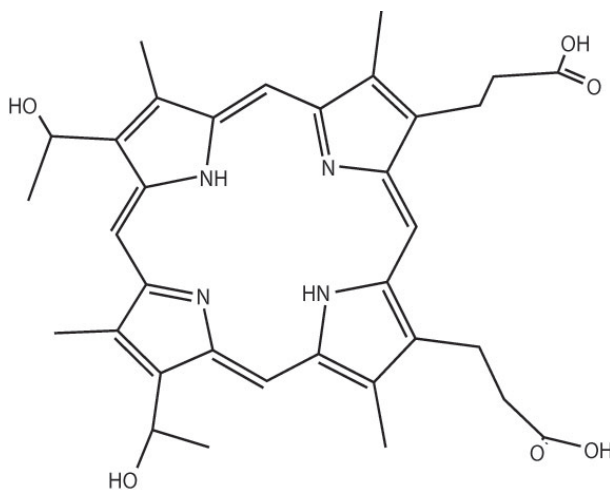


Figure 1.3: Hematoporphyrin [8].

5-Aminolevulinic Acid and protoporphyrin IX

5-Aminolevulinic Acid (ALA) is a naturally occurring amino acid that is a precursor to protoporphyrin IX. PpIX is converted into heme through the action of enzyme ferrochelatase. The exogenous administration of ALA forces the cells to produce PpIX faster than iron ferrochelatase can convert them into heme, then, PpIX accumulates in cells, allows a selective buildup of PpIX in tumor cells relative to normal cells. PpIX has a band I absorption maximum at 635 nm with extinction coefficient $\epsilon < 5,000 \text{ M}^{-1}\text{cm}^{-1}$. ALA induced PpIX

as a photosensitizer has been approved for the treatment of actinic keratosis and is being studied for treatment of basal cell carcinoma [9, 10].

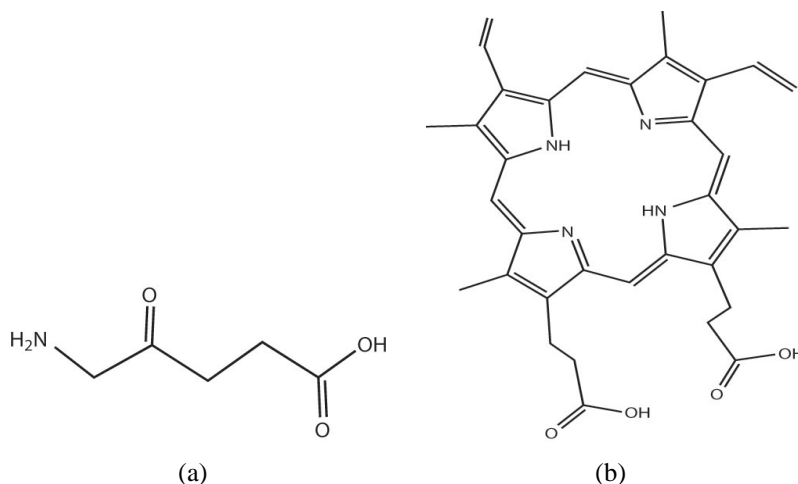


Figure 1.4: ALA (a) and PpIX (b) [10].

Phthalocyanines

Phthalocyanines absorb very strongly in the red region of the spectrum with absorption maxima in the 670 ~ 780 nm window and have a relatively high extinction coefficient $\epsilon > 100,000 \text{ M}^{-1}\text{cm}^{-1}$. Phthalocyanines can be made water soluble by addition of multiple sulfonation groups to the corners. Zinc, aluminum, and silicon phthalocyanine have been found useful for photodynamic therapy [11]. Silicon phthalocyanine Pc 4 is now undergoing clinical evaluation for cutaneous and subcutaneous lesions [12].

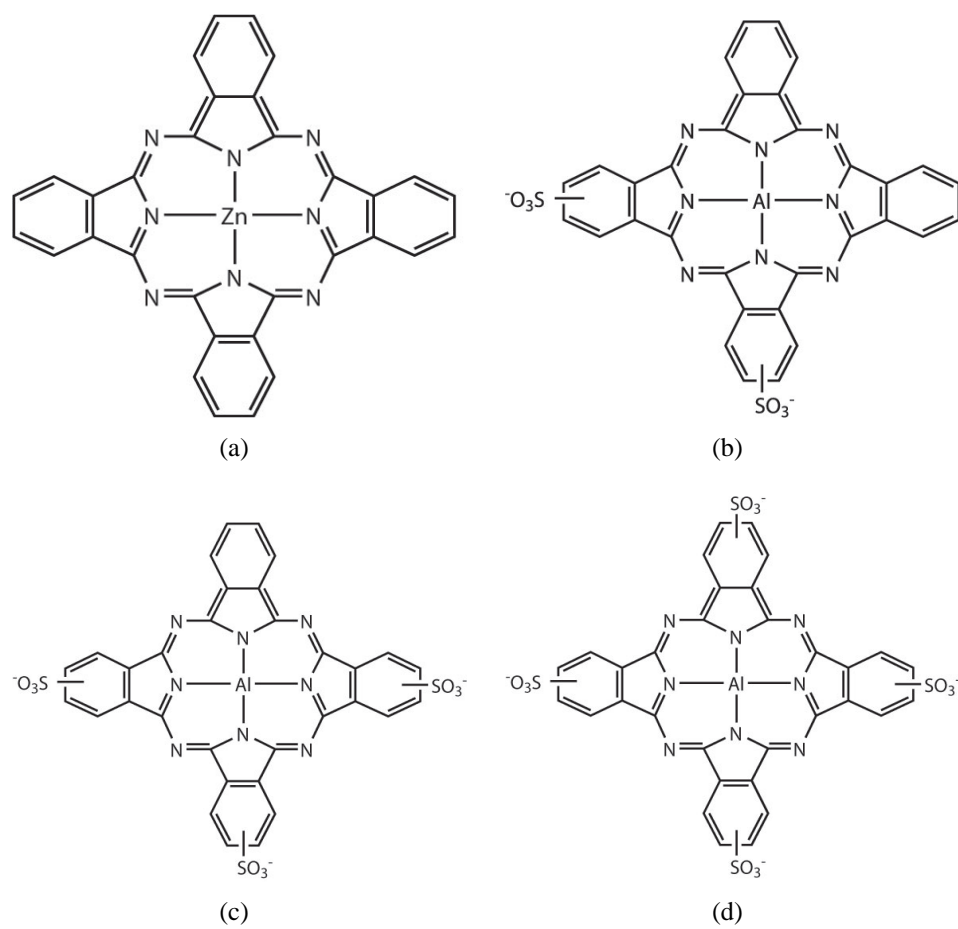


Figure 1.5: Phthalocyanines. (a) ZnPc; (b) AlPcS2; (c) AlPcS3; (d) AlPcS4 [8].

Chlorin and bacteriochlorin derivatives

Reduction of a pyrrole double bond on the porphyrin periphery gives the chlorin core, and further reduction of a second pyrrole double bond on the chlorin periphery gives bacteriochlorins. Both chlorin and bacteriochlorin have band I absorption maxima at longer wavelength $\lambda_{max} = 650 \sim 670$ nm for chlorin and $\lambda_{max} = 730 \sim 800$ nm for bacteriochlorin.

The first chlorin to be evaluated was the natural chlorin e_6 . Chlorin e_6 , which has a band I absorption maximum of 654 nm with extinction coefficient $\epsilon \approx 40,000 \text{ M}^{-1}\text{cm}^{-1}$. However, chlorin e_6 shows long-term skin photosensitivity and requires a high dose to be effective [13].

Bacteriochlorin derivatives have a band I absorption maxima between 737 and 805 nm, and show limited skin sensitivity [11].

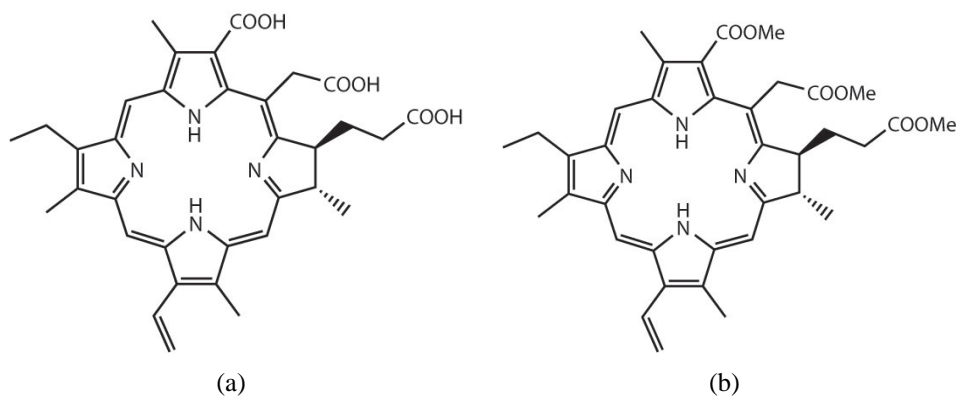


Figure 1.6: Chlorin e_6 (a) and Chlorin e_6 derivative (b) [8].

Benzoporphyrin derivatives (Verteporfin or Visudyne) have a band I absorption maximum at 689 nm and extinction of $\epsilon \approx 35,000 \text{ M}^{-1}\text{cm}^{-1}$. Verteporfin shows limited skin

sensitivity (3 ~ 5 days) and rapid clearance from tissues. Verteporfin is undergoing clinical trials for treatment of basal cell carcinoma, prostate. Verteporfin-for-injection has become the largest success in photodynamic therapy by becoming the recommended treatment for the wet form of age related macular degeneration (AMD) [14–16].

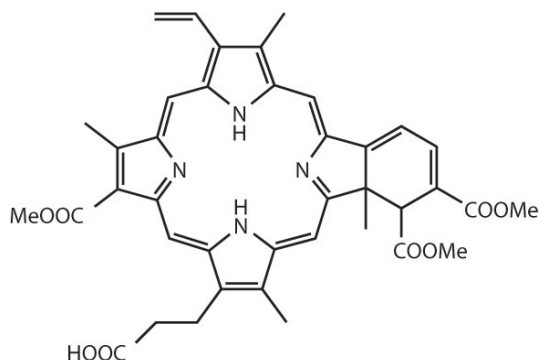


Figure 1.7: Verteporfin [8].

Tin etiopurpurin (SnET_2) is a metal chlorin derivative that is being evaluated for the treatment of cutaneous metastatic breast cancer and basal cell carcinoma, as well as age related macular degeneration. SnET_2 has a band I absorption maximum of 660 nm with $\epsilon \approx 28,000 \text{ M}^{-1} \text{ cm}^{-1}$. SnET_2 also shows long-term skin sensitivity and limits its general use .

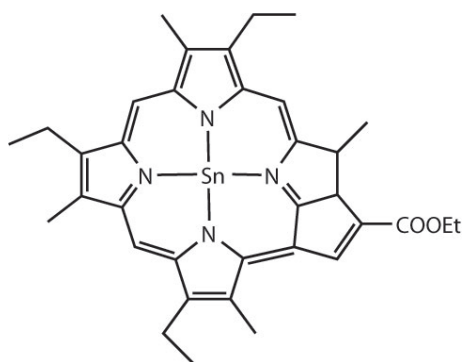


Figure 1.8: SnET_2 [8].

Tookad is another bacteriochlorin derivative, which has absorption maxima at 762 and 538 nm and shows very rapid clearance. Tookad is been evaluated as a photosensitizer for treatment of prostate cancer [17–23].

Synthetic chlorin 5,10,15,20-tetra(3-hydroxyphenyl)-2,3-dihydroporphyrin (*m*THPC) (Foscan, Biolitec Pharma, Scotland, U.K.) has been approved in Europe for use against head and neck, prostate, and pancreatic tumors. *m*THPC has a band I absorption maximum at 652 nm with extinction coefficient $\epsilon \approx 30,000 \text{ M}^{-1}\text{cm}^{-1}$. Unlike many other photosensitizers, *m*THPC, does not have the mitochondria as its primary target. Instead, Golgi apparatus and endoplasmic reticulum are thought to be inactivated by *m*THPC. However, *m*THPC shows up to six weeks of skin sensitivity, and this may limit its clinical usage [24–28].

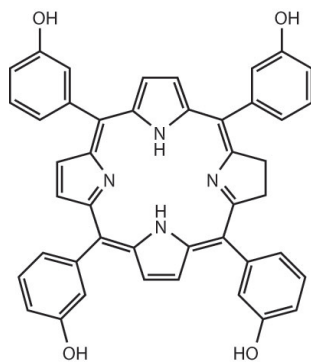


Figure 1.9: *m*THPC [8].

HPPH is another chlorin type photosensitizer proved to be potent in PDT. The synthetic chlorin derivative HPPH (Photochlor) has a band I absorption maximum at 665 nm and extinction coefficient $\epsilon \approx 47,500 \text{ M}^{-1}\text{cm}^{-1}$ [29–33].

1.2.2 Non-porphyrin Photosensitizers

Methylene blue and Nile blue

The phenothiazinium dye methylene blue has been used as a photosensitizer ($\lambda_{max} = 620 \text{ nm}$) for the inactivation of various pathogens contained in blood plasma.

Benzophenothiazines (Nile Blues) absorb light in the 600 ~ 650 nm window, and produce $^1\text{O}_2$ efficiently. Nile blues are reported to accumulate in the lysosomes of cancer cells.

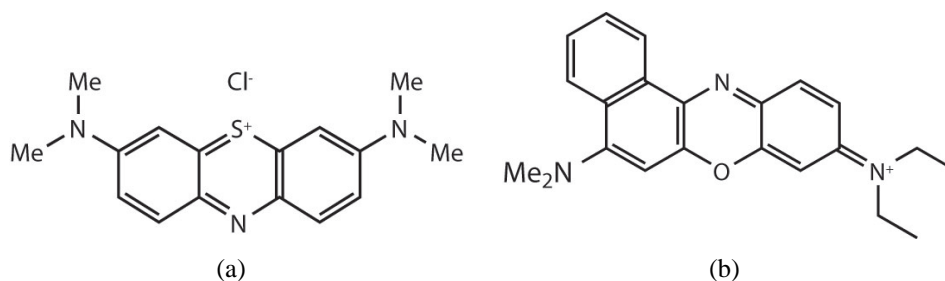


Figure 1.12: Methylene Blue (a) and Nile Blue (b) [3].

1.3 Biology of Photodynamic Therapy

1.3.1 Cellular Targeting Mechanism

Nuclear DNA is believed to be the primary target in radiation therapy for cell killing, with double-strand breaks being the principle mechanism of damage. DNA damage induced by PDT has also been shown in number of *in vitro* studies, although this is not widely recognized to be the main mechanism of tissue destruction. Direct DNA damage such as

	Photosensitizer	Commercial name	Wavelength (nm)	ϵ ($M^{-1} cm^{-1}$)	Hydrophobicity	
Porphyrin	HpD	Photofrin/Porfimer Sodium	630	1,170	hydrophobic	
	TPP		630	18,900	hydrophobic	
	TPPS4				hydrophilic	
Protoporphyrin	ALA-Protoporphyrin IX	Levulan/Metvix/Benzvix/Hexvix	635	5,000	hydrophilic	
Phthalocyanines	ZnPc	CGP55847	675	243,00	hydrophobic	
	AlPcS2				hydrophilic	
	AlPcS3				hydrophilic	
	AlPcS4				hydrophilic	
	Phthalocyanine-4				Pc 4	670
Chlorin	Ce6	Verteporfin/Visudyne	654	40,000	hydrophobic	
	BPD		690	35,000	hydrophobic	
	SnET ₂		Purlytin	660	28,000	hydrophobic
	Bacteriochlorin Derivative		Tookad	762, 538	108,600	hydrophobic
	<i>m</i> THPC		Temoporfin/Foscan	652	30,000	hydrophobic
	HPPH		Photochlor	665	47,500	hydrophobic
	Lutetium texaphyrin		Lutex/Lutrin/Antrin/Optrin	732	42,000	hydrophilic
	Methylene Blue		Methylene Blue	620	95,000	hydrophilic

Table 1.1: Lists of photosensitizers and fundamental clinical characteristics of the photosensitizers used in clinical and preclinical trials [45].

single-/double-strand breaks through attack at uracil and thymine sites and guanine moiety modification were demonstrated as increased levels of DNA-DNA and DNA-protein cross-links after PDT. Indirect DNA damage is through the deactivation of DNA repair enzymes which are extremely sensitive to singlet oxygen and other free radicals generated during PDT. This has been demonstrated by Boegheim *et al.*, showing inhibited DNA-damage repair mechanisms in haematoporphyrin PDT of murine L929 fibroblasts cells. However, there is very little uptake of lipophilic photosensitizers within the nucleus, as a consequence of which DNA is not directly subjected to PDT induced photo-damage.

Fluorescence microscopy studies showed hydrophilic photosensitizers accumulate to lysosomes, implicating that lysosomes might be a primary target in PDT [2, 46]. Geze *et*

al., suggested that following the disruption of lysosomes, hydrolases and other hydrolytic enzymes leak out of the damaged lysosomes and may cause necrotic cell death [47]. In contrast, Moan *et al.* suggested that lysosomes can be reservoirs for some photosensitizers, such that when targeted in PDT treatment [48–50]. Upon light radiation, lysosomes break and release the remaining photosensitizer, and this photosensitizer re-localizes to PDT targeting organelles such as mitochondria, causing further damage during the treatment time. This has been demonstrated and further exploited for photodynamic delivery of other molecules contained in micelles.

Hydrophobic anionic photosensitizers preferentially attach to the plasma and cellular membranes, *e.g.*, mitochondria and nuclear membranes [2, 46]. Membrane damage caused by PDT is introduced through the oxidation of unsaturated fatty acid residues and cholesterol, or through inactivation of membrane bound enzymes. In addition, this membrane damage is associated with the release of inflammatory and immune mediators, which initiate cascades of events responsible for immune effects against tumor cells.

1.3.2 Vascular Targeting Mechanism

The viability of tumor cells requires a functioning vascular network to provide oxygen and other nutrients and also to remove toxic waste products associated with cellular metabolism. It has been widely accepted that no solid tumor can grow larger than a critical size of 1 mm^3 without developing a blood supply network [51–53]. Targeting tumor vasculature is there-

fore one promising approach to cancer treatment. There have been a number of reports of PDT causing microvascular collapse [54–56], leading to severe tissue hypoxia and anoxia [57–59].

Vascular targeting PDT was first demonstrated by Henderson *et al.* in 1989 using photosensitizer Photofrin in a fibrosarcoma mouse model, where they showed Photofrin induced vascular shutdown, limiting the oxygen and nutrients supply to the tumor [60]. This PDT vascular effect was further examined by Fingar *et al.*, who treated tumor bearing animals within minutes of injection of Photofrin, to restrict the extravasation of photosensitizers and confine the photodynamic damage to the tumor vasculature. They observed pockets of necrosis regions remote from the damaged vessels [61]. Preclinical *in vivo* PDT studies with photosensitizer MV6401 (pyropheophorbide derivative, Miravant Medical Technologies, Santa Barbara, CA), showed a two-step vascular response following PDT treatment. The first phase response was acute, characterized by vasoconstriction. After three hours, the second chronic phase was characterized by thrombus formation. These vascular effects were associated with a delay in tumor growth [62].

In addition, Korbelik *et al.* reported that vascular destruction observed after PDT is similar to the inflammatory response observed after tissue injury or infection [63]. Endothelial cells normally produce a balance of vasoactive and vasoconstrictive substances that maintain a healthy vascular network [64]. When vascular targeting PDT exposes the basement membrane to the blood serum, cascade effects will occur and tip the balance to-

ward vasoconstriction [65]. Platelets and neutrophils adhere to the vessel wall, roll toward the constriction, aggregate and migrate to the surrounding tissue following the chemokine gradients [66].

The mechanism underlying the vascular effects of PDT differ greatly with different photosensitizers. Photofrin PDT leads to vessel constriction, vessel leakage, leukocyte adhesion and thrombus formation, all apparently linked to platelet activation and release of thromboxane [55, 67]. PDT with phthalocyanine causes primarily vascular leakage [68], and PDT with chlorin e_6 results in blood flow stasis primarily because of platelet aggregation [69].

1.3.3 Immune Effects

Although it is not completely understood, researchers have reported that PDT can activate or suppress the immune system, depending on the factors of the treatment regime. PDT treatment seems to alter the balance of agents that regulate the immune system and appears to be able to tip it toward activation or suppression of by release of specific cytokines.

PDT induced damage in membranes of cell (endothelial or tumor cell) or cellular organelles can trigger a cascade event, including enhanced expression of stress proteins, activation of apoptosis genes and upregulation of some cytokine genes [70]. Damage of cellular membranes also prompts a rapid activation of phospholipases leading to accelerated phospholipid degradation with massive release of lipid debris, and metabolites of

arachidonic acids which are powerful inflammatory mediators [2, 63, 71]. Another source of inflammation signaling relates to PDT induced vascular damage. Endothelial cells will contract and expose the basement membrane in the vessel wall. This is followed by rapid attachment of circulating neutrophils and platelets, leading to a progressive impairment of vascular function as well as a massive release of various inflammatory mediators [72].

A strong inflammatory reaction is a central event in the PDT induced tumor destruction. In the inflammatory process, a wide variety of potent mediators are released, including vasoactive substances, components of the complement and clotting cascades, acute phase proteins, proteinase, peroxidase, radicals, leukocyte chemoattractants, cytokines, growth factors and other immune regulators [2, 71, 72].

The release of inflammation mediators after PDT initiates recruitment of leukocytes from circulatory system and amplifies their activity. A massive invasion of neutrophils, mast cells, and monocytes/macrophages during and after PDT treatment has been reported in several animal studies [73, 74]. Neutrophils have profound impact on PDT mediated destruction of tumor tissues. In the tumor blood stream, neutrophils are key contributors to the infliction of endothelial damage. PDT induced endothelial cell contraction allows these neutrophils to extravasate in tumor interstitium, where neutrophils engage the destruction of tumor parenchyma. Toxic free radicals and myeloperoxidases are liberated through the degranulation of neutrophils. Chemotactic substances are also released by neutrophils attracting another wave of invasion of immune cells. Monocytes/macrophages are another

class of nonspecific immune cells activated by PDT. Macrophages were documented to release TNF- α following PDT and to preferentially recognize PDT treated tumor cells as their targets [2, 75, 76].

These nonspecific immune development processes may trigger tumor specific immune reactions. For example, tumor associated macrophages are prompted to phagocytize large numbers of PDT killed or damaged tumor cells. Antigen presenting cells will process tumor specific peptides and present them on the cell membrane. Tumor antigens will be recognized by helper T lymphocytes directed by the intensive inflammatory signals leading to fully developed tumor immunity [2].

All these factors add together to make the photochemical and photobiological effects of PDT to be fairly complex, and perhaps even more complex than in other therapies such as chemotherapy or radiation therapy. Even the change of photosensitizer or timing of delivery of light can affect the biochemical damage which occurs. Thus, the remainder of this thesis focuses on some specific mechanistic events which can occur in photodynamic therapy with verteporfin.

Chapter 2

Motivation, Specific Aims and Thesis

Overview

2.1 Motivation and Specific Aims

2.1.1 Patient Variation in Response to PDT

Photodynamic therapy can be viewed as a dual stage treatment modality. It contains similar processes to chemotherapy, *e.g.* with drug administration, drug absorption, drug distribution, drug metabolism and drug excretion, and similar to the process in radiation therapy, *e.g.* delivery of photons to the lesion. The benefit of PDT is mainly the dual selectivity: the preferential accumulation of photosensitizers and selective absorption of photons in the lesion area. However, this dual selectivity mechanism also leads to a dual complexity for

PDT treatment. The treatment resistance problems observed in chemotherapy and radiation therapy are also observed in some PDT treatments. For example, intermittent blood flow in tumor has been shown to be a major treatment resistance factor in radiation treatment because of the noncontinuous supply of oxygen inducing transient tumor hypoxia. Intermittent blood flow is also a factor that limits chemotherapy drug delivery. Tumor cells in poorly perfused areas always exhibit less drug uptake, and will survive and eventually regrow after the treatment. In PDT treatment, the effects of intermittent blood flow are two-fold: first, photosensitizer is not well delivered in the regions of poorly perfused areas; second, tumor cells in transient hypoxia areas cannot produce sufficient photochemical reaction to kill the tissue. Therefore, tumor cells surrounding nonconstant blood flow regions demonstrate more resistance to the PDT treatment, and will tend to regrow after the PDT treatment and cause failure of treatment. Other variability factors in these three treatment modalities are listed in Table 2.1.

Unfortunately, current clinical photodynamic therapy treatment plans are largely based on empirical escalation trials without much attention paid to the individual variation in photosensitizer pharmacokinetics and absorbed light doses between patients. The translation of advances in photodynamic therapy to clinical applications can be complicated by these inter-individual and intra-individual variation which can result in unpredicted toxicity or highly variable treatment efficacy, Table 2.2 [77].

	Chemotherapy		Photodynamic therapy		Radiation therapy	
	Process	Variability factors	Process	Variability factors	Process	Variability factors
Systemic level	administration	medication error patient compliance nursing error	administration	medication error patient compliance nursing error		
	absorption distribution metabolism excretion	serum protein level hepatic function renal function	absorption distribution metabolism excretion	serum protein level hepatic function renal function		
Tumor level	distribution	tumor vasculature intermittent blood flow transvascular transport interstitial transport lymphatic transport receptor function	distribution	tumor vasculature intermittent blood flow transvascular transport interstitial transport lymphatic transport receptor function	photon distribution oxygenation	tumor geometry intermittent blood flow
	cellular uptake cellular retention		cellular uptake cellular retention		photon distribution oxygenation	tumor geometry intermittent blood flow

Table 2.1: Variability factors in cancer chemotherapy, radiation therapy and photodynamic therapy.

Photosensitizer	Tumor Sites	Patients	Main Results	Ref
Photofrin	Barret's mucosa	100	Conversion of 75-80% to normal squamous epithelium in all patients Dysplasia eliminated in 78 patients, eliminated 10 of 13 tumors.	[78]
Foscan	Oral cancer	20	6 of 6 T3 lesions, 3 of 6 T4 lesions, and 9 of 14 T1/T2 cleared after single treatment.	[26]
Photofrin	Refractory transition-cell carcinoma of bladder	36	58% CR at 3 months; 10 of 21 with CR had recurrence at mean follow-up of 12 months.	[79]
Photofrin	Refractory carcinoma-in-situ of bladder	34	74% CR at 3 months; recurrence at 2 years in 14 of 18 CR follow-up 10 of 34 alive at 64 months mean follow-up.	[80]
Photofrin	BBC of skin	37	88% CR, 12% PR, 10% recurrence at 1 year	[81]
Topical ALA	BBC of skin	80	90% CR, 7.5% PR	[10]
Topical ALA	Bowen's disease	36	89% CR at median follow-up, 9% recurrence after 18 months	[82]
Photofrin	Chest wall recurrence breast cancer	20	20% CR, 45% PR, 35% NR	[83]
Photofrin	Oral cavity	41	87% CR, 13% PR, 25% recurrence over 5-53 months	[84]
Foscan	Oral cavity SCC	96	58% CR, 11% PR	[77]
Photofrin	Malignant pleural mesothelioma	31	Median survival 12 months	[85]
Photofrin	Cutaneous tumors	50	52% CR	[86]

Table 2.2: Variation in response to PDT. CR = complete response; PR = partial response; NR = no response; BBC = basal-cell carcinoma; SCC = squamous-cell carcinoma. Modified from [87].

2.1.2 Photon Distribution

Recently, considerable attention has been paid to the development of a light dosimeter, mainly because most of clinical PDT treatments are performed in radiation oncology departments, where the knowledge of radiation treatment planning based on patient anatomy information is more advanced and well-developed by professional medical physicists.

Current light dosimetry in PDT focuses on the following two issues:

1. Heterogeneous photon distribution in the tissue due to irregular geometry. Light distribution in cylindrical and spherical geometries (Overdosing and underdosing due to heterogeneous light distribution).
2. Heterogenous photon distribution due to heterogeneous optical properties of biological tissues. (Inter-patient and intra-patient variation in optical properties).

2.1.3 Photosensitizer Pharmacokinetics

Photosensitizer pharmacokinetics has been extensively investigated in both animal studies and clinical studies. Novel techniques in fluorescence spectroscopy enabled researchers and radiation oncologists to dynamically monitor the photosensitizer concentration in real time. However most of these studies focus on the dynamic change of the photosensitizer distribution in both normal and neoplastic tissues, and the goals of these studies are mainly developing optimal treatment protocols such that the treatment can most effectively kill

the tumor cells and spare the normal tissues. Most recently, a few investigators have reported that there exists large variation in photosensitizer uptake between patients for the same prescribed photosensitizer dose [88]. What are the sources of photosensitizer pharmacokinetics inter-individual variation? How does this variation affect the PDT treatment and how can this variation be reduced? These issues have had comparatively investigation devoted to them. The goal of this study is to identify the potential sources of photosensitizer pharmacokinetic variability during each of these steps, and seek strategies to reduce the variability, and individualize PDT treatments.

2.1.4 Specific Aims

How can the treatment efficacy variability of PDT be reduced and, at the same time, obtain maximum effect? This will require knowledge of the following:

1. Identification of potential sources of variability
2. Mathematical modeling of individual and population pharmacokinetics
3. Correlation between pharmacokinetics and the treatment outcome
4. Possible modulation of the drug pharmacokinetics
5. Development of strategies that will tailor doses to individual patients

We pursue the answers to the above questions at both the microscopic level (temporal and spatial dynamics inside the tumor) and the macroscopic level (systemic level).

At the microscopic level, the goals are (1) to analyze the microscopic heterogeneity of photosensitizer distribution, namely, to develop a fundamental understanding of the vascular and interstitial barriers to the delivery of photosensitizer molecules to solid tumors, their contribution to the inter-individual variability; (2) to formulate and test new strategies to overcome the physiological barriers, and reduce the photosensitizer pharmacokinetic variation. Specifically, investigate strategies to modulate photosensitizer transvascular transport to increase the photosensitizer tumor uptake and reduce the distribution heterogeneity.

At the macroscopic level, the goals are: (1) to quantify and analyze the macroscopic variation of photosensitizer uptake, namely, to correlate the variation at macroscopic level to microscopic heterogeneity, and to develop non-invasive photosensitizer dosimeter to monitor these variation; and (2) to establish a photosensitizer dosimetry-controlled PDT protocol based on photosensitizer macroscopic sampling technique to reduce the inter-individual variation in treatment response to PDT.

These goals are achieved using three approaches in this research:

1. A microscopic approach to directly visualize the tumor pathophysiological functions and photosensitizer dynamics.
2. A macroscopic approach using macro-sampling techniques to monitor photosensitizer uptake dynamics.
3. Mathematical modeling to integrate existing data and to guide the experimental stud-

ies.

2.2 Thesis Overview

This thesis is, the author believes, the first publication to propose the concept of photodynamic therapy treatment individualization. This thesis has four parts.

Part I is the introduction. The theories and mechanisms in photodynamic therapy are laid out here, and an introduction to the motivations, specific aims and rationales of this project are stated.

Chapter 1 provides a introduction to the current status of photodynamic therapy with emphasis on prostate PDT treatment.

Chapter 2 is a presentation of the motivations for this project, with specific aims and illustration of the rationale for design of the experiments.

Part II of the thesis presents a series of investigations to identify the potential sources of photosensitizer pharmacokinetic variability. A review of photosensitizer quantification technologies is also presented.

Chapter 3 is a review of each step in photosensitizer pharmacokinetics, *e.g.*, routes of administration, systemic distribution in circulatory system, distribution in tumor vasculature, transport across vessel wall, transport through tumor interstitium and finally metabolism/destruction and excretion. Factors that cause pharmacokinetic variability in each of these steps are also

discussed.

Chapter 4 is a comparison of the tumor micro-environment, photosensitizer pharmacokinetics and transport processes. The model system of a single tumor type inoculated in two host-sites is used. The orthotopic and subcutaneous locations illustrate how these factors affect PDT treatment outcome. This chapter emphasizes how transport parameters can affect verteporfin pharmacokinetics, and they influence the tumor response to cellular and vascular targeting PDT treatments.

Chapter 5 reports on analysis of the intra-individual and inter-individual variabilities in verteporfin transport processes and examination of correlation between these transport parameters and verteporfin pharmacokinetic variability.

Chapter 6 is a review of the current photosensitizer quantification technologies and discussion of the effects of sampling volume upon evaluation of photosensitizer distribution.

Part III of the thesis summarizes efforts to develop strategies to individualize PDT treatment.

Chapter 7 is an illustration of the correlation between intra-tumor variation and inter-tumor variation in photosensitizer levels, and a study of the correlation between photosensitizer pharmacokinetics and PDT treatment outcome. This chapter provides clues to the question of how to individualize PDT treatment in the planning process.

Chapter 8 is a discussion of the effects of inflammatory mediators such as Substance P on modulation of photosensitizer pharmacokinetics, and efficacy/individual variability of

PDT treatment.

Chapter 9 provides strategies to compensate the photosensitizer pharmacokinetic variability at macroscopic scale, namely, PDT treatment planning based on photosensitizer dosimetry information.

Part IV is the conclusion of this investigation and discuss the future directions of PDT treatment individualization.

Chapter 10 includes conclusions and future directions for this project and summarizes publications produced from this project along with the significance of each.

Part II

Quantification of Photosensitizer

Pharmacokinetic Variability

Chapter 3

Origins of Photosensitizer

Pharmacokinetic Variability

As discussed in Chapter 1 and 2, most patients in clinical PDT studies with a particular diagnosis are assumed to be identical in terms of the dosage to be delivered, and follow a pre-prescribed protocol. However, factors such as age, gender, race, organ function and tumor microenvironment can alter the pharmacokinetics of photosensitizers delivered in drug vehicles. This chapter will outline the potential sources of photosensitizer pharmacokinetic variability. Most photosensitizers are transported throughout the circulatory system and, except for vascular targeting PDT, end up within the parenchyma of the tissues and organs where their presence is beneficial (i.e. those tissues to be treated) and also in some areas where their presence may be detrimental. In the following sections, we will discuss the

consecutive steps of photosensitizer Administration, Distribution, Metabolism/Destruction and Excretion (ADME).

3.1 Photosensitizer Delivery with Liposomes

First-generation photosensitizers, represented by Photofrin, suffer from several drawbacks [2, 89]:

1. They are complex mixture of several partially unidentified porphyrins and they show poor selectivity in terms of tumor tissue/normal tissue ratios.
2. They have low extinction coefficients, and require relatively large amount of administration to obtain a satisfactory PDT therapeutic response.
3. They have absorption maximum at a relatively short wavelengths (630 nm) leading to a poor tissue penetration of light.
4. They present high accumulation rate in skin, lasting for up to 6-8 weeks after PDT treatment.

The problems encountered with these first-generation photosensitizers have led to the development of new photo-active molecules, the second generation photosensitizers such as porphyrin derivatives, phthalocyanines and chlorins. These photosensitizers can be made relatively pure and well-characterized. They are more effective at generating singlet oxygen

and have a stronger absorption in the range of 650-800 nm, where the light can penetrate to deeper tissue. They have high selectivity for diseased tissue, and relatively rapid elimination, therefore providing high therapeutic ratios [2, 3, 90]. Another important feature of these second generation photosensitizers is their hydrophobic property. Most of second generation photosensitizers are hydrophobic, this is a desired feature when the preferential accumulation in cellular hydrophobic loci is required, since these photosensitizer molecules must be able cross the cell lipid membrane [3, 8, 91, 92]. However, due to their poor solubility in water, intravenous administration of photosensitizer is greatly hampered. Thus, it is necessary to develop suitable delivery systems to effectively deliver the photosensitizer. Thus to improve tumor targeting and to reduce side effects. During the continuous search for photosensitizer delivery systems, liposomes with their high loading capacity and their flexibility to accommodate photosensitizer physicochemical properties, have received a lot of attention as a valuable carrier for variety of photosensitizers [29, 91].

The history of liposomes can trace back to the pioneer observation of Alec Bangham roughly 40 years ago, that phospholipid in aqueous systems can form closed bi-layered structures. Since then, liposomes have moved a long way from being just an exotic biophysical research to a pharmaceutical carrier for numerous practical applications [93, 94]. Liposomes are spherical, self-closed structures formed by one or several concentric lipid bi-layers with an aqueous phase inside and between the lipid bi-layers [94, 95].

These liposome carriers can be classified into three categories (Figure 3.1):

1. Conventional liposomes (Figure 3.1(a))
2. Passive targeting liposomes (Figure 3.1(b))
3. Active targeting liposomes (Figure 3.1(c), 3.1(d))

3.1.1 Conventional Liposomes

Conventional liposomes are used as the means to solubilize and formulate the both hydrophilic and highly hydrophobic photosensitizers for intravenous administration rather than using them to enhance tumor delivery of photosensitizers. Many second generation photosensitizers are designed to be water insoluble (hydrophobic), specifically because these hydrophobic photosensitizers are incorporated rapidly into the liposomal membrane (Figure 3.1(a) a), *e.g.*, BPD-MA, ZnPc. Water soluble (hydrophilic) photosensitizers, on the other hand, can be entrapped into the aqueous liposome interior (Figure 3.1(a) b), *e.g.*, ALPcS4.

After liposomal formulated photosensitizers enter into the blood stream, lipid exchange between liposomes and lipoproteins leads to an irreversible disintegration of the liposomes. The released photosensitizers in the blood stream subsequently associate with albumin, lipoproteins (both high and low density lipoproteins (HDLs, LDLs)) and other serum proteins, Figure 3.2 a2. As well, liposomal photosensitizers can be opsonized by serum proteins, and then taken up by the mononuclear phagocyte system (MPS), Figure 3.2 a1, [91].

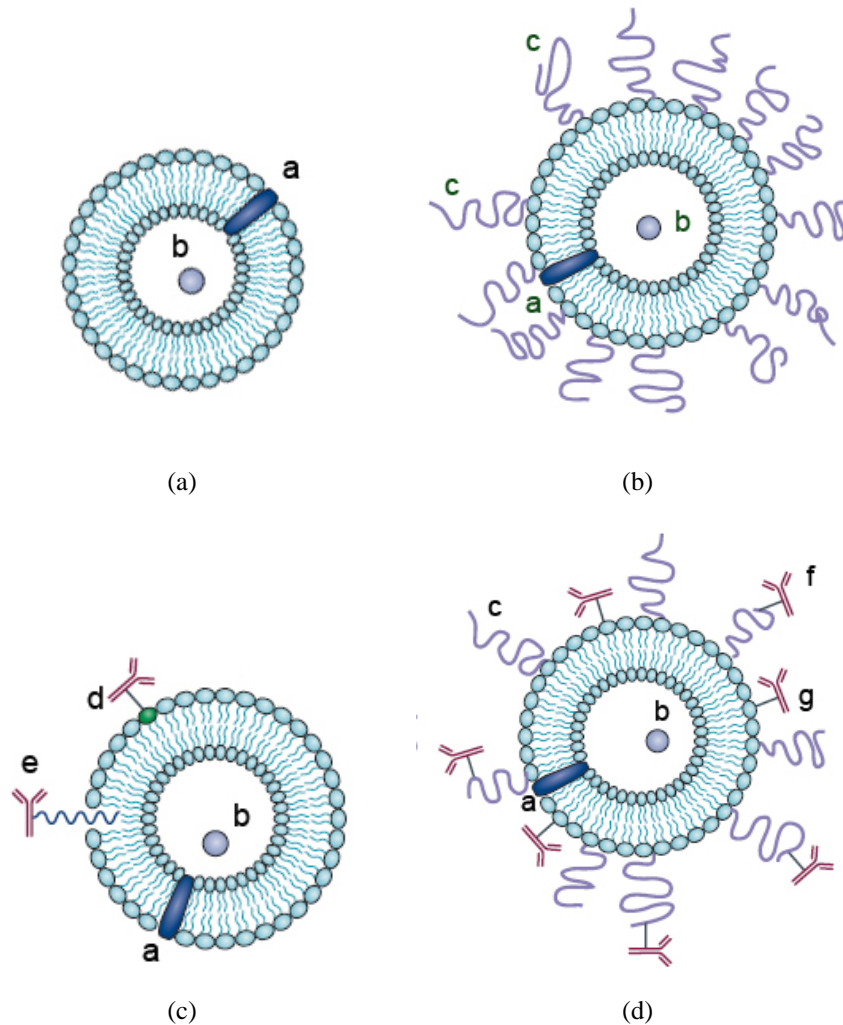


Figure 3.1: Three categories of liposomes. (a) early conventional liposomes with water insoluble photosensitizer **a** entrapped into the aqueous liposomes interior, and water soluble photosensitizer **b** incorporated into the liposomal membrane; (b) long-circulating liposomes grafted with a protective polymer **c**, such as PEG, which shields the liposome surface from the interaction with opsonizing proteins; (c) antibody-targeted immunoliposome with antibody covalently coupled **d** to the reactive phospholipids in the membrane or hydrophobically anchored **e** into the liposomal membrane after preliminary modification with a hydrophobic moiety; (d) long-circulating immunoliposomes simultaneously bearing both protective polymer and antibody, which can be attached to the liposome surface **g**, or preferably, to the distal end of the grafted polymeric chain. Modified from [94].

These two phenomena account for the very short plasma half-life (minutes) for most of the liposome photosensitizers. Of importance, since most of tumor cells are reported to express an elevated number of LDL-receptors on the cell membrane due to the rapid proliferation, the association with LDL might enhance the photosensitizer uptake by LDL-receptor mediated endocytosis. This process is illustrated in Figure 3.2 a3, [29, 91].

A significant amount of preclinical and clinical PDT has been done using liposomal formulations, and the following chapters will focus on the pharmacokinetics of photosensitizers of this kind, using Verteporfin-For-Injection as the main topic of study.

3.1.2 Passive Targeting Liposomes

Clinical applications of conventional liposomes have been limited due to the propensity of the MPS to rapidly remove these particles from the bloodstream. As a result, the uptake of these liposomes by tumor tissue is always found insufficient. Passive targeting liposomes are designed to be rendered 'invisible' for serum proteins and MPS so that these liposomes can be selectively extravasated, accumulated and retained in tumor tissues. Provided that they circulate sufficiently long, the 'enhanced permeability and retention (EPR)' effect [96–98] allows liposomes to passively accumulate in tumor tissue in high concentration.

The uptake of liposomes by phagocytic cells is prompted by the opsonization process, during which the opsonin make the liposomes more susceptible to phagocytosis [99]. *In vivo* studies revealed that the opsonization depends on the physicochemical properties of

the liposomes such as hydrophobicity, charge, size and fluidity of the liposome surface [100]. Generally speaking, the adsorption of opsonin is favored onto hydrophobic rather than hydrophilic surfaces so that the hydrophobic molecules are rapidly scavenged. Different methods have been suggested to achieve long circulation of liposomes *in vivo*, including coating the liposome surface with inert, bio-compatible polymers, such as polyethylene glycol (PEG), which forms a protective hydrophilic layer over the liposome surface and slows down liposome recognition by opsonin and therefore prolongs the circulation half-life to the order of tens of hours [101, 102](Figure 3.1(b)).

However, these long circulating passive targeting liposomes do not effectively interact with cells. The extravasated liposomes accumulate in the tumor interstitial space but cannot effectively transfer the photosensitizers to the tumor cells. This is illustrated in Figure 3.2 b. Gijssen, *et al.*, demonstrated that Stealth[®] liposomes containing hydrophilic photosensitizer ALPcS4 did not display any *in vitro* photocytotoxicity activity in the malignant cells, whereas the free ALPcS4 did [103]. This is explained by Gijssen that the hydrophilic ALPcS4 retains tightly in the liposomal formulation, and since the liposomes have limited interaction with cells, the photosensitizer uptake is therefore limited. On the contrary, the hydrophobic photosensitizer, BPD-MA, when incorporated into glucuronide-modified liposomes (PGlcUA-liposomes), was found more photo-toxic to subcutaneous sarcoma. In that study, Oku, *et al.*, demonstrated PGlcUA-liposomal BPD-MA exhibited a significant tumor regression and 80% cure rate compared with the 20% cure rate with conventional

formulated liposomal(DPPG-liposomes) BPD-MA [104]. This is probably due to the fact that after a prolonged accumulation in the tumor interstitial space, a certain amount of hydrophobic photosensitizer permeates from the liposomes to the tumor cells.

3.1.3 Active Targeting Liposomes

The surface of active targeting liposomes are coupled with specific targeting entities to enhance the selective interactions with tumor cell membranes. This targeting technique can be applied to conventional liposomes (Figure 3.1(c)), but it is more appealing for passive targeting of long circulation liposomes (Figure 3.1(d)), since sufficient extravasation at targeting tumor tissue is required. The active targeting liposomes have the following advantages [91]:

- high affinity of binding moiety to the receptor or antigen on the targeted cell surface
- direct and more specific localization with increased efficiency and selectivity

The effectiveness of active targeting liposome delivery depends on several factors:

- the stability of liposomes in the circulatory system
- the ability of liposomes to cross the physiological barriers and reach its site of recognition
- the non-toxicity, non-immunogenicity, and biodegradability of liposomes

Figure 3.2 illustrates active targeting liposomes entering the tumor cell by receptor-mediated endocytosis upon binding to an internalization receptor.

3.2 Photosensitizer Administration and Systemic Distribution

In clinics, most photosensitizers are administered in their drug formulation intravenously, orally, or topically. In preclinical animal studies, photosensitizers can also be administered intraperitoneally, or intramuscularly. Of all the administration methods, intravenous administration of the photosensitizer is the most direct route and results in rapid and complete bioavailability. Bioavailability is the term used to indicate the fraction of an administered dose that reaches systemic circulation. The bioavailability of oral, topical, intraperitoneal, and intramuscular administrations are subject to absorption barriers and first-pass effects. As a result, photosensitizer intravenous injection has far less pharmacokinetic variability compared with the other administration methods.

Serum proteins are predominantly responsible for the transport of photosensitizers throughout the body. Upon administration into the blood stream, conventional liposomes interact with lipoproteins, disintegrate, and release the encapsulated photosensitizers. These released photosensitizers subsequently associate with serum proteins. The nature of photosensitizer-serum protein interaction depends on the physicochemical properties of the photosensitizers

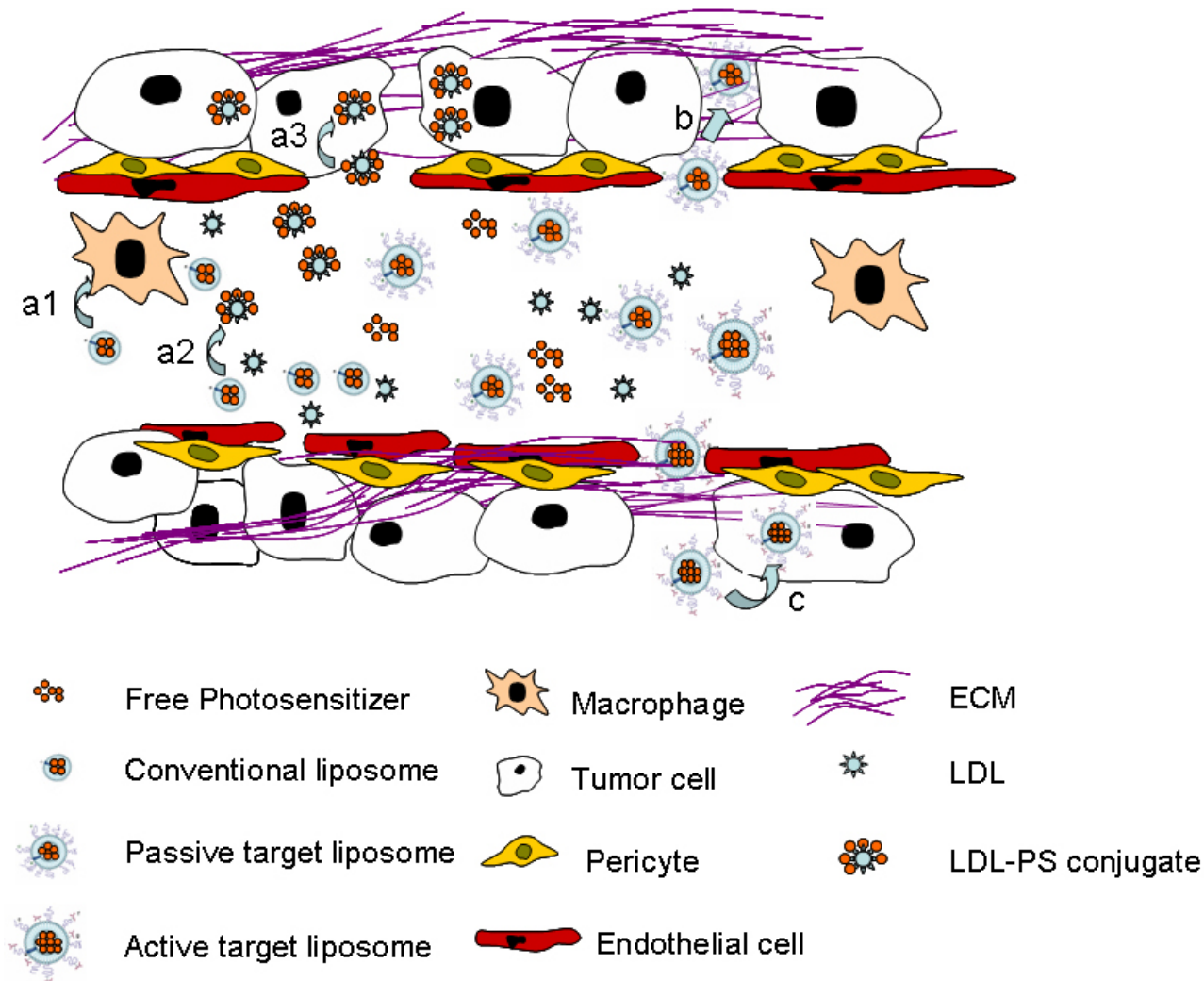


Figure 3.2: *In vivo* behavior of three types of liposome delivery systems. Conventional liposomes have a short plasma half-life either because they become absorbed by protein opsonins, followed by macrophage uptake (a1) or because of lipid exchange with plasma proteins, followed by liposome disintegration and subsequent photosensitizer release. The released photosensitizer might associate with plasma proteins and then enter the tumor cells mainly by LDL-receptor-mediated endocytosis (a2). A small fraction of the conventional liposomes reaches the tumor tissue in its original formulation and allows for intracellular uptake of the photosensitizer by direct binding to cell surface proteins (a3). Passively targeted liposomes accumulate in the tumor interstitium without actual intracellular uptake. Active targeted liposomes can either be directed to a non-internalizing target at the surface of the tumor cell or can enter the tumor cell by receptor-mediated endocytosis upon binding to an internalizing receptor (c). Drawn based on [91].

[91]. For example, hydrophilic photosensitizers such as aluminum tetrasulfonated phthalocyanine (AlPcS4) tend to associate with serum albumin, where more hydrophobic photosensitizers such as BPD-MA tend to conjugate with low density lipoproteins (LDLs) in the blood stream [105].

Albumin is the most abundant serum proteins in human, with concentration about 0.6 mM [106]. Human serum albumin (HSA) consists of 585 amino acids forming a single polypeptide, with molecular weight of 66,000 Da and diameter of 7 nm [107]. Albumin-conjugated photosensitizers being investigated include ZnPc, Hematoporphyrin, aluminum phthalocyanine, and chlorin e6 [105].

Lipoprotein is a particle consisting of a central core of hydrophobic lipids surrounded by a shell of hydrophilic polar lipids and apoproteins. LDLs are major carriers of cholesterol in the blood, and play an important role for drug delivery. LDLs have a diameter of 22nm and a mass approximately 3,000,000 Da [108]. LDLs are the carriers of Benzoporphyrin derivative (BPD, Verteporfin). Dynamics of LDL-BPD conjugate distribution has been investigated in a variety of *in vitro*, *in vivo* and clinical studies [109–124].

3.3 Photosensitizer Distribution in Tumor

A tumor is composed of more than just cancer cells. It consists of an intricate network of cell types and extracellular contents, including endothelial cells that comprise blood vessels, the stromal pericytes that stabilize the developing tumor vasculature and extracel-

Serum Proteins	Photosensitizer	Targets	Reference
BSA	HpD	Macrophage	[125, 126]
BSA	ZnPc	Marine mammary and human colon carcinoma	[127]
BSA	Ce6	Scavenger receptor	[128]
BSA	AlPcS4	Scavenger receptor	[129]
LDL	ZnPc	MS-2 fibrosarcoma	[130]
LDL	HpD	HT1080 fibroblast	[131]
LDL	BPD-MA	Choroidal melanomas, neovasculature	[123, 132, 133]
		LDL receptor	[125, 126, 134]
LDL	TPPS	LDL receptor	[135]
LDL	AlPc	Scavenger receptor	[136]
Transferrin	HpD	Transferrin receptor	[126]
Transferrin	Ce6	Adenocarcinoma	[137]

Table 3.1: Summary of photosensitizer-protein conjugates. Summarized based on [105].

lular matrix that stabilizes this network. Many other cell types, including stromal cells and immune cells, also surround the cancer cells and influence their development.

To reach the cancer cells in the tumor, albumin-photosensitizer or LDL-photosensitizer conjugates must preferentially accumulate in tumor vasculature, transport across the microvascular walls into the tumor interstitium and finally transport through the tumor interstitial compartment [138–150]. Specific liposome delivered photosensitizers of a given size, charge and configuration have specific pathways to reach the tumor cells. Transport processes of the protein-photosensitizer complex may involve diffusion and convection, depending on the physicochemical properties of the conjugates and pathophysiological properties of the tumor tissue.

Additionally, there is growing body of evidence that tumor-host interactions have significant effects on gene expression, angiogenesis, vascular morphology, vessel wall per-

meability, interstitial diffusivity, and metastasis [151–158], and therefore, modulate the pharmacokinetics of macromolecules entering and leaving the tissue.

3.3.1 Photosensitizer Distribution through the Tumor Vascular Network

The first barrier encountered by blood-borne photosensitizer molecules is the abnormal vascular architecture morphology. Tumor vasculature consists of a pre-existing vessel network of the host vasculature, and vessels formed in response to the tumor induced angiogenesis process. This latter process leads to the sprouting, bridging and intussusceptive growth of new vessels from existing vessel networks. Local hypoxia is believed to be the inducer of tumor angiogenesis, it activates the expression of various growth factors stimulating endothelial cells growth, including endothelial growth factors (VEGFs), angiopoietins and platelet-derived growth factors (PDGFs)[159–163]. This immature nascent vascular network reaches a mature level through recruitment of mural cells, generation of extracellular matrix, specialization of the vessel walls (endothelial cells, mural cells and extracellular matrix (inter-endothelial junction, fenestrated endothelium, surface-receptors, *etc*). Vasculature network maturation involves optimizing branching patterns, expanding and pruning [164].

Since the angiogenesis process in tumors is poorly regulated and heterogeneous, tumor vasculature does not follow the same regular artery-vein-capillary structure hierarchy as

in normal tissues [164–167], instead, it contains many tortuous vessels, shunts, vascular loops, widely variable intervascular distances, and large avascular areas; besides, tumor vessels are characterized by irregular diameters and thin vessel walls [165, 168, 169]. These geometric irregularities (*i.e.* vascular density, vessel length, vessel diameter and branching patterns of various blood vessels) in tumor vasculature architecture results in heterogeneous hemodynamics.

Blood flow in this vasculature topology is chaotic both spatially and temporally. Based on perfusion rate, specific tumor regions can be categorized roughly into four regions: an avascular, necrotic region; a semi-necrotic region; a stabilized microcirculation region and an advancing front [170, 171]. Blood flow rates in necrotic and semi-necrotic regions of tumors are found lower compared to those in non-necrotic, well-perfused areas.

Hemodynamics in solid tumors also demonstrate intermittent stagnation followed by high flow or reverse flow temporarily in isolated segmentation [171]. By repetitive injection of blood-borne markers, the dynamics of blood flow in tumor can be easily illustrated. Complete absence of one of the markers is convincing visual evidence that the vessels have been closed in the time interval between administration of drugs [171–173]. With quantitative image analysis techniques, Durand, *et al.*, have shown that dramatic changes such as complete cessation or re-perfusion occurs at most a few percentage of the vessels, whereas, the majority of the vessels show fluctuations with 2 fold flow variation [174–178].

Considering these spatial and temporal heterogeneities in blood supply coupled with

variation in vascular morphology at both microscopic and macroscopic scales, it is not surprising that the spatial distribution of anti-cancer drugs in tumors is heterogeneous, and thus affects the response to chemotherapy in patients. In addition, spatially and temporally heterogeneous blood supply induces tumor hypoxia. This appears in the form of either chronic hypoxia, which is diffusion limited, and/or acute hypoxia, which is perfusion limited. As a result, this heterogeneous perfusion causes tumor radioresistance, as the presence of oxygen increases radical production and DNA damage during therapy.

3.3.2 Transport of Photosensitizers across Microvascular Walls

Transvascular transport model

Once the blood-borne macromolecules have reached the exchanging vessels, their extravasation, J_s (g/s), occurs by diffusion or convection, and/or transcytosis [179]. Although changes in macromolecular microvessel transport are often reported in terms of changes in fluid or solute fluxes between the plasma and interstitium, the permeability coefficients are often used as the functional measurements of microvascular fluid/solute exchange that represent the properties of the microvascular wall. Because most of the fluid/solute microvascular exchange is passive, the permeability coefficients relate the net fluxes of fluid and solute to the pressure and concentration gradients that drive them across the vessel wall.

Based on irreversible thermodynamics, Kedem and Katchalsky [180–182] derived a set

of equations to describe the flow of solvent and solute across homoporous and heteroporous membranes.

According to Starling hypothesis, net fluid flow across a vessel wall is given by:

$$J_f = L_p S (\Delta P - \sigma \Delta \pi) \quad (3.1)$$

and net solute flux through a homoporous membrane is given by the Staverman-Kedem-Katchalsky equation [180–182]:

$$J_s = J_f (1 - \sigma) \bar{C} + P_d S \Delta C \quad (3.2)$$

where $L_p S$ represents the hydraulic conductance, the product of hydraulic conductivity (L_p) and membrane surface area (S); ΔP is the transmembrane hydrostatic pressure gradient; σ is the reflection coefficient of the membrane to the solute; $\Delta \pi$ is the transmembrane osmotic pressure gradient; P_d is the diffusive permeability; $\Delta C = (C_p - C_i)$ is the solute concentration gradient, where C_p and C_i stand for solute concentration in plasma and interstitium, respectively; and \bar{C} is the mean intra-membrane solute concentration.

Integration of Equation 3.2 across the membrane and between the boundary conditions C_p and C_i yields Patlak equation [183]:

$$J_s = J_f (1 - \sigma) \frac{C_p - C_i e^{-Pe}}{1 - e^{-Pe}} \quad (3.3)$$

where Pe is referred to as the Peclet number, and is given by:

$$Pe = \frac{J_f(1 - \sigma)}{P_d S} \quad (3.4)$$

The Peclet number indicates the importance of convective transport with respect to diffusive transport. When Pe is small, the diffusive transport is dominant, and both Equation 3.2 and 3.3 can be approximated as:

$$J_s = P_{dEff} S (C_p - C_i) \quad (3.5)$$

where P_{dEff} is referred to as the effective permeability and it includes the dominant diffusive component as well as less dominant convective component.

These transvascular transport parameters: P_d (diffusive permeability, vascular permeability coefficient); L_p (hydraulic conductivity, filtration coefficient) and σ (osmotic reflection coefficient) depend on physicochemical properties of solute molecules, *e.g.*, molecular size, charge and configuration as well as the physiological and physicochemical properties of tumor vessel wall, *e.g.*, vessel wall ultrastructure, transport pathways, and charge. The hydrostatic and osmotic pressure gradients are also dependent on the pathophysiological properties of the tumor tissue. Discussion about the methods of evaluation of these permeability coefficients is beyond the scope of this thesis, so for a more detailed discussion refer to review articles [179, 183]

Evaluation of the permeability coefficient (P)

Macroscopic Methods In tissue uptake studies, test molecules are injected into the blood stream, the uptake in the tumor is evaluated invasively (tissue extraction) or non-invasively (MRI, PET and optical techniques). Tissue uptake studies provide a global estimation of the transport parameters and yet little temporal and spatial heterogeneous information for individual capillaries. Also, it does not count the contribution of temporal and spatial variation in blood flow in the tumor. Despite these disadvantages, this technique is most widely used for the relative measurement of permeability of different tumor types [179, 180], or permeability changes after tumor treatment [184].

Microscopic Methods Microscopically, permeability of molecules is measured by monitoring the concentration of the molecules in and outside vessels. Single vessel methods measure the permeability to solute of a single capillary; lose the ability of characterizing all the capillaries in the tissues, especially in heterogeneous tumors [185]. With the development of intravital fluorescence microscope and window chamber models, the heterogeneous permeability of microvascular beds has been measured, including counting the number of spots where the tracer has leaked out from the vasculature, measuring the concentration of tracers around the vessels, and measuring the extravasation rate using digital video image analysis [186, 187].

Characterization of permeability coefficients

1. Values of permeability coefficient for macromolecules (larger than serum albumin: 3.6nm) decrease much less rapidly with increasing molecular size, indicating there exists different pathways or mechanisms for large and small molecule transvascular transport.
2. Diffusion of small molecule solutes is through water-filled pores or channels with diameters larger than the diameter of the molecules.
3. The reflection coefficient has no correlation to hydraulic permeability (macromolecules)
4. Hydraulic conductivity is proportional to permeability for small hydraulic molecules: so that differences in permeability of different tissue is the consequence of variation in number of channels per unit area of vessel wall instead of pore size.

Transport Pathways: Structure-Function Relationships

The ultrastructural shape of the vascular walls can be divided into two groups. The first is called fenestrated endothelium which are vessel walls with high values of L_p ($>10^{-6}$ cm/cmH₂O·s), where the transport across these vessel walls is through the fenestrae; For intermediate sized molecules, the transport pathway is "restricted diffusion" and for macromolecules the reflection coefficient is similar to vessels with continuous endothelium. The second group of

wall shapes are continuous endothelium which are walls of vessels with lower values of L_p , where the transvascular transport is through intercellular clefts.

Transvascular transport pathways include:

1. Trans-endothelial exchange water and small hydrophilic solutes, *e.g.*, glucose, amino acid and urea). Although this pathway exists, the quantitative contribution of this pathway to the net flux of water and small hydrophilic molecules can be negligible;
2. Extracellular exchange: transport is through either small pores (4-5 nm) available for small and intermediate-sized molecules [188] or large pores (20-30 nm) responsible for macromolecules [189].

Although small and intermediate-sized molecules pass through the large pores, since the relative number of small pores to large pores falls in the range of 4,000 to 1 (muscle) to <1,000 to 1 [190], the transvascular transport of these molecules depends on the frequency of small pores per unit area of vessel walls. The permeability to macromolecules is entirely determined by the frequency and dimension of the large pores.

Variabilities in transvascular transport

Considerable numbers of reports have shown that tumor tissues are more permeable than normal tissues, which is a result of the distinguished vasculature structure. This phenomenon is good for cancer chemotherapy and photodynamic therapy, which depend on passive delivery of agents to tumor. But the heterogeneous feature of tumor permeability

brings non-uniform drug distribution problems, and makes the treatment more variable. It has been demonstrated that local microenvironment plays an important role in controlling the vascular permeability. For example, HGL21, a human glioma is found more leaky at subcutaneous inoculation sites, but exhibits blood-brain barrier properties in the cranial window. The hypothesis is that host tumor interactions control the expression of a variety of cytokines including the ones associated with permeability changes, *i.e.*, VPF/VEGF and its inhibitors. As discussed above, this cytokine expression demonstrates a spatially heterogeneous feature. So it is not surprising that the permeability in solid tumors is also heterogeneous. These variations have been observed at both macroscopic and microscopic levels. Hobbs, *et al*, presented the difference in permeability at different host-sites even for the same tumor cell lines. His study also showed that this permeability difference is partly due to the characteristic pore cutoff size of the tumors, which is regulated by the growth factor [154]. Similar study from Yuan [187] and Fukumura [152] also demonstrated that the local micro-environment of tumors can control the permeability. Recent work from Baluk [191] and Yuan [192] showed that temporal changes exist as well in the number and morphology of endothelial gaps, and accounts for the temporal changes in tumor permeability and plasma leakage. In addition, interstitial fluid pressure, average vascular surface area are also determinants of transvascular transport. For example, experimental tumors often exhibit a uniformly high pressure inside the tumor, but a significant drop to normal values in tumor's periphery or peri-tumor regions [138–140, 145, 193]. Thus convective transport of macromolecules is often more pronounced at the periphery of a tumor, since convection

depends on the fluid pressure gradient. Additionally, the average vascular surface area per unit tissue weight decreases with tumor growth, hence, larger tumors always demonstrate reduced transvascular transport compared to small tumors [193, 194].

Manipulation of tumor vessel permeability

Both physical (radiation, heat, PDT) and chemical factors (protease, cytokines, *etc*) can alter the tumor permeability. Radiation [195–197] and PDT [61, 198] increase the tumor permeability via:

1. Direct damage to the endothelial cells;
2. Increase blood flow;
3. Increase the exchange surface area;
4. Damage to the extracellular matrix structure;
5. Alter the interstitial fluid pressure.

Mediators and inhibitors on macromolecular permeability have been studied; they are believed to regulate the endothelial gaps. Such agents include bradykinin, nitric oxide, peroxynitrite, VPF and VEGF, and some tumor necrosis factors [97, 199–201].

3.3.3 Transport of Photosensitizers through Tumor Interstitium

Interstitial transport model

Interstitial solute transport is an effect caused by the macromolecular concentration profile in the tumor interstitium. Molecules migrate and move through the interstitium by diffusion and convection processes [202]. Diffusion is proportional to the molecular concentration gradient in the interstitium. The ratio of diffusive flux to the concentration gradient is interstitial diffusion coefficient D (cm^2/s). Convection is proportional to interstitial fluid velocity \vec{u} (cm/s), which is proportional to the pressure gradient in interstitium. The ratio of interstitial fluid velocity to the pressure gradient is interstitial hydraulic conductivity K ($\text{cm}^2/\text{mmHg}\cdot\text{s}$).

The diffusion flux and convection flux can be expressed as:

Diffusion flux:

$$\vec{J}_D = -D\nabla C_i \quad (3.6)$$

Convection flux:

$$\vec{J}_C = C_i R_f \vec{u} = C_i R_f L_{p,i} \nabla p \quad (3.7)$$

where C_i (mol/ml , g/ml or number of molecules/ ml) is the concentration of transport molecules at different locations in the tumor interstitium; R_f is the retardant factor (ratio of solute velocity to fluid velocity), $L_{p,i}$ ($\text{cm}/\text{mmHg}\cdot\text{s}$) is interstitial hydraulic conductivity.

The microscopic interstitial transport of solute can then be modeled as a convection-diffusion equation [203]:

$$\frac{\partial C_i}{\partial t} = \nabla \cdot (D \cdot \nabla C_i) - \nabla \cdot (R_f \vec{u}_i C_i) + \Phi_s - \Phi_b + \Phi_d - \Phi_k \quad (3.8)$$

The boundary condition for transvascular solute flux is given by Starling's Law, expressed in Patlak Equation [202]:

$$\left(-D \cdot \nabla C_i + \nabla \cdot (R_f \vec{u}_i C_i) \right) \Big|_{\Gamma} = \nabla \cdot \vec{u}_i (1 - \sigma) \left(\frac{C_p e^{Pe} - C_i}{e^{Pe} - 1} \right) \Big|_{\Gamma} \quad (3.9)$$

where Φ_s , Φ_b , Φ_d , and Φ_k are solute source, binding, dissociation, and consumption terms in the unit of mol/ml·s; Γ is the intravascular-extravascular boundary, $(\nabla \cdot \vec{u}_i)_{\Gamma}$ is normal velocity at the vessel wall, Pe is transvascular Peclet number, defined as the ration of convection to diffusion flux ($Pe = (\nabla \cdot \vec{u}_i)_{\Gamma} (1 - \sigma) \frac{1}{P}$).

For simplicity, most macromolecule interstitial transport analysis ignores the fluid exchange between intravascular and extravascular compartments, since the diffusion is much more dominant in this process [193, 194, 202–204]. Thus the interstitial transport model can be simplified as:

$$\frac{\partial C_i}{\partial t} = \nabla \cdot (D \nabla C_i) - \Phi_b + \Phi_d - \Phi_k \quad (3.10)$$

and the Patlak boundary condition for solute flux can be rewritten as:

$$-DS\nabla C = \vec{J}_s = PS\vec{S}(C_{i,\Gamma} - C_p) \quad (3.11)$$

where P is the diffusive permeability coefficient, which is discussed as in the transvascular transport section, $\vec{S} = S\hat{n}$ is the tumor vasculature surface area vector, $C_{i,\Gamma}$ is drug concentration at the intravascular-extravascular compartment interfaces, C_p is drug concentration in vascular compartment. Note that the source term Φ_s has been omitted in the interstitial diffusion equation Equation 3.10, since a solute source boundary condition has been applied in Equation 3.11.

Evaluation of diffusion coefficient (D)

Cussler has summarized a *ex vivo* method to evaluate diffusion coefficients of various macromolecules [205]. The process involves measuring the solute flux at a known concentration gradient or measuring the relaxation of the concentration gradient as a function of time in the tissue slices *in vitro* or in gels as a model for tumor interstitium, fitting of these measurement data to steady or unsteady state diffusion equation, and extracting the diffusion coefficients. With the development of quantitative fluorescence intravital microscope, several investigators [206–208] have evaluated the tumor interstitial diffusion coefficients *in vivo* non-invasively. The diffusion coefficient was calculated based on the spatial distribution of fluorescence dyes (*e.g.* fluorescence labeled dextran and protein) in tumor cham-

ber model or other thin tissue preparations. Relaxation of the concentration gradient was recorded as the molecules extravasated and distributed into the tumor interstitium, and diffusion coefficient of specific molecules was evaluated by fitting the concentration gradient to the non-steady-state diffusion equation. The drawback of this method is that the calculated effective diffusion coefficients include both diffusive and convective components. To distinguish diffusion from convection, Chary and Jain [209] adapted photobleaching recovery after photobleaching (FRAP) method to measure the diffusion coefficients of different macromolecules in the rabbit ear chamber. The FRAP method involves local equilibrated accumulation of fluorescence labeled macromolecules, extensive light illumination causing local photobleaching, and relaxation of concentration profile. Diffusion coefficients of macromolecules with different molecular weights in water and normal tissues have been published by several investigators, and can be described as:

$$D = aM_r^{-b} \quad (3.12)$$

Coefficients a and b are tabulated in Jain's review paper [202], showing that the diffusion coefficients in tissue deviate from the diffusion coefficients in water, suggesting that the diffusion coefficient depends not only on the physicochemical properties of the macromolecule being investigated, but also on the physiological and physicochemical properties of interstitial compartment.

Transport Pathways: Structure-Function Relations

The interstitium is defined as the space located between capillary walls and the cells, the basic structure of interstitium includes: fiber framework composed of collagen, salt solution and proteins derived from plasma [210]. Tumor interstitium is characterized by large interstitial space, high collagen concentration, low proteoglycan and hyaluronate concentrations, high interstitial fluid pressure and absence of anatomically well-defined functional lymphatic networks [202].

Tumor and stromal cells produce and assemble a network composed of collagen, proteoglycans, and other molecules, hindering the transport of macromolecules transportation in interstitium [211, 212]. Various *in vitro* and *in vivo* studies have shown that resistance to water and solute transport is generally attributed to stabilized polysaccharide network (hyaluronate and proteoglycans) enmeshed in the collagen network. The authors attribute the higher resistance of macromolecular diffusion to the higher content of glycosaminoglycan (GAG) [213–215] and hyaluronic acid (HA). Tumor tissue has substantial structural differences in composition and assembly patterns of ECM compared with normal tissues, Netti showed that interstitial movement of macromolecules does not correlate the GAG content, instead, the total collagen content of each tissue appears to mirror the measurements of macromolecule mobility, besides, the organization of collagen addition to absolute content plays an important role in interstitial transport [197].

Variability in interstitial transport

Different tumor types or different tumor host-sites have different ECM composition, structure and distributions. This will lead to different diffusion dynamics for specific macromolecules. Pluen [216], *et al*, using FRAP technique, measured the diffusion coefficients of proteins, dextran, and liposomes in two different tumor host-sites (dorsal chamber and cranial window) in mice, and reported slower diffusion rate in DC tumors. Microscopically, immunohistochemistry and electron microscopy studies of ECM ultra-structures in these two tumor types showed heterogeneous distribution of each ECM components. According to interstitial transport pathway theory, the variabilities in content of different contents of ECM and their heterogeneous distribution inside tumor affects the macromolecules interstitial transport process, and thus affects the intra-tumor distribution and inter-individual variability in drug uptake. Another factor that causes non-uniform distribution of endogenous macromolecules is interstitial fluid pressure, as mentioned earlier, which is high in the center of a solid tumor and low at periphery and surrounding normal tissue. Thus the extravasated macromolecules tend to move to the tumor periphery and normal tissue following the fluid pressure gradient through convection. These macromolecules have to overcome this outward convection to diffuse back into the tumor.

Manipulation of diffusion coefficient

Since the organization of ECM contributes to most of the resistance for the macromolecules in their interstitial transport, the degradation of these structures will increase the molecules mobility in the tumor interstitium. According to Netti's report, local administration of collagenase can significantly increase the diffusion coefficients in HSTS and U87 tumors measured by the FRAP method [201]. Eikenes, *et al.*, also showed that collagenase modulates the ECM, reduces the interstitial fluid pressure and enhances the interstitial transportation of osteosarcoma-associated monoclonal antibodies (TP-3) [217].

3.3.4 Summary of Barriers to Photosensitizer Distribution in Tumor

Causes of microscopic and macroscopic variation are

1. Irregular vasculature topology
2. Heterogeneous blood supply
3. Heterogeneous vascular permeability coefficients
4. Heterogeneous interstitial diffusion coefficients
5. Non-uniform interstitial fluid pressure

3.3.5 Photosensitizer Photobleaching

In addition to the variation in photosensitizer transvascular and interstitial transport, there exist variation in photobleaching during the light illumination. This photosensitizer destruction process potentially induces photosensitizer redistribution during the time of irradiation and causes photosensitizer intra-tumor distribution variability. There are large numbers of reports exhibiting photobleaching, reducing photosensitivity both *in vitro* and *in vivo*, and as a result, leading to less effective PDT treatment [27, 218–223]. Several investigators have used measurement of photobleaching as another dosimetric parameter for PDT [224, 225]. However, the mechanisms of photobleaching for different photosensitizer molecules are quite different, and not well-understood, and possibly not readily predictable. Microscopically, photobleaching depends on the photosensitizer distribution, and may or may not link to the oxygen distribution in the tumor [226–228]. Photobleaching induced photosensitizer redistribution has been reported at both tumor tissue [229] and intra-cellular level [50, 230–232]. Moan, *et al*, showed that aluminum phthalocynine (AlPcS2) can undergo intra-cellular redistribution during light irradiation, yet without increased photo-toxicity [50]. While other photosensitizer molecules, Zn(II) phthalocynine [232], and Nile blue derivatives [230, 231] have shown an increase photo-toxicity with the intracellular redistribution. These phenomena make the photosensitizer dynamic distribution more complicated, and bring obstacles for building better PDT treatment protocols. An on-line microscopic evaluation of photosensitizer distribution along with the tumor mi-

crossopic oxygenation profile will provide a better picture of photobleaching mechanisms and help to find ways to optimize PDT treatment.

3.4 Photosensitizer Metabolism and Excretion

3.4.1 Metabolism

Metabolism and excretion are the two processes by which photosensitizers are eliminated from the body. Metabolism, also called biotransformation, is the elimination of drugs through enzymatic alteration of the chemical structure of molecules to form metabolites. The drug is eliminated from the body by conversion to a new chemical entity that is more water-soluble and more readily excreted from the body. The major organ responsible for drug metabolism is the liver. Liver blood flow and enzyme activity determine the liver metabolism of the drug. Metabolism is process varies among individuals and within individuals over time. Genetic inheritance is the major source of individual variation in drug metabolism. Developmental and environmental factors also have profound effects on drug metabolism.

3.4.2 Excretion

Excretion involves the removal process of photosensitizers, active metabolites or inactive metabolites from the body. Renal elimination through the urine is the most common route

of elimination. Biliary excretion is another common route of elimination. Decreased excretion can result in accumulation of photosensitizer and possible toxicity.

3.4.3 Photosensitizer Clearance and Half-life

The measure of photosensitizer elimination by all routes of metabolism and excretion is clearance, which is defined as the rate of removal of photosensitizer in proportion to plasma concentration. Clearance is reported as the volume of plasma cleared of the photosensitizer per unit time. The concept of clearance is useful in understanding the elimination characteristics of a photosensitizer, and in its pharmacokinetic calculations.

Another parameter characterizing drug elimination is half-life, which is defined as the amount of time required for half of the drug to be eliminated from the body. It can be measured as the amount of time it takes for the plasma concentration of photosensitizer to decline by 50%. Because the photosensitizer in peripheral compartment and the photosensitizer in plasma compartment are at equilibrium, changes in concentration of the drug in plasma represents changes of the total amount of photosensitizer in the body, regardless of whether the drug is primarily located in the circulatory system or primarily sequestered in the peripheral tissue. Therefore, a drop in plasma concentration of 50% means that the total drug in the whole body has dropped by 50%.

Chapter 4

Effects of Tumor Host-site on Verteporfin Pharmacokinetics and PDT Treatment

Chapter 3 outlines the potential sources for photosensitizer intra-tumor and inter-individual pharmacokinetic variability in parallel to four pharmacokinetic phases after drug administration. Reviews of pharmacokinetic models, transport models and parameter characteristics of these models are also presented. In this chapter, the focus is on the pharmacokinetics of Verteporfin (BPD-MA) in a rat prostate tumor model called the Dunning MAT-LyLu. A series of experimental comparisons are made using MAT-LyLu tumors inoculated at two distinct sites: orthotopic and subcutaneous host-sites. The comparisons include:

- Tumor microenvironment, *i.e.*, tumor vasculature architecture, VEGF expression, and tumor oxygenation;
- Verteporfin transport parameters, *i.e.*, plasma pharmacokinetics, vascular permeability, and interstitial diffusion coefficients;
- Tumor response to vascular and cellular-targeting PDT treatments.

This chapter provides an extreme case study of photosensitizer inter-individual pharmacokinetic variability, since tumors at distinct host-sites have different transport parameters, *i.e.*, tumor vasculature network, vascular permeability, and interstitial diffusion coefficients, leading to different photosensitizer pharmacokinetics, and thus behave differently in response to PDT treatment.

4.1 Introduction

A growing number of studies suggest that PDT can be a promising treatment for prostate cancer [21, 233]. Studies on the optical characteristics of human and animal prostate tissue/cancer indicate that it is possible to provide an entire prostate treatment with optical fibers [234–238]. The effectiveness in prostate tumor management has been shown in various rat and mouse tumor models [21, 239–243]. However, most of these studies have been conducted on prostate tumors induced at the subcutaneous (s.c.) site (ectopic) and only two PDT studies on the orthotopic prostate tumor models have been reported [21, 240]. This is

Comparison	Key Conclusions	Ref
Cranium v.s. dorsal skin	Faster angiogenesis in cranial site	[249]
	Blood barrier formation only formed in cranial site	[142]
	Smaller vascular pore cutoff size in cranial site	[154]
	Lower vascular permeability in cranial site after VEGF administration	[192]
	Higher interstitial diffusion in cranial site attributable to less collagen	[156]
	Tumor host-site influences the endothelial differentiation	[151]
	Higher Flk1 and Flt1 mRNA expression, less fenestrated endothelium in cranial site	[157]
	Absence of host-site influence on angiogenesis, blood flow and permeability	[245]
Cranial v.s. mammary fat pad	Higher permeability but lower angiogenesis in fat pad site	[155]
Liver v.s. subcutaneous	Higher vascular permeability in liver site	[250]
Liver v.s. dorsal skin	Lower VEGF expression and angiogenesis, higher vascular permeability in liver	[152]
Gallbladder v.s. subcutaneous	Higher expression of endogenous anti-angiogenesis factor in orthotopic site	[248]
Bladder v.s. subcutaneous	Enhanced tumor outgrowth and invasiveness	[251]
Pancreas v.s. abdominal wall	High VEGF expression, angiogenesis and tumor growth in pancreas	[158]
Prostate v.s. subcutaneous	Increased metastasis after Laser-induced hyperthermia in orthotopic site	[247]

Table 4.1: Role of tumor host microenvironment in pathophysiological and physical functions of tumor. Summarized based on [155].

presumably because the subcutaneous tumor is easy to produce and convenient to study.

However, accumulating evidence shows that the tumor host micro-environment affects tumor gene expression and has a significant effect upon tumor physiologic characteristics such as growth pattern, vascularities, angiogenesis, and metastasis [155, 158, 244–246]. Furthermore, these changes in gene expression impact the interactions which ultimately affect the macromolecule delivery pathways, *i.e.*, macromolecule transvascular transport [154, 192], and interstitial transport [156]. This inevitably affects the delivery of anti-cancer drugs to the tumor, and thus affects the treatment efficacy [247, 248]. Evaluation of cancer therapies in a non-physiologically relevant tumor models may hamper the transition of experimental results to the clinical application, since tumors grown in different host-sites might respond differently to the same treatment.

Table 4.1 lists several publications that discuss the effects of tumor host-site for pathophysiological and physical functions.

In addition, since different tumor inoculation sites present distinct pathophysiological features, and are characterized by different drug distribution pharmacokinetics, study of photosensitizer pharmacokinetics at two different tumor inoculation sites will help us gain knowledge of how different tumor microenvironment will affect those pharmacokinetic parameters, and how it affects the PDT treatment.

The objectives of this study are:

1. Evaluate the effects of inoculation sites on tumor microenvironment, *i.e.* VEGF expression, tumor vascularities and tumor oxygenation.
2. Evaluate the influence of tumor inoculation sites on photosensitizer pharmacokinetics, *i.e.*, plasma pharmacokinetics, transvascular transport, and interstitial transport.
3. Determine the host-site effects on PDT treatment efficacy.

4.2 Materials and Methods

4.2.1 Photosensitizer

A lipid formulation of the photosensitizer benzoporphyrin derivative (BPD)[114], called Verteporfin for Injection, was provided by QLT Inc. (Vancouver, BC, Canada), in powder form, and was reconstituted in saline to 1.0 mg/ml. Rats received 1.0 mg/Kg of verteporfin via tail vein, and were sacrificed 15 minutes or 3 hours after photosensitizer administration.

The vascular marker DiOC7₍₃₎ (Molecular Probes, Eugene, OR) was used as a probe to obtain information of tumor vasculature location and shape with fluorescence microscopy from frozen sections. Injections were administrated i.v. 1 minute before sacrifice at a concentration of 1 mg/Kg (dissolved in 75% dimethyl sulphoxide in phosphate buffered saline)[114, 173, 252]. To prevent the further diffusion of DiOC7₍₃₎ and BPD, tumors were isolated and put into liquid nitrogen and then further sliced to 10 μ m slides (near the center of the tumor) for fluorescence microscopy studies.

4.2.2 Animals and Tumor Models

Male Copenhagen rats (6-8 weeks old), obtained from Charles River Laboratories (Wilmington, MA), were used throughout the study. All animal procedures were carried out according to protocols approved by the Dartmouth College Animal Care and Use Committee. The R3327 MAT-LyLu Dunning prostate tumor is an androgen independent carcinoma, syngeneic to the Copenhagen rats, and highly metastatic to both lung and lymph nodes [253]. R3327 MAT-LyLu prostate cancer cells were cultured in RPMI-1640 with glutamine (Mediatech, Herndon, VA) supplemented with 10% fetal bovine serum (HyClone, Logan, UT) and 100 units/ml penicillin-streptomycin (Mediatech). The subcutaneous MAT-LyLu tumors were induced by injecting approximately 1×10^5 MAT-LyLu cells (suspended in 0.05 ml PBS) subcutaneous into the shaved rat flank. Tumor growth was documented regularly by external measurements with calipers. Tumors were used for the experiment at 9

to 12 days after inoculation, with a surface diameter of 7 to 9 mm and a thickness of 2 to 4 mm. The orthotopic MAT-LyLu rat prostate cancer model was reproduced as previously described [240]. Briefly, animals were anesthetized with an injection (i.p.) of ketamine (90 mg/Kg) and xylazine (9 mg/Kg). After anesthesia, a 2-cm longitudinal incision was made on the lower abdomen just above the pubic bone, pulling the bladder aside to expose the prostate. The tumors were induced by injecting 1×10^5 MAT-LyLu cells (in 0.05 ml PBS) into the prostate ventral lobe. The injection site was cleaned with 70% ethanol to kill any possible residual tumor cells and the incision was closed aseptically. Tumors were used for experiment at 7 to 8 days after implantation when reaching a size of 6 to 9 mm in diameter. Both subcutaneous and orthotopic tumors had similar size (6-9 mm in diameter) and observed no spontaneous necrosis at the time of PDT treatment.

4.2.3 Analysis of Tumor Host-site Effects on Tumor Microenvironment

Analysis of Functional Tumor Vasculature

Tumor bearing animals were i.v. injected with a carbocyanine dye DiOC7₍₃₎ (Molecular Probes, Eugene, OR), a marker of functional vasculature, at a dose of 1 mg/Kg, 1 minute before sacrificing the animals. The tumor tissue was harvested, embedded in the TissueTek medium and snap-frozen in liquid nitrogen-cooled isopentane. Cryosections with thickness of 10 μm were taken from the tumor and imaged with a Nikon Diaphot-TMD fluorescence

microscope (excitation, 480/20 nm; emission, 540/40 nm) equipped with Qimaging Micropublisher Imaging System (Burnaby, BC, Canada), which includes a high resolution CCD digital camera and the image acquisition software. To quantify the functional vessel density and the average vessel size in the subcutaneous versus the orthotopic tumor, five to seven microscopic fields under a 10X objective lens (with an area of 1 mm²) were randomly taken from each section. Three sections were examined for each tumor and 10 animals were included in each of the subcutaneous and orthotopic tumor groups, resulting in a large sampling of the tumor vasculature patterns. The fluorescence images (682 × 512 pixels, 1 pixel = 1.69 μm), captured with the same exposure conditions, were analyzed with NIH ImageJ software with an automatic threshold setting to generate the functional vessel count and average vessel size.

Measurement of Tumor Oxygenation

Tumor oxygen partial pressure (pO₂) distribution was measured by using an Eppendorf polarographic oxygen electrode (Eppendorf, Hamburg, Germany; [254]). Before and between measurements, the 300 μm electrode probe was calibrated in physiologic saline by flushing alternatively with air (100% oxygenated) and nitrogen (0% oxygenated). Tumor-bearing animals were anesthetized with inhalation of 1.5% isoflurane mixed with air. For the subcutaneous tumor, a small cut was made on the rat skin to facilitate the probe insertion. An abdominal incision was made to expose the orthotopic tumors. The oxygen

electrode was first inserted into the tumor. After the pO₂ value became stable, the probe was set to advance automatically through the tissue in a 0.7 mm increments, followed by a 0.3 mm backward step before measurement. The probe track length was predetermined by the tumor size and three diagonal tracks were made through each tumor. From the pO₂ values obtained for each tumor, the median and mean pO₂ values and the percentage of readings <5 mmHg were calculated. The values of each group and the SD were obtained based on the data of each tumor in the group. To show the pO₂ distribution, a histogram was generated by pooling all the values from animals in each group and displaying the percentage of pO₂ values in each pO₂ range category.

VEGF-A ELISA Assay

Proteins were extracted from the orthotopic and subcutaneous MAT-LyLu tumors. Briefly, frozen tumors were pulverized into powder in a tissue homogenizer and thawed in 1 ml/mg lysis buffer containing protease inhibitors (1% NP40, 0.5% sodium deoxycholate, 0.1% SDS, 10 mg/ml PMSF, 100 mmol/L sodium orthovanadate, and protease inhibitors cocktail). Extracts were incubated on ice for 30 minutes with vortexing every 5 minutes followed by centrifuging at 10,000 × g for 10 minutes at 4 °C. The supernatant was transferred and centrifuged again. Protein samples were stored at -80 °C until ELISA assay. A rat VEGF Duo Set ELISA development system (R&D Systems, Minneapolis, MN2) was used, according to the manufacturer's instruction, to quantify rat VEGF levels in tumor

extracts. Results were normalized to protein concentrations. Four tumors were included in each group.

4.2.4 Analysis of Tumor Host-site Effects on Verteporfin Tumor Uptake

Tissue distribution of verteporfin was studied by fluorescence microscopy at 15 minutes and 3 hours following drug administration (i.v., 1 mg/Kg). To visualize the perfused blood vessels, perfusion marker DiOC7₍₃₎ was injected (i.v.) at a dose of 1 mg/Kg, 1 minute before excising the tumor tissue. Cryosections (10 μ m) were cut from the tumor and the same microscopic fields (with an objective lens of 10X) were imaged for both verteporfin (excitation, 425/40 nm; emission, 700/30 nm) and perfusion marker DiOC7₍₃₎ (excitation, 480/20 nm; emission, 540/40 nm) with a Nikon Diaphot-TMD fluorescence microscope. To quantify verteporfin fluorescence intensity in the subcutaneous and orthotopic tumors, five to seven microscopic fields (with an area of 1 mm²) were randomly taken from each section. Three sections were examined for each tumor and 5 or 6 animals were included in each group. The intensity of the fluorescence image (682 \times 512 pixels, 1 pixel = 1.69 μ m) was measured with NIH ImageJ software. With the same exposure setting, background images were also taken from control tumors, which were injected only with DiOC7₍₃₎. The average intensity of these background images was subtracted from the values of verteporfin fluorescence intensity.

4.2.5 Analysis of Tumor Host-site Effects on Transport Parameters

Transvascular transport process

Macroscopic evaluation: Evans blue tissue uptake The permeability of tumor blood vessels in the orthotopic and subcutaneous MAT-LyLu tumors was assessed by the Evans blue extravasation assay [255]. Evans blue (10 mg/ml in PBS) was injected at a dose of 10 mg/Kg intravenously to the tumor-bearing animals. Tumors were excised at 15 minutes, 1, 3, and 24 hours after the administration. Before harvesting the tumor tissue, animals were perfused with 50 ml physiologic saline to remove the Evans blue dye in the circulation. Tumors were weighed, minced, and extracted with formamide (1 ml per 100 mg tumor tissue) for 72 hours. The solutions were centrifuged and the absorbance of Evans blue in the supernatant was measured at 620 nm by a spectrophotometer. The absorbance data were all normalized to the highest value obtained to generate relative results for comparison between tumors in different sites. At least three animals were included in each group.

Microscopic evaluation: verteporfin transvascular transport model Verteporfin permeability (P) was determined from BPD fluorescence images taken from tissues that were removed at 15 minutes post verteporfin injection. Details about the permeability mathematical model will be discussed in Chapter 5. In general, effective permeability coefficients of BPD in MAT-LyLu tumors were calculated as:

$$P_{dEff} = (1 - H_t) \frac{V}{S} \frac{dI_i/dt}{I_{p,0}} \quad (4.1)$$

where H_t is average hematocrit in tumor vessels, V and S are the total volume and surface area of vessels within the tissue volume captured by the fluorescence microscope, $\frac{dI_i}{dt}$ is the total fluorescence intensity change per unit time, $I_{p,0}$ is intravascular fluorescence intensity at time of verteporfin injection. 5 to 7 microscopic fields (with an area of 1 mm²) were randomly taken from each section. Three sections were examined for each tumor and 5 and 6 animals were included in the subcutaneous and orthotopic tumor groups.

Interstitial transport processes

The interstitial diffusion coefficient of verteporfin at two tumor inoculation sites was determined via a 2-dimensional finite element diffusion model based on the vascular geometry obtained from fluorescence perfusion images. Details about the interstitial transport model will be discussed in Chapter 5. The effective diffusion coefficient D was calculated via parameter estimation through fitting the data to predictions by the diffusion equation:

$$\frac{\partial C_i}{\partial t} = \nabla \cdot (D \nabla C_i) \quad (4.2)$$

with Patlak boundary condition for solute flux at the boundary of vessel wall:

$$-DS\nabla C = \vec{J}_s = P_{dEff}\vec{S}(C_{i,\Gamma} - C_p) \quad (4.3)$$

where P_{dEff} is the diffusive permeability coefficient, which is discussed as in the transvascular transport section, $\vec{S} = S\hat{n}$ is the tumor vasculature surface area vector, $C_{i,\Gamma}$ is the drug concentration at the intravascular-extravascular compartment interfaces, C_p is the drug concentration in vascular compartment.

The same set of fluorescence images were analyzed for permeability and diffusion coefficient evaluation, which include 5 to 7 randomly selected $1 \times 1 \text{ mm}^2$ microscopic fields from each section, 3 sections from each animal and 5 or 6 animals from the subcutaneous and orthotopic tumor groups.

4.2.6 Analysis of Tumor Host-site Effects on PDT Treatment

A diode laser system (Applied Optronics, Newport, CT) with 690 nm wavelength was used throughout this study. The light was delivered through an optical fiber (140 μm core diameter) and irradiated the tumor surface over a 1 cm diameter beam spot using a fiber optic collimator. The MAT-LyLu tumors in both sites were exposed to an incident fluence rate of 50 mW/cm² for 1,000 seconds (50 J/cm²), as measured by a Thorlabs optical power meter (Thorlabs, Inc., North Newton, NJ). Animals were anesthetized with an injection (i.p.) of ketamine (90 mg/Kg) and xylazine (9 mg/Kg) and placed on a heating pad, maintained at 37 °C, throughout the treatments. For the orthotopic MAT-LyLu tumors, abdominal surgery

was made to expose the tumor in the prostate for light treatment. To ensure the delivery of the same light dose (50 J/cm^2), skin over the subcutaneous MAT-LyLu tumor was surgically retracted during the light treatment and sutured after treatment. The same operation was done on all control tumors. PDT-induced tumor necrosis was measured histologically at 2 days after treatment [256]. Briefly, H&E stained tumor images were digitally recorded using an Olympus BX50 microscope with an Olympus C3030 CCD camera. An objective of 1.25X was used to cover the whole tumor section. The whole tumor area was outlined on the computer screen using a freehand drawing tool and measured with NIH ImageJ software. The tumor necrotic area was outlined and measured in a similar way. Tumor outlines were confirmed by visual inspection of tissue slides under 10X or 40X magnification.

4.2.7 Statistical Analysis

The values of vessel density and average vessel size were transformed to a log scale for correlation analysis and probability estimation, which was calculated by the number of occurrence over the total sample size. A standard unpaired t-test was used to compare the statistical significance of vessel density, vessel size, and VEGF release between different groups. Statistical analysis of vascular permeability and percentage of pO_2 values was completed by a nonparametric Wilcoxon test. Analysis of fluorescence intensity and percentage of tumor necrosis among different groups was done by nonparametric ANOVA test (Kruskal-Wallis test). Statistical significance was accepted at $p < 0.05$.

4.3 Results

4.3.1 Effect of Tumor Host-site on MAT-LyLu Tumor Growth and Histology

The MAT-LyLu tumor growth in the prostatic and subcutaneous environment was compared by implanting the same amount of (1×10^5) cells in both sites. Tumors were excised and weighed at 14 days after implantation. The average tumor weight was 2.84 ± 0.77 g ($N = 5$) and 6.58 ± 1.86 g ($N = 5$) for the subcutaneous and orthotopic MAT-LyLu tumors, respectively. H&E staining of tumor sections revealed that both subcutaneous and orthotopic MAT-LyLu tumors were poorly differentiated adenocarcinomas (Figure 4.1). The occurrence of several mitotic nuclei throughout the entire tumor sections indicated that the tumor had a high growth rate. Infiltration of macrophage and lymphocytes were often observed, especially in the orthotopic tumor. No significant difference in tumor cell morphology was found between tumors in different sites.

4.3.2 Effect of Tumor Host-sites on MAT-LyLu Tumor Vasculature Morphology

The functional vasculature of the MAT-LyLu tumors was stained by intravenously injecting a fluorescent perfusion marker DiOC7₍₃₎ and the representative images are shown in Figure 4.8. The number of functional blood vessels and average vessel size in each fluorescence

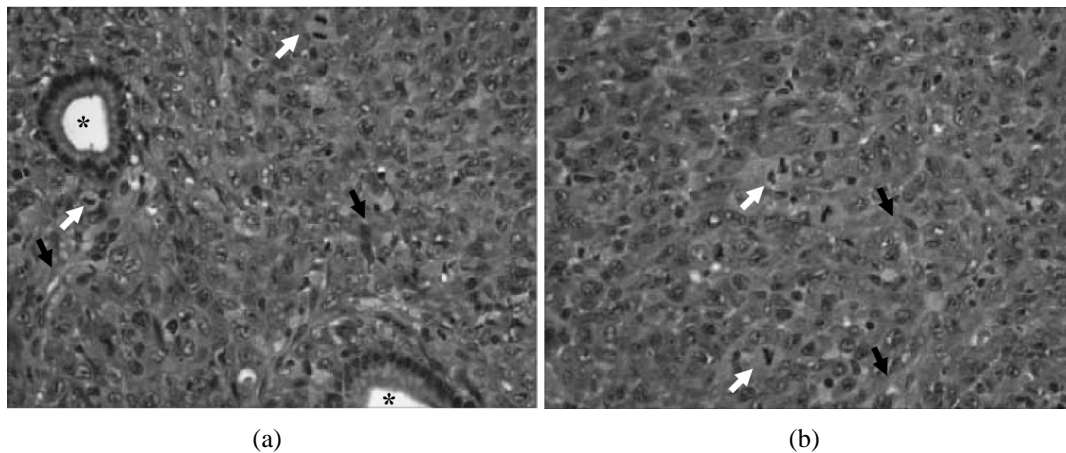


Figure 4.1: H&E staining histology images of orthotopic (a) and subcutaneous tumors (b)(40X). Tumor cells at two host-sites showed no significant different in cell morphology and both sites are present with poorly differentiated adenocarcinoma. Note many mitotic nuclei (*white arrows*) presented at both tumor host-sites, and the present of prostate glandular tissue (★) in the orthotopic sites, *Black arrows*, some blood vessels.

microscopic field (10X, with an area of 1 mm²) was analyzed with NIH ImageJ using an automatic threshold. As shown in Figure 4.2, substantial heterogeneity in tumor vessel size and density is observed in both orthotopic and subcutaneous MAT-LyLu tumors. A slight but statistically significant inverse correlation between the vessel density and the average vessel size was established in both cases. The correlation coefficient was - 0.20 and - 0.31 for the orthotopic and subcutaneous tumor, respectively. The averaged probability distributions of tumor vessel density and average vessel size in the orthotopic and subcutaneous MAT-LyLu tumors, generated from a summation of 209 orthotopic and 191 subcutaneous tumor images, are shown in Figure 4.2(b). It was found that the orthotopic MAT-LyLu tumors tended to have a higher vessel density but smaller vessel size than the subcutaneous ones ($p < 0.01$). The orthotopic tumor had a mean of 85 functional vessels per mm² and

the mean vessel size was $443 \mu\text{m}^2$, whereas the mean vessel density in the subcutaneous tumor was 73 vessels/mm^2 and the mean vessel size was $511 \mu\text{m}^2$.

4.3.3 Effect of Tumor Host-site on Tumor VEGF level

VEGF protein levels in the orthotopic and subcutaneous MAT-LyLu tumors were determined by a rat VEGF ELISA kit. As shown in Figure 4.3, average VEGF level in the orthotopic tumors was more than twice that in the subcutaneous tumors.

4.3.4 Effect of Tumor Host-site on Tumor Oxygenation

Tumor oxygenation was assessed with Eppendorf measurements and the resulting histograms of assembled data are shown in Figure 4.4. The figure shows results from 198 points for the orthotopic and 365 points for the subcutaneous tumors. The averaged mean pO_2 , median pO_2 , and the percentage of values $<5 \text{ mmHg}$ from all tumors in each group together with SD are summarized in Table 4.2. Whereas the mean and median values are not significantly different between the tumors at two different sites, the percentage $<5 \text{ mmHg}$ (hypoxic values) is significantly different, with $11.8 \pm 3.9 \text{ mmHg}$ in the orthotopic and $30.1 \pm 29.5 \text{ mmHg}$ in the subcutaneous case, suggesting fewer hypoxic areas in the orthotopic tumor.

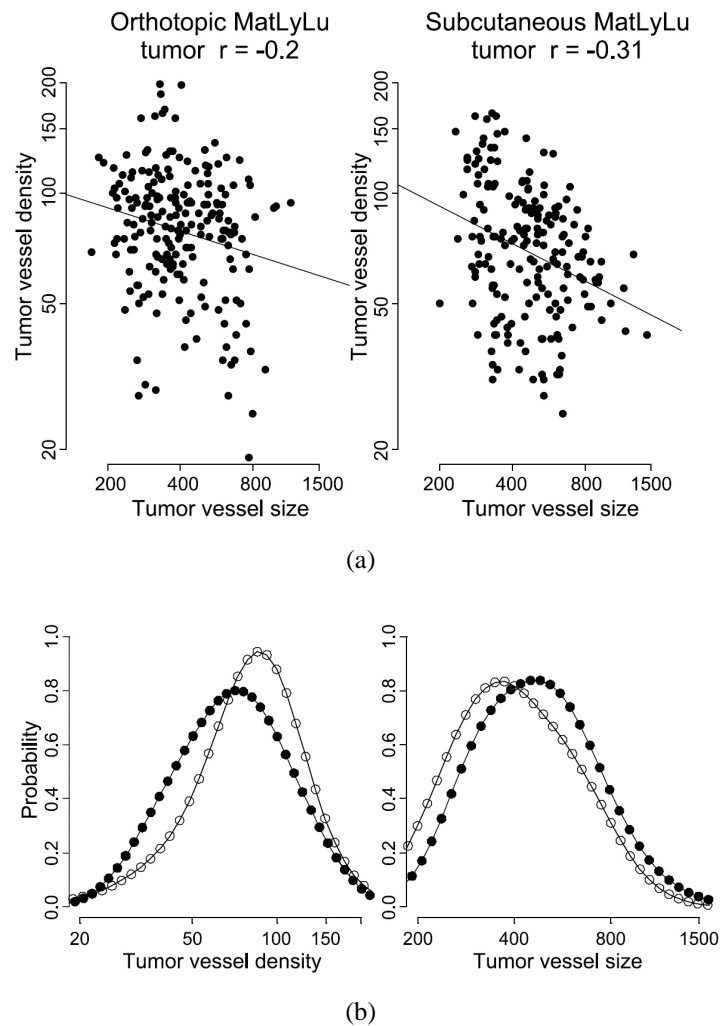


Figure 4.2: (a), as a scatter plot showing an inverse correlation between vascular density (vessels/ mm^2) and average vessel size (μm^2) in both orthotopic and subcutaneous MAT-LyLu tumors; (b) probability estimation of tumor vessel density and average vessel size in the orthotopic (white) and subcutaneous (black) MAT-LyLu tumors. Functional tumor vasculature was stained by injecting a perfusion marker DiOC7₍₃₎ (1 mg/kg, i.v.) to the tumor-bearing animal. Tumor vessel density and vessel size data were generated by analyzing 209 orthotopic and 191 subcutaneous tumor images with NIH ImageJ

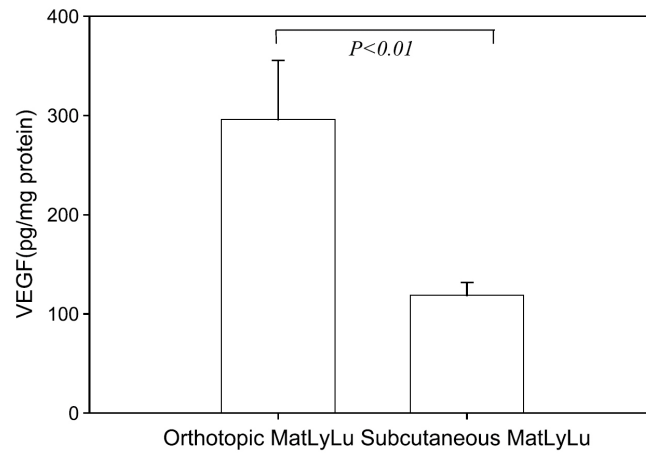


Figure 4.3: Difference in tumor VEGF release between orthotopic and subcutaneous tumors. Total tumor proteins were extracted from tumors in both sites and VEGF level was quantified by ELISA assay. Four tumors were included in each group.

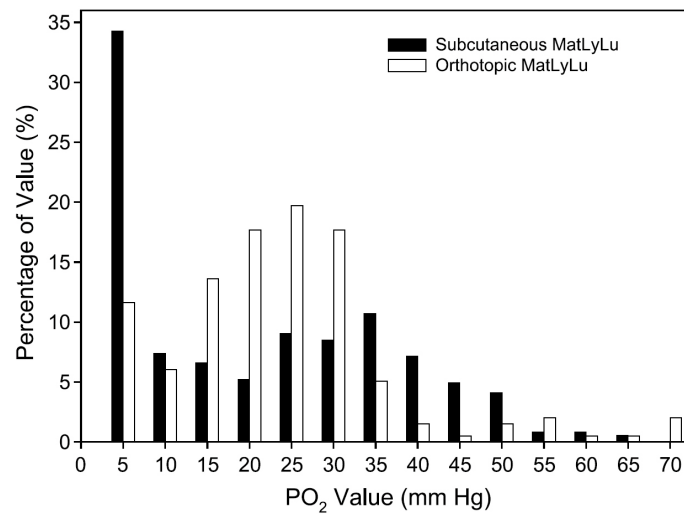


Figure 4.4: Difference in tumor oxygenation profiles between orthotopic and subcutaneous tumors. Oxygen partial pressure was measured by Eppendorf polarographic oxygen electrode. The histogram was generated by pooling all the measurements from tumors in subcutaneous (n = 7) and orthotopic (n = 5) tumor groups.

	Number of samples	pO ₂ Mean ± Stdev (mmHg)	pO ₂ Median ± Stdev (mmHg)	< 5mmHg Percentage ± Stdev
Orthotopic	198 (n = 5)	20.8 ± 4.6	20.8 ± 3.0	11.8 ± 3.9
Subcutaneous	365 (n =7)	19.8 ± 9.5	16.9 ± 11.6	30.1 ± 29.5 *

Table 4.2: Difference in tumor oxygen partial pressure between orthotopic and subcutaneous tumors.

4.3.5 Effect of Tumor Host-sites on Macroscopic Permeability

Vascular permeability in the MAT-LyLu tumors implanted in orthotopic and subcutaneous sites was assessed by Evans blue tumor uptake (Figure 4.5). Uptake of Evans blue dye was significantly higher in the orthotopic tumor than the subcutaneous one at 15 minutes after injection ($p < 0.01$). No significant difference in tumor Evans blue level was found at 1 hour after administration ($p > 0.05$) and by 24 hours after injection, the same amount of Evans blue dye was detected in the orthotopic and subcutaneous tumors.

4.3.6 Effect of Tumor Host-site on Microscopic Permeability

The mean effective permeability coefficient of both tumor host-sites are shown in Figure 4.6. The subcutaneous tumors exhibited a significantly lower effective permeability coefficient as compared with orthotopic tumors ($0.02565 \pm 0.00425 \mu\text{m/s}$; $0.03858 \pm 0.00661 \mu\text{m/s}$; $p < 0.005$; Figure 4.6).

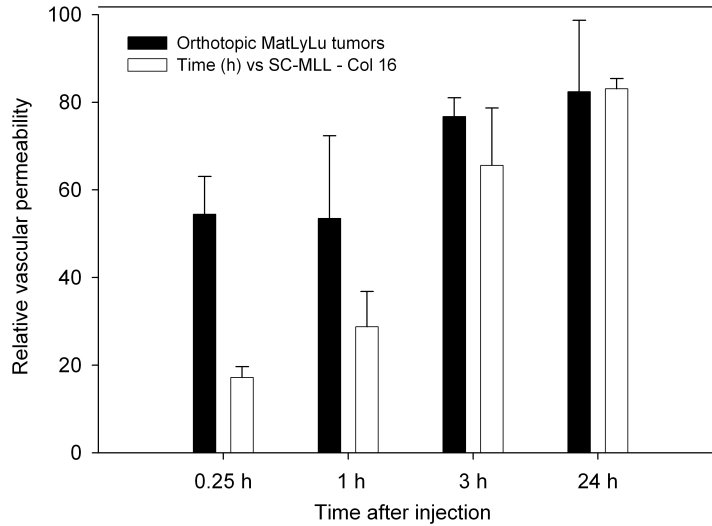


Figure 4.5: Difference in tumor vascular permeability to Evans Blue between orthotopic and subcutaneous tumors. Tumors were excised at different time points after i.v. injection of Evans Blue (10 mg/Kg in PBS). The uptake of Evans Blue was measured by spectrophotometry after tissue extraction with formamide. Each group includes 3 to 5 animals.

4.3.7 Effect of Tumor Host-sites on Interstitial Diffusion Coefficient

The average estimates of diffusion coefficients for both tumor implantation sites are shown in Figure 4.7. The subcutaneous tumors exhibited a significantly lower diffusion rate as compared with orthotopic tumors ($0.88 \pm 0.12 \mu\text{m}^2/\text{s}$; $1.59 \pm 0.20 \mu\text{m}^2/\text{s}$; $p = 0.005$; Figure 4.7).

4.3.8 Effect of Tumor Host Micro-environment on Verteporfin Uptake

To begin assessing the effectiveness of PDT with verteporfin in the orthotopic and subcutaneous MAT-LyLu tumors, the uptake of verteporfin was first quantified by fluorescence

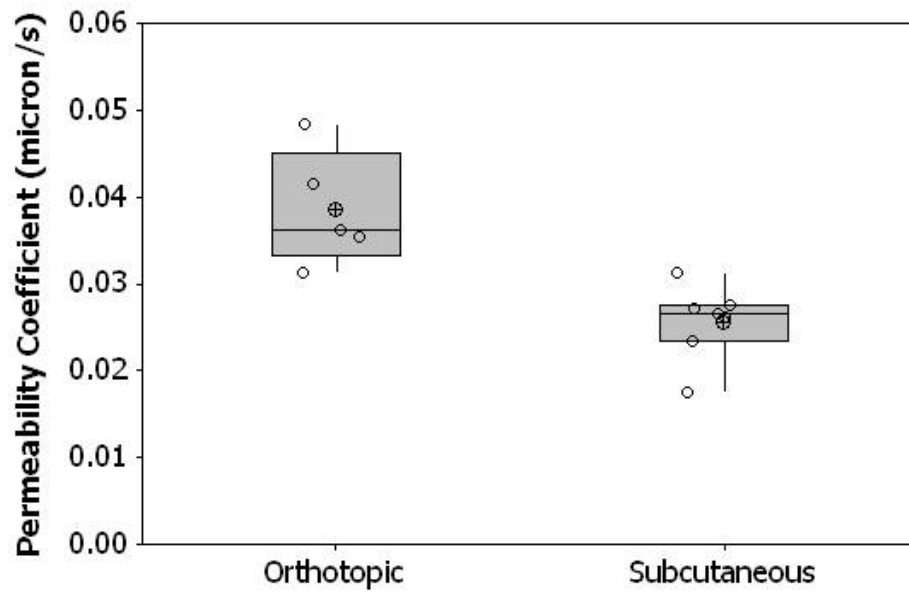


Figure 4.6: Averaged calculated effective diffusive permeability coefficients for subcutaneous ($n=6$) and orthotopic ($n=5$) tumors. Subcutaneous tumors showed a significantly lower transvascular permeability compared to orthotopic tumors ($0.02565 \pm 0.00425 \mu\text{m/s}$; $0.03858 \pm 0.00661 \mu\text{m/s}$; $p < 0.005$).

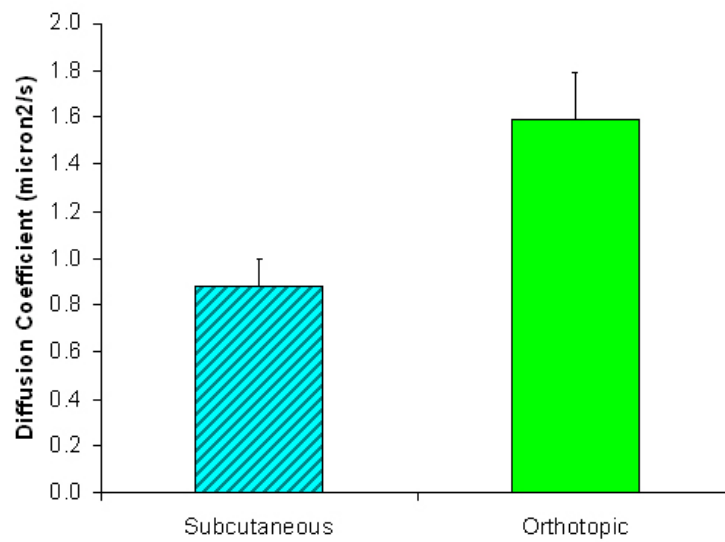


Figure 4.7: The average estimates of diffusion coefficients are shown for the subcutaneous and orthotopic tumor models ($n = 4$ for each group). The diffusion coefficients of three areas per tumor were determined via iterative inverse model fitting to the diffusion prediction. The mean diffusion coefficient is significantly higher in the orthotopic tumors than the subcutaneous tumors. Data are expressed as Mean \pm SE. $p < 0.05$ as compared with subcutaneous tumors.

microscopy. Representative fluorescence images of verteporfin and corresponding perfusion marker DiOC7₍₃₎ images are shown in Figure 4.8. The distribution of verteporfin in the subcutaneous tumor at 15 minutes after administration was almost identical to the perfusion marker, indicating a typical intravascular localization [257]. However, verteporfin distribution in the orthotopic tumor displayed a more diffused pattern compared with the subcutaneous tumor. Verteporfin fluorescence was generally observed throughout the entire tumor section in both orthotopic and subcutaneous tumors at 3 hours after injection. Verteporfin fluorescence intensity was quantified by analyzing 75 to 100 microscopic images from 5 or 6 animals in each group and the results are shown in Figure 4.9 as a box-plot to illustrate the variance (distribution heterogeneity), mean, and median values. Nonparametric ANOVA test indicated that the fluorescence intensity from the orthotopic tumor samples was significantly higher ($p < 0.05$) than from the subcutaneous tumor samples at 15 minutes after injection. However, no significant difference in verteporfin fluorescence intensity was found at 3 hours after injection.

4.3.9 Tumor response to PDT

To assess the PDT treatment effect, tumor necrotic area was measured histopathologically at 2 days after treatments, as described previously [256]. Five tumors were included in each group. The untreated control group had no or minimal (< 5%) spontaneous necrosis. Table 4.3 shows the percentage of tumor necrosis over the entire tumor tissue in each treat-

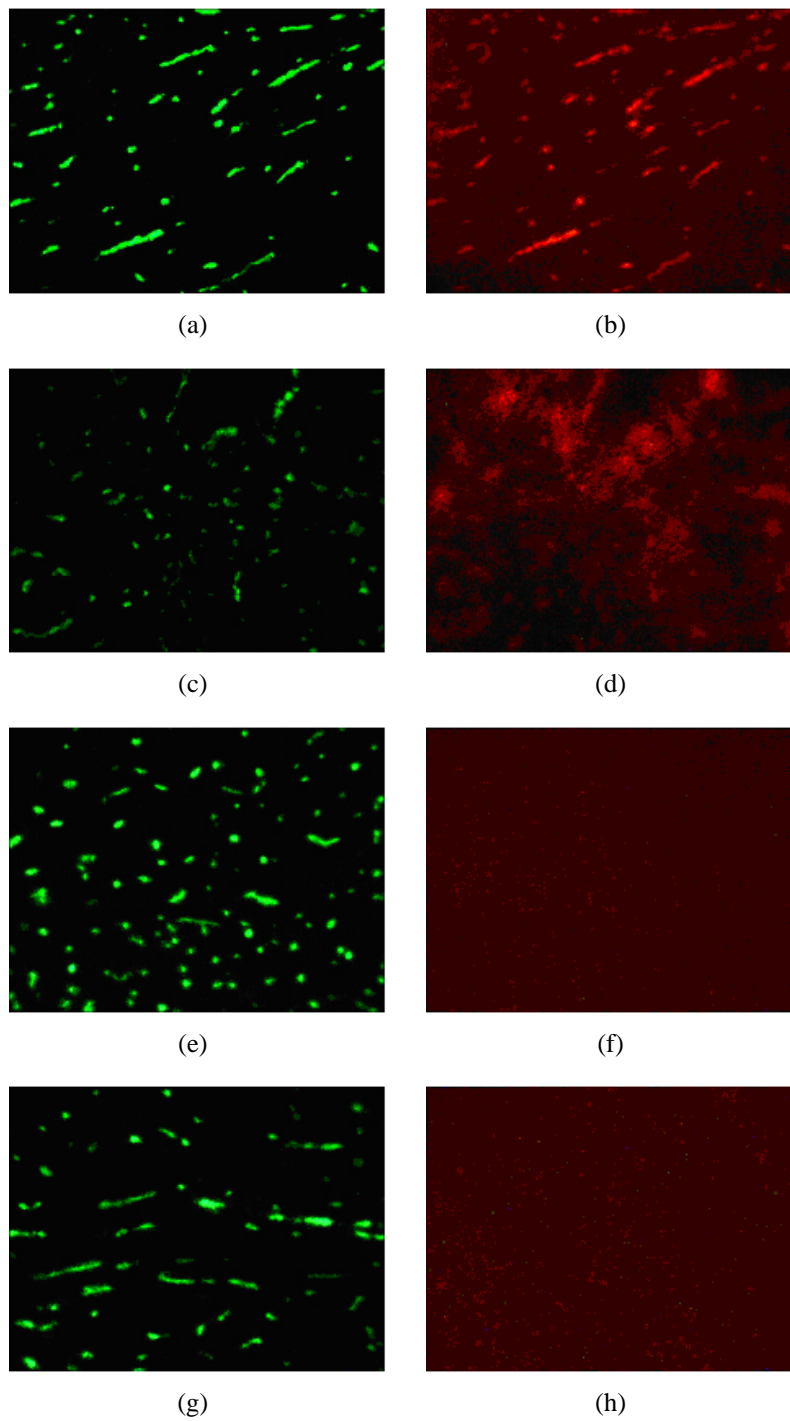


Figure 4.8: Fluorescence images of verteporfin in the orthotopic and subcutaneous MAT-LyLu tumors at 15 minutes or 3 hours after verteporfin i.v. injection (1 mg/Kg). The perfusion marker DiOC7₍₃₎ (1 mg/Kg, i.v.) was injected 1 minute before animal sacrifice to visualize the functional blood vessels. The same microscopic field (objective lens of 10X) was imaged for both DiOC7₍₃₎ (green) and verteporfin (red) by using different filter set. Bar, 100 μm .

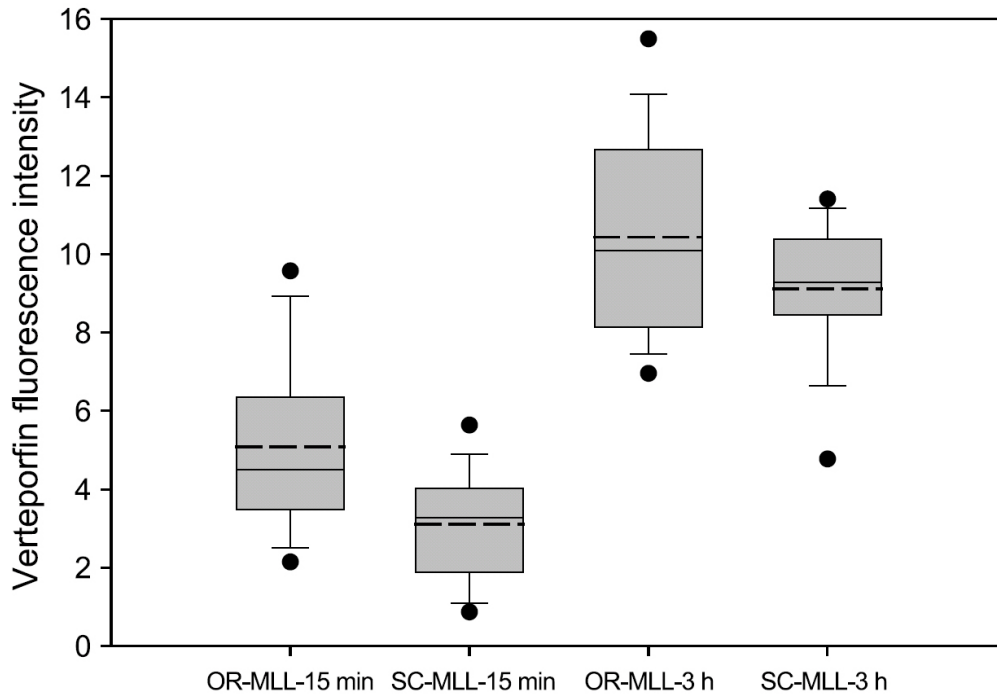


Figure 4.9: Effect of tumor host-sites on verteoporfin uptake in MAT-LyLu tumors. Verteoporfin distribution in orthotopic and subcutaneous tumors was studied by fluorescence microscopy at 15 min and 3 hours following administration (1 mg/Kg, i.v.). Verteoporfin tumor uptake was quantified by measuring fluorescence intensity using ImageJ. Each group included 75 to 100 microscopic images randomly taken from frozen sections obtained from 5 to 6 tumors. The results are presented in a box-plot to illustrate the level and heterogeneity in drug distribution. In the box, 25 percentile data (lower boundary) to 75 percentile data (higher boundary) is shown, while the dots show 5 percentile data to 95 percentile data. The solid line is the median and the dashed line is the mean. Verteoporfin levels in the orthotopic tumor at 15 minutes after injection (OR-MAT-LyLu-15 min) are significantly higher than in the subcutaneous tumor (SC-MAT-LyLu-15 min). Fluorescence intensity increased significantly from the 15 minute time point to the 3 hour timepoint, in both orthotopic and subcutaneous tumors. There is no significant difference in fluorescence intensity between the orthotopic (OR-MAT-LyLu-3 h) and subcutaneous (SC-MAT-LyLu-3 h) tumors at 3 hours after injection.

ment group, with error bars showing the SD. The difference between groups treated with 15 minute drug-light interval PDT was not significant, $84.4 \pm 0.99\%$ necrosis in the subcutaneous tumor and $90.9 \pm 10.1\%$ in the orthotopic tumor. In the case of 3 hours drug-light interval PDT, the percentage of tumor necrosis induced was $28.8 \pm 8.7\%$ and $64.0 \pm 9.2\%$ for the subcutaneous and orthotopic tumors, respectively ($p < 0.01$).

	Vascular-targeting PDT 15-m drug-light interval	Cellular-targeting PDT 3-h drug-light interval
Orthotopic	90.9 ± 10.1	64.0 ± 9.2 ★
Subcutaneous	84.4 ± 0.99	28.8 ± 8.7

Table 4.3: Effect of tumor host environment on tumor necrotic area induced by verteporfin PDTs. ★ indicates $p < 0.01$, significant difference between two host-sites.

4.4 Discussion

As discussed in Chapter 2 and 3, we hypothesize that inter-individual variability in response to PDT treatment is due to the intra-individual and inter-individual pharmacokinetic variabilities, which we believe, are caused by heterogeneous transport processes during the delivery of photosensitizer to the tumor. Before entering the study of inter-individual and intra-individual pharmacokinetic variability, it is essential to test this hypothesis in two populations that represent different physiological characteristics. In this study, we used a rat prostate tumor model inoculated at two host-sits, subcutaneous and orthotopic. We have investigated the tumor host-site effects on tumor microenvironment, transport processes, photosensitizer pharmacokinetics, and response to cellular and vascular-targeting PDTs.

Specifically, we are interested in looking for the answers to the questions: how do transport parameters affect photosensitizer pharmacokinetics, and how do these pharmacokinetics influence the PDT treatment at two tumor inoculation sites?

In addition to this, the report presented here systematically examines the validity of using experimental tumor models to study PDT treatment. This issue becomes even more important when considering that most current PDT studies are done on tumors grown in the ectopic tumor environments (such as subcutaneous space) rather than in their native orthotopic organ environment.

One striking difference between the orthotopic and subcutaneous MAT-LyLu tumor is the growth potential. It was found that tumors in the prostate weighed more than twice than tumors in the subcutaneous space at 14 days after implantation. This result, consistent with the previous studies [247, 258], shows that the prostate environment is more favorable for MAT-LyLu tumor growth. The increased tumor growth in the orthotopic environment is likely related to its high vessel density, which can provide a good supply of nutrients and oxygen to the tumor tissue. Since subcutaneous MAT-LyLu tumors have a lower vascular density than the orthotopic ones, the intervascular space could be larger, which leads to regions of low oxygenation due to limited oxygen diffusion distance [259]. As shown, tumor oxygenation measured by the Eppendorf electrode confirmed that the subcutaneous MAT-LyLu tumor had a higher fraction of hypoxic area ($pO_2 < 5$ mmHg) than the orthotopic tumor (Table 4.2).

The difference in vessel density between the subcutaneous and orthotopic MAT-LyLu tumor can be partially explained by the difference in the VEGF level in the tumor tissue. To maintain a sustained growth, tumors need to develop new vasculature to fulfill the requirements for oxygen and nutrients. This angiogenic process is often triggered by the release of proangiogenic factors such as VEGF and basic fibroblast growth factor [159]. VEGF is the most potent proangiogenic factor detected in various tumors [161]. We found in this study that the VEGF level in the orthotopic MAT-LyLu tumor was about 2.5-fold greater than in the subcutaneous tumor. This is in agreement with the higher vascular density (Figure 4.2) and vessel permeability (Figure 4.5 and 4.6) observed in the orthotopic tumor vasculature, suggesting a stronger angiogenic stimulus in the orthotopic environment [155, 260]. Higher expression of other angiogenic factors has also been reported in some human prostate tumor lines orthotopically implanted in the mouse prostate [244, 246, 261]. Thus, prostate cancer cells grew in the orthotopic site displayed much higher growth potential than cells in the ectopic (subcutaneous) host environment.

Effective delivery of photosensitizer depends on the transport barriers photosensitizer molecules encountered during the transport processes. After verteporfin injection, verteporfin molecules distribute in the systemic circulatory system, distribute in tumor vasculature, transport across tumor vessel wall, and distribute through tumor interstitium (Chapter 3). At the tumor level, the vessel density, transvascular transport and interstitial transport are the dominant factors for the effective drug delivery. From the tumor microenvironment

study here, it was established that the orthotopic tumors present a significantly higher vessel density (Figure 4.2(b)), higher effective vascular permeability (Figure 4.5 and 4.6) and interstitial diffusion coefficient (Figure 4.7). These transport parameters in orthotopic tumors indicate a higher verteporfin transport rate in orthotopic tumor site, leading to a higher verteporfin uptake in orthotopic tumors. Indeed, we have found a significantly higher verteporfin uptake in orthotopic tumor tissues at 15 minutes after injection (Figure 4.9). However, surprisingly, we found there is no significant difference of verteporfin tumor uptake at the 3 hour time point, comparing two tumor host-sites. This phenomena is accompanied with the fact that there are huge variation among individuals within orthotopic and subcutaneous tumor groups. Thus the comparison between two tumor groups shows no significant difference. Analysis of inter-individual and intra-individual verteporfin pharmacokinetic variabilities and their relations to the transport parameters will be discussed in Chapter 5.

PDT-induced tumor necrosis was measured to compare the tumor response at different sites. We attempted to isolate the direct tumor cellular effect and the secondary vascular effect by using the drug-light intervals at either 15 minutes or 3 hours. In previous studies, we have shown that these two regimens can determine where the damage largely occurs [257, 262]. It is interesting to find that the vascular targeting approach (15 minutes drug-light interval) yielded similar tissue damage (near 85-90%) for both types of tumors (Table 4.3), although there was a significant difference in photosensitizer uptake and tumor

hypoxic area. This result suggests that vascular targeting PDT is not sensitive to tumor micro-environment issues related to photosensitizer and oxygen delivery since the vessels may have an adequate supply of both. A recent study shows that vascular targeting PDT can even circumvent the multi-drug resistance in cancer cells for an improved cancer therapy [263]. Another explanation for this is that, in vascular targeting PDT, tissue damage is introduced by the inflammation effects triggered by the damage to tumor endothelial cells. This inflammatory effect might homogenize the PDT effect, and produce equally effective treatment even though verteporfin tumor uptake levels are significant different at two tumor sites. This homogenization effect is also found reduce the inter-individual variability in response to PDT within each host-sit group. The coefficient of variation (standard deviation, mean ratio) in tumor necrotic area in vascular targeting PDT is lower compared with cellular targeting PDT (11.1% *v.s.* 14.2% at orthotopic sites, and 1.2% *v.s.* 30.2% at subcutaneous sites).

In contrast, the cellular targeting PDT treatment (3 hours drug-light interval) did show strong dependence on tumor host-site. Significant difference in tissue damage was observed in the subcutaneous versus the orthotopic tumors. Photosensitizer uptake apparently is not a major cause for this difference since the drug level was found to be similar at the time of PDT treatment. The difference in tumor response to the cellular targeting PDT is likely due to different tumor vasculature and oxygenation status observed in the orthotopic and subcutaneous tumor micro-environment. It has been shown that micro-regional differences

in vascular density affect oxygen delivery, and that a larger intercapillary spacing pattern can decrease PDT efficacy due to the limitation of oxygen delivery, thereby reducing the amount of singlet oxygen produced in the tissue [264, 265]. Thus, lower vascular density and higher hypoxic fractions observed in the subcutaneous MAT-LyLu tumors might be the major reason for limited tumor response. Detailed discussion about the intra-individual and inter-individual verteporfin pharmacokinetic variabilities and their effects on vascular and cellular targeting PDT treatment will be presented in Chapter 7.

4.5 Conclusions

In summary, it was shown that the R3327-MAT-LyLu tumors, grown orthotopically in the prostate and subcutaneous, display difference in tumor vasculature, oxygenation and the level of VEGF expression. Orthotopic tumors exhibit 16.4% higher vessel density, 13.3% smaller vessel size, 60.8% more hypoxia fraction and one fold higher VEGF expression level compared to subcutaneous tumors. The difference in tumor pathophysiologic properties induced by tumor host environment affects photosensitizer transport parameters, photosensitizer uptake and response to PDT. Microscopic transvascular permeability of orthotopic tumors shows 50% higher than subcutaneous, whereas, the interstitial diffusion coefficient of orthotopic tumors is 80% higher compared with subcutaneous tumors. 66% higher BPD tumor uptake was found in orthotopic tumors 15 minutes after verteporfin i.v. administration. Cellular targeting PDT (long drug-light interval) was found sensitive to

tumor host microenvironment (orthotopic tumors exhibit one fold larger necrotic area than subcutaneous tumors), whereas the vascular targeting PDT (short drug-light interval) was insensitive to such variation.

Chapter 5

Correlation between Verteporfin

Transport Parameters and Verteporfin

Pharmacokinetics

The transport parameters have been characterized at two tumor inoculation sites, relative to their effects on verteporfin tumor uptake and tumor responses to PDT. We concluded that orthotopic tumors have a higher vessel density, higher vascular permeability, and higher interstitial diffusion rate, which one of these parameters determines the verteporfin tumor uptake levels remains unknown. In addition, a large inter-individual and intra-individual variability exists in the verteporfin concentration. In Chapter 3, we have discussed the theory of drug delivery to tumors, and proposed a hypothesis that intra-tumor and inter-tumor

variabilities of transport parameters, *e.g.*, transvascular permeability, interstitial diffusion rate, all contribute to cause the variation observed in verteporfin uptake. In this chapter, these microscopic transport processes are discussed, and are found to be the most dominant factors for verteporfin distribution in tumor.

5.1 Introduction

The transport of drugs in tissue has been an extensive area of study, yet tools to accurately interpret these processes have largely been limited in accuracy by the use of simplistic geometries and because of problems associated with variation in transport between tumor types. We have developed transvascular transport models and interstitial transport models to simulate photosensitizer transport processes in complex geometries, as defined by histology images. These parameters were examined as to how they affect the photosensitizer intra-tumor distribution at two tumor inoculation sites, namely the subcutaneous and orthotopic locations.

As discussed in Chapter 1, in photodynamic therapy, the photosensitizer transport issue is especially problematic as the treatment efficacy is a non-linear function of the amount of photosensitizer present combined with the total light irradiation dose and the oxygenation of the tissue. In recent years, the dosimetry issues with photodynamic therapy have shown that there are complex temporal and spatial heterogeneity issues related to the oxygen supply, the photosensitizer supply and the photobleaching of photosensitizer. One important

aspect of understanding the treatment efficacy is to have a clear understanding and modeling of the photosensitizer transport processes inside the tumor, namely, the distribution in the tumor vasculature, transvascular transport, interstitial transport and elimination from tumor vascular/lymphatic networks.

The vasculature in solid tumors have high spatial heterogeneity and this results in observable changes in photosensitizer transport. Tumor vessels have irregular structure, diameters and branching patterns [165, 167, 168, 266], as well as thin walls, and incomplete basement membrane and abnormal pericytes [169, 267–269]. These anatomic abnormalities are likely the origin of the unusual leakiness, intermittent blood flow, low pressure, spontaneous hemorrhage and stasis which are all observed in local regions of the tumor [141, 171–173, 252, 270, 271]. These abnormalities influence the delivery of therapeutic molecules to the interior of solid tumors, and in turn, affects treatment efficacy. As experimental models for tumors have been established, it has become clear that many factors influence the transport process of drugs in solid tumors, to the point where tumors that are simply grown in different locations can have dramatically different vascular characteristics [156, 251, 272], and different responses to a given therapy [273, 274].

Photodynamic therapy involves treating the solid malignancies with tissue penetrating light following the systematic administration of certain photosensitizers that can be localized somewhat preferentially in neoplastic tissues. These photosensitizers are activated by the appropriate wavelength of light, and subsequently produce reactive oxygen species such

as singlet oxygen ($^1\text{O}_2$) to induced cellular toxicity [90, 275]. The photosensitizer distribution is one of the key factors that influences the treatment efficacy of photodynamic therapy. Our previous studies indicated the dynamic distribution of BPD in the RIF-1 tumor model [257], observing that the distribution is dominated by the vascular localization initially, and that this is gradually transported out into the tissue to a relatively homogeneous distribution within the time scale of 3 hours after intravenous administration. While this observation was shown in drug concentration, it also dominated the treatment effect, in that the vascular damage was dominant in tumor destruction at short drug-light intervals, while the cellular death mechanism was more dominant with 3 hour drug-light time intervals. Thus, developing a complete model-based understanding of photosensitizer transport processes inside the tumor will provide useful insight into how to maximize treatment efficacy with this type of therapy. In addition, there have been numerous reports illustrating inter-individual variability in response to PDT treatment. This inter-individual variability is thought to be caused by photosensitizer pharmacokinetic variability between the individuals. From observations in this work in orthoptic and subcutaneous tumors, a hypothesis was developed that inter-individual pharmacokinetic variability is caused by heterogenous transport processes between individuals. If this is true, mathematical modeling of photosensitizer transport inside the tumor can facilitate a better understanding of the dominant transport factors that affect this distribution and possibly elucidate the origins of inter-individual variability.

Entering into this study, it is important to clearly acknowledge that developing a com-

plete mathematical description of the transport process is likely not possible due to the overwhelming heterogeneity of the tumor and the mixture of causes of these transport processes. However, approaching the problem from a heuristic perspective, we observe verteporfin that enters the tumor vasculature reaches the cancer cells and interstitial space via transport processes due to the concentration gradient present. Provided that the interstitial fluid pressure inside the solid tumor is significantly higher than the normal tissue, then convection due the fluid exchange can be ignored (Chapter 3). There are many other factors influencing the transport such as convection, leakage, pressure changes, but if the dominant process is thought to be diffusion then we can approach the transvascular transport and interstitial transport as a diffusion problem. Indeed, most transvascular transport and interstitial transport analysis has been performed based on diffusion theory, where the exchange flux of molecules are proportional to the molecular concentration gradients(Chapter 3).

This chapter presents a lumped transvascular transport model and a distributed 2-dimensional heterogeneous diffusion model of BPD transport inside the tumor. A carbocyanine fluorescence vessel marker DiOC7₍₃₎ was used to obtain unambiguous information about the geometry of the perfused tumor vasculature. The permeability coefficient was solved using an intravascular-extravascular compartment model. The interstitial diffusion transport equation was solved using the finite element method with a simplified Patlak boundary condition for solute flux on the intravascular-extravascular boundary. Once the forward solver was implemented, an inverse problem solver was built comparing pixel values in the

simulation to the intensities observed in the experimentally obtained fluorescence images of the tumor. The molecular diffusion coefficient was iteratively updated after each forward calculation until the optimal interstitial diffusion parameter was found. While the processes are not completely diffusive, we can still define an 'effective' permeability coefficient and an 'effective' interstitial diffusion coefficient and examine how these parameters are altered intra-individually and inter-individually, and how these transport parameters affect the photosensitizer tumor uptake.

5.2 Materials and Methods

5.2.1 Photosensitizer

Verteporfin (lipid-formulated benzoporphyrin derivative monoacid ring A) was obtained from QLT, Inc. (Vancouver, Canada). A stock saline solution of verteporfin was reconstituted according to the manufacturer's instructions and stored at 4 °C in the dark. It was injected intravenously to the animals at the dose of 0.25 mg/Kg at 15 minutes or 1.0 mg/Kg at 3 hours before light irradiation.

5.2.2 Animals and Tumor Models

Male Copenhagen rats with average 120 g-150 g body weight (Charles River Laboratories, Wilmington, MA) were used for this study. All animals were housed in the animal facility

with 12-h light/dark cycles, having temperature control and free access to water and standard laboratory diet. All procedures and experiments were approved by the Animal Care and Use Committee of Dartmouth College. For all procedures, the rats were anesthetized with an intra-muscular injection of a mixture of Ketamine and Xylazine (90:9 ratio). The rat abdomen area and hind flanks were shaved and cleaned with Betadine solution. In some animals, a subcutaneous tumor was introduced by injection of 1×10^5 cells of the R3327 MAT-LyLu (Metastatic AT-Lymph Node and Lung) [253] Dunning rat prostate tumor on the right flank in a volume of 50 μ l. In some animals, a lower laparotomy was performed during the orthotopic tumor injection; the bladder was pulled aside in order to expose the prostate. In these animals, an orthotopic tumor was induced by injecting 1×10^5 cells of the same tumor line in 50 μ l PBS into the prostate ventral lobe. The injection site was cleaned by 70% ethanol to kill any possible leaky cancer cells and the incision was closed aseptically. Animals were followed daily to track the tumor growth, and it was observed that reasonably sized tumors were observed after seven days post implantation.

5.2.3 Verteporfin Plasma Pharmacokinetics

Verteporfin plasma concentrations were measured in eight Copenhagen rats for 8 hours. The animals were anesthetized and lipid formulated BPD was injected at 1.0 mg/Kg as described above. 200 μ l blood were drawn from the Jugular vein of each animal. The plasma was separated from the blood by centrifugation at 8000 rpm at 4°C. The plasma was

diluted by a factor of 10 in 1% SDS in PBS and placed in a 2.5 ml cuvette. The fluorescence spectrum was recorded by FluoroMax-2 (Jobin Yvon Inc., Edison, NJ) excited at 430 nm. The peak fluorescence intensities at 690 nm were converted to g/ml using the fluorescence intensity-BPD concentration calibration curve obtained by the fluorospectrometer.

5.2.4 Microscopy and Image Analysis

Fluorescence microscopy was completed with a Nikon Diaphot-TMD microscope using a 100 Watt Mercury Lamp and Q-imaging Micropublisher CCD Camera (Burnaby, BC, Canada). The system used a 10 X objective magnification to carry out the photography of the fluorescence images, resulting in 682×512 pixels² or 1150×863 μm^2 images. A narrow excitation band (470-490 nm) fluorescein cube (DM510, B1E; Nikon, Garden City, NY) with 520-560 nm emission filter and a 405-445 nm excitation with 685-715 nm emission filter (560DCXR, C36848, Chroma Technology Corp., VT) were used for DiOC7₍₃₎ and BPD fluorescence images respectively. In order to analyze images of fluorescence from BPD as a function of distance from the capillaries, a custom MATLAB (MathWorks, Inc.) program was developed to read in the DiOC7₍₃₎ image along with the co-localized BPD image, and track out spatially from the edge of each vessel and calculate the fluorescence per pixel as a function of distance from the vessel wall. This program is described briefly in our previous work [257] and is available as an online calculator at (<http://biolight.thayer.dartmouth.edu>). This procedure allows reasonably good

estimation of the intravascular drug profile as a function of distance from a single or a few sets of fluorescence images.

5.2.5 Verteporfin Transvascular Transport

In this study, we have derived several approximate relations to calculate the average effective diffusive permeability coefficient (P_d) based on the fluorescence images taken at 15 minutes after verteporfin i.v. injection. The average effective permeability coefficient (P_d) is defined as the ratio of extravasating flux (J_s) of the photosensitizer to its transvascular photosensitizer concentration gradient ($\Delta C = C_v - C_{i,0}$) per unit vessel wall surface area [186, 187]:

$$P_d = \frac{J_s}{S (C_v - C_{i,0})} \quad (5.1)$$

Assuming that at time zero, photosensitizer concentration in the interstitial space is negligible, Equation 5.1 can be approximated as:

$$P_d = \frac{J_s}{S (C_v)} \quad (5.2)$$

Rate of interstitial accumulation of photosensitizer molecules is: $\frac{dN_i(t)}{dt}$.

For a large tissue region which include many blood vessels, the flux J_s should be approximately equal to the rate at which photosensitizers accumulate in this region, provided

that lymphatic removal of photosensitizer molecules is negligible [186, 187]. Thus,

$$P_d = \frac{dN_i(t)}{S(C_v)} \quad (5.3)$$

Since no variation is likely to exist in the photosensitizer concentration in plasma among vessels included in tissue region, then, the number of photosensitizer molecules in vascular compartment can be approximated as:

$$N_v(t) = \sum_j (C_v V_{v,j} (1 - H_{T,j})) = C_v V_v (1 - H_T) \quad (5.4)$$

where $V_{v,j}$ and $H_{T,j}$ are the vascular volume and hematocrit of vessel j , respectively, and H_T is the mean hematocrit weighted with the vascular volume: $H_T = \frac{\sum (V_{v,j} H_{T,j})}{\sum V_{v,j}}$.

Photosensitizer plasma concentration and interstitial concentration can be approximated as [186, 187]:

$$C_v = \frac{N_v(t)}{V_v (1 - H_T)} \quad (5.5)$$

$$C_i = \frac{N_i(t)}{V_i} \quad (5.6)$$

Substituting Equation 5.5 and 5.6 to Equation 5.4, and assuming linearity exists between the number of photosensitizer molecules ($N(t)$) and the average fluorescence in-

tensity, $(I(t))$, for both vascular and interstitial compartments, then the average effective diffusive permeability can be expressed as [186, 187]:

$$P_d = \frac{V_v (1 - H_T) \frac{dI_i}{dt}}{S I_{v,0}} \quad (5.7)$$

where I_i is the total fluorescence intensity in interstitium and $I_{v,0}$ is the total fluorescence intensity in the intravascular compartment at time of photosensitizer i.v. injection, which can be approximated as $C_v(t = 0) = C_v(t = 15m) \times \frac{C_p(t=0)}{C_p(t=15m)}$, assuming the drug concentration in the tumor vasculature has the same concentration temporal dynamic profile as systemic circulation.

5.2.6 Verteporfin Interstitial Transport

The theory of blood-born molecule transportation in interstitium was well-established since Krogh's cylinder model [276, 277], which showed the analytical prediction of oxygen delivery through the capillary. Many physiological and pathological experiments as well as mathematical modeling of molecular transport have been completed [277], including the small molecules (oxygen, some therapeutic drugs) and larger macromolecules [193, 194, 203, 204]. The transport of macromolecules in tumor interstitium could be simplified as a diffusion process, which is governed by the following diffusion equation:

$$\frac{\partial C_i(x, y, t)}{\partial t} = \nabla \cdot (D \nabla C_i(x, y, t)) \quad (5.8)$$

with Patlak boundary condition for solute flux on the boundary between intravascular and extravascular compartment:

$$(-DS \nabla C)_\Gamma = \vec{J}_s = P \vec{S} (C_{i,\Gamma} - C_v) \quad (5.9)$$

where $C_i(x, y, t)$ is the photosensitizer concentration at position (x, y) ; D is the diffusion coefficient for photosensitizer in the tumor; P is the diffusive permeability coefficient, as discussed in the transvascular transport section; $\vec{S} = S \hat{n}$ is the tumor vasculature surface area vector; $C_{i,\Gamma}$ is drug concentration at the intravascular-extravascular compartment interfaces, C_v is drug concentration in vascular compartment.

For simplicity, the diffusion coefficient is assumed to be spatially-independent and time-independent, which may not be true for the heterogeneous tumor micro-environment. In addition, there may be multiple components of the photosensitizer such as albumin-bound, free, and lipid bound components, however for simplicity these are all grouped together here. The implications and limitations of this will be reviewed in the Discussion section.

Finite Element Numerical Implementation

Equation 5.8 was solved using a standard finite element method in a two dimensional domain using linear triangular elements [278], which assume the photosensitizer concentration at each point at time t , $\tilde{C}^{(e)}(x, y; a)$ (finite element approximation), can be interpolated as a linear combination of concentration at its three element nodes, as shown here,

$$\tilde{C}^{(e)}(x, y; a) = \sum_{j=1}^3 a_j \Phi_j^{(e)}(x, y) \quad (5.10)$$

where a_j is the concentration value at element node, and $\Phi_j^{(e)}(x, y)$ is the basis function used in finite element computations. Following the Galerkin Weighted-Residuals Method [278], Equation 5.8 was converted to a discretized linear system by integrating the equation multiplied by the basis functions $\Phi^{(e)}(x, y)$. The diffusion equation can then be written in the matrix equation form as follows:

$$\begin{bmatrix} M_{11}^{(e)} & M_{12}^{(e)} & M_{13}^{(e)} \\ M_{21}^{(e)} & M_{22}^{(e)} & M_{23}^{(e)} \\ M_{31}^{(e)} & M_{32}^{(e)} & M_{33}^{(e)} \end{bmatrix} \begin{Bmatrix} \partial a_1 / \partial t \\ \partial a_2 / \partial t \\ \partial a_3 / \partial t \end{Bmatrix} + \begin{bmatrix} K_{12}^{(e)} & K_{12}^{(e)} & K_{13}^{(e)} \\ K_{22}^{(e)} & K_{22}^{(e)} & K_{23}^{(e)} \\ K_{31}^{(e)} & K_{32}^{(e)} & K_{33}^{(e)} \end{bmatrix} \begin{Bmatrix} a_1 \\ a_2 \\ a_3 \end{Bmatrix} = \begin{Bmatrix} F_1^{(e)} \\ F_2^{(e)} \\ F_3^{(e)} \end{Bmatrix} \quad (5.11)$$

where

$$M_{ij}^{(e)} = \iint \Phi_i^{(e)} \Phi_j^{(e)} dx dy \quad (5.12)$$

$$K_{ij}^{(e)} = D \iint \frac{\partial \Phi_i^{(e)}}{\partial x} \frac{\partial \Phi_j^{(e)}}{\partial x} dx dy + D \iint \frac{\partial \Phi_i^{(e)}}{\partial y} \frac{\partial \Phi_j^{(e)}}{\partial y} dx dy \quad (5.13)$$

$$F_{ij}^{(e)} = \oint \tilde{\tau}_{-n}^{(e)} \Phi_i^{(e)} ds \quad (5.14)$$

$\oint \tilde{\tau}_{-n}^{(e)} \Phi_i^{(e)} ds$ is the boundary flux integral, related to the Patlak boundary condition (Equation 5.9). Following the Crank-Nicolson-Galerkin scheme [279] to insure the stability and second order accuracy in both temporal and spatial domain, the diffusion equation governing the whole domain becomes the following assembled matrix equation:

$$\{[M] + \frac{\Delta t}{2}[K]\}\{a(t_{n+1})\} = \{[M] - \frac{\Delta t}{2}[K]\}\{a(t_n)\} + \{F(t_n)\} \quad (5.15)$$

In this study, the DiOC7₍₃₎ fluorescence images were loaded into MATLAB, converted to black-white images and partitioned to intravascular and extravascular compartment. A finite element mesh was then created in MATLAB PDE Toolbox contained 8,000 ~ 10,000 nodal points for the 1,150×863 μm images, as shown in Figure 5.1.

In MATLAB, three arrays contain all the geometry and vasculature structure information of the fluorescence image, in the node, element and boundary element arrays, which are used to create files for computation on. The repetitive solution of Equation 5.11 formally requires the computation, storage and multiplication of $\{[M] + \frac{\Delta t}{2}[K]\}^{-1}$. If approached di-

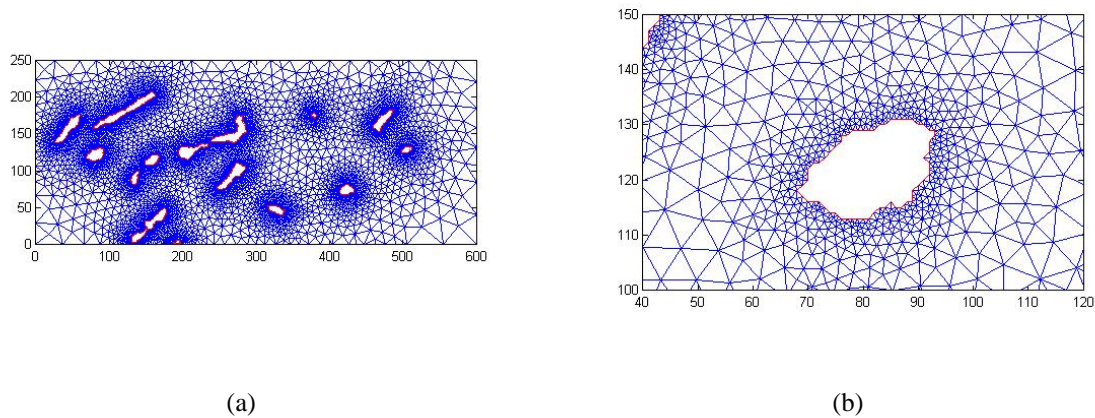


Figure 5.1: An example finite element mesh for tumor interstitium is shown here. The blank areas are the functional capillaries and the light areas are the tumor parenchyma. In this mesh, 16,838 triangle elements were used with 8,536 nodes. (b) shows a magnified interstitial region around a vessel.

rectly, this would require full matrix storage (N^2 for a mesh of N nodes) and excessive runtime (N^3 operations). Thus, it was essential to take advantage of banded matrix storage and computation techniques. The program was written in Fortran, and the subroutine library LAPACK (Linear Algebra PACKage, <http://www.netlib.org/lapack/>) was used for solving the linear inversion problems. In this study, the Mode 3 banded matrix storage method and SGEMM (Single precision GEneral Matrix Multiplication), SGBSV (Single precision General Band Simple driVer) subroutines were used for storage, multiplication, and matrix equation calculation respectively. To use these storage mode and subroutines efficiently, small half-bandwidth is required. However, the mesh generated by the MATLAB PDE (Partial Differential Equation) toolbox usually contained a very large bandwidth due to node numbering scheme that was not optimized for banded matrices. Thus, to solve this

problem, the node, element and boundary element files were further modified by a custom Collins-type bandwidth reduction program [280]. New node, element and boundary element files were created, and used for the matrix calculation. The bandwidth reduced files decreased the half-bandwidth of original node numbering scheme from 8,000 to 115 nodes, thereby minimizing the storage and computational resources needed to solve the matrix inversion to solve Equation 5.11.

Diffusion Coefficient Estimation

An inverse model developed was used for the calculation of diffusion coefficient of the photosensitizer, based on the photosensitizer fluorescence images (assumed to be the measurement data a_m). A set of diffusion coefficients ranging from $D_0 = 0.1 \mu\text{m}^2/\text{s}$ to $D_1 = 10.0 \mu\text{m}^2/\text{s}$ with an interval $\Delta D = 0.1 \mu\text{m}^2/\text{s}$ (D_0, D_1 obtained from experimental data [156]) were used for the forward model to calculate the photosensitizer distribution at certain time point, t (15 minutes in this study). The Root Mean Square (RMS) error between the forward simulation result with diffusion coefficient D , and photosensitizer fluorescence images was calculated according to the following formula:

$$RMS(D) = \sqrt{\frac{\sum_{i=1}^{nnode} (a_m(i) - a_c(i))^2}{nnode}} \quad (5.16)$$

where $a_m(i)$ is the photosensitizer concentration measurement at node i , $a_c(i)$ is the calculated photosensitizer concentration at node i , $nnode$ is total number of nodes in the area of interests. The objective of the inverse model was to find the unique optimal diffusion coefficient D , which would minimize the RMS error. A total number of twelve fluorescence image sets (three fluorescence images from each animal and four animals from each group) was used as measurement data and an average effective diffusion coefficient of BPD for subcutaneous and orthotopic tumors were obtained.

5.3 Results

5.3.1 Verteporfin Plasma Pharmacokinetics

The BPD plasma concentration at different time points after BPD injection were acquired from 8 animals. Samples of the blood were extracted and the BPD concentrations were quantified using a cuvette-based spectrofluorometer. Each set of BPD plasma pharmacokinetic data, one per animal, was normalized to the mean BPD plasma concentration at time of injection. These normalized data were then fitted to a two-compartment model, the four empirical parameters (A , B , $\tau_{\frac{1}{2}\alpha}$, and $\tau_{\frac{1}{2}\beta}$) were estimated. Each animal set of four empirical parameters was listed in Table 5.1. The final global fitted double-exponential decay model can be expressed as:

$$C(t) = 0.82e^{-6.04t} + 0.18e^{-0.12t} \quad (5.17)$$

where t is the time after BPD administration (in hours) and $C(t)$ is the normalized BPD concentration. The experiment data and fitted curve are shown in Figure 5.2. Thus the two metabolic lifetimes are then 9.6 minutes for the first rapid decay, and 8.3 hours for the secondary slower decrease.

Animal ID	Age (Weeks)	Body Weight (g)	A (A.U.)	B (A.U.)	$\tau_{\frac{1}{2}\alpha}$ (mins)	$\tau_{\frac{1}{2}\beta}$ (hrs)
1	6	195	0.59	0.20	7.92	4.22
2	5	185	0.66	0.16	9.56	6.32
3	5	155	0.86	0.18	7.13	5.27
4	5	180	0.99	0.20	5.72	5.59
5	6	160	0.95	0.16	8.76	6.88
6	7	155	1.11	0.18	5.67	6.82
7	5	165	0.78	0.20	4.11	4.53
8	5	185	0.82	0.17	8.17	8.80

Table 5.1: Two-compartment model parameter estimations for individual animals. Each pharmacokinetic data set was fitted to $C(t) = Ae^{-\alpha t} + Be^{-\beta t}$, elimination half-lives $\tau_{\frac{1}{2}\alpha} = \ln 2/\alpha$ and $\tau_{\frac{1}{2}\beta} = \ln 2/\beta$.

In Figure 5.2, the final global fitted model is represented by a red thick curve, and the raw data are represented by the black thin curves.

5.3.2 BPD localization changes over time

Co-staining with DiOC7₍₃₎ showed that at the 15 minute time point after VFI injection, most verteporfin molecules were localized proximal to DiOC7₍₃₎ positive structures. This

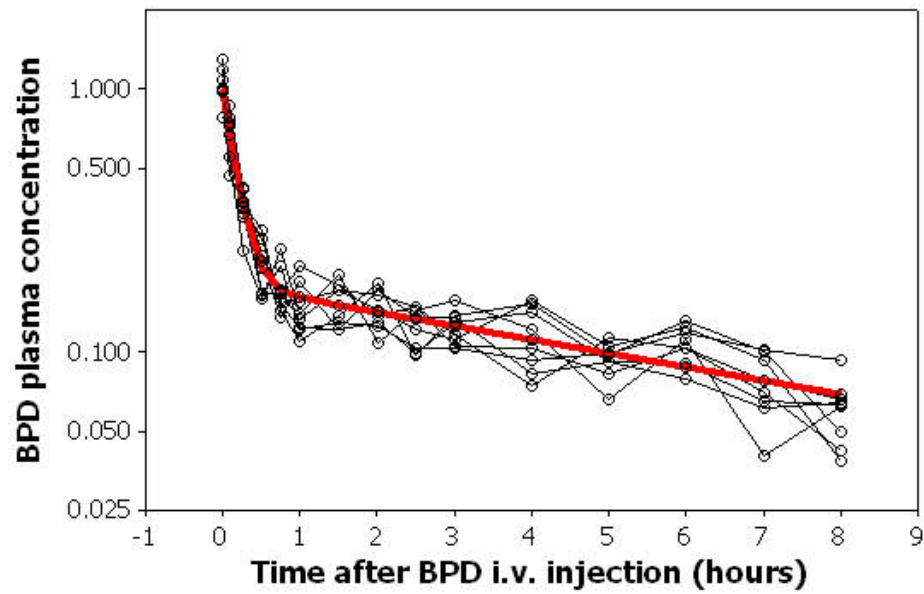


Figure 5.2: The normalized BPD plasma concentration is shown as quantified from samples taken from eight rats. The mean data was fitted to bi-phase exponential decay model, with the result shown by the red thick line. The connected points are normalized raw data from the measurements at each point for individual animals.

indicated that BPD was confined to the functional vascular compartment in these early time points, and not much molecules extravasate into tumor interstitium (see Figure 5.3(a), 5.3(b), 5.3(c), 5.3(d)). The photographs in Figure 5.3 illustrate the BPD fluorescence image of orthotopic tumor and its corresponding DiOC7₍₃₎ vasculature image from the same animal in co-localized measurements of the same section. BPD fluorescence was found not only confined within the tumor vasculature, but also leaked out from the tumor capillaries compared with the subcutaneous tumor, at the 15 minute time point after injection (Figure 5.3(a), 5.3(b), 5.3(c), 5.3(d)). It was assumed that the BPD concentration inside the tumor capillaries were at the same level in both the subcutaneous tumor and orthotopic tumor, since the tumors were both grown in the same animal. Figure 5.3(e), 5.3(f), 5.3(g), 5.3(h) shows the BPD distribution in subcutaneous and orthotopic tumors at 3 hours after i.v. injection along with their corresponding co-localized DiOC7₍₃₎ fluorescence images. BPD molecular fluorescence was found distributed nearly homogeneously in the tumor parenchyma in both subcutaneous and orthotopic tumors.

5.3.3 BPD fluorescence intravascular and extravascular distribution

Using co-stained DiOC7₍₃₎ fluorescence images, BPD fluorescence images can be partitioned to two compartments: DiOC7₍₃₎ positive region indicating a vascular space, and DiOC7₍₃₎ negative region representing the tumor extravascular space. Figure 5.4(a) through Figure 5.4(d) illustrate the DiOC7₍₃₎, BPD fluorescence images, as well as the partitioned

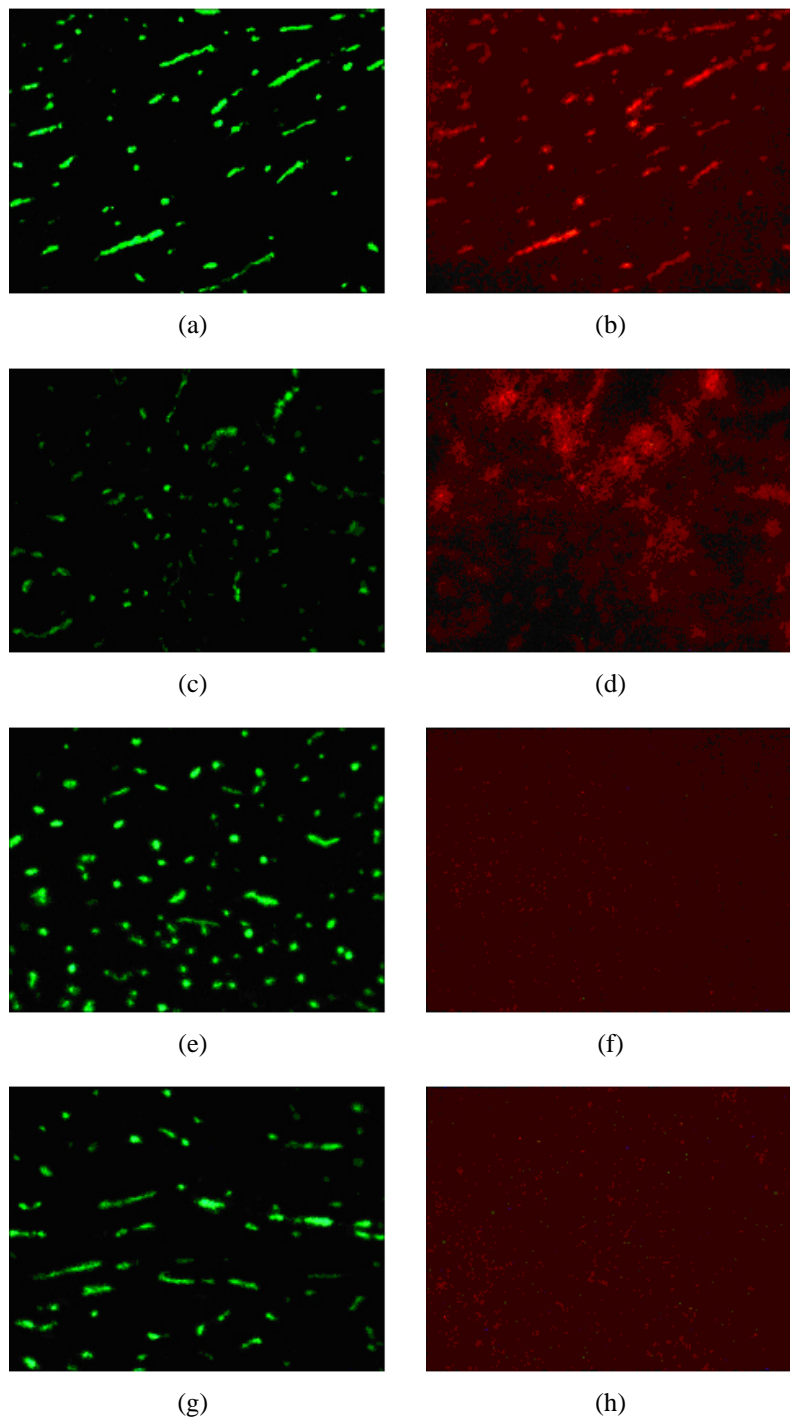


Figure 5.3: Fluorescence images of the subcutaneous tumor ((a) & (b), (e) & (f) and orthotopic tumor (c) & (d), (g) & (h) are shown. The DiOC7₍₃₎ (green) images in (a) & (c) show the locations of the perfused vasculature, and the BPD fluorescence (red) images in (b) & (d) show a snapshot in time of the drug as it diffuses out of the vasculature at 15 minutes after i.v. injection. Similar to (a) & (c), DiOC7₍₃₎ (green) images in (e) & (g) show the locations of the perfused vasculature, and the BPD fluorescence (red) images in (f) & (h) show the drug fluorescence 3 hours after i.v. injection, after it has clearly diffused out of the vasculature.

BPD fluorescence images showing BPD fluorescence in intravascular and extravascular compartments.

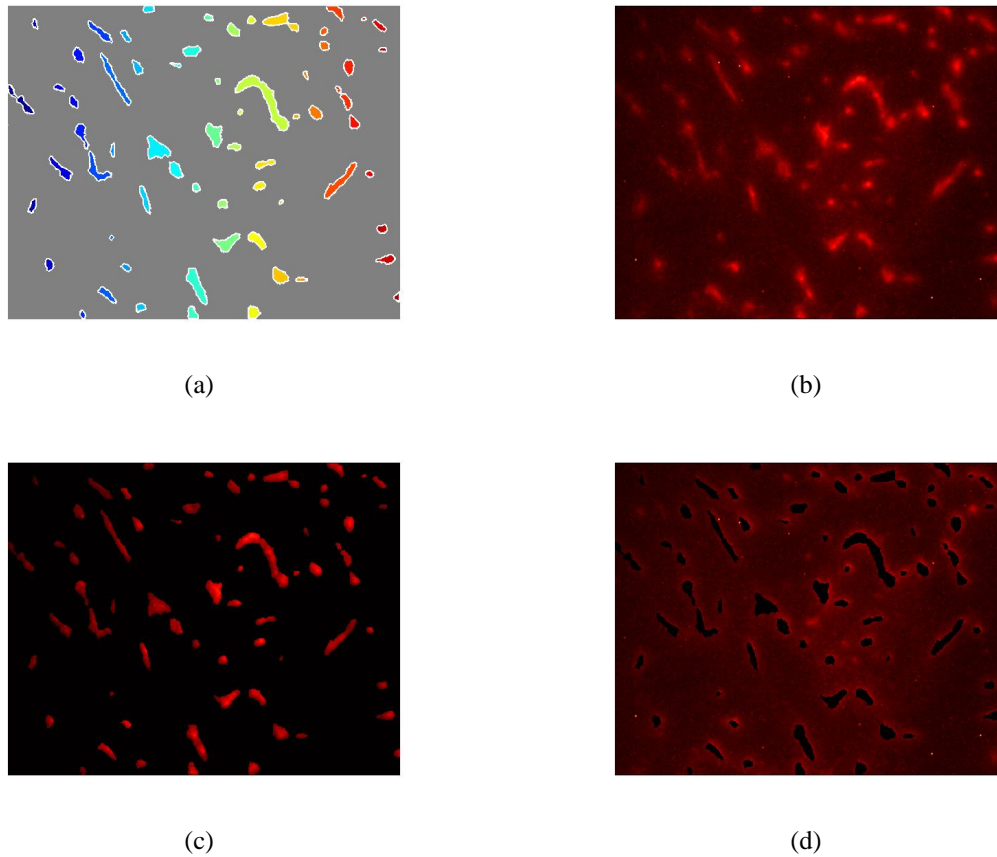


Figure 5.4: Intravascular and extravascular compartment segmentation. (a) tumor vasculature geometry illustrated in a color-labeled image; (b) corresponding BPD fluorescence image; (c) segmented intravascular BPD fluorescence image; (d) segmented extravascular BPD fluorescence image.

The mean fluorescence intensity in intravascular and extravascular spaces were evaluated using a customized MATLAB program. Figure 5.5(a) shows the distribution of measured intravascular BPD fluorescence intensity of 90 sampling sites from 5 subcutaneous tumor bearing animals and extravascular BPD fluorescence intensity from the same animals

comparing with Figure 5.5(b) showing the intravascular and extravascular fluorescence intensities from orthotopic tumor bearing animals (108 sampling sites, 5 animals).

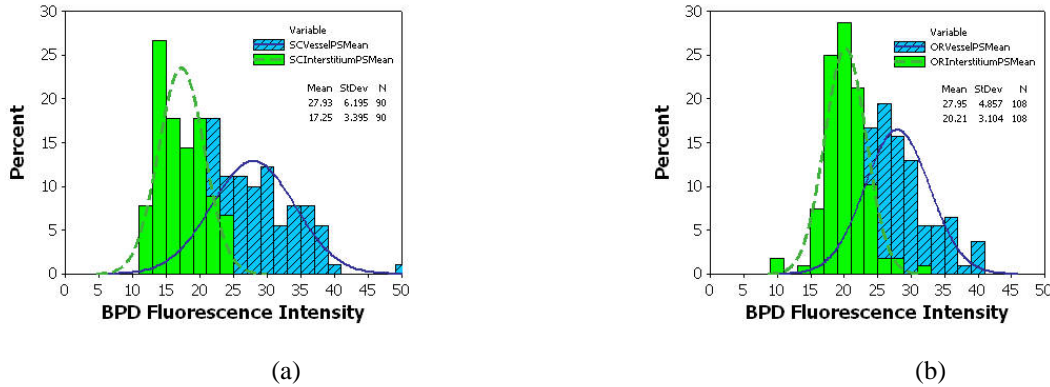


Figure 5.5: Histogram of BPD fluorescence intensity in intravascular and extravascular spaces from subcutaneous tumors (a) and orthotopic tumors (b). The histograms were generated by analyzing 90 fluorescence images from 5 subcutaneous tumors and 108 images from 5 orthotopic tumors.

In Figure 5.7, the calculated profiles of BPD fluorescence intensity (after background subtraction) are shown as a function of distance from tumor capillary wall, for both subcutaneous and orthotopic tumors in the short (15 minutes) and long (3 hours) time points. These profiles were calculated by the automated program that uses the vessel locations and tracks outwards from each vessel to calculate the average fluorescence per pixel as a function of the distance from the vessel wall, as described in the microscopy methods section. Overall, it can be observed from Figure 5.7, that the concentration of photosensitizer in the orthotopic tumor is higher than in the subcutaneous tumor at all distances from the vessel wall. In addition, BPD radial concentration profile exhibits a steeper gradient as compared

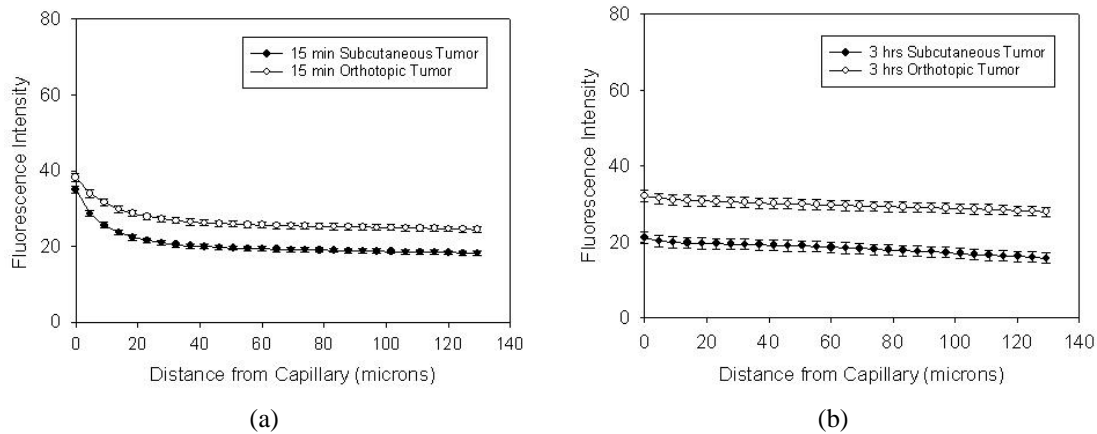


Figure 5.6: The average BPD fluorescence intensity is shown as a function of distance from capillaries. BPD fluorescence images along with their corresponding DiOC7₍₃₎ fluorescence images were used and the averaged pixel intensity in tumor parenchyma at each distance away from a capillary was calculated. The graph in (a) is the analysis of subcutaneous and orthotopic tumors 15 minutes after BPD i.v. administration. The graph in (b) shows the 3 hour groups of BPD distributions.

with orthotopic tumors. The time course of this interstitium diffusion process is difficult to observe from these static pictures of drug distribution, but simulations allow a visual presentation of the transport process. From this figure, a higher transvascular permeability coefficient and a higher interstitial diffusion coefficient are implicated in the orthotopic tumor model as compared to the subcutaneous model, as the amount of drug appears higher outside the vessels and the diffusion gradient is less steep in orthotopic tumors.

Interstitial BPD fluorescence intensity radial distribution is evaluated from different sampling sites of the same tumor and is presented in Figure 5.7(a) for a subcutaneous tumor (sampling sites) and Figure 5.7(b) for an orthotopic tumor (sampling sites) at 15 mins after verteporfin i.v. injection. The gradients of BPD intensity function varied considerably in

both subcutaneous and orthotopic tumors, indicating that there exist variation in effective interstitial diffusion coefficients in both tumor types.

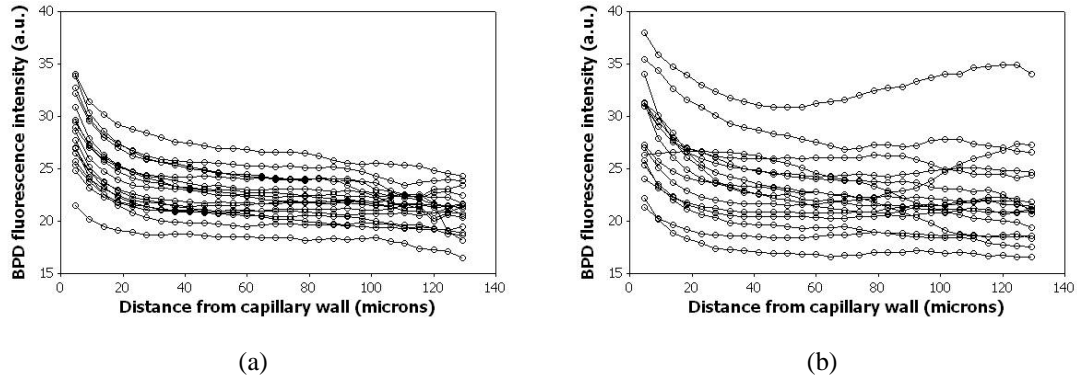


Figure 5.7: BPD fluorescence radial distributions at different sampling sites for a subcutaneous (a) (17 sampling sites) and an orthotopic tumor (b) (17 sampling sites).

5.3.4 Microscopic Permeability

The mean fluorescence intensity from intravascular and extravascular regions were used to calculate the average effective diffusive permeability coefficient of subcutaneous and orthotopic tumors.

The effective diffusive permeability coefficients were found to vary considerably among different locations of the tumor in both subcutaneous and orthotopic tumors. Figure 5.8 illustrates the overall intra-tumor variation of effective permeability of subcutaneous (7 animals, 102 sampling sites) and orthotopic tumors (5 animals with 103 sampling sites).

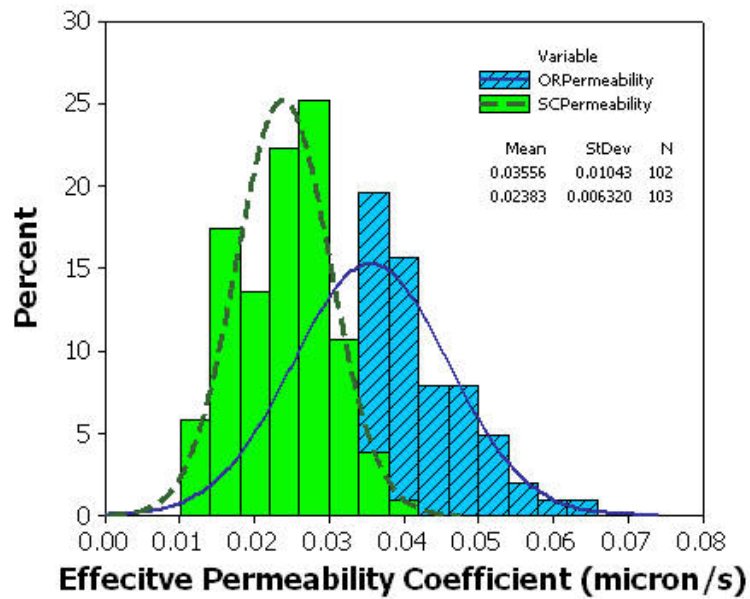


Figure 5.8: Distribution of diffusive permeability coefficients evaluated from $1 \times 1 \text{ mm}^2$ fluorescence images. The histograms were generated by analyzing 102 fluorescence images in 7 subcutaneous tumors and 103 fluorescence images in 5 orthotopic tumors.

5.3.5 Interstitial Diffusion

Forward simulation of photosensitizer diffusion

Figure 5.9(c) shows the BPD concentration profiles in an orthotopic tumor slice following i.v. injection, Figure 5.9(a) shows the accompanying vascular marker image and Figure 5.9(b) shows the geometry of thresholded vasculature. The remaining images in Figure 5.9(d) through Figure 5.9(h) show simulations of the diffusion process, at different times after the projected injection time. The diffusion coefficient used in this simulation was $1.4 \mu\text{m}^2/\text{s}$, which was determined to be an optimal fit to generate matched data to the fluorescence image. Each profile corresponds to a different time in simulation, as indicated in the figure caption. The BPD concentration inside the tumor capillaries was assumed to be uniform throughout the tumor, and decayed temporally according to the BPD plasma concentration curve shown in Figure 5.2. The diffusion coefficient was assumed to be homogeneous in the tumor parenchyma, and time-independent. Figure 5.10(c), shows the same diffusion process for a subcutaneous tumor, with Figure 5.10(a) being the accompanying co-localized vascular marker image. The simulations for this drug diffusion process are shown at different time points in Figure 5.10(d) through 5.10(h), as denoted in the caption. In this case, the diffusion coefficient used was $0.6 \mu\text{m}^2/\text{s}$, which provided the optimal match to the fluorescence image data. It is interesting to note in these images that the vessels are larger and the diffusion coefficient is significantly smaller in the subcutaneous case than in the orthotopic case.

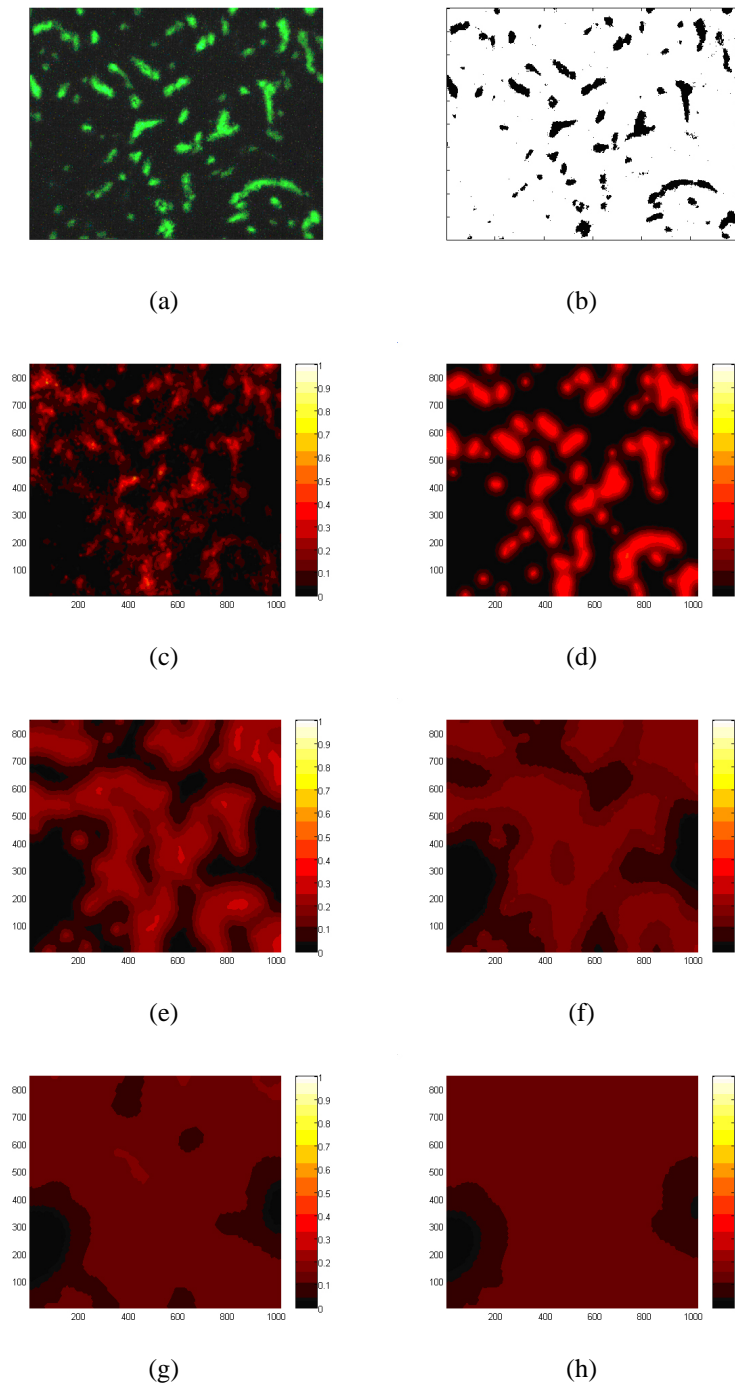


Figure 5.9: Simulations of BPD distribution in the orthotopic tumor model are shown. The image in (a) is the DiOC7₍₃₎ fluorescence image of perfused vessels and image (b) is the segmented geometry of vasculature derived from (a). Image (c) shows the BPD fluorescence image in an orthotopic tumor 15 minutes after BPD i.v. injection. Images (d) through (h) show the simulations of the diffusion process, at 15 minutes, 30 minutes, 1 hour, 2 hours and 3 hours after BPD administration. The effective diffusion coefficient used here was $1.4 \mu\text{m}^2/\text{s}$, which was the optimal fit to the measured image data (c).

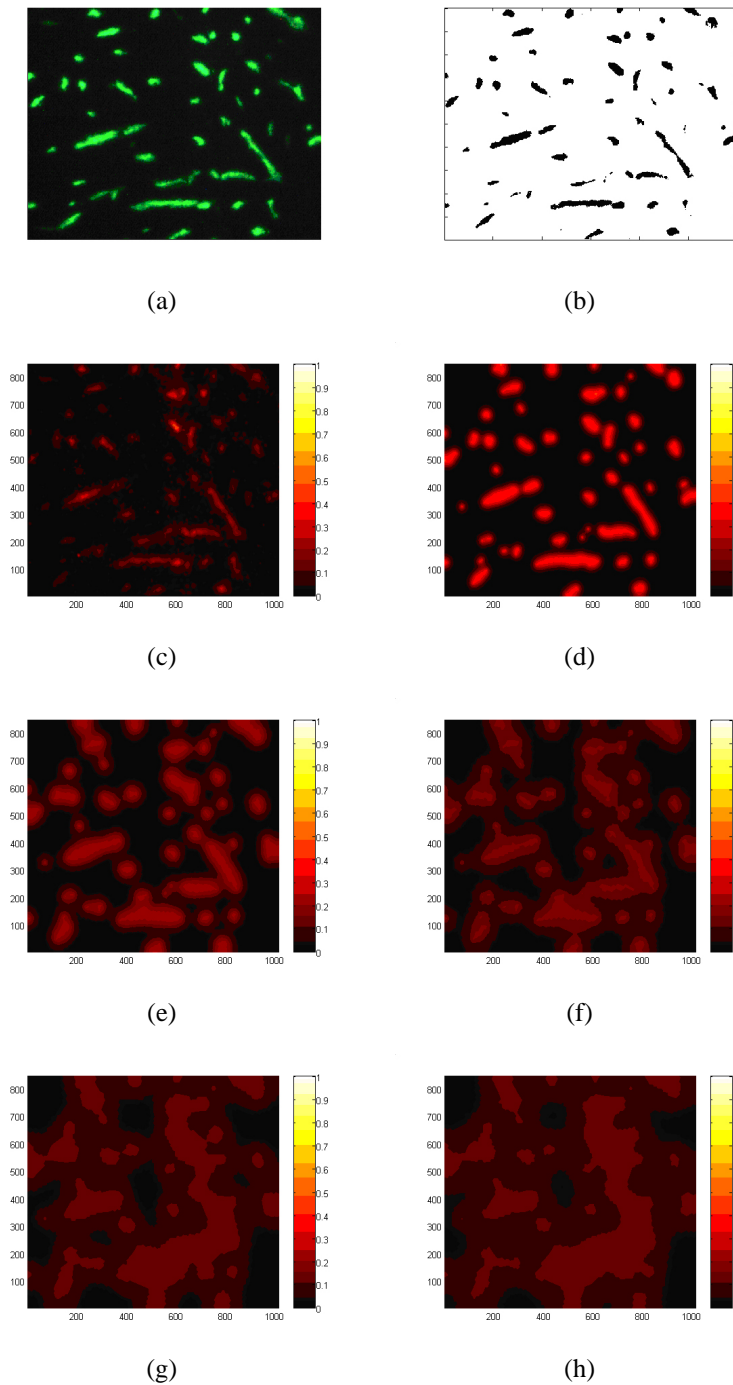


Figure 5.10: Similar to Figure 5.9, these images show the simulation profile of a subcutaneous tumor. The image in (a) is the DiOC7₍₃₎ fluorescence image and (b) is the segmented geometry of the vasculature. A BPD fluorescence image obtained 15 minutes after BPD i.v. administration is shown in (c). The images in (d) through (h) show the simulations of the diffusion process, at 15 minutes, 30 minutes, 1 hour, 2 hours and 3 hours after BPD i.v. administration. The effective diffusion coefficient used here was $0.6 \mu\text{m}^2/\text{s}$, which provided the optimum fit to the measured image, (c).

Estimation of BPD effective diffusion coefficient in subcutaneous and orthotopic tumor

Figure 5.6(a) indicates diffusion rates at different locations of the same tumor are different. This is confirmed with the evaluation of effective diffusion coefficient at different locations of the tumor. Figure 5.11 illustrates the overall intra-tumor variation of diffusion coefficients evaluated from $1 \times 1 \text{ mm}^2$ tumor tissues for both tumor types.

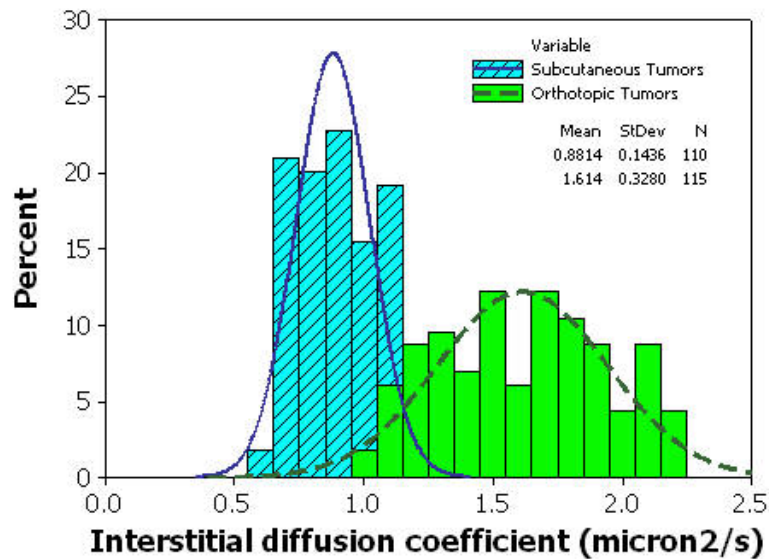


Figure 5.11: Distribution of interstitial diffusion coefficients evaluated from $1 \times 1 \text{ mm}^2$ sampling sites. The histograms were generated by analyzing 110 fluorescence images in 7 subcutaneous tumors and 115 fluorescence images in 5 orthotopic tumors.

5.3.6 Correlation between Transport Parameters and Verteporfin Pharmacokinetics

Mean fluorescence intensity of each fluorescence image were plotted as a function of vascular volume, vascular permeability (P) and interstitial diffusion coefficient (D) to illustrate the dominant factors determining the mean fluorescence intensity of that image. 5 orthotopic tumor bearing animals (99 images) and 7 subcutaneous tumor bearing animals (121 images) were included in this study. Tumor vascular volume in two dimensional image analysis are represented by the vessel area (pixel²), effective permeability and interstitial diffusion coefficient were calculated as discussed in the above sections. We have found a significant correlation between tumor vascular volume and mean fluorescence intensity at both tumor inoculation sites ($R^2 = 64.1\%$ in subcutaneous tumors, $R^2 = 63.6\%$ in orthotopic tumors, $p < 0.001$). But there is no significant correlation between mean fluorescence intensity and other transport parameters at any inoculation site. The regression analysis is shown in Figure 5.12.

The average transport parameters and verteporfin mean fluorescence intensity for individual animals were analyzed in the same manner to illustrate how the average transport parameters affect the mean photosensitizer uptake on an individual based comparison. Verteporfin tumor uptake which is assumed proportional to the average fluorescence intensity at multiple arbitrarily sampled locations was found correlate to the total vascular volume at both subcutaneous and orthotopic tumor host-sites ($p < 0.05$). The regression

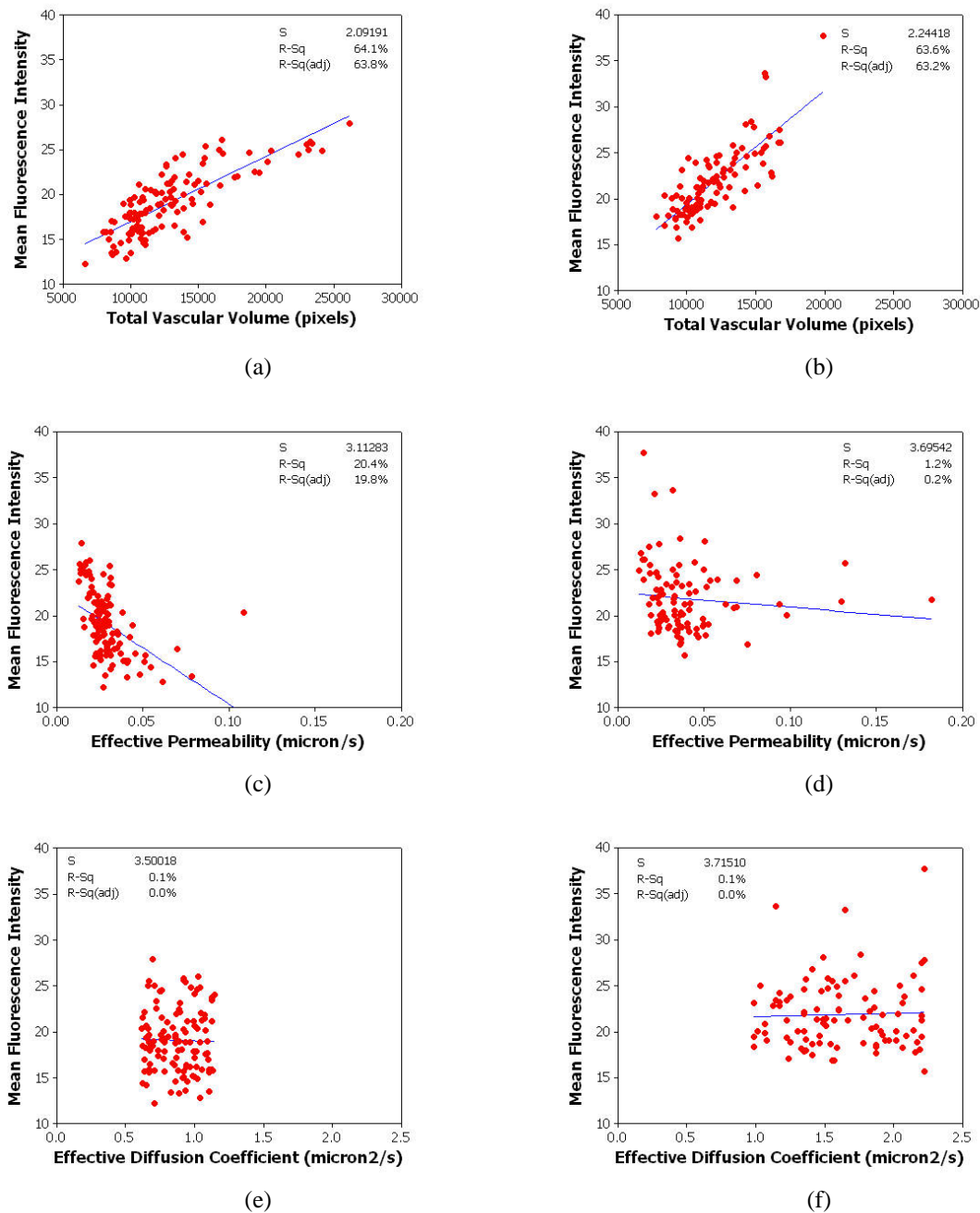


Figure 5.12: Correlation between intra-individual variability in transport parameters and mean fluorescence intensity. The scatter plots were generated from analysis of 102 fluorescence images in 7 subcutaneous tumors ((a), (c) and (e)) and 103 fluorescence images in 5 orthotopic tumors ((b), (d) and (f)). BPD fluorescence intensity were plotted as a function of tumor vessel area ((a) & (b)), transvascular permeability ((c) & (d)), and interstitial diffusion coefficient ((e) & (f)).

analysis of transport parameters and verteporfin individual tumor uptake were shown in Figure 5.13.

5.4 Discussion

As discussed in Chapter 3, there are variety of factors that affect the photosensitizer pharmacokinetics. These factors contribute in every step of the photosensitizer pharmacokinetic process, *i.e.*, including administration, distribution, metabolism, and excretion. According to a dimensional scale of their impact, these factors can be classified into two categories: the factors that affect the photosensitizer pharmacokinetics at a systemic level, *e.g.*, photosensitizer systemic distribution, drug excretion and then at a tumor level, *e.g.*, such as drug distribution in the tumor. Upon intravenous injection, verteporfin photosensitizer distributes in the systemic circulatory system, distributes in the tumor vasculature, transports across tumor vessel walls, and distributes through the tumor interstitium. This is a complex biological process characterized by temporal and spatial heterogeneity and high variability among individuals. The objective of this study is to investigate the relationship between photosensitizer transport parameters and photosensitizer mean fluorescence intensity and search for the origins of intra-individual and inter-individual photosensitizer pharmacokinetic variability.

To quantify verteporfin inter-individual plasma pharmacokinetic variability, BPD plasma concentrations of eight tumor bearing animals were followed for 8 hours. Verteporfin

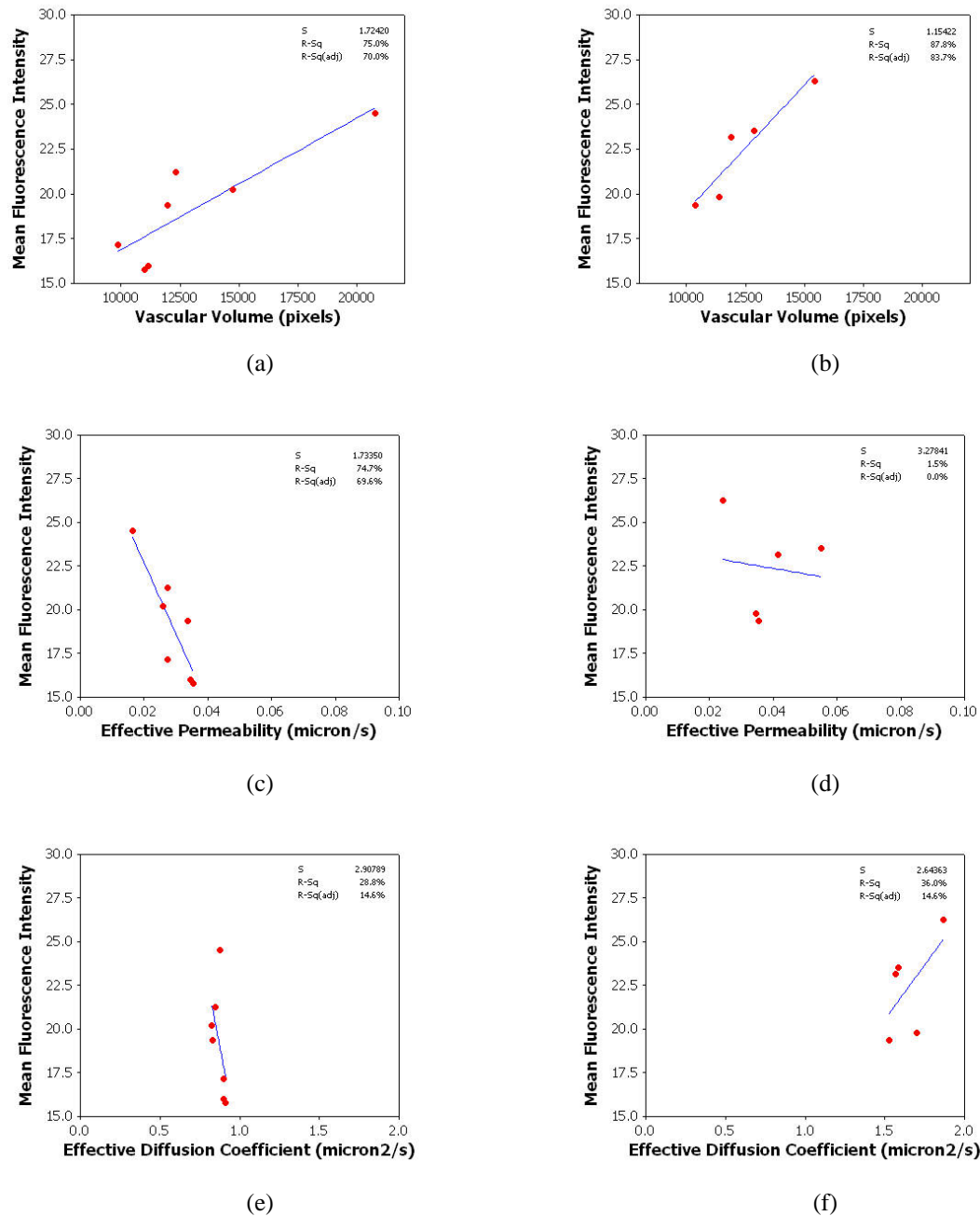


Figure 5.13: Correlation between inter-individual variability in transport parameters and mean fluorescence intensity as measured by fluorescence microscopy. The scatter plots were generated from 7 subcutaneous tumors ((a), (c) and (e)) and orthotopic tumors ((b), (d) and (f)). BPD fluorescence intensity were plotted as a function of average tumor vessel area ((a) & (b)), average transvascular permeability ((c) & (d)), and average interstitial diffusion coefficient ((e) & (f)).

plasma pharmacokinetic data were then fitted with a double-exponential decay model. Individual plasma concentration profiles were normalized to their mean concentration at time $t = 0$ min after drug i.v. injection. The data were processed this way so that the variation between individuals could be preserved. Figure 5.2 illustrates the individual plasma pharmacokinetics, showing that there is about 20% variation in the parameter A and 9% in parameter B , 25%, 24% variation in the elimination half-life value $\tau_{\frac{1}{2}\alpha}$ and $\tau_{\frac{1}{2}\beta}$ among individuals (Table 5.1).

This observed variation in parameter A and B could be due to variation in the photosensitizer i.v. administration process ,e.g., human errors in tail vein injection. A possible explanation for the variation in elimination half-lives involves the binding process of verteporfin to low density lipoproteins (LDLs), and the activities of the macrophage systems. Plasma LDL concentration varies from individual to individual, and for the same individual, varies from day to day. The unbound hydrophobic photosensitizers are taken up by macrophage system and eliminated from the body, and thus results in a faster clearance. It has been reported that the serum protein concentration, such as human serum albumin (HSA), LDL, and transferrin, tends to decrease with age [281]. Older animals may have more unbound hydrophobic verteporfin molecules and likely have a faster clearance, yet also changes in animal health will likely cause some variation in this level.

The BPD distribution kinetics were compared in two tumor implantation sites. The BPD fluorescence images shown in Figure 5.3 along with the co-registered DiOC7₍₃₎ fluo-

rescence images demonstrating that verteporfin is predominantly in the tumor vasculature at early time points after administration (*i.e.* 15 min or less), and for longer drug-light intervals (*i.e.* 3 hours), more verteporfin is transported across the tumor vessel wall, diffused through tumor interstitium and distributed homogeneously in the tumor parenchyma.

These fluorescence images can be analyzed in two ways, first, verteporfin fluorescence images can be segmented into intravascular and extravascular compartments using co-stained DiOC7₍₃₎ fluorescence images. The mean fluorescence intensity in the two different segmentations can then be analyzed. This two-compartment model has also been used to characterize the transvascular transport process, thus this analysis is in parallel to transvascular transport process. In the second approach, the spatial distribution of verteporfin has been analyzed by studying the fluorescence intensity radial profile. This analysis looks at the spatial distribution of verteporfin as a function of distance from vessel wall. Indeed, this is an equivalent one dimensional interstitial diffusion model where the shape of the radial profile is determined by the effective diffusion coefficient. Thus this analysis is in parallel to interstitial transport processes.

Using co-stained DiOC7₍₃₎ fluorescence images, each BPD fluorescence image was partitioned into intravascular and extravascular compartments (Figure 5.4), the mean fluorescence intensity of each compartment in the two implantation sites is shown in Figure 5.5. Mean fluorescence intensity in the intravascular compartment was found to be significantly higher than the extravascular compartment. This indicates that at 15 minutes

after verteporfin injection, most verteporfin photosensitizer molecules are in the intravascular compartment, only a portion of verteporfin molecules extravasate from the vessel into the tumor interstitium compartment. Comparisons between two tumor inoculation sites showed that subcutaneous tumors and orthotopic tumors have same mean intravascular fluorescence intensity, but the intra-individual variability in this quantity is significant higher in subcutaneous tumors compared to orthotopic tumors (CV% = 22% for subcutaneous tumors and 17% for orthotopic tumors). This comparison indicates that blood flow in subcutaneous tumors are more spatially heterogeneous. The inter-vessel fluorescence intensity variation might be caused by the chaotic flow pattern in the subcutaneous tumors. There might be more intermittent flow, reduced flow in these tumors. On the other hand, comparison of extravascular fluorescence intensity showed that orthotopic tumors have a significantly higher and less variable verteporfin mean fluorescence intensity in the extravascular compartment (CV% = 19.7% for subcutaneous tumors and 15.3% for orthotopic tumors). It is not surprising that the mean fluorescence intensity in the extravascular space is higher in orthotopic tumors, since orthotopic tumors present significant higher transvascular permeability coefficient compared to subcutaneous tumors (Figure 4.5, Figure 4.6, and Figure 5.8). However, it has been illustrated that the effective permeability is spatially heterogeneous and highly variable compared to subcutaneous tumors. A higher variability in extravascular fluorescence intensity should be observed in orthotopic tumors. The only possible reason for this might be the highly variable intravascular fluorescence intensity observed in subcutaneous tumors. Although the transvascular permeability is lower

and less variable in subcutaneous tumors, the intravascular fluorescence intensity variation causes variability in transvascular photosensitizer concentration gradient. Thus although the permeability is less heterogeneous, the solute flux are still higher variable due to the heterogeneous concentration gradient.

In the second approach, we calculated verteporfin fluorescence intensity as a function of distance from vessel wall. The average verteporfin radial profile is shown in Figure 5.7. Comparison between subcutaneous and orthotopic tumors showed a steeper BPD radial profile. This indicates subcutaneous tumor have a lower interstitial diffusion coefficient compared to orthotopic tumors. Pluen *et al.* [216] estimated the effective diffusion coefficients of macromolecules and liposomes in cranial windows (CW) and dorsal chambers (DC) using a technique called fluorescence recovery after photobleaching (FRAP) [282]. In their case, they used this method to show a 5 to 10 fold slower diffusion process of large molecules in the DC tumor as compared with the CW tumor. Similarly, in this study, the BPD distribution kinetics in two tumor implantation sites were compared for the prostate tumor and it was found that BPD diffused faster in the orthotopic MAT-LyLu tumor model as compared with the subcutaneous model. To quantify the difference of diffusion coefficient in these models, a numerical diffusion model was used, using the assumption that diffusion was the dominant process for BPD distribution. The effective diffusion coefficient was calculated by minimizing root-mean-square between the simulation results and normalized BPD fluorescence images. Another observation from this is that the orthotopic

fluorescence intensity radial profile is above the subcutaneous one at any distance from the vessel wall. Mean verteporfin fluorescence intensity in the extravascular space is the area under this radial profile curve, thus a higher value of radial profile indicates there is more photosensitizer in the extravascular space. This result further confirms the fact that the vascular permeability present in orthotopic tumors is higher than in subcutaneous tumors.

Another interesting observation is that the verteporfin radial profile evaluated from different locations within a tumor is highly variable. This phenomena is clearly demonstrated in Figure 5.7(a) and 5.7(b). Each graph shows verteporfin fluorescence radial profiles from 17 sampling sites from each tumor of the same animal. Comparing the intra-tumor variation, these verteporfin gradient profiles showed less variable among different locations in the subcutaneous tumor, whereas, they are highly variable in an orthotopic tumor. If the interstitial diffusion coefficient at different locations of the tumor are the same, the radial profiles calculated from these images should have the same shape, but might shift in the y-axis due to the difference in transvascular solute flux, which depends on both effective permeability and transvascular solute concentration gradient. The radial profiles shown in the subcutaneous tumor are of similar shape, with some variable shift along the y-axis. This indicates that the diffusion coefficient in subcutaneous tumors are less variable compared to orthotopic tumors. This is further confirmed by the histogram analysis pooled together all the sampling locations from different animals (Figure 5.11) (CV% = 16% for subcutaneous tumors and 20% for orthotopic tumors). The variation in the highest value

on the curve (just outside vessel wall) represent the variation of the solute flux exchange between intravascular and extravascular compartment. This variation is found higher in orthotopic tumor, in this particular animal, this might be due to the variation in permeability or the variation in the solute transvascular concentration gradient. However, it has been shown in this study, verteporfin concentration intervascular variation is less in orthotopic tumors. Thus this higher variability in the highest value on the radial profile is likely due to heterogeneous permeability (Figure 5.8).

While the physical measurement change is interesting, it is also important here to discuss benefits and limitations of approaches to modeling the photosensitizer transport that we have developed. A limitation of these mathematical models is that a spatially-independent vascular permeability and interstitial diffusion coefficient are assumed for the transvascular transport and interstitial transport in a tumor tissue of area approximately $1 \times 1 \text{ mm}^2$. Yet in looking at the figures, it is obvious that there is significant spatial heterogeneity at early times in the drug transport process.

For the short drug-light interval simulations (Figure 5.9(c) v.s. 5.9(d) and Figure 5.10(c) v.s. 5.10(d)), the image results have some spatially variant differences from the image data. This implies that a heterogeneous transport occurs in these tumor regions with the area less than $1 \times 1 \text{ mm}^2$, and the origins may be due to the intervascular photosensitizer concentration variation, vascular permeability variation and interstitial diffusion coefficient variation at a lower dimensional scale than we have investigated.

We have illustrated the mean verteporfin intravascular concentration variation among $1 \times 1 \text{ mm}^2$ sampling areas which contains approximately 80-100 vessels. This variability can be clearly observed on a single vessel basis. The dynamic changes in the blood flow have been observed with double injections of blood-born fluorescence markers [172, 173, 252], allowing time for the vessels to open and close. For short BPD drug-light interval combined with the injection of DiOC7₍₃₎ ten minutes later, the difference in intensities of DiOC7₍₃₎ and BPD in the vascular areas provides evidence that the vessel has a heterogeneity of dynamic changes in flow or perfusion over time. This variation appears to be more frequent in the subcutaneous tumor model as compared with the orthotopic model (Figure 5.5).

Transvascular permeability and interstitial diffusion coefficients evaluated from $1 \times 1 \text{ mm}^2$ tumor tissues exhibit higher variability among different sampling locations. These variabilities seem to be less in subcutaneous tumors compared to orthotopic tumors (Figure 5.8 and 5.11). Variability in these parameters at a lower dimensional scale can be also observed, *e.g.*, areas around a single vessel. This requires using these transport models at a smaller scale, for example, calculating the solute flux across a single vessel and fluorescence intensity radial profile around that vessel, so that the permeability for that single vessel and interstitial diffusion rate around vessel can be calculated. Perhaps more effort should be spent on quantifying the microscopic heterogeneity of these transport parameters on single vessel bases, such as developing histograms of permeability and diffusion coefficient. However, using an entire image of data provides an excellent opportunity to

average data together, thereby maximizing the signal to noise of the measurement. This is not readily achieved in single point estimates such as FRAP analysis for diffusion coefficient [282], and single vessel analysis for permeability [283]. An additional benefit of this image analysis approach is that standard histological sectioning can be used for the analysis, as long as the tissue is preserved in a manner that retains the fluorescence, such as frozen section sampling. Another important issue is that this simulation is based upon a single time-point, whereas FRAP type analysis and intravital fluorescence microscopy permeability analysis measure data from a number of time points and use the data to better match the model. However, for molecules with low permeability and low diffusion rate, the intravital fluorescence microscopy and FRAP processes require cumbersome experiments where the animal must remain anesthetized for a number of hours, compromising blood flow, photobleaching of fluorescence tracer molecules and making the experiment difficult.

Another important issue in these transport models is the assumption that the transport parameters, transvascular permeability, diffusion coefficients are time-independent parameters. However, several investigations have pointed out that these transport processes are not only spatially heterogeneous, but also temporally heterogeneous. Heterogeneous blood flow inside tumor has been extensively investigated by several research groups [171]. It has been shown that dramatic changes such as complete cessation or re-perfusion occurs in few percentage of vessels, and majority of the vessels showed fluctuations with 2-fold flow variation [174–178]. The temporal heterogeneity in transvascular transport in tumor has

been shown in Monsky's report, where he showed the change to albumin ranges from 9.18×10^{-7} to -5.33×10^{-7} cm/s over 24 h [200]. Hypoxia, hypoglycemia, and low pH have been shown up-regulate VEGF expression. These factors are themselves spatially and temporally heterogeneous inside the tumor. Thus expression of VEGF and its receptors varies spatially and temporally, and this might be responsible for the heterogeneity in permeability [200]. Interstitial fluid and solute transport have been shown strongly dependent upon the volume, structure, interaction and distribution of extracellular matrix molecules. Since these properties do not have temporal heterogeneity, the diffusion process in the tumor interstitium should present very little or no temporal variation.

Once these photosensitizer transport models have been validated, they were then used for searching for the dominant transport parameters for the mean fluorescence intensity. All the fluorescence mean intensities for all the images taken for subcutaneous and orthotopic tumors have been pooled together, and plotted as a function of tumor vessel volume, permeability, and interstitial diffusion coefficient. Strong correlation was found between vessel volume and mean photosensitizer fluorescence intensity (Figure 5.12). This is not surprising, since the majority of photosensitizer molecules are confined in the intravascular compartment, so that this higher fluorescence intensity will be averaged out when integrating over the interstitial space. However, if the vessel volume is high, there will be more total photosensitizer molecules in the intravascular space, and in the sampling tissue region, thus an increase in the mean fluorescence intensity readings will be seen. A few

hours after verteporfin i.v. injection, most photosensitizer molecules extravasate from intravascular compartment into tumor interstitium. Photosensitizer molecules in the tumor interstitium then determine the mean fluorescence intensity observed. Thus the mean fluorescence intensity should not correlate with vessel volume, but rather with the permeability and/or interstitial diffusion coefficient. However, as shown in Figure 5.6(b), the diffusion gradient is dissipated at 3 hr post i.v. injection for both subcutaneous and orthotopic tumors, indicating that a steady state has been reached in the tumor interstitium. The total number of photosensitizer molecules in extravascular compartment is mainly dependent on the permeability. Hence, the mean fluorescence intensity should positively correlate with the transvascular permeability (data not shown).

5.5 Conclusion

In summary, pathology image-based numerical models were presented to evaluate the effective transvascular permeability and interstitial diffusion coefficient of BPD in delivery via Verteporfin for Injection. Microscopic mathematical models were used to quantify the rates of effective transvascular transport and interstitial diffusion in subcutaneous and orthotopic Dunning prostate MAT-LyLu tumor models, since they represent very different vascular architectures, yet have the same cellular origin. Using a fluorescence vascular marker, the geometry of the tumor vasculature was obtained and then the co-localized fluorescence images of BPD were used along with an experimentally derived plasma concentration curve,

to simulate the transvascular and interstitial transport process. Despite the limitations of the models, such as 2-dimensional model, microscopic spatial homogeneity and time invariant, these models can be used to determine the effective vascular permeability and diffusion coefficients of the tumor tissues and quantify the changes of photosensitizer transport rate after treatment. Up to 25% of inter-tumor variation in BPD plasma pharmacokinetics was showed in this study. The inter-tumor and intra-tumor variation in transvascular permeability were found 16.6% and 26.5% in subcutaneous tumors and 17.1% and 29.3% in orthotopic tumors. Interstitial diffusion coefficient evaluated showed 12.6% inter-tumor variation and 16.3% intra-tumor variation in subcutaneous tumors and 13.6% inter-tumor variation and 20.3% intra-tumor variation in orthotopic tumors. The effects of the inter-tumor and intra-tumor variation in these transport parameters on the mean fluorescence intensity was then analyzed. At early time points after verteporfin injection, the mean fluorescence intensity is positively correlated with the vessel volume in the tumor ($R^2 = 64.1\%$, $p < 0.001$ for subcutaneous tumors, and $R^2 = 63.6\%$, $p < 0.001$ for orthotopic tumors), whereas, at longer time points, when the photosensitizer molecules are distributed in the tumor interstitium, the mean fluorescence intensity correlates with tumor transvascular permeability values. These results suggest that approaches to increase the vascular volume at early time points post verteporfin injection can increase the drug retention in tumor, while techniques to enhance transvascular permeability, such as, introducing inflammation mediators, can increase the photosensitizer uptake level in the tumor.

Chapter 6

Photosensitizer Dosimetry: Effects of sampling volume

Photosensitizer microscopic transport processes have been extensively discussed in Chapter 3 to 5. These photosensitizer transport models are based on the tumor microvasculature geometry obtained from microscopic histology images. Based on these transport analysis at microscopic level, we have correlated the photosensitizer fluorescence intensity quantified by the fluorescence microscopy and the transport parameters extracted from microscopic transport models. *Ex vivo* fluorescence microscopy analysis is perhaps the most accurate way to sample the photosensitizer fluorescence intensity in tumor tissue at a microscopic level. In addition, through analyzing the fluorescence intensity histogram of multiple microscopic images, an intra-tumor photosensitizer uptake variability can be

evaluated. Comparisons of the mean and standard deviation of these multiple fluorescence measurement between individuals provide information about the intra-individual and inter-individual photosensitizer pharmacokinetic variability. However, *ex vivo* fluorescence microscopy analysis requires slicing the frozen tumor into many sections and imaging on a standard fluorescence microscope, which is not readily accessible in clinical settings. Despite its accuracy and information provided at microscopic level, this biopsy type analysis is rarely in use in clinical PDTs. The ability to track the spatial and temporal dynamics of photosensitizer concentrations in tissue non-invasively is of importance for the photosensitizer pharmacological research and for clinical PDT applications. Recently many fluorescence *in vivo* detection techniques have been developed, including fiber optics based dosimeters and wide-field fluorescence imaging dosimeters. These dosimeters utilize non-invasive fluorescence sensing techniques, thus are very promising for clinical applications. However, these dosimetry techniques sample the fluorophores from a bulk tissue, and this might not be representative for the true fluorophore concentration inside tissue. How does this macroscopic or mesoscopic quantifications relate to the microscopic quantification is of particular importance in this study. The key to this question will provide links among photosensitizer concentration microscopic, mesoscopic and macroscopic quantifications, thus connect the microscopic transport analysis to the photosensitizer macroscopic quantification.

6.1 Introduction

Effective PDT treatment require accumulation of photosensitizer molecules and light activation at targeting sites. Most PDT treatment protocols are developed through extensive dose escalation studies, and are always in terms of photosensitizer dose, drug-light interval and light dose. However, as discussed in Chapter 3, 4 and 5, during photosensitizer molecules delivery process, there are a various factor that may limit the effective photosensitizer delivery to the tumor cells, thus cause intra-tumor heterogeneous distribution. Indeed, this intra-tumor variability in photosensitizer distribution have been reported in numerous pre-clinical and clinical PDT treatments. As a consequence, in some cases, PDT treatment is ineffective, in others, there might be excessive damage to the surrounding normal tissues. Therefore, a real-time monitoring of photosensitizer spatial and temporal dynamics would be much appealing in clinical PDTs [284, 285]. In clinical settings, photosensitizer concentration in tissues is usually determined by invasive procedures such as blood sampling [281] or taking biopsies and performing photosensitizer fluorescence analysis [286]. Recently, variety of non-invasive drug quantification techniques have been developed. According to their quantification mechanisms. they can be categorized as reflectance measurement, absorption measurement, and fluorescence measurement. They can also be classified as fiber optics based measurement and wide-field imaging measurement.

Solonenko *et al.* [38] measured photosensitizer Lutex concentration, blood oxygenation and optical properties *in vivo* in canine large bowels, kidneys and prostates. They observed

significant variability in Lutex uptake between organs and even between the same organ in different dogs. Weersink *et al.* [287] measured AlPcS4 concentration on rabbits, and found measurements on the liver yielded accurate estimation, but are affected by the multi-layer structure in the skin. Mourant *et al.* [288] developed single fiber source-detector configuration pair to measure the absorption of some chemotherapy drugs in an animal tumor model. Although there is a linear correlation between the measurement and extracted concentration but a systematical underestimation was found compared to the extraction data, possibly due to the absorption model they incorporated. At Dartmouth, we have developed fiber-optic probe spectroscopic system, Aurora spectrometer [289], and validated this system on MTGB marine tumor model using photosensitizer AlPcS2 [290]. An *ex vivo* calibration curve was used as a lookup table to quantify the AlPcS2 concentration in tumor tissue, muscle, and liver. Cubeddu *et al.* [291] used a fluorescence imaging system to monitor AlPcS2 emission during the PDT of murine tumors, and found the fluorescence intensity and absorption spectrum changed before and after PDT.

The drug quantification methods clearly impact the magnitude of the signal [292–294]. While in general, careful calibration can be used to interpret the signal and yield a semi-quantitative measurement, the problem still remains that different approaches to sampling fluorescence yield vary the results, and cannot easily be compared. In addition, fluorescence within tumors is known to be highly heterogeneous, with a variance that can be as high as 100% of the mean value [295], and inspection of any fluorescence microscope

image will reveal a microscopic-level heterogeneity which changes from near zero to extremely high values [296–298]. In this chapter, the problem of measuring fluorescence was examined in detail, using flow cytometry, fluorescence microscopy and *in vivo* measurements with Aurora spectrometer. The interpretation of *in vivo* fluorescence measurements is the key problem, but in order to fully interpret the meaning of these measurement, a comprehensive analysis of intensity and variance is required. The distribution of fluorescence intensities observed in tissue is analyzed with a histogram interpretation of the heterogeneity, and this allows comparison between microscopy data and *in vivo* fluorometer data.

One of the major problems in drug quantification is that the sampling volume varies, and the drug is invariably partitioned between different spaces of the tissue, such as vascular, interstitial fluid, extra cellular matrix and cellular areas. While several studies have been completed comparing *in vivo* fluorescence sampling to dye quantification via tissue extraction methods [299, 300], the results are still confounded by this partitioning issue. In particular, aggregation and micro-environment biophysical changes alter the fluorescence quantum yield [115, 301, 302], and this will cause differences between the *in vivo* fluorescence and the *ex vivo* fluorescence intensities. *ex vivo* methods typically involve tissue digestion and chemical extraction in a NaOH-type solvent with SDS or some other emulsifying agent [284, 299]. This results in a quasi-monomeric solution which should have a maximal fluorescence yield. However, *in vivo* the fluorescence within different compartments of the tissue may have significantly different fluorescence yield values, resulting in

a cumulative signal which is not linear with increased drug or not consistently linear over time with the actual drug concentration in the bulk tissue. These changes are quite difficult to prove conclusively, yet, perhaps the most important part of this observation is that the fluorescence yield *in vivo* is likely a better reporter of photo-physically active compound [115]. There are enough data to support the contention that *in vivo* fluorescence should be used to predict *in vivo* photo-activity [303, 304]. Dosimetry based upon *in vivo* fluorescence is widely accepted in PDT studies, and methods for advanced interpretation of the *in vivo* signal have been proposed in several recent studies [305].

This chapter focuses on a more subtle problem than the *ex vivo/in vivo* issue, namely that the size of the sampling volume affects the magnitude and variance of the detected fluorescence signal. In a recent series of studies, the development of an optimized fiber probe was outlined and tested in phantoms and animal tissues [289, 290, 295]. The design of the probe was developed around the idea that when the sampling volume is smaller in dimension than the average scattering distance in tissue (approximately 100 microns), then the detected fluorescence signal was not highly affected by the tissue optical properties [289, 306]. This design was coupled with the idea of using many small sampling fibers, spaced apart by enough distance to minimize crosstalk between them. This design proved useful and is now in routine pre-clinical and human use for PDT dosimetry [256]. However, it is still not obvious that this measured signal is a good representation of the mean and variance of the photosensitizer concentration *in vivo*. Indeed, systematic comparisons be-

tween fluorescence microscopy on frozen tissue sections and *in vivo* fluorescence still yield differences in the signal mean and variance [256]. This difference between fluorescence detection methods is the subject examined here, with a particular focus on how well the system measures the spatial variance of the fluorescence *in vivo*. The specific size scales examined here are between 10 microns and 1 mm sampling volume, where the smallest size presents the sampling at a size which is smaller than the typical inter-capillary spacing. This distance scale is important as it presents a primary barrier of drug delivery into tumor parenchyma. Yet sampling of larger volumes is often desired because it can be done macroscopically and feasibly both in pre-clinical and clinical treatment plans.

In this study, tissues from the same animals are used to compare fluorescence measured *in vivo*, to measurements *ex vivo* on frozen sections using microscopy. The histogram distribution of values are examined and compared. Finally, the partitioning between vascular and stromal spaces is quantitatively analyzed with image processing software, to examine how the transition from vascular localization to stromal localization affects the measurements. This was completed with the clinically used drug verteporfin for injection, which is a lipid formulation of the photosensitizer molecule benzoporphyrin derivative. The photo-physical activity of such a mixture is complex, making an interpretation of the sampling volume and micro-environmental effects even more important for accurate dosimetry measurements.

6.2 Materials and Methods

6.2.1 Photosensitizer

The photosensitizer verteporfin was used in this study, which is a lipid formulation of benzoporphyrin derivative (BPD)[111, 112, 301]. This was obtained from QLT Inc. (Vancouver, Canada). A stock saline solution of verteporfin was reconstituted according to the manufacturer's instructions and stored at 4 °C in a covered tube. This stock solution was injected intravenously to animals at various times prior to use, with a dose of 1.0 mg/Kg. The time points of 15 minutes, 3 hours, and 6 hours were analyzed for most studies, to examine the fluorescence as a function of time after injection. The fluorescent molecule is referred to as BPD in this study, whereas the injected agent is commonly called verteporfin, which includes the BPD and the lipid carrier with solution.

6.2.2 Tumor and Animal Models

The R3327-MAT-LyLu Dunning prostate tumor model was used in this study, which is an androgen-independent carcinoma, syngeneic to the Copenhagen rat. These R3327-MAT-LyLu prostate cancer cells were obtained from Tayyaba Hasan's laboratory, and were cultured in RPMI-1640 with glutamine (Mediatech, Herndon, VA) supplemented with 10% fetal bovine serum (HyClone, Logan, UT) and 100 units/ml penicillin-streptomycin (Mediatech). All animal procedures were carried out according to a protocol approved by the

Dartmouth College Institutional Animal Care and Use Committee (IACUC). Copenhagen rats (male, 6-8 weeks old) were used in this study, and were obtained from Charles River Laboratories (Wilmington, MA). Subcutaneous MAT-LyLu tumors were induced by injecting approximately 1×10^5 MAT-LyLu cells (suspended in 0.05 ml PBS) subcutaneously into the animal flank after shaving. The tumor growth was measured daily with calipers. Tumors were used for the experiment at 9-12 days after inoculation, with a surface diameter of 7-9 mm and a thickness of 2-4 mm.

6.2.3 Flow Cytometry

Tumor tissues were excised at 15 min and 3 h after injection of verteporfin (1 mg/Kg, i.v.) and minced under sterile and subdued light condition. The minced tumor tissue was digested in sterile PBS containing 0.05% protease (Sigma type IX), 0.02% DNase (Sigma type I) and 0.02% collagenase (Sigma type IV) under continuous shaking at 37 C for 40 min, as described previously [257]. The resultant single cell suspension was passed through a cell strainer (BD Biosciences) to remove any remaining tissue clumps and cell aggregates. Verteporfin fluorescence intensity was analyzed by a FACScan (BD Biosciences). 10000 cells were captured from each sample and verteporfin signal was read in FL32 channel (488 nm excitation and 610 nm long-pass emission) using a log amplifier.

6.2.4 Fluorescence Microscopy

The fluorescence of verteporfin was analyzed by fluorescence microscopy of the frozen tumor sections, at time points of 15 min, 3 hrs and 6 hrs following drug injection. To visualize the perfused blood vessels, a carbocyanine dye perfusion marker DiOC7₍₃₎ (Molecular Probes, Eugene, OR) was also injected intravenously at a dose of 1 mg/Kg one minute before excising the tumor tissue. Tumors were surgically removed from the animal immediately after sacrifice, and the tumors were embedded in TissueTek medium and snap-frozen immediately in liquid nitrogen cooled isopentane. Cryosections of 10 micron thickness were cut from the frozen tumor and the same microscopic fields were imaged for both verteporfin (excitation: 425/40 nm, emission: 700/30 nm) and the perfusion marker DiOC7₍₃₎ (excitation: 480/20 nm, emission: 540/40 nm) with a Nikon Diaphot-TMD fluorescence microscope.

6.2.5 *In vivo* Fluorescence Quantification

In vivo measurements were taken with a specially designed fluorimeter fiber-based system which micro-samples the tissue volume [256, 289, 290, 295]. The probe end was designed with 100 micron diameter fibers to constrain the volume of tissue sampled to be smaller than the average scattering distance of tissue (typically 100-200 microns) [289]. The system has been tested in several phantoms and animal studies, and has been systematically compared to tissue extraction values, using the photosensitizer tetrasulphonated aluminum

phthalocyanine [290]. In this study, the system was used to monitor fluorescence at multiple sites on the surface of the tumor, using 20 distinct locations and sampling 10 times from each site. The system was designed to sample each location for 0.5 seconds, and leave less than 1% bleached from each spot for each measurement. In practice the repeated measurements from each location were analyzed to determine that photobleaching had not caused a significant systematic decrease in the values during the 10 repeated measurements. The set of 200 data points for each animal were used to generate a histogram of fluorescence intensities for each animal. The histograms of individual animals were then cumulatively analyzed to create an average histogram for animals injected 15 minutes prior to measurements, and animals injected 3 hours prior to measurements.

6.2.6 Image Analysis and Statistical Analysis

Image analysis was completed on several microscopic fields from each section of the tumors. The intensity of the fluorescence in each pixel and in each image was assessed with custom written MATLAB programs [307] to quantify the fluorescence as a function of distance from the capillary wall in the tumor tissue. Paired images of capillaries, stained with DiOC7₍₃₎, and images of BPD fluorescence were used for the analysis, and the average intensity per pixel was quantified for each distance from the vessel wall (software can be run online or downloaded from <http://biolight.thayer.dartmouth.edu>). Assessment was completed for histogram-based analysis of the data, as well as analysis of fluorescence

as a function of distance from the capillaries. The analysis of histograms mean and variance values was completed with standard students t -test and f -test statistics. For differences in the mean of two distributions, the unpaired t -test provided the p -values for these. For comparisons where the variance was thought to change due to sampling volume changes, the f -test statistic was used, which is defined as the ratio of the variances. Using all the raw data, a p -value is calculated for the hypothesis that the two distributions have equal variance values, with a low p -value indicating that the variances are not equal. Thus a low p -value indicates that the distribution shapes are significantly different, even if the mean values are found to be the same.

6.3 Results

6.3.1 Flow Cytometry Analysis of Cellular Fluorescence

Histogram data from the cell flow cytometry experiments is shown in Figure 6.3.1. The data includes three groups of cells including: (1) control tumor cells having no verteporfin *in vivo*, (2) tumor cells extracted 15 minutes after verteporfin injection *in vivo*, and (3) tumor cells extracted 3 hours after verteporfin injection *in vivo*. Animals were used with injection at the same concentration of 1 mg/Kg of verteporfin. The flow cytometry results show histograms of fluorescence intensity (x-axis) versus number of cells (y-axis). This distribution of fluorescence values is routinely displayed on a logarithmic scale in flow

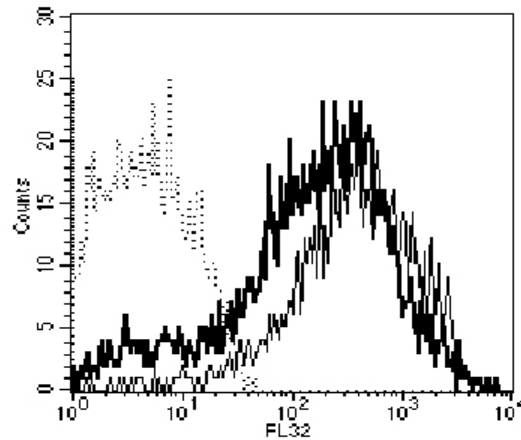


Figure 6.1: Flow cytometry histograms showing cellular uptake of verteporfin *in vivo*, assayed *ex vivo* after the tumor cells were removed and disaggregated. Control (dotted line); 15 min after verteporfin injection (thick line); 3 h after verteporfin injection (thin line).

cytometry analysis, as the signal was amplified in this manner, thus the resulting graph is shown in a linear representation of the signal intensity. Representative flow cytometry histograms are shown in Figure 6.3.1. The width of each histogram indicates that a large variation exists in the amount of photosensitizer per cell. The mean fluorescence intensity of the control sample is 7.4 and the mean intensity values increase to 342.6 and 611.4 at 15 min and 3 h after injection, respectively ($p < 0.01$). This experiment was repeated three times and they all showed the same trend. The potential wash out of BPD from the cells during the processing is a potential artifact of the procedure, but one which cannot be readily solved in this type of assay.

6.3.2 Fluorescence Microscopy of Frozen Tumor Sections

To quantify verteporfin fluorescence intensity in the tumors, several approaches were taken in interpretation of the images. For each tumor, several magnifications were used for sampling the tumor. The images shown in Figure 6.2, illustrate one aspect of the BPD distribution observed in these tumors, which is that the fluorescence intensity observed is significantly higher in the periphery of the tumor as compared to the center. This is a common observation of some experimental tumors, yet in any given field at higher magnification, Figure 6.2(a), the BPD distribution can appear quite homogeneous. These images were taken from tissue removed at 3 hours after BPD injection. Interestingly, the BPD fluorescence pattern in 6.2(b) is not representative of the perfused vascular pattern, shown in Figure 6.2(b), but the periphery of the image is on average 2 times as high in fluorescence as compared to the center of the image. This estimate of a factor of 2, is a bulk average value, estimated by quantifying the fluorescence in ImageJ software taking the average over the exterior 100 microns periphery to the interior volume inside this 100 micron ring around the tumor rim.

In addition to this observation, many sample images were taken at 40X magnification to analyze the fluorescence per pixel across average regions of the tumor. Representative images are shown in Figure 6.3, with the perfused blood vessels areas shown by DiOC7₍₃₎ fluorescence (Figure 6.3(a), 6.3(c) and 6.3(e)), and the second set of fluorescence images (right column) being BPD. Images were taken at 15 minutes, 3 hours and 6 hours post

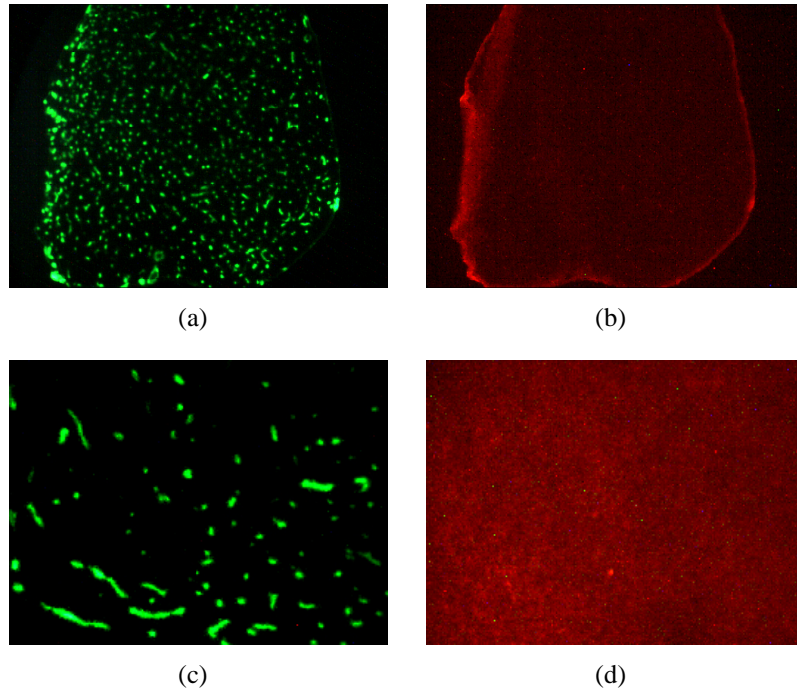


Figure 6.2: Images of vascular marker DiOC7₍₃₎ ((a), (c)) and BPD fluorescence ((b), (d)) at different magnification views of the same tumor type, including 4X on the top row ((a), (b)) and 40X on the bottom row ((c), (d)). These images were acquired 3 hours after verteporfin injection, and illustrate the macroscopic variation that exists from the edge to the center of the tumor (b), which is not reflected in the vascular pattern (a).

injection. Control images with no verteporfin injected were also taken and had very low levels of fluorescence intensity in the BPD images, as is reported in the next figure. All animals were injected with 1 mg/Kg of BPD in verteporfin. These type of images were acquired from 3 to 5 animals in each time point, and 3 sections were taken from each tumor. Within each section up to 12 microscopic fields were randomly sampled. The fluorescence per pixel histograms were calculated for the different time points, using frozen tumor sections from multiple animals, to quantify average cumulative histograms of the fluorescence at 15 minutes, 3 hours and 6 hours after injection of verteporfin.

These histograms are shown in Figure 6.4(a). Because small amounts of fluorescence are present in un-injected animals with tumors as well due to autofluorescence and leakage through the filters, the same analysis was completed in un-injected control tumors. In general, the un-injected animal tissues had low fluorescence on this setting (mean near 15 arb.units), the 15 minute time point showed higher fluorescence (mean near 19 a.u.), and the 3 hour data and 6 hour data had respectively higher mean values (near 27 and 29 a.u., respectively). This analysis was completed without subtracting the background fluorescence from the sample data, whereas in the data presented in the next figure (Figure 6.5) all histograms have more data included, and have a background subtraction. The spatial heterogeneity in these images was analyzed using a MATLAB program which found the vessel locations and then binned intensity values radially outward from the vessel walls. The values summed from multiple images are reported in Figure 6.4(b), showing the con-

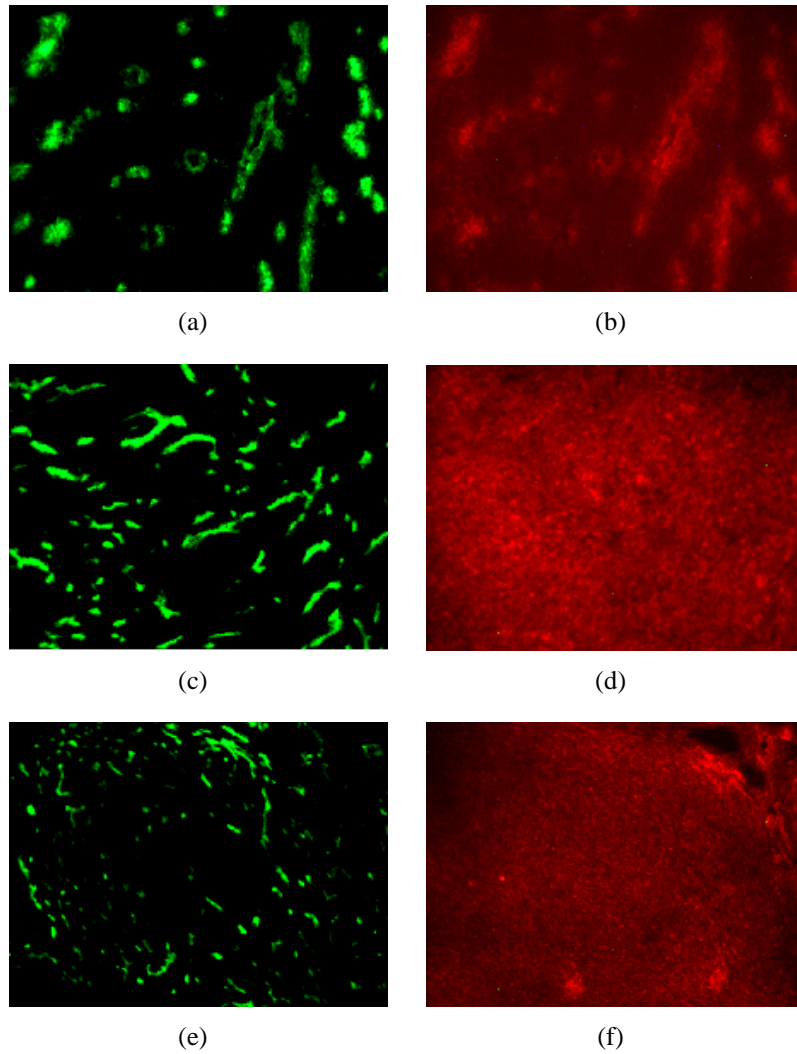


Figure 6.3: Images of vascular perfusion marker DiOC7₍₃₎ ((a), (c), (e)) and BPD fluorescence ((b), (d), (f)) and are shown superimposed together from frozen tissue slices of tumor. The three images show representative distributions where the tumor tissue was resected and frozen at different times after BPD injection, including 15 minutes (a), 3 hours (b) and 6 hours (c). The DiOC7₍₃₎ was injected within 5 minutes before the tumor resection in all cases.

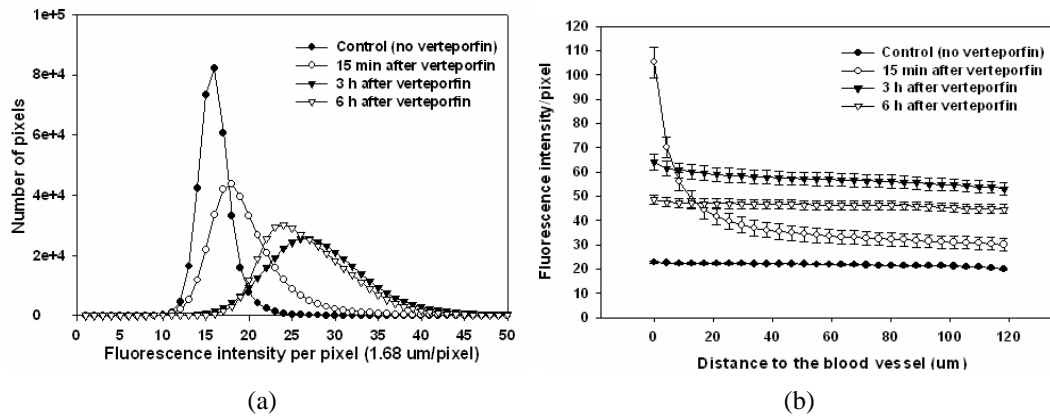


Figure 6.4: Fluorescence in tumor tissue as quantified by microscopy analysis is shown in (a) as histograms showing the distribution of fluorescence intensity and (b) as a function of distance from the capillaries. Analysis was completed on about 40 frozen sections images from 3 animals in each group.

control, 15 minute, 3 hour and 6 hour tissue data. The higher concentration near the vessel wall at 15 minutes illustrates the diffusion gradient of drug coming out from the vessel at this early time. Whereas the longer time points of 3 and 6 hours show comparatively flatter distributions, indicating there was no strong gradient.

6.3.3 Histogram Analysis of Fluorescence Microscopy

The histogram data from fluorescence microscopy was analyzed in two ways. Since multiple animals and multiple sections were used, there is sufficient data to quantify the fluorescence on different spatial scales. The fluorescence intensity per pixel was quantified for each image, and these were summed into a single histogram, reported in Figure 6.5(a) and 6.5(c), for the 15 minute and 3 hour time points, respectively. Next, the fluorescence intensity per image was quantified as well, providing a fluorescence intensity measure which

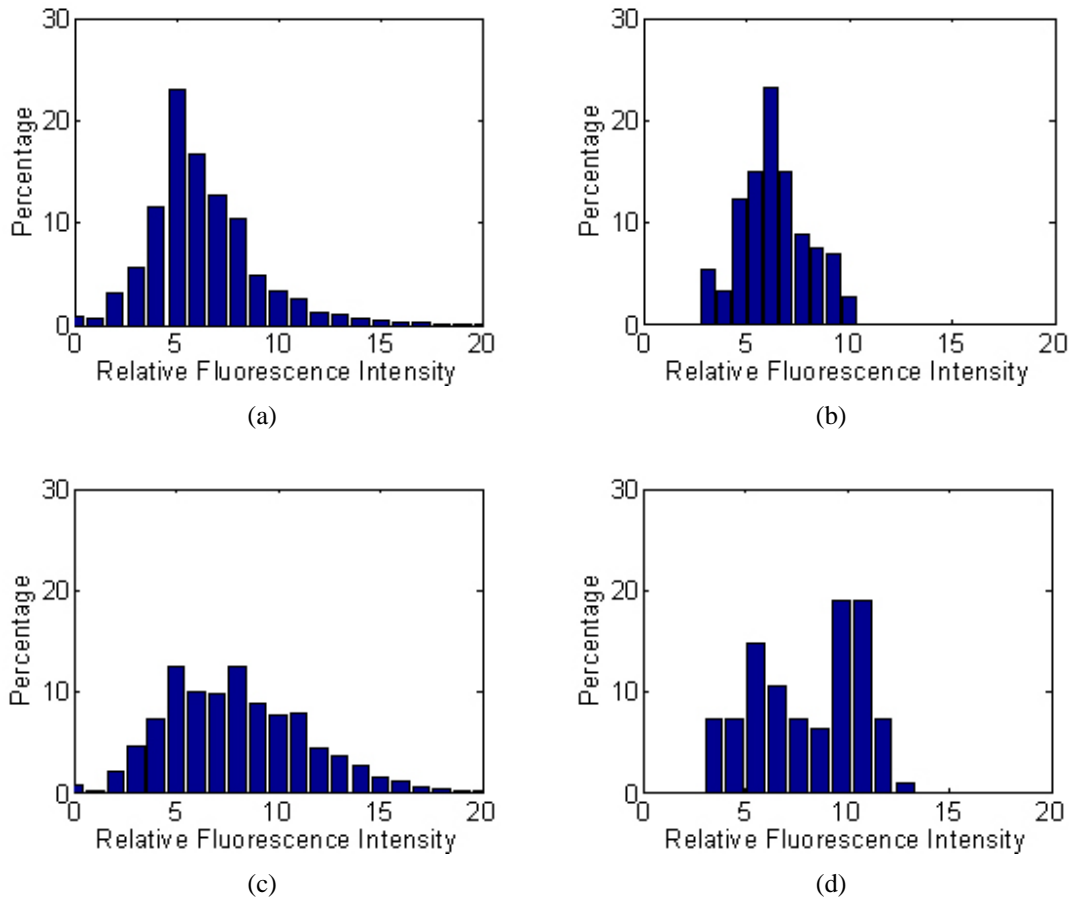


Figure 6.5: Histograms of fluorescence intensity are shown for analysis from frozen section microscopy data as listed in the previous figure, with the tissue resected 15 minutes after verteporfin injection (top row) and 3 hours after injection (bottom row). The two sets of graphs show the analysis completed where each pixel was taken separately and all pixels in all images were used (left column graphs), and then also the data is reported (in the right column) where the entire image fluorescence intensities were used, such that each histogram represents a higher spatial averaging. The data is taken from 6-7 animals in each group, using 3 slice sections for each tumor, and 147 and 95 images total, for the 15 minute and 3 hr data, respectively. For the pixel data, all pixels in the image were used, corresponding to 349,133 values per image. Analysis of the histogram differences and similarities is quantified in Table 6.1

Histogram	Number of samples	Mean \pm Std ($\langle f \rangle \pm \sigma$)	Mean t -test p value for $\langle f_i \rangle \neq \langle f_p \rangle$	f -test statistics σ_i^2 / σ_p^2	Variance f -test p value for $\sigma_i^2 = \sigma_p^2$
15 min Pixel	5.1×10^7	6.4 ± 3.2	0.008	0.29	0
15 min Image	147	6.4 ± 1.7			
3 hr Pixel	3.3×10^7	8.1 ± 3.9	0.009	0.5	0
3 hr Image	95	8.1 ± 2.7			

Table 6.1: Statistical data for the histograms shown in Figure 6.5, for 15 minute data 6.5(a) and 6.5(b), and 3 hour data 6.5(c) and 6.5(d). The mean ($\langle f \rangle$) and standard deviation (σ) for each histogram is shown in the 3rd column. The 4th column reports on the p -value that the means of the pixel and image values are different (*i.e.* $\langle f_i \rangle \neq \langle f_p \rangle$), with the results showing that the two 15 minute histograms are significantly the same, and the two 3 hr histograms are as well, in terms of their mean values. In the 5th column the results of the f -statistic are shown which is the ratio of the variances. In the 6th column the f -test p -values are shown for the hypothesis that the variances are equal (*i.e.* $\sigma_i^2 = \sigma_p^2$), showing that the probability is zero that these variances at the pixel level and image level are equal.

averages a considerably larger volume of tissue (1 mm^2), rather than for each pixel in the images. This latter approach was used to create histograms as well, and these are shown in Figure 6.5(b) and 6.5(d). While the data in these two sets of graphs is derived from the same images, the resulting histograms have differences from each other, notably that the variance is reduced in the latter cases 6.5(b) and 6.5(d), as compared to 6.5(a) and 6.5(c). The data was fit to a normal distribution, and clearly the data sets in 6.5(a) and 6.5(c) are more optimal for this, as they have larger numbers of data. The mean values and variance of each distribution can be calculated for the distributions in 6.5(b) and 6.5(d), which are analogous to the *in vivo* measurements, reported in the next section. As stated in the previous section (discussing Figure 6.4), the histograms in Figure 6.5 include a larger number of samples and have background subtracted values reported, to exclude the signal due to

the background fluorescence. For the 15 minute data, the mean is 6.4 for both pixel and image level sampling and yet the variance was 1.7 for image level sampling and 3.2 for pixel level sampling. This difference in the variance is statistically different, as shown by the f -test statistic in Table 6.1, where the probability that the variances are equal is determined to be 0.000. For the 3 hour data, the mean is 8.1 for both the pixel and image level sampling of the fluorescence and yet the variance was 2.7 for image level sampling and 3.9 for pixel level sampling. Again, this is significantly different (Table 6.1), indicating that the distributions are fluorescence are different based upon the size scale of sampling.

6.3.4 *In vivo* Fluorescence Measurements

In vivo measurements of BPD fluorescence were taken using several animals as discussed in the materials section. The histogram of fluorescence intensities for two individual animals can be seen in Figure 6.6(a) and 6.6(b), for the cases of 15 minutes and 3 hours post injection of verteporfin. These individual data are shown to illustrate how each animal typically has a smaller variance in the data distribution, as compared to the overall variance observed in the data summarized for five animals, shown in Figure 6.6(c). Even though 100 data points were acquired from each tumor, as shown in 6.6(a) and 6.6(b), the histograms do not show a lot of high and low values, as compared to the cumulative graph 6.6(c). In Figure 6.6(a), the mean and variance values are tabulated in Table 6.2, as 0.13 and 0.05 for rat 1, and 0.09 and 0.05 for rat 2.. These two distributions have a similar variance, but

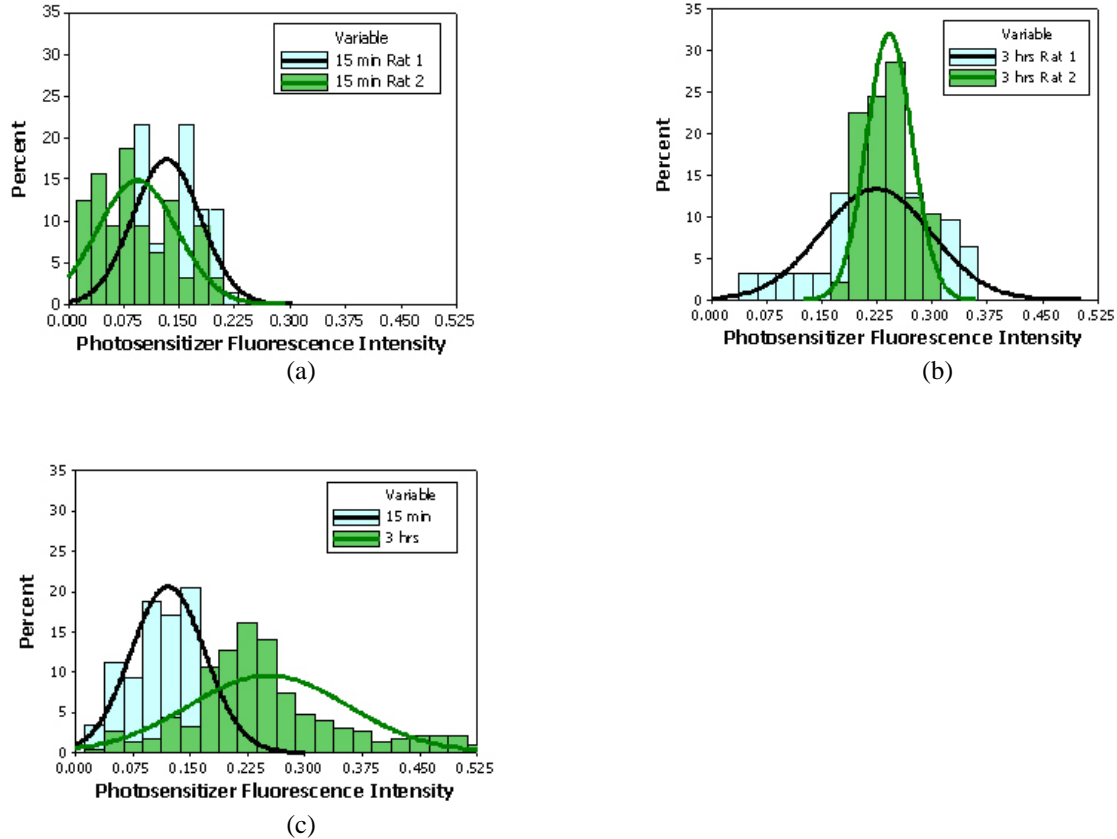


Figure 6.6: Histograms of fluorescence intensity are shown for analysis from frozen section microscopy data as listed in the previous figure, with the tissue resected 15 minutes after verteporfin injection (top row) and 3 hours after injection (bottom row). The two sets of graphs show the analysis completed where each pixel was taken separately and all pixels in all images were used (left column graphs), and then also the data is reported (in the right column) where the entire image fluorescence intensities were used, such that each histogram represents a higher spatial averaging. The data is taken from 6-7 animals in each group, using 3 slice sections for each tumor, and 147 and 95 images total, for the 15 minute and 3 hr data, respectively. For the pixel data, all pixels in the image were used, corresponding to 349,133 values per image. Analysis of the histogram differences and similarities is quantified in Table 6.1

Histogram	Number of samples	Mean \pm Std ($\langle f \rangle \pm \sigma$)	Mean t -test p value for $\langle f_i \rangle \neq \langle f_p \rangle$	f -test statistics σ_i^2 / σ_p^2	Variance f -test p value for $\sigma_i^2 = \sigma_p^2$
Rat 1, 15 min	70	0.13 ± 0.05	0.008	0.73	0.283
Rat 2, 15 min	32	0.09 ± 0.05			
Rat 1, 3 hr	31	0.22 ± 0.07	0.009	0.17	0
Rat 2, 3 hr	49	0.24 ± 0.03			
Summary 15 min	117	0.12 ± 0.05	0	0.21	0
Summary 3 hr	300	0.25 ± 0.10			

Table 6.2: Statistical data for the histograms shown in Figure 6.6 of the two sample rats shown for 15 minute data in 6.6(a), 3 hour data in 6.6(b), summary data shown in 6.6(c). The mean and standard deviation for each histogram is shown in the 3rd column. The 4th column reports on the p -value that the means are the same, with the results showing that the two 15 minute histograms are significantly different, and the two 3 hr histograms are as well, in terms of their mean values. In the 5th and 6th columns the results of the f -statistic are shown, where the variance is significantly lower in the image histogram for the 3 hr case, but not the 15 minute case. When comparing the 15 min data to the 3 hr data, the variance is also significantly different.

different mean values. These two samples are simply illustrative of an overall trend which is seen from sampling many different animals, which is that the variance of the distribution is often the same, but the mean value between animals can be different. In Figure 6.6(b) the mean and variance values are tabulated in Table 6.2 as well, and are 0.22 and 0.07 for rat 1, and 0.24 and 0.03 for rat 2. In this case the drug has distributed more homogeneously in the tissue, and the mean values are much closer between animals, and the variance of the distribution is seen to be different. In Figure 6.6(c) when the composite data is plotted for both the 15 min and 3 hour time points using several animals, the mean and variance values are listed in Table 6.2, and are 0.12 and 0.05 for 15 minutes, and 0.25 and 0.10 for 3 hours. These two distributions have different mean values and different variances, where both the mean and the variance increase by a factor of 2, between the 15 minute and the 3 hour time points.

6.4 Discussion

While a large number of research studies use fluorescence measurements from tissue as a tool to assess concentration or relative changes in concentration of photosensitizer, comparably little has been published upon the effect of how the measurements are done. In the past two decades or so, knowledge of how the tissue scattering affects the detected signal has significantly improved, to the point where it is possible to simulate and predict measured signals, given predictions of the bulk tissue optical properties. However, in all these

studies, both simulations and experimental, the micro-regional fluctuations in optical properties and the micro-regional changes in drug compartmentalization are largely ignored. This is a practical issue, as compensating or accommodating these changes is exceptionally difficult, however in this study the focus has been upon understanding these changes spatially and temporally, to allow a full understanding of the limitations of our measured signal.

When the photosensitizer is injected in the animal and is distributed by the vascular tree, the diffusion of the drug occurs into the tissue, and there are two levels of heterogeneity that were observed here. First, there is considerable macroscopic heterogeneity which is induced by the physical features of the tumor, as shown in Figure 6.2(b), where the concentration in the peripheral regions of the mass are on average about 2 times as high as in the center of the image. This large degree of macroscopic spatial heterogeneity is clearly problematic, yet well documented in both chemotherapy and photodynamic therapy drug distribution studies. The origins of macroscopic spatial heterogeneities are still not well understood, even after considerable research, yet are largely attributed to pressure gradients slowing the diffusive process [308]. This is a static phenomenon which needs to be understood and used when interpreting measurements from the surface of tumors. The current fiber optic design used here [256, 289, 290, 295], was designed specifically to sample shallow regions of tissue because of the need for reducing the effect of tissue light scattering upon the measured signal. The design works well for what it is proposed

for, but will ultimately only sample the most superficial 200-300 microns of tissue, which is the region where the drug concentration is highest. Thus, this design of a fiber probe is not ideal for the tumor type where the periphery of the tumor is so substantially higher than the interior. An interstitial fiber probe or a macroscopic diffuse sampling probe would be required to measure from the interior of the tumor. This is a static problem in drug sampling from tissue, which can confound many studies of drug delivery *in vivo*.

The origin of the spatial heterogeneity observed in Figure 6.3(b) at the 15 minute time point is due to the diffusion time required for drug to make it from the higher concentration in the vessel out to the distant sites of the tumor epithelium. This spatial concentration gradient induces the diffusive transport of the drug, once it has passed out of the endothelial barrier. Measurement of the drug concentration at early times will always be confounded by this compartmentalization issue. However, the data plotted in Figures 6.5(a) and 6.5(b) illustrate the different signals which would be measured from a small sampling region and a larger sampling region. In general, the mean values of these two distributions appear the same (p -values in Table 6.1), being 6.4 for the 15 minute data and near 8.1 for the 3 hour data. However while the means of the distributions appear similar, the obvious difference is that the lowest and highest values of the distribution are lost, in this latter case. The variances are significantly different, as shown by the f -test statistic and p -values shown in Table 6.1, illustrating that the distribution observed with pixel-level sampling is wider than the distribution observed when sampling is done over larger areas of tissue.

Thus, sampling fluorescence from larger and larger regions has the affect of averaging the distribution function toward the mean value, and there is a loss of the lowest and highest parts of the histogram. It is not yet clear what implications these areas with very high and low drug level may have on PDT treatment outcome. If measurement of the lowest and highest photosensitizer concentrations is important or useful for predicting tumor response, then sampling with smaller fibers and detectors will be important. However sampling of many points on each tumor would then also be essential, similar to how Eppendorf oxygen electrode measurements of tumors require multiple points and multiple tracks to be used for a useful measurement of the oxygen distribution in a tumor [309]. It is possible that the mean value of photosensitizer concentration is all that is required, and then sampling with larger fibers should be sufficient.

We compare these microscopic data to the *in vivo* fiber measurements, plotted in Figure 6.6, and similar histograms are seen. The quantification of the mean and variance values of these distributions in Table 6.2, shows that the mean values between different animals can easily be different, and the variance values may or may not be different, depending upon the physical characteristics of the drug diffusion and the sampling. The most important observation in this data set is that the distributions are similar to those observed in Figure 6.5, when image level sampling was completed, such that the ratio of the variance to the mean of the distribution is small. The cumulative data for any one animal show a histogram which has a variance which is in reasonable agreement with the microscopic data, yet

appears as though the lowest and highest values of the histogram are not well represented (see Figure 6.6(b)). When data are pooled from several animals (Figure 6.6(c)), then the full histogram appears more like a normal distribution, with values down to zero and up to the higher values. Thus, for any one animal, multiple sampling of the tumor is still useful, yet will not show the range of low and high values present in the tissue and the microscopic scale. This is a fundamental observation, that macroscopic sampling can likely never reveal the true range of concentrations existing in the tissue, because the distribution achieved has systematically averaged out the lowest and highest values. The only way to achieve the full distribution of values in the tissue is to sample at the tissue many times on a distance scale which is smaller than the inter-capillary spacing.

However, the choice of which size scale is presents the "true" distribution is also a good question, and an extension of this study might also be to sample the tissue at the distance scale of the cell, or of sub-cellular organelles. These distance scales are also likely to present histogram distributions which are different than that observed on the intercapillary spacing distance scale. However, since the dominant factor in drug distribution is the diffusion or transport from the capillaries into the parenchyma, this study has focused on this latter scale, as compared to a macroscopic sampling scale of nearer 1 mm.

This study has not addressed the question of what the pertinent measurement of photosensitizer concentration is *in vivo*. It has been implied that the mean value of the concentration is the important parameter, and clearly photodynamic therapy effect scales with

the drug dose in the tissue [305, 310, 311]. However, it is interesting to compare the photosensitizer histogram to the oxygen histogram observed in Eppendorf electrode studies [312]. In both radiation therapy and photodynamic therapy, there is good evidence to support the idea that the fraction of the tumor at the lowest oxygen tension is ultimately what limits the efficacy of therapy [309, 313–315]. Thus, it is also conceivable that the fraction of the tumor which has low photosensitizer concentration is what limits the efficacy of photodynamic therapy. However, currently this is just a hypothesis, and as yet untested. The main purpose of the present study was simply to understand what the measurement of fluorescence *in vivo* represents in terms of the true photosensitizer concentration in the tissue.

6.5 Conclusions

In conclusion, when fluorescence is measured *in vivo* the size of the region sampled appears to affect the measurement histogram of values, but does not strongly affect the mean value. As the region sampled is increased to larger than the typical inter-vascular distance, the histogram of values observed tends to lose the lowest and highest parts of the histogram. This is typically what can be observed with *in vivo* sampling of tissue with fiber optic probes. The macroscopic heterogeneity observed in many experimental tumors is an important issue for sampling of tumors, because if the measurement is taken from the exterior of the tumor, then the signal will be biased towards higher values than is representative of the

full tumor. These effects upon the sampled signal are likely difficult to avoid or correct for, but need to be well understood when interpreting *in vivo* data. Further study of this effect could be carried out with fiber probes of varying diameter, and this work is ongoing presently. This study presents an initial interpretation of the size scales of heterogeneity observed in this experimental tumor system, using microscopy and a current working fiber probe system.

Part III

Strategies for PDT Treatment

Individualization

Chapter 7

Correlation between Photosensitizer Pharmacokinetics and PDT Outcome

In **Part II**, we have discussed the sources of the photosensitizer pharmacokinetic variability, pharmacokinetic models of photosensitizer systemic distribution and distribution inside tumor tissue, and tumor microenvironment effects upon the photosensitizer pharmacokinetics. Once these pharmacokinetic variabilities have been recognized and the potential sources of variabilities have been identified, the next question is how can these pharmacokinetic variabilities be reduced? To find the answers to this, we first need to understand the correlation between photosensitizer pharmacokinetics and treatment outcome. In this chapter, we will explore the connection between these on the individual level.

7.1 Introduction

In photodynamic therapy, it is assumed that the photosensitizer should be preferentially delivered to, or retained in the tumor for the best therapeutic effect. This concept has determined the design of new photosensitizers/photosensitizer delivery systems and clinical PDT treatment protocols. For example, the development of liposome photosensitizer delivery systems has enabled the tumor cell specific targeting through the surface modification of liposomes. Active targeting liposomes can remain stabilized in the circulatory system, and preferentially extravasate at the tumor site. They accumulate in the tumor interstitium and enter the tumor cells via tumor specific antibody-receptor endocytosis. Usually, in defining optimal PDT treatment protocols, standard dose escalation methods are used to explore the optimal drug-light interval at which there is maximal difference between photosensitizer uptake in tumor and the surrounding normal tissues. However, it has not been possible to ensure the amount of photosensitizer molecules delivered to the targeting tumor cells, due to variety of factors in the process of photosensitizer delivery which have been discussed in Chapter 3 and 4. In addition to these microscopic intra-tumor photosensitizer variabilities, there is growing evidence that the distribution of photosensitizer between individuals fluctuates significantly. But the connection of how photosensitizer pharmacokinetic variation affects the PDT treatment efficacy has not yet been investigated. In this study, these relations between intra-tumor and inter-tumor variability in photosensitizer uptake are examined, and the correlation between inter-individual photosensitizer

pharmacokinetic variability and responses to cellular-targeting and vascular-targeting PDT treatment.

7.2 Material and Methods

7.2.1 Animals and Tumor Model

The R3327-MAT-LyLu Dunning prostate tumor model was used in this study, which is an androgen-independent carcinoma, syngeneic to the Copenhagen rat. These R3327-MAT-LyLu prostate cancer cells were cultured in RPMI-1640 with glutamine (Mediatech, Herndon, VA) supplemented with 10% fetal bovine serum (HyClone, Logan, UT) and 100 units/ml penicillin-streptomycin (Mediatech). All animal procedures were carried out according to a protocol approved by the Dartmouth College Institutional Animal Care and Use Committee (IACUC). Copenhagen rats (male, 6-8 weeks old) were used in this study, and were obtained from Charles River Laboratories (Wilmington, MA). Subcutaneous MAT-LyLu tumors were induced by injecting approximately 1×10^5 MAT-LyLu cells (suspended in 0.05 ml PBS) subcutaneously into the animal flank after shaving. The tumor growth was measured daily with calipers. Tumors were used for the experiment at 9-12 days after inoculation, with a surface diameter of 7-9 mm and a thickness of 2-4 mm.

7.2.2 Cellular and Vascular Targeting Photodynamic Therapy

A 690 nm wavelength diode laser system (Applied Optronics, CT) was used throughout the study for irradiation of tumor. The light was delivered through a 140 μm optical fiber, and illuminated the tumor surface over 1 cm diameter beam spot after passing through a fiber optic collimator. The MAT-LyLu tumors were exposed to an incident fluence rate of 50 mW/cm^2 , as measured by an optical power meter (Thorlabs Inc., North Newton, NJ). Animals were anesthetized with an intramuscular injection of ketamine-xylazine (90 mg/Kg and 9 mg/Kg) and placed on a heating pad maintained at 37 $^\circ\text{C}$, throughout the treatments.

In the vascular targeting PDT treatment group (vPDT), animals received verteporfin intravenously at a dose of 0.25 mg/kg BPD-MA per bodyweight. Tumors ($n = 11$) in vPDT group were exposed to 75 J/cm^2 total light dose 15 min after verteporfin administration. Animals in the cellular targeting PDT treatment group (cPDT) ($n = 20$) received 1 mg/kg BPD-MA via i.v. injection, and were exposed to a same total light dose 3 hours after verteporfin injection. Tumors in the control group (CTRL) ($n = 20$) also received 1 mg/Kg BPD-MA, but were not exposed to light illumination.

7.2.3 Tumor Regrowth Assay

A tumor regrowth assay was used to quantify the treatment effects of photodynamic therapy. Width (a), length (b) and height (c) were measured with slide calipers to determine

the tumor volume, and calculations were performed using the formula $V = \frac{\pi}{6} \times a \times b \times c$. The longitudinal tumor volume data, as a function of time (in days) after treatment, are displayed on a semi-logarithmic scale. The advantage of the semi-logarithmic versus regular scale is that exponentially growing tumors follow a straight line so that the effects of the tumor growth delay are clearly seen. Moreover, expressing observations as $v_t = \ln(V_t)$, where V_t is the tumor volume at time t , facilitates modeling of tumor growth and regrowth in treatment groups and their statistical comparison [316]. The following tumor regrowth model [316] has been applied to mathematically to describe the dynamics of treated tumors: $v_t = \alpha + \beta t - \ln(SF\%)(e^{-\delta t} - 1)$, where α is the log tumor volume before the treatment, β is the growth rate of unaffected tumor cells, δ is a cell loss constant at which the treated cells die, and $SF\%$ is survival fraction. This model allows computing other treatment endpoints such as tumor regrowth delay (TGD) computed as and doubling time (DT) as the solution to the equation. Tumor regrowth delay (TGD), doubling time (DT) and survival fraction ($SF\%$) were used to determine variation of tumor response within and between groups.

7.2.4 Photosensitizer Pharmacokinetics Quantification

Verteporfin plasma concentration quantification

In the vPDT treatment group, animals were anesthetized and verteporfin was injected at 0.25 mg/Kg BPD-MA as described above. Verteporfin plasma concentrations from each animal were measured at different time points after photosensitizer i.v. injection. At these

times, 200 μ l blood was drawn from the Jugular vein of each animal at 3, 5, 10, and 15 min. Animals then received light treatment as described above. The plasma was separated from the blood by centrifugation at 8000 rpm at 4°C. The plasma was diluted by a factor of 10 in a solution of 1% SDS in PBS and placed in a 2.5 ml cuvette. The fluorescence spectrum was recorded by a FluoroMax-2 (Jobin Yvon Inc., Edison, NJ) excited at 430 nm. The peak fluorescence intensities at 690 nm were converted to g/ml using the fluorescence intensity for the BPD concentration calibration curve.

Verteporfin tissue concentration *in vivo* quantification by Aurora Fluorometer

In the cPDT group, animals were injected verteporfin intravenously at a dose of 1.0 mg/Kg. At 3 hours after photosensitizer administration, *in vivo* measurements were taken with the Aurora fluorometer [256, 289, 290, 295]. The probe end was designed with 100 micron diameter fibers to constrain the volume of tissue sampled to be smaller than the average scattering distance of tissue (typically 100-200 microns) [289]. The system has been tested in several phantoms and animal studies, and has been systematically compared to tissue extraction values, using the photosensitizer tetrasulphonated aluminum phthalocyanine [290]. In this study, the system was used to monitor fluorescence at multiple sites on the surface of the tumor, using 20 distinct locations and sampling 10 times from each site. The system was designed to sample each location for 0.5 seconds, and leave less than 1% bleached from each spot for the measurements. In practice the repeated measurements from each location

were analyzed to determine that photobleaching had not caused a significant systematic decrease in the values during the 10 repeated measurements. The set of 200 data points for each animal were used to analyze the verteporfin distribution heterogeneity within a tumor for each animal. The average of these 200 data points were used to represent the verteporfin tumor uptake and to analyze the uptake variation between individual animals.

Verteporfin tissue concentration *ex vivo* quantification by Fluorescence Microscopy

In a separate group, tumor bearing animals received i.v. injection of verteporfin at 1.0 mg/Kg. At 15 min or 3 hours post drug administration, animals were sacrificed and tumor tissues were rapidly dissected, embedded in TissueTek medium and snap-frozen in liquid nitrogen. Cryosections of 10 micron thickness were cut from the frozen tumor, and fluorescence of BPD-MA was then analyzed with a Nikon Diaphot-TMD fluorescence microscope equipped with a chroma filter set specially designed for this fluorophore (excitation: 425/40 nm, emission: 700/30 nm).

7.3 Results

7.3.1 Intra-tumor and Inter-tumor Variation in Verteporfin Pharmacokinetics

Verteporfin plasma pharmacokinetics

Verteporfin plasma pharmacokinetic profiles after a single bolus i.v. injection of verteporfin in tumor bearing rats are shown in Figure 7.1. The plasma concentration decreased rapidly during the time course of monitoring. The individual normalized data were then fitted to a single exponential decay model $C(t) = Ae^{-\alpha t}$, and then verteporfin elimination half-lives were calculated by $\tau_{\frac{1}{2}\alpha} = \ln 2/\alpha$. Table 7.1 listed these verteporfin plasma pharmacokinetic parameters were for the 11 animals in the vPDT group. The final global fitted single-exponential decay model can be expressed as:

$$C(t) = 0.995e^{-0.072t} \quad (7.1)$$

where t is the time after verteporfin injection (in minutes) and $C(t)$ is the normalized verteporfin plasma concentration. The metabolic half-life for verteporfin is thus 9.61 minutes which is consistent with our previous results Chapter 4.

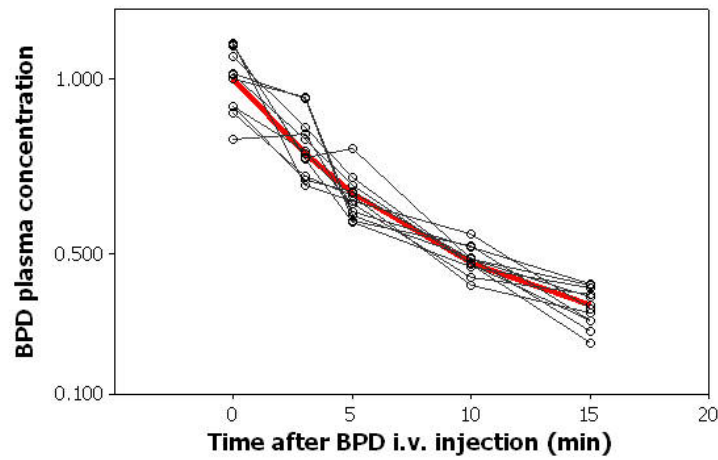


Figure 7.1: Normalized verteporfin plasma concentration as a function of time after a single i.v. injection. Individual plasma concentration profiles were normalized to their mean concentration at time zero. The normalized individual profiles were plotted in thin black lines with black circles, and the fitted curve to the mean was plotted in a red thick curve.

Animal ID	Age (Weeks)	Body Weight (g)	A (A.U.)	$\tau_{\frac{1}{2}\alpha}$ (mins)
1	7	175	0.91	9.84
2	7	170	0.93	10.48
3	6	180	1.07	9.48
4	7	175	1.02	9.24
5	7	185	1.04	8.99
6	6	195	0.87	14.04
7	6	170	1.04	8.28
8	7	180	1.08	8.51
9	6	185	1.05	8.53
10	7	175	1.03	8.73
11	7	185	0.89	9.38

Table 7.1: One compartment model parameter estimations for individual animals. Each pharmacokinetic data set was fitted to $C(t) = Ae^{-\alpha t}$, elimination half-lives $\tau_{\frac{1}{2}\alpha} = \ln 2 / \alpha$.

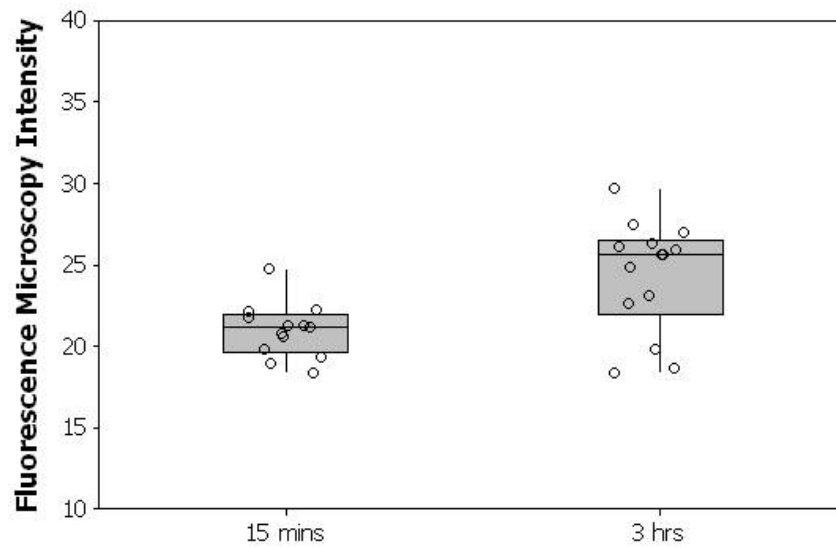
Verteporfin tissue concentration variability evaluated by fluorescence microscopy

To quantify the variation of BPD-MA fluorescence intensity at different locations within a tumor, and the mean fluorescence intensity between tumors, 40X magnification was used for sampling the fluorescence in frozen tissues. Each fluorescence image contained 682×512 pixels which is equivalent to $1150 \times 863 \mu\text{m}^2$. At least ten $1150 \times 863 \mu\text{m}^2$ fluorescence images were obtained at different locations within a tumor from each animal, and 13 and 14 animals were included in the 15 min and 3 hr time point groups, respectively.

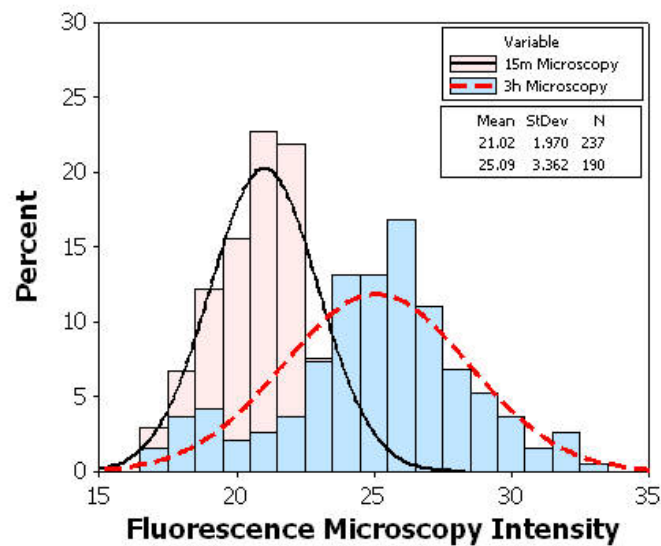
Verteporfin fluorescence intensity of each $1150 \times 863 \mu\text{m}^2$ sampling area was quantified. The averages of fluorescence intensities measured from different images from the same tumor were used to represent the uptake level for that individual. Comparison of individual tumor uptake between 15 min group and 3 hr groups is shown in Figure 7.2(a) and Table 7.2. Verteporfin fluorescence intensity was found significantly higher in the 3 hr group compared to 15 min group ($p < 0.05$).

The fluorescence intensities of each image from individual animals were pooled together and summarized in the histogram (Figure 7.2(b)) for the analysis of intra-tumor variation of verteporfin uptake. The coefficient of variation (standard deviation mean ratio) was used to evaluate the variabilities of verteporfin concentration level at distinct locations within the tumor. Statistical analysis of these fluorescence microscopy data are listed in Table 7.2.

The coefficient of variation (CV%) and mean values of each set of verteporfin fluo-



(a)



(b)

Figure 7.2: Verteporfin tumor uptake evaluated by fluorescence microscopy. Vascular targeting PDT group (15 m) included 237 fluorescence images from 13 animals, whereas cellular targeting PDT group (3 h) included 190 fluorescence images from 14 animals. Comparisons were presented in box-plot (a) and histogram (b) to illustrate the inter-tumor and intra-tumor variation in BPD distribution.

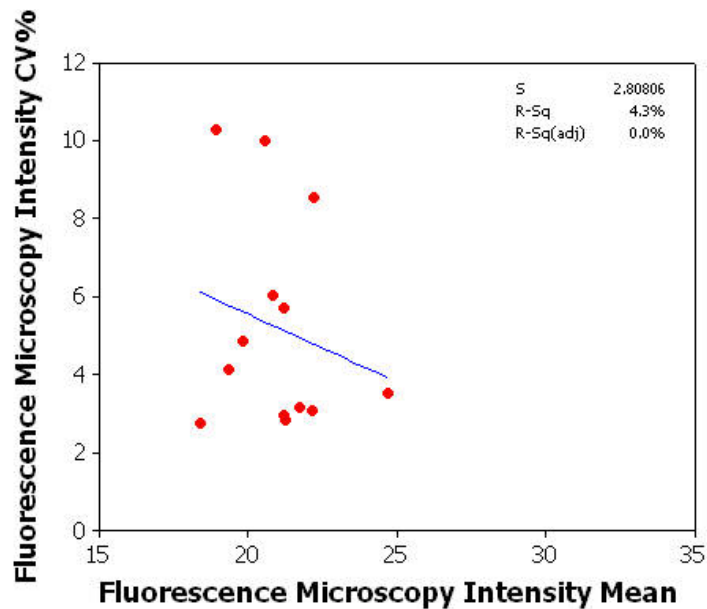
Histogram	Number of samples	Mean \pm Std ($\langle f \rangle \pm \sigma$)	CV%	Mean t -test p value for $\langle f_i \rangle \neq \langle f_p \rangle$	f -test statistics σ_l^2 / σ_p^2	Variance f -test p value for $\sigma_l^2 = \sigma_p^2$
15-min image	237	21.02 \pm 1.97	9.37	0.000	0.34	0.000
3-h image	190	25.09 \pm 3.36	13.39			
15-m individual	13	20.95 \pm 1.65	7.88	0.003	0.23	0.017
3-h individual	14	24.37 \pm 3.42	14.03			

Table 7.2: Statistical analysis for histograms shown in Figure 7.2., for intra-tumor variation 7.2(b), and inter-tumor variation 7.2(a). The mean ($\langle f \rangle$) and standard deviation (σ) for each histogram is shown in the 3rd column. The 4th column shows the coefficient of variation representing the extent of variation. The 5th column reports on the p -value that the means of the vascular targeting PDT group and cellular targeting PDT group are different (*i.e.* $\langle f_i \rangle \neq \langle f_p \rangle$). In the 6th column the results of the f -statistic are shown which is the ratio of the variances. In the 7th column the f -test p -values are shown for the hypothesis that the variances are equal (*i.e.* $\sigma_l^2 = \sigma_p^2$).

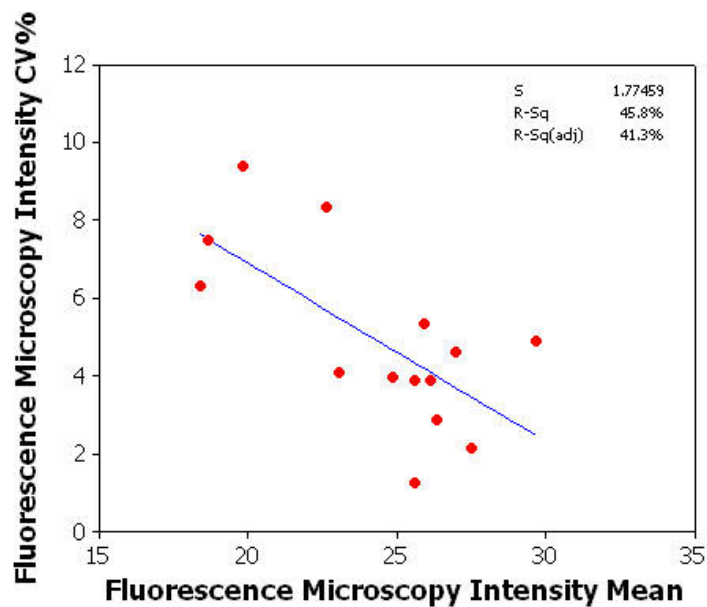
rescence measurements were used to analyze the photosensitizer fluorescence intra-tumor variability and inter-tumor variability. Figure 7.3 illustrates that there is an inverse correlation between tumor verteporfin uptake and the extent of photosensitizer variability (CV%) inside the tumors in the 3 hr group ($R^2 = 45.8\%$, $p = 0.008$). However, no such correlation was found in the animals in the 15 min group ($R^2 = 4.3\%$, $p = 0.495$).

Verteporfin tissue concentration variability evaluated by the Aurora fluorometer

Similar analysis was performed on verteporfin *in vivo* quantification data. Measurements were taken using 30 animals in the 15 min group and 40 animals in the 3 hr group. The mean fluorescence intensity of 100 data points was evaluated from 20 locations on the tumor and these were used to represent the verteporfin uptake level in that tumor. The



(a)



(b)

Figure 7.3: Correlation between verteporfin uptake intra-tumor variability and inter-tumor variability analyzed for vascular targeting PDT (15 m)(a) and cellular targeting PDT (3 h)(b).

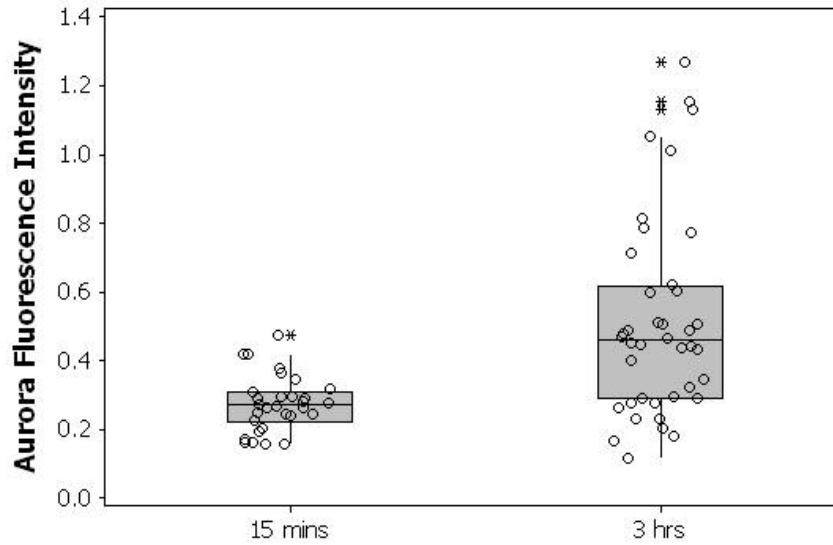
coefficient of variation represented the intra-tumor variation of verteporfin uptake.

The box-plot of verteporfin uptake for individual tumors from both groups can be seen in Figure 7.4(a). Consistent with the observation from fluorescence microscopy analysis, verteporfin uptake levels were found significantly higher at 3 hrs after verteporfin i.v. injection ($p = 0.000$). Both the coefficient of variation analysis and two population F -test indicated that the inter-individual variation in verteporfin uptake was significant higher in this group (Table 7.3). Overall intra-tumor variation from both groups can be seen from the histogram in Figure 7.4(b). The mean, standard deviation, t -test, and f -test were listed in Table 7.3.

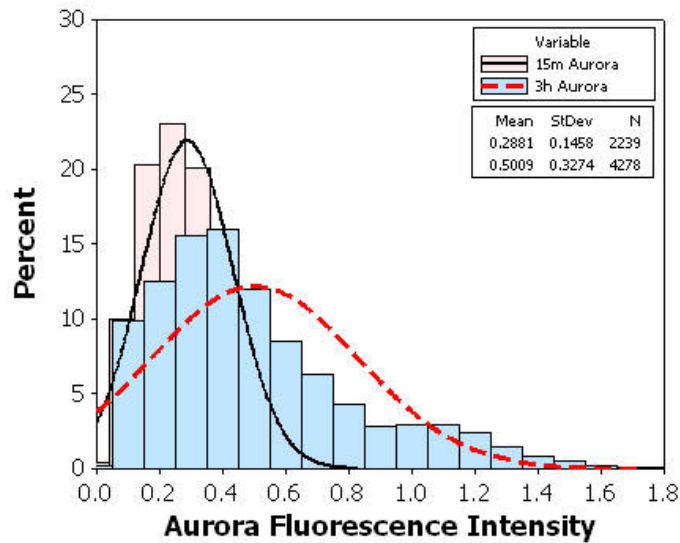
Histogram	Number of samples	Mean \pm Std ($\langle f \rangle \pm \sigma$)	CV%	Mean t -test p value for $\langle f_i \rangle \neq \langle f_p \rangle$	f -test statistics σ_i^2 / σ_p^2	Variance f -test p value for $\sigma_i^2 = \sigma_p^2$
15-min regional	2239	0.28 ± 0.15	53.57	0.000	0.20	0.000
3-h regional	4278	0.50 ± 0.33	66.00			
15-m individual	30	0.27 ± 0.08	29.63	0.003	0.08	0.000
3-h individual	40	0.51 ± 0.29	56.86			

Table 7.3: Statistics for histograms shown in Figure 7.4 of inter-tumor variation in 7.4(a), and intra-tumor variation in 7.4(b). The mean and standard deviation for each histogram is shown in the 3rd column. The 4th column is the coefficient of variation. The 5th column reports on the p -value that the means are the different. In the 6th and 7th columns the results of the f -statistic are shown comparing the variance.

Analysis of the correlation between intra-tumor variation and verteporfin uptake were performed in a similar way as discussed above. An inverse correlation was observed between tumor verteporfin uptake and the extent of photosensitizer variability (CV%) in the 3 hr group ($R^2 = 43.3\%$, $p = 0.000$). No such correlation was found in the animals in 15



(a)



(b)

Figure 7.4: Verteporfin tumor uptake evaluated by the Aurora fluorometer. Vascular targeting PDT group (15 m) included 2239 samplings from 30 animals, whereas cellular targeting PDT group (3 h) included 4278 samplings from 40 animals. Similar to Figure 7.2, comparisons were presented in box-plot (a) and histogram (b) to illustrate the inter-tumor and intra-tumor variation in BPD distribution.

min group ($R^2 = 0.1\%$, $p = 0.897$) Figure 7.5.

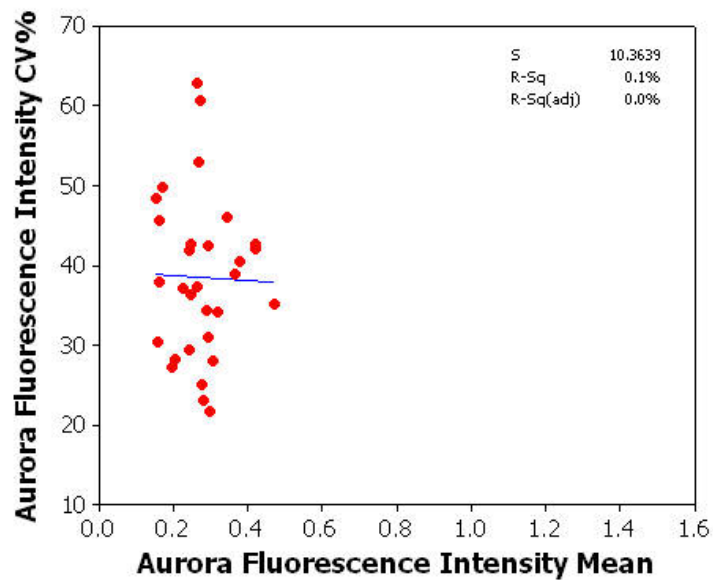
7.3.2 Growth Dynamics post Cellular and Vascular Targeting PDT

To assess the tumor response to different types of PDT treatments, the tumor volume was measured daily immediately following PDT treatment. The growth dynamics were then fitted to a double exponential model [316] to characterize the biological response to the treatment.

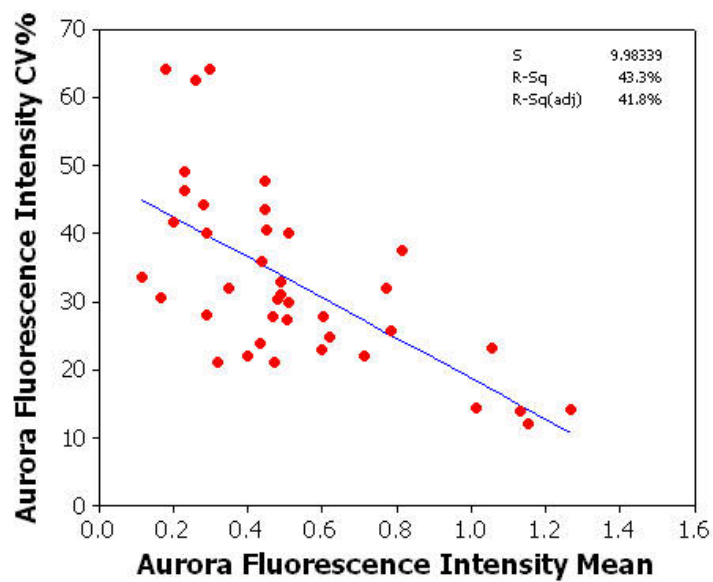
The animals in the photosensitizer-only control group showed faster and less variable growth dynamics (Figure 7.6(a)). The mean \pm standard variation of tumor volume on day one and day six were $213 \pm 71 \text{ mm}^3$ and $2224 \pm 735 \text{ mm}^3$. The coefficients of variation were 33.4% and 33.1%, respectively.

The animals in the cPDT treatment group showed considerably more variation in growth dynamics after treatment. On day one, the mean tumor volume was 204 mm^3 with a standard deviation of 55 mm^3 , which corresponds to a coefficient of variation of 26.9%. On day eight, the mean tumor volume increased to $1753 \pm 1151 \text{ mm}^3$, corresponding to coefficient of variation of 65.7%.

However, animals in the vPDT group responded differently after treatment. On day one, the mean tumor volume was 208 mm^3 with a standard deviation of 30 mm^3 , which corresponds to a coefficient of variation of 14.2%. Vascular targeting PDT controlled the tumor more effectively compared to cellular targeting PDT. On day ten, the mean tumor



(a)



(b)

Figure 7.5: Correlation between verteporfin intra-tumor variability and inter-tumor variability analyzed from the Aurora Fluorometer. Coefficient of variation were plotted as a function of the mean fluorescence intensity for tumors in vascular targeting PDT group (n = 13)(a) and cellular targeting PDT groups (n = 14)(b).

volume increased to $1529 \pm 336 \text{ mm}^3$, corresponding to coefficient of variation of 21.9%.

By fitting the tumor volume to a double-exponential regrowth model, the control tumors were found to grow at an exponential rate of $e^{0.467 \times \text{days}}$, with a doubling time of 1.45 days. Cellular targeting PDT treated tumors showed an average growth delay of 3.65 days (standard deviation: 0.39, coefficient of variation: 10.6%), tumor doubling time 3.50 ± 0.45 days (coefficient of variation: 12.8%) and surviving fraction of $18.7 \pm 4.2\%$ (coefficient of variation 22.7%). Vascular targeting PDT showed a growth delay of 5.16 ± 0.14 days, tumor doubling time 6.32 ± 0.13 days, and surviving fraction of $8.47 \pm 0.86\%$. The standard deviation and coefficient of variation for each parameter are listed in Table 7.4.

Group	DT	TGD	SF%
CTRL	1.45 ± 0.03 (2.1%)	NA	NA
cPDT	3.65 ± 0.38 (10.6%)	3.50 ± 0.45 (12.8%)	18.77 ± 4.26 (22.7%)
vPDT	6.32 ± 0.13 (2.1%)	5.16 ± 0.14 (2.7%)	8.48 ± 0.86 (10.2%)

Table 7.4: Summary of tumor doubling time, tumor growth delay and surviving fraction for all treatment groups.

7.3.3 Correlation between Verteporfin Pharmacokinetics and PDT Treatment Outcome

Relation between tumor response to vPDT and verteporfin plasma pharmacokinetics

Tumor response to PDT was evaluated as a function of normalized verteporfin plasma concentration at $t = 15$ min measured by FluoroMax as described in the Materials and Methods session. Survival fraction ($SF\%$) was used to represent the tumor response to the PDT treat-

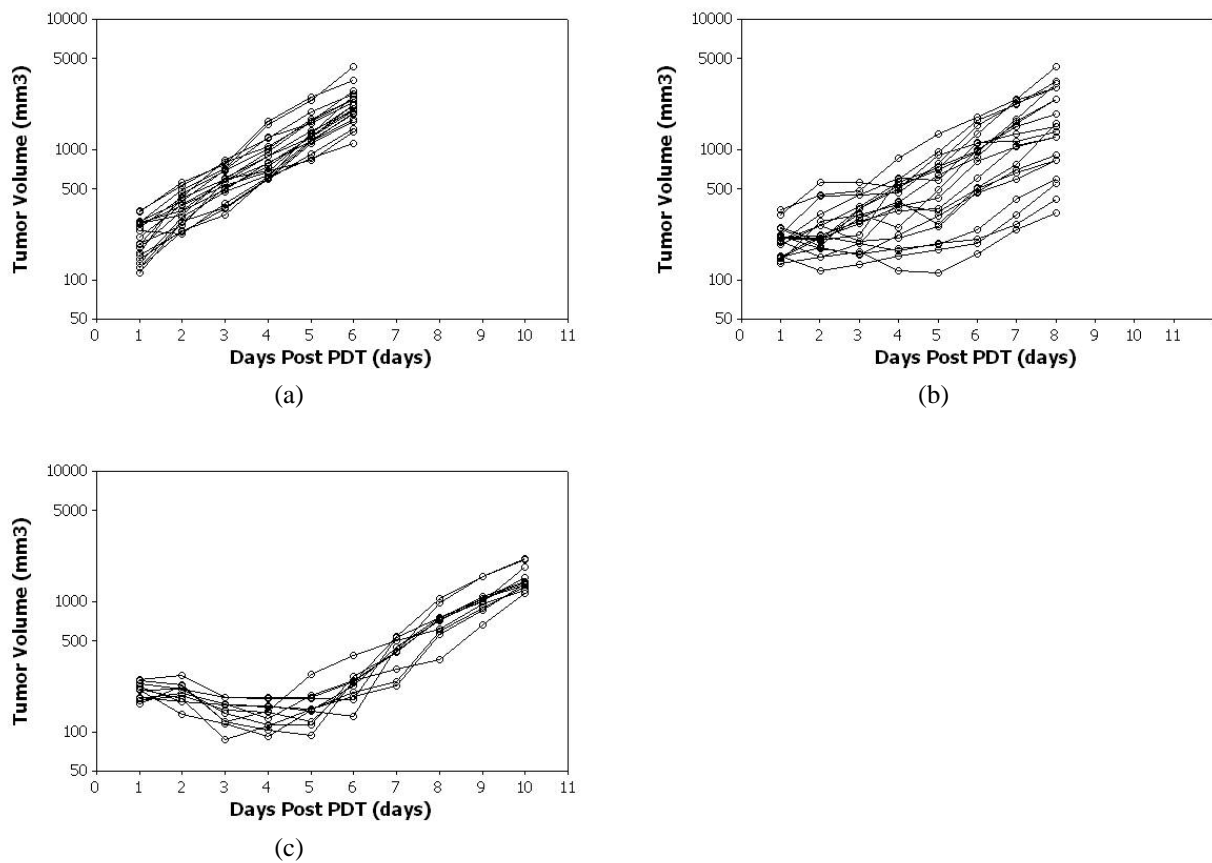


Figure 7.6: Tumor growth dynamics of animals in the CTRL (a), cPDT (b) and vPDT groups (c). Coefficients of variation for tumor volumes were 33.4% and 33.1% at day one and day six for CTRL animals, and 26.9% and 65.7% at day one and day eight for the cPDT animals; 14.2% and 21.9% at day one and day ten for the vPDT animals.

ment. The survival fraction was found inversely correlated with the normalized verteporfin concentration at time $t = 15$ min as illustrated in Figure 7.7. The regression analysis showed $R^2 = 44.0\%$ and $p = 0.026$.

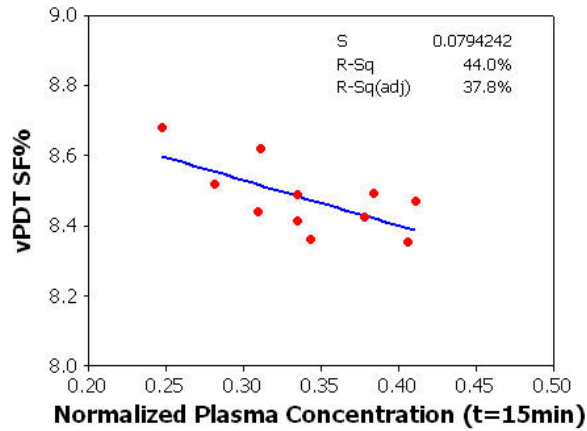


Figure 7.7: Correlation between normalized verteporfin plasma concentration and vascular-targeting PDT treatment response. Survival fraction of treated tumors in vascular targeting PDT group were plotted as a function of normalized plasma concentration at time $t = 15$ m, showing an inverse correlation between these parameters ($p = 0.026$).

Relation between tumor response to cPDT and verteporfin tissue distribution

Tumor response to PDT was evaluated as a function of verteporfin uptake in the tumor at the time of illumination measured by the Aurora fluorometer, as described in the Materials and Methods session. Survival fraction ($SF\%$) was used to represent the tumor response to the PDT treatment. The survival fraction was found inversely correlated with the verteporfin tumor uptake (the mean of 100 measurements) as illustrated in Figure 7.8. The regression analysis showed $R^2 = 44.1\%$ and $p = 0.001$.

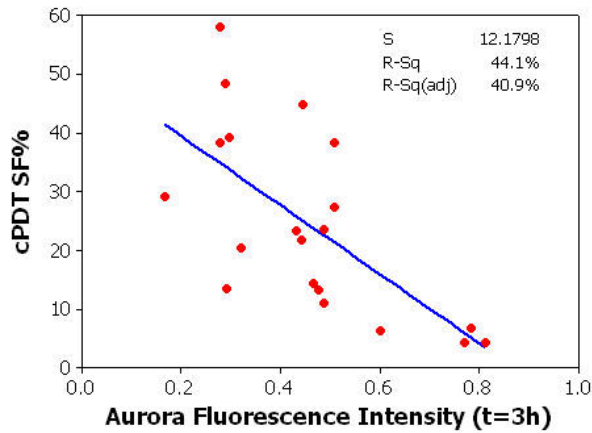


Figure 7.8: Correlation between verteporfin level and cellular targeting PDT treatment responses. Survival fraction of treated tumors in cellular targeting PDT group were plotted as a function of mean fluorescence intensity measured by Aurora fluorometer at time $t = 3$ h, showing an inverse correlation between these parameters ($p = 0.001$).

7.4 Discussion

PDT treatment using verteporfin has been approved for the treatment of wet form AMD, and is under clinical trials for cutaneous non-melanoma skin cancer and psoriasis. Extensive preclinical research has been carried out using verteporfin as therapy for prostate cancer, Barretts' esophagus [122] and multiple sclerosis [317]. We have previously demonstrated that verteporfin can be used to primarily target tumor vasculature or tumor cells by adjusting the drug-light interval. For a short drug-light interval, *e.g.*, verteporfin molecules concentrate in the tumor vascular compartment. Most photodynamic reactions take place in the tumor vasculature. Whereas, for a long drug-light interval, verteporfin molecules transport across the vascular wall and diffuse through tumor interstitium, and accumulate

in tumor cells, when the light treatment is performed, the photodynamic action happens inside the tumor cells.

In theoretical estimates of the threshold dose, the threshold PDT dose is defined as the minimum number of photons absorbed by the photosensitizer per unit tissue volume [305] to kill the tissue. The concentration of photosensitizer molecules at the site of photodynamic reaction is clearly a determinant factor in this calculation. However, there are substantial variation in photosensitizer uptake between tumors and within a tumor. How do these microscopic variation correlate with the inter-tumor variation, and how does this pharmacokinetic variability affect PDT treatment? The objectives of this part of the study were first to characterize the verteporfin pharmacokinetic variability at systemic and tumor levels, and second to relate the verteporfin intra-tumor variability to inter-individual variability, and last to relate verteporfin pharmacokinetic parameters to the biological responses to cellular and vascular targeting PDT treatment.

In Chapter 4, we reported the verteporfin plasma concentration as a function of time after drug i.v. injection. In that study, verteporfin concentration in plasma was measured up to 8 hours post administration, and was fitted to a double-exponential decay model. Here, we performed a plasma pharmacokinetic study on 11 tumor bearing animals, and followed the plasma concentration up to 15 minutes post administration when the animals received light treatment. Verteporfin plasma pharmacokinetic data was then fitted with an exponential decay model. The elimination half-life was consistent with the first decay half-life observed

in our previous work. Individual plasma concentration profiles were normalized to their mean concentration at time $t = 0$ min after drug i.v. injection. The data were processed this way so that the variation between individuals could be preserved. Figure 7.1 illustrated the individual plasma pharmacokinetics, showing that there were about 8% variation in the parameter A and 17% variation in the elimination half-life among individuals (Table 7.1). This observed variation in parameter A can be due to variation in the photosensitizer i.v. administration process, *e.g.*, human errors in tail vein injection, or variation in the subjects health. This latter issue occurs if health issues lead to variation in the binding process of verteporfin to low density lipoproteins (LDLs). Plasma LDL concentration varies from individual to individual, and for the same individual, varies from day to day. The unbound hydrophobic photosensitizers are taken up by the macrophage system and eliminated from the body, and this process results in a faster clearance. It has been reported that the serum protein concentration, such as human serum albumin (HSA), LDL, and transferrin, tends to decrease with age [281]. Older animals or those with compromised health may have more unbound hydrophobic verteporfin molecules and likely have a faster clearance.

The verteporfin tumor uptake study focused on variability of photosensitizer concentration between individual animals and in the microscopic variability within a tumor. Two drug quantification methods were used, *ex vivo* fluorescence microscopy and *in vivo* Aurora micro-fluorometry. In Chapter 6, the effect of sampling region size upon quantification of tissue verteporfin concentration was examined, showing that the observed spatial

heterogeneity decreases as the sampling size increases due to the signal averaging over a larger volume of tissue. Thus it is important to be cautious when these measurement data are interpreted. Figure 7.2(b) and 7.4(b) illustrate the inter-individual and intra-individual variability in verteporfin concentration measured by these two methods.

There are several interesting facts demonstrated in these graphs. First, verteporfin concentration levels were significantly higher at 3 hours post injection in contrast to 15 min. This can be observed by either comparing the individual tumor uptake, or the histograms of verteporfin intra-tumor distribution using both microscopy and fluorometry methods, as illustrated in Figure 7.2(a) and 7.4(a). We have discussed the drug distribution process in Chapter 3 and 4, and demonstrated that after i.v. injection, photosensitizer distributes in the systemic circulatory system, tumor vasculature, and transport across the tumor vessel wall, and then diffuses through tumor interstitium. At early time points, photosensitizer molecules are constrained in the vasculature compartment due to the limited vascular permeability. Photosensitizer quantification was performed through fluorescence intensity measurement over a tumor tissue region of size approximately $1 \times 1 \text{ mm}^2$ which contains an average of 73 vessels (Chapter 5). The fluorescence intensity readings are the average of photosensitizer fluorescence intensity in the vasculature compartment over the $1 \times 1 \text{ mm}^2$ tumor tissue region. Hence it lowers the fluorescence readings. Another cause of lower fluorescence intensity readings at 15 min is that there could be photosensitizer quenching processes, where photosensitizer molecules undergo non-radiative relaxation with adjacent

molecules.

Second, the inter-individual verteporfin uptake variability was more pronounced at 3 hours compared to the inter-individual variability observed at 15 minutes. This phenomena was observed from the measurements obtained by both quantification techniques (Figure 7.2(a) and 7.4(a)). As listed in Table 7.2 and 7.3, inter-individual Variation values were 14.03% *v.s.* 7.8% from the microscopy study, and 56.86% *v.s.* 29.63%, for 15-m and 3-h groups. The *f*-test for equal covariance showed significantly less variability in 15-m microscopy and Aurora measurements groups ($p = 0.017$ and $p = 0.000$ for microscopy and Aurora measurements respectively). This observation is accompanied with the fact that verteporfin intra-tumor variabilities are significant higher in 3-h groups (Figure 7.2(b) and 7.4(b), Table 7.2 and 7.3). Again, this can be explained by the distribution processes of photosensitizer inside the tumor. At 15 minutes after i.v. injection, most verteporfin molecules are in the vascular compartment, verteporfin concentration in the tumor vasculature should be related to systemic plasma concentration, where only about 10% of variability was found among individuals in this study (Figure 7.1). This variability was further averaged out when the verteporfin concentration was quantified over a $1 \times 1 \text{ mm}^2$ tumor tissue region. On the other hand, at 3 hours, verteporfin molecules flow across the tumor vessel walls, diffuse through tumor interstitium, and then transport into the tumor cells through LDL-receptor endocytosis. Each three of these processes contain factors that cause verteporfin distribution heterogeneity (Chapter 3 and 4).

Taking transvascular transport as an example, it was demonstrated that the effective permeability coefficient of verteporfin in subcutaneous tumors varied from individual to individual (CV% = 16%) and from different locations within a tumor (CV% = 26%) (Chapter 4). This phenomena was further confirmed by the correlation study of intra-tumor variability and verteporfin individual tumor uptake, as shown in Figure 7.3(a), 7.5(b), 7.3(b) and 7.5(b). In both fluorescence microscopy and Aurora fluorometry studies, an inverse correlation between verteporfin fluorescence intra-tumor variation and tumor uptake was found at 3 hrs. This variation is caused by the variability factors of different transport processes, *e.g.*, heterogeneous permeability and heterogeneous interstitial diffusion rate. However, at 15 min, the causes of intra-tumor variation are photosensitizer systemic plasma concentration, vessel densities around the sample area, and regional hemodynamics of tumor vasculature. Also, verteporfin concentration variation in tumor vasculature might be averaged out when a $1 \times 1 \text{ mm}^2$ area of tumor tissue is sampled.

It is interesting to compare measurement data using two different photosensitizer quantification techniques. Fluorescence microscopy analysis of photosensitizer tumor distribution is by far the most reliable technique to study the drug spatial distributions at different microscopic levels, *e.g.*, drug intracellular distribution, drug concentration in tumor intravascular or extravascular compartment. However, it is an invasive *ex vivo* quantification technique and limits its usage in clinical settings. Spectrofluorometry techniques offer non-invasive quantification of drug levels in the tumor, but lack the ability to measure

drug concentration at the microscopic level (Chapter 6). As illustrated in 7.2(b) and 7.4(b), Table 7.2 and 7.3, verteporfin concentrations measured by the Aurora fluorometer exhibit higher variabilities compared to fluorescence microscopy analysis. The configuration of the detection probe used in this Aurora fluorometry study has been discussed elsewhere [256, 289, 290, 295]. It represents a sampling volume of roughly $3 \times 3 \text{ mm}^2$. In theory, the variation observed in Aurora measurements should be less compared with the fluorescence microscopy analysis where a sampling volume of approximately $1 \times 1 \text{ mm}^2$ tissue is measured. However, verteporfin quantification via the Aurora spectrometer were performed with repetitive samplings at different tumor locations. This will inevitably increase the standard deviation of the measurement due to the photobleaching of photosensitizer. Although the sampling volume of fluorescence microscopy is small, there is not much photobleaching of photosensitizer during the study, thus the variation remain less.

At both 15 min and 3 hrs, intra-tumor variabilities are found larger than the inter-individual variabilities using both quantification methods. To illustrate these comparisons, each measurement of verteporfin concentration at distinct locations and the mean values for individual animals were plotted side by side in Figure 7.9. This phenomena can be explained in a similar manner as we explored the sampling size effect on verteporfin quantification. That is: by averaging the multiple measurements at different locations within the tumor, the microscopic heterogeneities of photosensitizer distribution can be suppressed. Thus the mean value of these multiple measurements can be used to represent the photo-

sensitizer uptake level of the whole tumor regardless of the spatial distribution of photosensitizer molecules inside the tumor. This can be problematic when the photosensitizer concentration in a specific compartment of the tumor dominates the treatment efficacy, such as in vPDT.

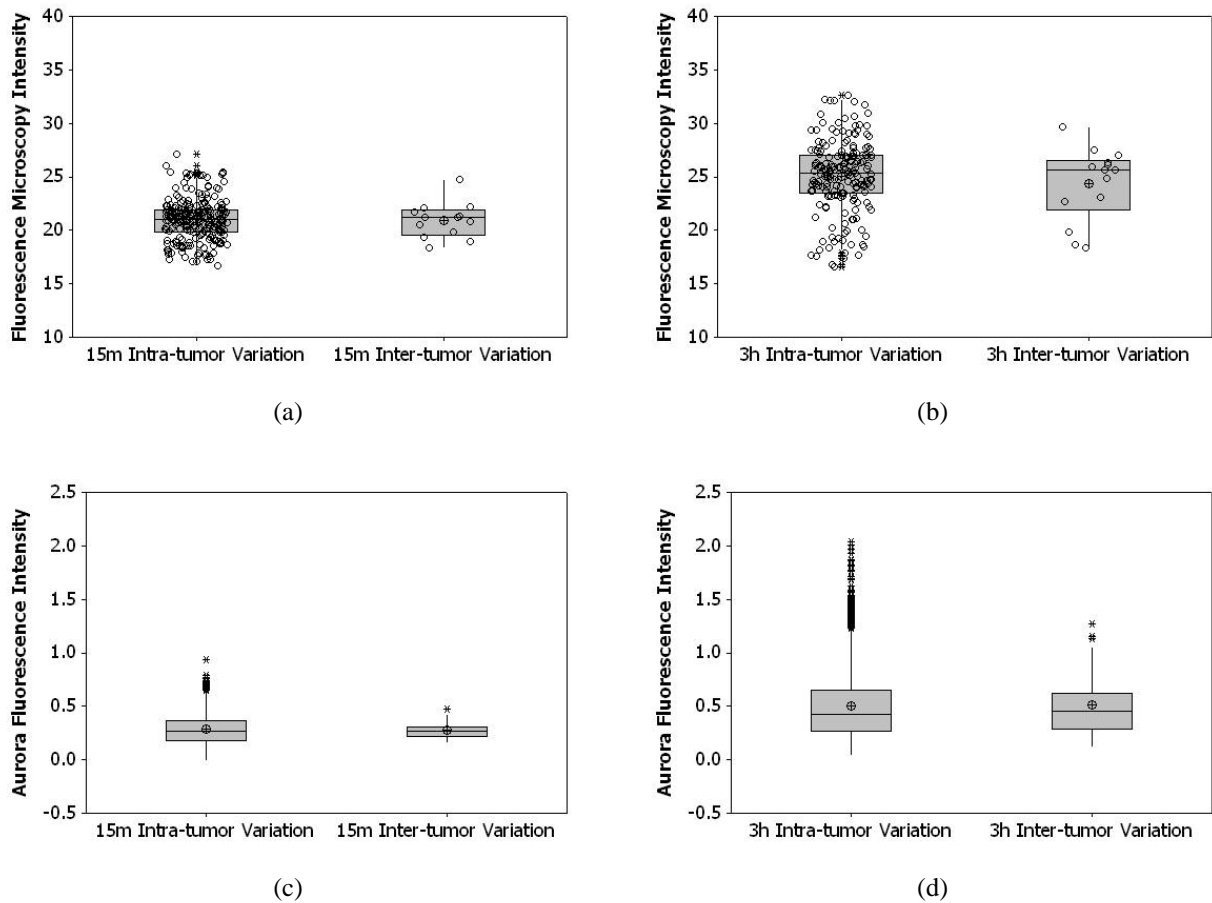


Figure 7.9: Comparison of verteporfin concentration intra-tumor variation and inter-tumor variation. The box-plots illustrate the intra-tumor variation and inter-tumor variation in BPD fluorescence intensity measured by fluorescence microscopy (a) & (b), and Aurora fluorometer (c) & (d).

Vascular targeting PDT now has become a common area of development in clinical

PDT treatments aimed at debulking solid tumors, because of its effectiveness and limited skin sensitivity. Extensive vascular targeting PDT studies have been conducted using a short drug-light interval after verteporfin injection and showed vessel constriction, leakage and vascular shutdown after treatment. Consistent with our previous findings and investigations by Fingar and Kurohane, vascular targeting PDT exhibited a more effective control of tumor, which can be seen from Figure 7.6. Another feature observed from this study is that variation in biological response to vascular targeting PDT was found much less than the biological response to cellular targeting PDT 7.4. There are two possible explanations for this. Firstly, PDT reactions take place in the tumor vasculature, where the verteporfin concentration variation is much less between individuals, besides, there is enough oxygen supply for the production of singlet oxygen. Secondly, vascular targeting PDT damages the tumor endothelial cells, and triggers inflammatory response of the tumor after treatment. This process might spatially homogenize the treatment effect, and produce a homogeneous macroscopic necrosis in the tumor. To further explore the effect of verteporfin plasma pharmacokinetic variability on vascular targeting efficacy, the survival fractions of individual tumor were plotted against the AUC (area under curve) of verteporfin plasma pharmacokinetics. A weak but statistically significant correlation was found between these two parameters. The weak correlation might be due to the heterogeneous and intermittent blood flow inside the tumor as we have discussed in Chapter 3 and 4.

Using a longer drug-light interval protocol, verteporfin molecules extravasate from tu-

mor vasculature, and distribute in the tumor parenchyma, primary PDT reactions take place in the extravascular compartment. Thus verteporfin concentration in tumor parenchyma determines the biological response. This less heterogeneous verteporfin distribution does not require microscopic quantification of verteporfin in specific compartments. Thus a non-invasive, fiber bundle based spectrometer can provide enough information about verteporfin concentration in the tumor tissue. Indeed, verteporfin concentration measured by multiple sampling using the Aurora fluorometer correlated well with the surviving fraction, as can be seen from Figure 7.8. In Chapter 5, we have discussed the effect of tumor micro-environment on cellular and vascular PDT treatment, and concluded that the higher hypoxia fraction observed in subcutaneous tumor limited the effectiveness of cellular targeting PDT. In comparison to that, we hypothesized that an indicator paralleled to hypoxic fraction in the oxygen histogram analysis should be a determinant for cellular targeting PDT treatment. For example, the lower quartile of verteporfin concentration histogram generated from the multiple measurements within a tumor might correlate to this. However, no such correlation was found between the lower-quartiles and treatment efficacy of cellular PDT (data not shown). This can be explained by the large intra-tumor variability observed at 3 hours after verteporfin injection. The lower readings are a mixture of locations where there is either limited drug delivery or photobleaching during the measurement. Another possible explanation is that the inflammatory response in cellular targeting PDT might even out the low photosensitizer areas where limited PDT reactions occur.

7.5 Conclusion

In summary, there was 15% inter-tumor variation in BPD plasma concentration at the time of light irradiation in vascular targeting PDT group, 40% inter-individual variation in BPD fluorescence intensity measured by Aurora fluorometer at the time of irradiation in cellular targeting PDT group. Tumor response to treatment were found significantly less variable to vascular targeting PDT than to cellular targeting PDT. 22.7% inter-individual variation was found in tumor survival fraction in response to cellular targeting PDT whereas it was 10.2% in vascular targeting PDT group. The inter-individual variability in response to vascular targeting PDT is mainly due to the verteporfin plasma pharmacokinetic variability ($R^2 = 44\%$, $p = 0.026$); whereas, the inter-individual variability observed in cellular targeting PDT is caused by the heterogeneity in the drug transport processes ($R^2 = 44\%$, $p = 0.001$). This implies that different photosensitizer monitoring techniques should be utilized in vascular targeting and cellular targeting PDT, but applied in different manner where they sample the pertinent fraction of the tissue to be targeted.

Chapter 8

Photosensitizer Pharmacokinetic Modulation

The transport processes of verteporfin have been characterized using two MAT-LyLu tumor inoculation sites, and it was determined that orthotopic tumors have a higher vessel density, vascular permeability and higher interstitial diffusion rate as compared to subcutaneous tumors. This higher transport rate leads to higher verteporfin uptake in orthotopic tumors at 15 mins after intravenous injection, but not at 3 hrs. The inter-individual and intra-individual verteporfin pharmacokinetic variability study presented in Chapter 5 indicated that at 15 minutes post verteporfin injection, most verteporfin molecules are confined in the intravascular compartment of the tumor. The mean fluorescence intensity signal, measured by either fluorescence microscopy or by the Aurora fluorometer, was dominated

by the total number of photosensitizer molecules in the intravascular compartment. However, at the 3 hr time point after verteporfin intravenous injection, most photosensitizer has extravasated from the intravascular space into the tumor interstitium, via a passive diffusion processes, because of the concentration gradient across the vessel wall. These extravasated molecules follow the concentration gradient in the tumor interstitium and diffuse through the interstitial space. Using mathematical modeling, it was estimated that for the interstitial diffusion process, 3 hrs is rather a long diffusion time. The rule of thumb for interstitial diffusion is that the time constant (τ_D), for a specific molecule, with diffusion coefficient D , to diffuse across distance L is approximately $L^2/4D$. For diffusion coefficient of verteporfin in MAT-LyLu tumors ($0.88 \mu\text{m}^2/\text{s}$ for subcutaneous tumors, and $1.59 \mu\text{m}^2/\text{s}$ for orthotopic tumors), τ_D is of order of 47 mins and 26 mins for $100 \mu\text{m}$ distance in subcutaneous and orthotopic tumors respectively. In addition, since most molecules are in the extravascular space, the mean fluorescence intensity of a tumor region with $1 \times 1 \text{ mm}^2$ area is determined by the total number of photosensitizer molecules in tumor interstitium. Thus, transvascular permeability appears to be the parameter that determines the mean fluorescence intensity the most.

In Chapter 7, it was established that there was a correlation between mean fluorescence intensity and the PDT treatment efficacy. This conclusion was drawn based upon the fact that cellular targeting PDT is less effective and much more variable, as compared to vascular targeting PDT. This higher inter-individual variability observed in cellular tar-

getting PDT is explained by the verteporfin inter-individual pharmacokinetic variability, especially the variability in intra-tumor distribution processes, such as distribution in tumor vasculature, transvascular transport and interstitial transport. This spatially heterogeneous transport processes results in a highly spatially variant BPD-MA distribution, leading to inter-individual variation in BPD-MA pharmacokinetics. Of all three transport parameters, transvascular permeability showed an important role in determining BPD-MA concentration level at 3 hrs post drug administration. This implies that by enhancing the transvascular transport process, *e.g.*, increasing the vascular permeability (P), a higher photosensitizer concentration can be achieved and thus reduce the inter-individual variation in photosensitizer tumor uptake, and as a result, reduce the inter-individual variability in response to cellular targeting PDT treatment.

8.1 Introduction

The rationale of this study comes from the cause-effect relationship that was found in photosensitizer transport parameters, as related to the PDT treatment efficacy. Cellular targeting PDT requires preferential accumulation of photosensitizer molecules in the tumor parenchyma. Thus the effective delivery of photosensitizer to the tumor cells is important for an effective cellular targeting PDT treatment. This type of treatment is achieved by lengthen the drug-light interval, in a way such that allows the photosensitizer to transport across the tumor vessel walls, and diffuse through tumor interstitium. However, each step

of these transport processes presents a high spatial and temporal heterogeneity. Most importantly for the 3 hr drug-light interval, the transvascular transport parameter permeability (P), seems to be a dominant factor affecting the BPD tumor uptake, and as a result, it influences the cellular targeting PDT treatment efficacy.

The increase vascular permeability induced by the inflammatory mediators is of particular interest to cellular targeting PDT, where the photosensitizer tumor uptake is limited by the lower permeability and heterogeneous transvascular transport processes inside the tumor. Inflammatory mediators, such as histamine, bradykinin, and Substance P (SP), are known to increase the permeability of venule, resulting in tissue edema [318, 319]. The mechanism underlying this increases permeability has been extensively studied. It has been demonstrated from the pathology studies that these inflammatory mediators cause gap formation at venular endothelial junctions, and the permeability increase is due to the formation of such gaps. Gaps formation is thought to result from the contraction of endothelial cells [320, 321]. This induced increase in permeability has been shown to be transient, even during the continuous infusion of inflammatory mediators, such as histamine and SP. Fox *et al.* demonstrated that during 60-min exposure to histamine, cat and rat mesenteries exhibited leaky sites just 1 or 2 minutes after the onset of topical application of histamine, and peaked at 5 to 10 minutes, and then disappeared at 20-30 minutes [322]. In Weidner's study, SP was applied intradermally via large cut-off plasmapheresis capillaries and it was found to induce dose-dependent vasodilation and protein extravasation characterized by a

fast onset and a desensitization within a time course of 30 minutes [323]. The mechanism for this permeability recovery phenomenon is believed attributed to the enclosure of the endothelial gaps triggered by the signaling pathways in the cytokine network [324]. In this study, the effect of SP application upon the photosensitizer verteporfin transvascular transport process was investigated, with a focus on the pharmacokinetics and possible improvements to cellular targeting PDT treatment efficacy.

8.2 Materials and Methods

8.2.1 Tumor and Animal Model

Male Copenhagen rats (6-8 weeks old), obtained from Charles River Laboratories (Wilmington, MA), were used throughout the study. The R3327 MAT-LyLu Dunning prostate tumor cells [253] were cultured as discussed in previous chapters. The subcutaneous MAT-LyLu tumors were induced by injecting approximately 1×10^5 MAT-LyLu cells (suspended in 0.05 ml PBS) subcutaneously into the shaved rat flank. Tumors were used for experiment at 7 to 8 days after implantation when they reached a size of 6 to 9 mm in diameter. No spontaneous necrosis was observed at the time experiment.

8.2.2 Photosensitizer and Inflammatory Mediator

Verteporfin, obtained from QLT Inc. (Vancouver, Canada), was used in this study. Verteporfin was reconstituted according to the manufacturer's instructions. This stock solution was injected intravenously to animals at various times prior to use, with a dose of 1.0 mg/Kg. Substance P (5 μ g/ml, Peninsula Laboratories, Belmont, CA) was dissolved in 100 mM acetic acid containing 0.9% NaCl.

8.2.3 Laser Doppler Blood Flow Monitoring

Laser Doppler blood flow measurement was taken with Moore Instruments Laser Doppler Perfusion Monitoring System (Wilmington, DE). Optical fiber probe with a diameter of 200 μ m was inserted in the tumor tissue through a 28-gauge needle. Blood flow was monitored for 1 hour after SP intra-tumor injection. All the flow data were normalized to the average pre-SP injection value for all animals.

8.2.4 Transvascular Permeability Coefficient Evaluation

Macroscopic permeability evaluation

Evans blue was used to assess tumor vascular permeability change after SP application. Quantification of the leakage of Evans blue, which binds to albumin in systemic circulation, provided a measurement of plasma protein leakage. Tumors were excised from the

animals at 15 minutes, 1 hour, 3 hours and 24 hours after Evans blue injection. Tumors were weighed, minced, and extracted with formamide (1 ml per 100 mg tumor tissue) for 72 hours. The solutions were centrifuged and the absorbance of Evans blue in the supernatant was measured at 620 nm by a spectrophotometer. The absorbance data were all normalized to the highest value obtained to generate relative results for comparison between SP treated group and control group.

Microscopic permeability evaluation

Verteporfin permeability (P) was determined from BPD fluorescence images taken from tissues that were removed at 15 minutes post verteporfin injection. Animals in the control group received i.v. injection of verteporfin at a dose of 1 mg/Kg, the tumors in SP treated group received the intra-tumor injection of SP followed immediately verteporfin i.v. injection at the same dose as animals in the control group. 15 minutes later, animals were injected DiOC7₍₃₎ (Molecular Probes, Eugene, OR) to obtain information of tumor vasculature location and shape with fluorescence microscopy from frozen sections. Injections were administrated i.v. 1 minute before sacrifice at a concentration of 1 mg/Kg (dissolved in 75% dimethyl sulphoxide in phosphate buffered saline)[114, 173, 252]. To prevent the further diffusion of DiOC7₍₃₎ and BPD, tumors were isolated and frozen in OCT with liquid nitrogen and then further sliced to 10 μ m slides (near the center of the tumor) for fluorescence microscopy studies.

Details about the permeability mathematical model has been discussed in Chapter 5. In general, effective permeability coefficients of BPD in MAT-LyLu tumors were calculated as:

$$P_{dEff} = (1 - H_t) \frac{V}{S} \frac{dI_i/dt}{I_{p,0}} \quad (8.1)$$

where H_t is average hematocrit in tumor vessels [325], V and S are the total volume and surface area of vessels within the tissue volume captured by the fluorescence microscope, $\frac{dI_i}{dt}$ is the total fluorescence intensity change per unit time, $I_{p,0}$ is intravascular fluorescence intensity at time of verteporfin injection [187]. A total of 5 to 7 microscopic fields (with an area of 1 mm²) were randomly taken from each section. Three sections were examined for each tumor and 5 and 6 animals were included in the SP treated and control groups, respectively.

8.2.5 Verteporfin Plasma Pharmacokinetics

To illustrate the effect of SP application on verteporfin systemic pharmacokinetics, animals were anesthetized and verteporfin was injected at 1 mg/Kg BPD-MA, for the animals in SP treated group, 50 μ l 5 μ g/ml SP were injected in tumor at the same time. Verteporfin plasma concentrations from each animal were measured at different time points after photosensitizer i.v. injection. 200 μ l blood was drawn from the Jugular vein of each animal at 5, 10, 15, 30 minutes and 1, 2, 3, 4, 6 and 8 hours. The plasma was separated from the

blood by centrifugation at 8000 rpm at 4°C. The plasma was diluted by a factor of 10 in a solution of 1% SDS in PBS and placed in a 2.5 ml cuvette. The fluorescence spectrum was recorded by a FluoroMax-2 (Jobin Yvon Inc., Edison, NJ) excited at 430 nm. The peak fluorescence intensities at 690 nm were converted to g/ml using the fluorescence intensity for the BPD concentration calibration curve.

8.2.6 Verteporfin Tumor Pharmacokinetics

Verteporfin tissue concentration *in vivo* quantification by Aurora Fluorometer

In both groups, animals were injected with verteporfin intravenously at a dose of 1.0 mg/Kg. For the animals in SP treated group, before verteporfin i.v. injection, 50 μ l SP solution was injected in the subcutaneous tumors. At 3 hours after photosensitizer administration, *in vivo* measurements were taken with the Aurora fluorometer [256, 289, 290, 295]. The configuration of this system has been discussed in Chapter 6 and 7. In a similar manner, the system was used to monitor fluorescence at multiple sites on the surface of the tumor, using 20 distinct locations and sampling 10 times from each site. The set of 200 data points for each animal were used to analyze the verteporfin distribution heterogeneity within a tumor for each animal. The average of these 200 data points were used to represent the verteporfin tumor uptake and to analyze the uptake variation between individual animals.

Verteporfin tissue concentration *ex vivo* quantification by Fluorescence Microscopy

In a separate group, tumor bearing animals received i.v. injection of verteporfin at 1.0 mg/Kg. At 3 hours post drug administration, animals were sacrificed and tumor tissues were rapidly dissected, embedded in TissueTek medium and snap-frozen in liquid nitrogen. Cryosections of 10 micron thickness were cut from the frozen tumor, and fluorescence of BPD-MA was then analyzed with a Nikon Diaphot-TMD fluorescence microscope equipped with a chroma filter set specially designed for this fluorophore (excitation: 425/40 nm, emission: 700/30 nm). Up to 30 to 40 $1 \times 1 \text{ mm}^2$ distinct locations were randomly selected to evaluate the BPD tumor pharmacokinetics.

8.2.7 PDT Treatment and Tumor Regrowth Assay

Tumor bearing animals were divided into four groups: PDT group (n = 6), SP+PDT group (n = 6), SP only control group (n = 5), verteporfin only control group (n = 6), and SP vehicle control group (n = 4). Animals in the PDT group received 1 mg/Kg verteporfin i.v. injection followed 3 h drug-light interval, and received 50 mW/cm², 75 J/cm² light treatment. Animals in SP+PDT group received intra-tumor injection of 50 μl SP, and 1 mg/Kg verteporfin i.v. injection, followed 3 h drug-light interval and same light delivery as in PDT group. In the verteporfin only group, animals received 1 mg/Kg verteporfin intravenously, and no light treatment was performed. In SP, and SP vehicle control groups, animals were injected 50 μl SP and 50 μl NaCl in the tumor respectively, and no light treatment was

delivered.

Width (a), length (b) and height (c) were measured with slide calipers to determine the tumor volume, and calculations were performed using the formula $V = \frac{\pi}{6} \times a \times b \times c$. The longitudinal tumor volume data, as a function of time (in days) after treatment, are then displayed on a semi-logarithmic scale.

8.3 Results

8.3.1 Verteporfin Plasma Pharmacokinetics

Verteporfin plasma pharmacokinetics in SP treated animals showed no significant difference compared to the animals in control group ($p > 0.05$). Verteporfin plasma pharmacokinetics were fitted to a two-compartment model, the four empirical parameters (A , B , $\tau_{\frac{1}{2}\alpha}$, and $\tau_{\frac{1}{2}\beta}$) were estimated. Each animal set of four empirical parameters was listed in Table 8.1. The experiment data and fitted curve are shown in Figure 8.1. No significant difference in these parameter between two groups ($p > 0.05$). In Figure 8.1, the final global fitted model is represented by a red thick curve, and the raw data are represented by the black thin curves.

	A (A.U.)	B (A.U.)	$\tau_{\frac{1}{2}\alpha}$ (mins)	$\tau_{\frac{1}{2}\beta}$ (hrs)
Ctrl	0.84 ± 0.08	0.18 ± 0.02	6.28 ± 2.07	5.84 ± 1.13
SP	0.84 ± 0.12	0.17 ± 0.04	8.27 ± 4.52	7.35 ± 2.49

Table 8.1: Two-compartment model parameter estimations for SP treated animals and control animals. Each pharmacokinetic data set was fitted to $C(t) = Ae^{-\alpha t} + Be^{-\beta t}$, elimination half-lives $\tau_{\frac{1}{2}\alpha} = \ln 2/\alpha$ and $\tau_{\frac{1}{2}\beta} = \ln 2/\beta$.

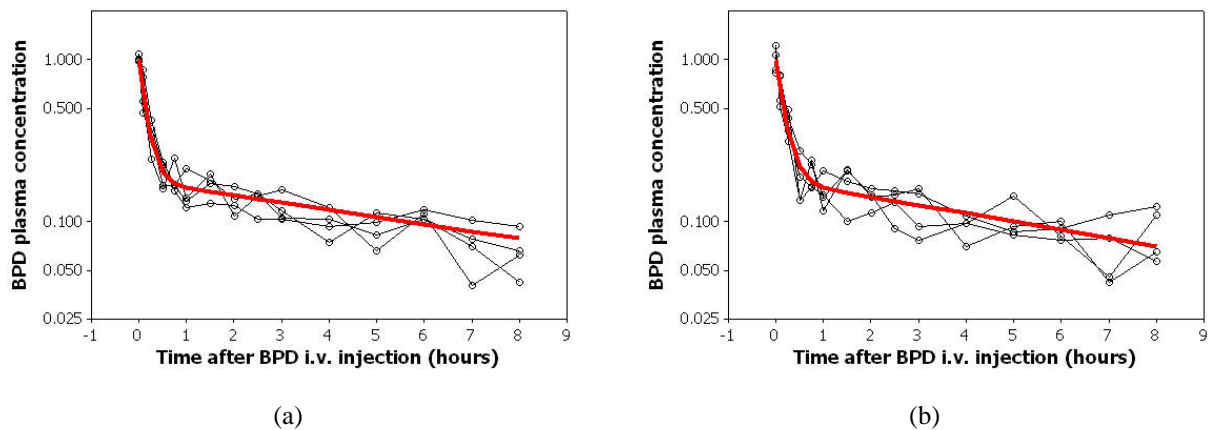


Figure 8.1: The normalized BPD plasma concentration is shown as quantified from samples taken from four rats of each group. The mean data was fitted to bi-phase exponential decay model, with the result shown by the red thick line. The connected points are normalized raw data from the measurements at each point for individual animals. No significant difference was observed between two groups ($p > 0.05$).

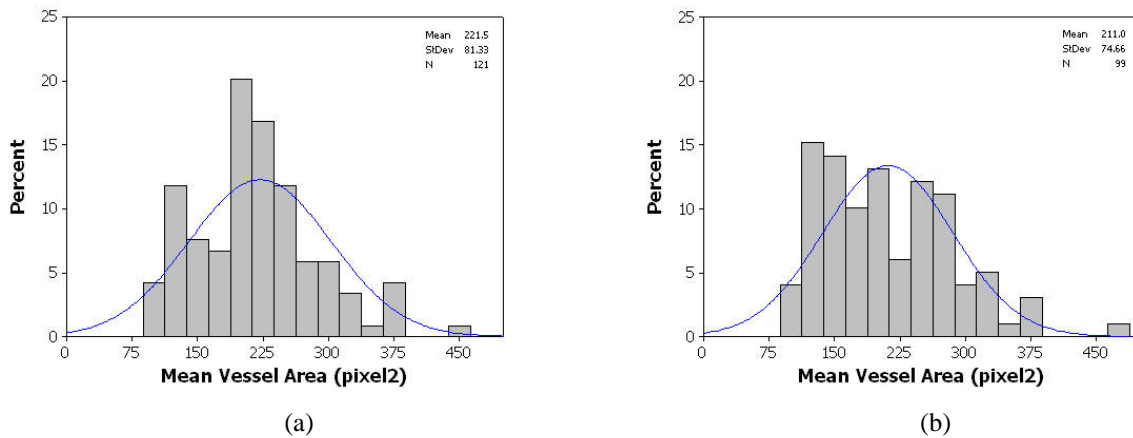


Figure 8.2: Histogram of average tumor vessel area in control tumors (a) and Substance P treated tumors (b). Functional tumor vasculature was stained by injecting a perfusion marker DiOC7₍₃₎ (1 mg/Kg, i.v.) to the tumor-bearing animal. Tumor vessel size data were generated by analyzing 121 control tumor images and 99 Substance P treated tumor images with NIH ImageJ. No significant difference in vessel area between two groups ($p = 0.323$).

8.3.2 Tumor Vasculature Morphology

The functional vasculature of MAT-LyLu tumors was stained by intravenously injecting a fluorescent perfusion marker DiOC7₍₃₎ and the representative images. The number of functional blood vessels and average vessel size in each fluorescence microscopic field (10X, with an area of 1 mm²) was analyzed with NIH ImageJ using an automatic threshold. As shown in Figure 8.2, no significantly different vessel area is found for the SP injection group and control group 15 minutes post SP intra-tumor injection. The average area of vessels were 211.0 ± 74.7 pixel² and 221.5 ± 81.3 pixel² for SP treated group and control group ($p = 0.323$).

8.3.3 Change of Tumor Vascular Permeability to Evans Blue

Vascular permeability in the MAT-LyLu tumors were assessed by Evans blue tumor uptake (Figure 8.3). Uptake of Evans blue dye was significantly higher in the SP treated tumors than the control animals at 1 hour and 3 hours after injection ($p < 0.05$). No significant difference in tumor Evans blue level was found at 15 min and 24 hours after administration ($p > 0.05$).

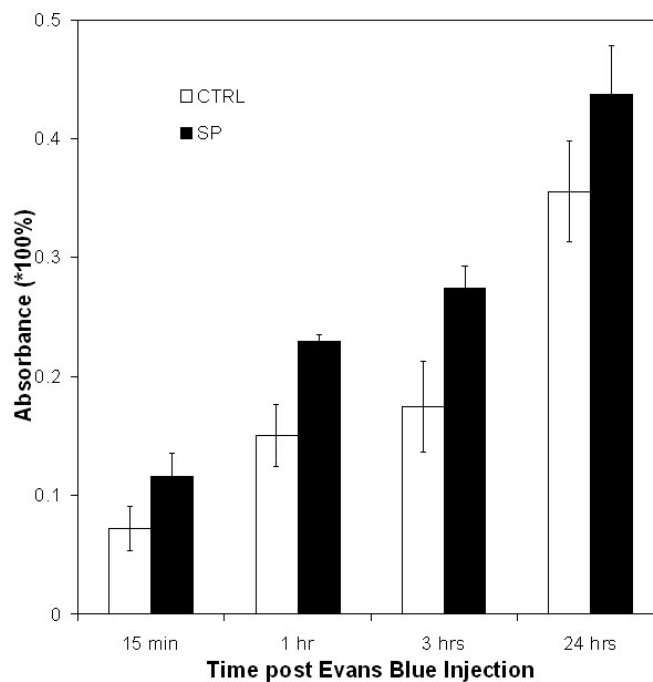


Figure 8.3: Effects of SP on vascular permeability to Evans blue. Tumors were excised at different time points after i.v. injection of Evans Blue (10 mg/Kg in PBS). The uptake of Evans Blue was measured by spectrophotometry after tissue extraction with formamide. Each group includes 3 to 5 animals.

8.3.4 Change of Tumor Microscopic Vascular Permeability

The mean effective permeability coefficients of tumors in both groups are shown in Figure 8.4. The SP treated tumors exhibited a significantly higher effective permeability coefficient as compared with control tumors ($0.04268 \pm 0.01226 \mu\text{m/s}$; $0.02608 \pm 0.00432 \mu\text{m/s}$; $p < 0.005$; Figure 8.4).

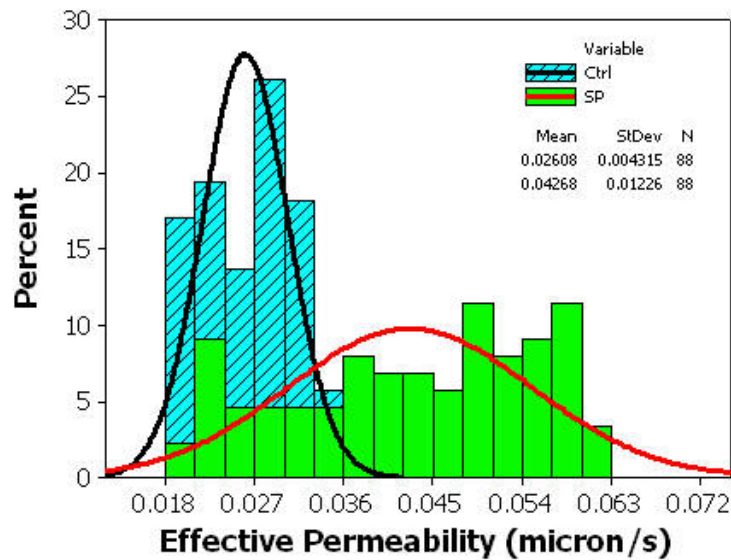


Figure 8.4: Average effective permeability coefficients before and after SP application. SP application significantly increase the microscopic vascular permeability ($p < 0.005$). Data shown in this graph were obtained from 88 fluorescence images from 5 animals in each group.

8.3.5 Change of Verteporfin Tumor Pharmacokinetics

Effect of SP on verteporfin tumor pharmacokinetics was analyzed through two photosensitizer quantification methods. In *ex vivo* fluorescence microscopy analysis, the mean fluorescence intensity of verteporfin in a $1 \times 1 \text{ mm}^2$ region was measured using a 40X magnification objective. These data were pooled together and used to generate fluorescence intensity histogram to illustrate the intra-tumor variation in verteporfin tumor pharmacokinetics. These intra-tumor variabilities in the SP and control groups are shown in Figure 8.5(a). Animals in the SP treated group showed a significantly higher verteporfin level compared to control tumors ($p < 0.05$). The averages of fluorescence intensities measured from different images from the same tumor were used to represent the uptake level for that individual. Comparison of individual tumor uptake between the SP treated group and the control group are shown in Figure 8.5(b). Verteporfin fluorescence intensity was found to be significantly higher in the SP treated group ($p < 0.05$).

In the second approach, verteporfin *in vivo* quantification were taken using 5 animals in the SP treated group and 5 animals in the control group. The mean fluorescence intensity of 100 data points was evaluated from 20 locations on the tumor and these were used to represent the verteporfin uptake level in that tumor. The coefficient of variation represented the intra-tumor variation of verteporfin uptake. The box-plot of verteporfin uptake for individual tumors from both groups can be seen in Figure 8.6(b). Consistent with the observation from fluorescence microscopy analysis, verteporfin uptake levels were found

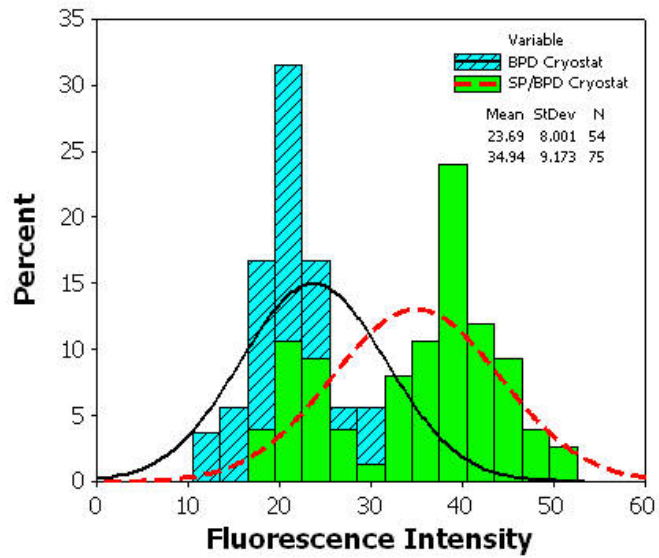
significantly higher in SP treated animals ($p < 0.05$).

8.3.6 Change of Tumor Blood Flow

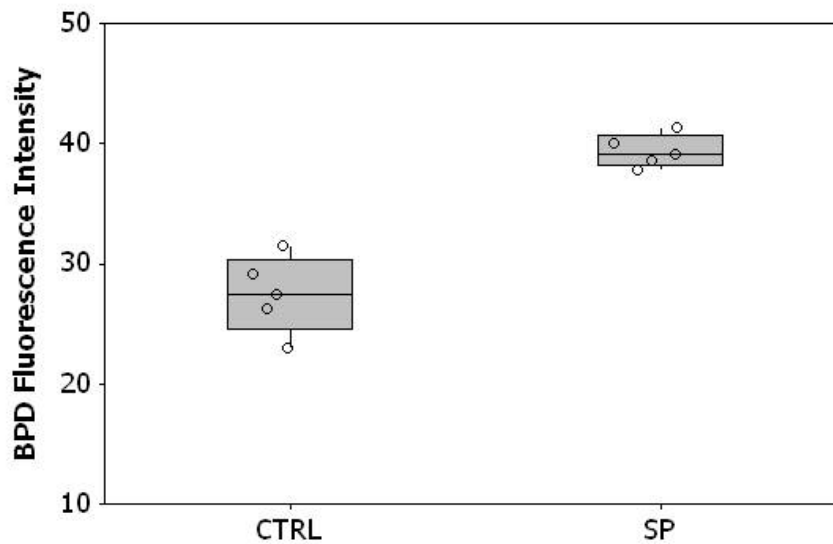
Intra-tumor injection of SP (50 μ l) led to significantly increased blood flow very shortly after injection. This response gradually declined, possibly due to the desensitization process. The blood flow dropped down to the control values at time point 6.4 ± 1.7 min ($n = 6$) (Figure 8.7). Blood flow dynamics of animals in the SP group are shown in black with circles, and the SP vehicle (NaCl) control animals ($n = 3$) plotted in red lines.

8.3.7 Enhancement of PDT Treatment Efficacy

Tumor regrowth measurements are shown for different treatment groups and control groups in Figure 8.8. Data points represent the average tumor volume for 6 animals in each group, and error bars show the standard deviation for these mean values. PDT treatments and PDT+SP treatment both induced tumor regrowth delay, and the SP+PDT group was found to be clearly more effective than the PDT only group. Animals in SP control group also demonstrated a slight tumor regrowth delay at days 5 post treatment (Figure 8.8).

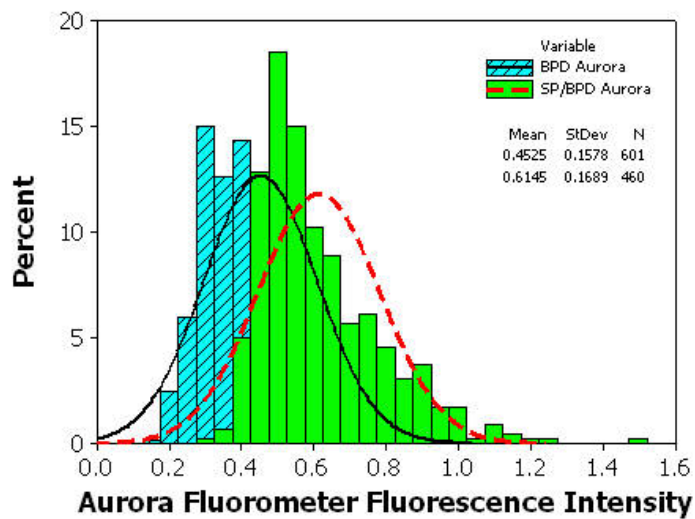


(a)

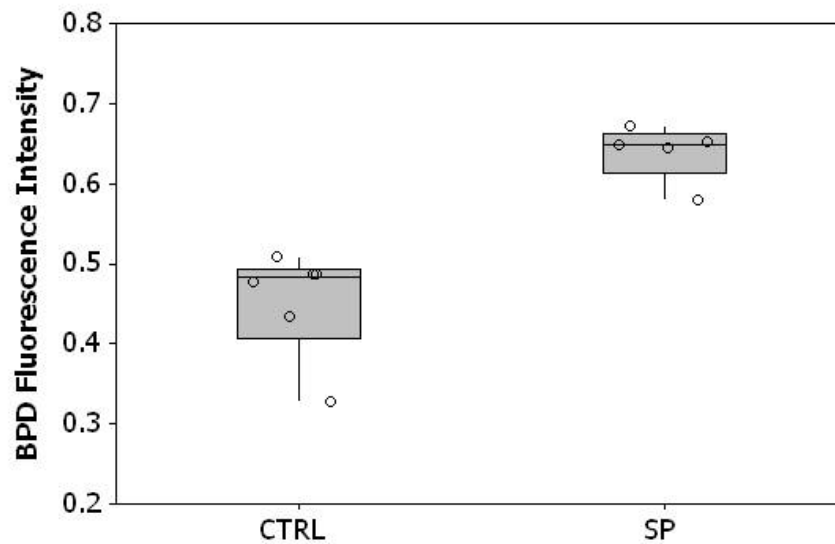


(b)

Figure 8.5: Verteporfin tumor uptake evaluated by the fluorescence microscopy. Comparisons between SP treated group and control group were presented in a histogram (a) and a box-plot (b) to illustrate the effects of SP on BPD fluorescence inter-tumor and intra-tumor variation. 5 animals were included in each group.



(a)



(b)

Figure 8.6: Verteporfin tumor uptake evaluated by the Aurora fluorometer. Comparisons between SP treated group and control group were presented in a histogram (a) and a box-plot (b) to illustrate the effects of SP on BPD fluorescence inter-tumor and intra-tumor variation. 4 and 5 animals were included in control and SP treated group respectively.

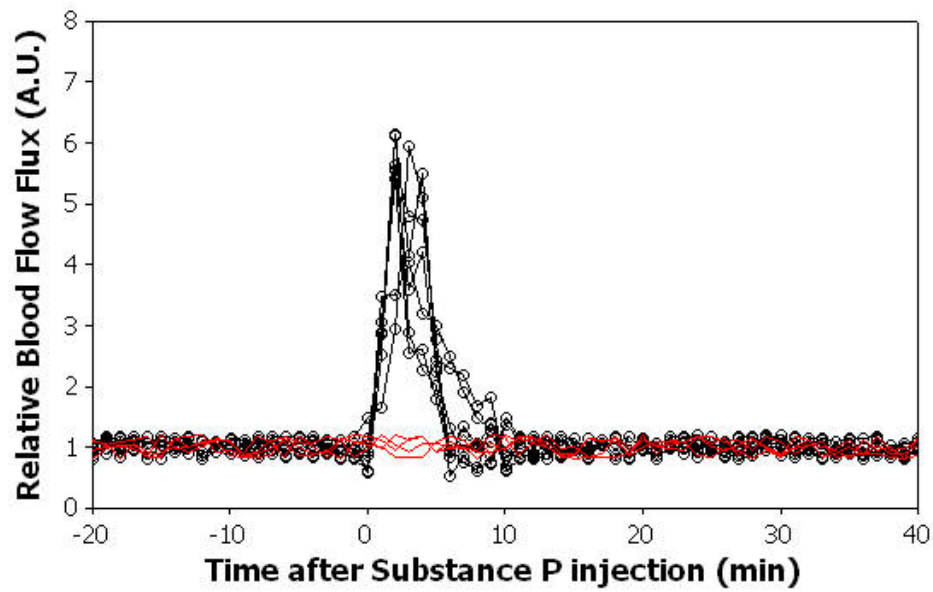


Figure 8.7: Blood flow changes after SP application recorded in MAT-LyLu tumors using a laser Doppler blood flow system. Normalized blood flow dynamics were plotted for individual animals. SP treated tumors ($n = 6$) are plotted in black line with circle; control tumors ($n = 4$) are plotted in red lines.

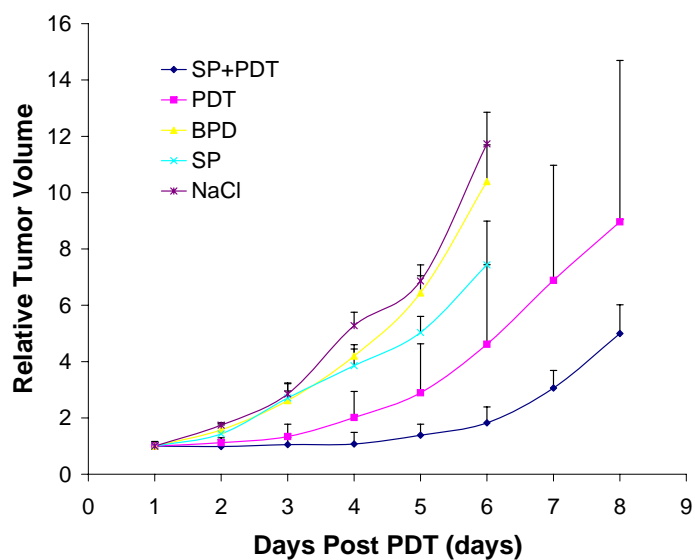


Figure 8.8: Tumor volume changes in response to PDT treatments. Animals in the PDT group received 1 mg/Kg verteporfin and were exposed to 75 J/cm² light illumination at 3 hrs. Animals in PDT+SP group received 50 μ l intratumor injection of SP before verteporfin administration, tumors received the same photosensitizer dose and light dose as in the PDT group. Animals in control groups received SP, NaCl or Verteporfin without light treatment. There were 6 animals in each group.

8.4 Discussion

In Chapter 5 and 7, it was established that there were connections between photosensitizer transport parameters, photosensitizer pharmacokinetics, and PDT treatment efficacy. The cause-effect relations among these parameters implies that individual photosensitizer pharmacokinetic variability can be modulated by manipulating the transport processes during the photosensitizer delivery process, and as a result, inter-individual variability in response to PDT treatment can be reduced. Cellular targeting PDT requires effective delivery of photosensitizer molecules to the tumor parenchyma. Photosensitizer inter-individual variability and intra-individual pharmacokinetic variability is severe, and, not surprisingly, inter-individual variability in response to cellular targeting PDT has been found to be the most variable when compared to vascular targeting PDT.

In the 3-h drug-light interval cellular-targeting PDT protocol, verteporfin tumor cell uptake is limited mainly by the transvascular transport process, rather than photosensitizer interstitial transport process. This is due to the time constant τ_D , which is much shorter than the drug-light interval 3-h. Thus, inter-individual variability in photosensitizer tumor uptake can be modulated by controlling the transvascular transport process, and in turn reduce the inter-individual variability in response to cellular targeting PDT.

There are variety of approaches to modulate the macromolecule transvascular transport process in solid tumor. These approaches modulate the process through one or more of the following pathways:

1. Direct damage to the endothelial cells;
2. Increase blood flow;
3. Increase the exchange surface area;
4. Alter the interstitial fluid pressure.

Perhaps, the most frequently and widely studied increased vascular permeability phenomenon is the large increase in permeability in acute or chronically inflamed tissues. Extensive studies have been performed to investigate the effects of the inflammatory mediators on various tissues, such as, trachea, striated muscle, mesentery, skin and airway mucosa. SP is one of the neurogenic inflammatory mediators present in sensory nerves [326], triggers neurogenic inflammation, in which plasma leakage is prominent feature.

The purpose of this study present here is to investigate the effect of SP on photosensitizer transport process, photosensitizer tumor pharmacokinetics, and its effect on cellular targeting PDT efficacy.

Verteporfin plasma pharmacokinetics have are not affected by the intra-tumor injection of SP, as can be seen from Figure 8.1 and Table 8.1. This is an attractive feature since a localized permeability increase is desired in the tumor. In our early studies of SP, an intravenous injection through tail vein was been examined. Verteporfin tumor uptake in these animals did not show any increase, and even exhibited a decrease in tumor uptake (data not shown). This might be due to the fact that post-capillary venules are the vessels

that are most sensitive to inflammatory stimuli, which are often found an absence in the tumor sites. By injecting SP locally, a localized transvascular transport modulation can be achieved, thus limiting photosensitizer pharmacokinetic modulation locally.

Vasodilation has been reported for in many SP inflammation studies. Brook *et al.* demonstrated that the percentage of dilated vessels is between 40-80% in small arterioles in the rat cremaster muscle [327]. However, in our study, the range of average vessel areas are comparable in SP treated and control tumors (Figure 8.2). This can be explained by the temporal dynamics of SP vasodilation effect. In Brook's study, the vessel diameter was evaluated via television microscopy, thus the temporal dynamics of the vessel morphology can be evaluated. In this study, we used fluorescence microscopic perfusion images at 15 minutes after SP administration. At this time point, vasodilation might have already recovered to the normal level. Thus, SP treated tumors did not show differences compared to the control animals. This temporal effect can be confirmed from the blood flow dynamics post SP injection. Figure 8.7 indicates that shortly after SP administration, the blood flow increases about 5 fold higher compared to the controls. This increased blood flow relaxed back to the baseline within an average 6 minutes (Figure 8.7). Therefore, the observed vessel area at 15 minutes would be comparable to the controls.

Substance P induced vascular leakage is transient and followed by a rapid desensitization process. This is explained by the endothelial gaps formation and re-closure after exposure to SP. This gaps formation process is accompanied by vessel dilation and increased

blood flow observed shortly after SP treatment. Thus increased blood flow and exchange area is another factor that affect the transvascular transport. We evaluated the vascular permeability via macroscopic tumor Evans blue extravasation assay and microscopic fluorescence microscopy. In Evans blue analysis, an increased Evans blue extravasation was found at 1 hour and 3 hours post administration (Figure 8.3). At 15 minute, there is slightly but not significant difference between the SP treated and control group. This is probably due to the localization of Evans blue-albumin conjugates. Since at early time point post Evans blue administration, Evans blue-albumin conjugates accumulates in the intravascular compartment, the total Evans blue tumor level is determined by the concentration in the intravascular compartment. However, after a longer period of time, Evans blue-albumin conjugates extravasate across tumor vessel wall and distributed in tumor interstitium. Thus the number of conjugates extravasated determines the total tumor uptake. Therefore, SP induced transvascular permeability increases are more pronounced at 1 and 3 hours.

An inflammatory mediator induced vascular permeability increase has been extensively studied. Wu *et al.* measured the effective permeability coefficient to α -lactalbumin in the rat mesentery during 15 min of 10^{-3} M histamine suffusion, and showed a maximum 15 fold higher permeability at 4 min, and approximately 6 fold higher at 15 min [328]. We have found approximately 60% increase in the microscopic transvascular permeability coefficient (Figure 8.4). This value is much smaller than the results shown by other investigators. These investigations were performed mostly on the post-capillary venules in normal

tissues, such as trachea, mesentery, and skin, where the interstitial pressure is much lower than inside the tumor. As a result, the transvascular transport process is dominated by convection rather than diffusion. After SP injection, molecules extravasate through these gaps via the fluid exchange across the vessel wall. However, in the tumor tissue, the interstitial fluid pressure is much higher. Even though the gaps have formed providing enough space for transvascular transport, photosensitizer molecules still have to follow the concentration gradient to diffuse into tumor interstitium.

The increased permeability induced by Substance P led to a higher verteporfin uptake in tumor at 3 hours after injection. This can be seen from both fluorescence microscopy analysis and Aurora fluorometry analysis showing there is about 40 to 50% increase in verteporfin fluorescence intensity (Figure 8.5 and 8.6). It is interesting to see that in Figure 8.5(a), the fluorescence intensity intra-tumor distribution seemed more heterogeneous in the SP treated group. This heterogeneity is characterized by one peak centered around the mean value and a smaller peak centered at the control mean value. This phenomenon might be due to the heterogeneous SP intra-tumor administration. For a small portion of regions inside the tumor, there is limited SP delivered, thus the transvascular transport is not affected by SP injection. However, when integrated to the whole tumor, this effect is less pronounced, and the inter-individual variability in verteporfin uptake is reduced (Figure 8.5(b) and 8.6(b)).

PDT induced tumor growth delay was measured to examine the effect of SP on tumor

treatment response. It is not surprising that SP+PDT treatment controlled the tumor growth best, since SP administration enhances the photosensitizer transvascular transport, and increases the photosensitizer uptake. One interesting fact observed from the tumor growth analysis is that the inter-individual variability in response to PDT in SP+PDT group seemed to be less compared to the PDT treated group. This can be seen from Figure 8.9. There are two possible reasons for these. First, by modulating the photosensitizer transvascular transport process, less inter-individual variability in verteporfin tumor uptake was achieved, at 3 hours. Secondly, an inflammatory condition is of importance to PDT treatment. More and more evidence has pointed to the fact that PDT damage is induced through the disintegration of cellular membrane which triggers the inflammation process. Endogenous injection of inflammatory mediators seemed to enhance this PDT-induced inflammatory process, and show a better control of tumor. At the same time, this inflammatory process homogenizes the heterogeneous distribution of photosensitizer inside the tumor, and reduces the inter-individual variability in response to PDT.

8.5 Conclusions

In this study, the intra-tumor application of Substance P was shown to increase the photosensitizer transvascular permeability 64%, enhance the photosensitizer BPD uptake by 48% measured by fluorescence microscopy and and 35% quantified by Aurora fluorometer. Inter-individual pharmacokinetic variability and inter-individual variability in response

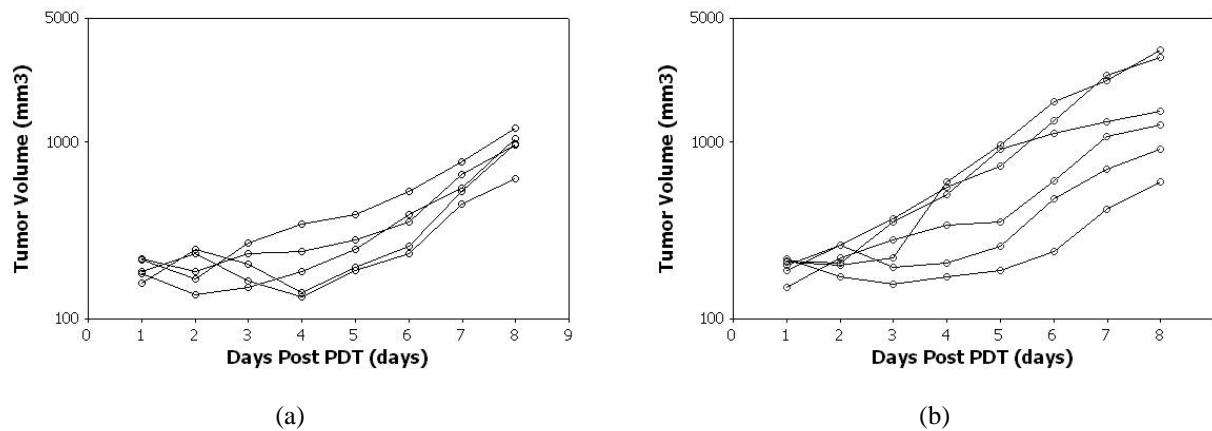


Figure 8.9: Individual growth dynamics for SP+PDT (a) and PDT group (b). Coefficients of variation for tumor volumes are 12.5% and 20.5% at day one and day eight for SP+PDT treated animals, and 12.7% and 63.9% at day one and day eight for PDT treated animals.

to cellular targeting PDT was found reduced by 40% and 50% after application of Substance P. The treatment with Substance P and cellular targeting PDT exhibited a better control of tumor. This study implies that increasing photosensitizer transport may be a useful mechanism for reducing the inter-individual variability in standard PDT treatment.

Chapter 9

Photosensitizer Dosimetry Controlled PDT Treatment Planning

9.1 Introduction

Over the past 30 years, PDT protocols have been developed for numerous types of cancers and pre-cancers conditions. FDA approved PDT sites include skin, head and neck and gastrointestinal tract [77, 87, 329].

To date, most clinical PDT treatments have been performed using a predetermined PS dose, a fixed time interval between photosensitizer and light administration, and a stipulated irradiation time with a fixed incident light irradiance (in units of mW/cm^2 for surfaces, or specified as mW/cm for cylindrical illuminators). Using this protocol, most pre-clinical

and clinical PDT studies indicate a considerable variation in the treatment response [77]. Although some of this treatment response variation can be due to the biologic variation in response to therapy for different histologic subtypes or different tumor geometries, the issue of varying photosensitizer concentration in the tumor tissue would seem to be a contributing factor. As a matter of fact, significant heterogeneity in PS tumor uptake has been demonstrated in both animal and human tumors [88, 330]. Yet this issue is also the one that can be readily addressed with *in vivo* dosimetry measurements, by simply adding more light dose where there is lower drug dose. There is a well known reciprocity between drug and light dose, which has been demonstrated in experimental tumors for several years [310, 331–333]. Or through developing an integrated treatment plan which integrates the fluorescence in real time during the treatment to estimate the overall dose [REF Wilson paper]

Recent developments of fluorescence detection techniques have made online dosimetry of PS possible. Both fiber based dosimeters [289] and wide-field fluorescence imaging dosimeters [291, 300, 334, 335] have been designed and tested in phantom, animal and clinical studies. These fluorescence measurements can provide information about photosensitizer concentration in different tumors and in different areas within a tumor. Currently, most PS dosimetry systems focus on the overall change of PS concentration without enough attention on the variation of measurements within each subject. This is partially because some PS dosimetry systems tend to sample large tissue volumes and therefore are not able

to detect PS uptake heterogeneity. The micro-sampling probe in the dosimeter system used in this study allows detection of PS variation in tumor tissue on the size scale of 100 microns. It is generally accepted that photodynamic therapy dose is defined as the number of photons absorbed by photosensitizer per unit volume of tissue [336, 337]. This determination is readily calculated by multiplying the concentration of PS by its extinction coefficient and the light fluence incident in that location. Thus, in order to deliver the same PDT dose, as the concentration of PS changes, the light fluence should be adjusted accordingly to compensate for this PS inter-subject variation.

The objective of this study was to examine the feasibility and outcome of an individual PDT regimen based on PS dosimetry measurements in a well-characterized rat prostate tumor model. The PS tumor uptake variation was assessed using the micro-sampling PS dosimetry system and, based on these measurements, the light dose was adjusted to determine whether such a modification would improve treatment outcome. If this overall hypothesis is true, it would open up the possibility of subject-customized PDT dosimetry along the lines of radiation therapy treatment planning.

9.2 Materials and Methods

9.2.1 Animals and tumor model

Male Copenhagen rats with an average body weight of 120 g-150 g, were used for this study (Charles River Laboratories, Wilmington, MA). All animals were housed in the Dartmouth Medical School animal facility. This facility and program are AAACAC accredited and adhere to all USDA guidelines for animal research use. The animals were housed in a temperature controlled environment with a 12-hr light/dark cycles, having free access to water and standard laboratory diet. All procedures and experiments were approved by the Dartmouth College Institutional Animal Care and Use Committee. The animals were anesthetized using an intra-muscular injection of a mixture of Ketamine and Xylazine at a dose of 90 mg/Kg and 10 mg/Kg respectively. A subcutaneous tumor was introduced by injection of 1×10^5 cells of the Dunning prostate tumor R3327 MAT-LyLu (Metastatic AT-Lymph Node and Lung) [253], on the right flank in a volume of 50 μ l. Animals were followed daily to track the tumor growth. Tumors were treated when they reach 150-300 mm³ (approximately 7 days post injection).

9.2.2 Photosensitizer

A liposomal formulation of the photosensitizer benzoporphyrin derivative (BPD) [111, 115], verteporfin-for-injection (QLT Inc., Vancouver, BC, Canada), was used for all stud-

ies. Following reconstitution, animals received 1.0 mg/Kg BPD intravenously (tail vein). Photosensitizer dosimetry was then performed, and tumors were irradiated 3 hours after PS administration.

9.2.3 Photosensitizer dosimetry

Immediately prior to light treatment, the skin over the tumor area was carefully removed for measurement of the PS fluorescence in the tissue. The surrounding vasculature was preserved as much as possible to minimize bleeding and changes in optical properties of the tumor. PS concentration measurement was achieved using a customized commercial fluorimeter system (Aurora Optics, Inc., Hanover, New Hampshire) at 20 distinct locations, sampling 5 times at each site. A set of 100 data points for each animal was used to analyze the intra-tumor variation of fluorescence intensity for each animal. The average of these 100 data points was used to represent the PS uptake for individual animals and for the analysis of inter-tumor variation. All the measurements were recorded 3 hours after PS administration. The fluorimeter system employed a 405 nm diode laser, a 660 nm long-pass filter and a photomultiplier tube for detection. The fiber bundle contained 6 detection fibers and a center excitation fiber. The six detection fibers each has 100 micron diameter in order to constrain the distance of tissue sampled to be smaller than the average scattering distance (mean free path) of tissue, which is typically 100-200 microns. The sampling time for each measurement was limited within 0.5 seconds, so that less than 10% photobleaching

occurred when a repeated sampling was taken from an individual spot on the tissue [256, 290, 295].

9.2.4 Photodynamic dose calculation and Photodynamic therapy treatment

Irradiation of tumors was achieved using a 1 Watt maximum, 690 nm wavelength diode laser (Applied Optronics, CT) delivered via a 140 μm diameter optical fiber. Laser beam was collimated through a coupling lens on the end of the fiber to a 1cm diameter beam spot over the tumor surface. The tumors received an average incident irradiance 50 mW/cm^2 , as evaluated by an optical power meter (Thorlabs Inc, NJ). The time of irradiation was fixed for the first two groups, and then varied in the latter three groups to maintain a group where each animal received a fixed total dose, as defined below. Tumor-bearing animals were divided into five groups of 11-20 animals. The control group and standard PDT group were as follows: (a) PS-only Control group (CTRL): 20 animals were injected verteporfin intravenously and received PS dosimetry without laser illumination 3 hours post injection. (b) Non-Compensated PDT treatment group (NC-PDT): 20 animals received the i.v. injection of Verteporfin-For-Injection, and photosensitizer dosimetry 3 hours post injection. Animals received the PDT irradiation right after PS dosimetry with total light dose of 75 J/cm^2 and an average light irradiance of 50 mW/cm^2 . Photodynamic dose was estimated by multiplying the photosensitizer uptake of each individual and the total light dose of 75 J/cm^2 . The

effect of compensating the light dose to the photosensitizer concentration was examined in three ways. Since the fluorescence from each animal was measured in up to 100 samples, each subject had a distribution of values from which to estimate the photosensitizer dose *in vivo*. It was hypothesized that compensating the light dose of each animal to achieve a total PDT dose equivalent to that calculated by the mean PS dose multiplied by 75 J/cm^2 might be optimal. However, alternative measures of the photosensitizer dose based upon the histogram of values from each animal, would be to use the lower quartile of the distribution, or possibly the upper quartile of the distribution. In order to test if the mean lower quartile, or mean upper quartile values of the PDT dose were better suited to reduce variance in treatment effect, treatment groups were included which received PDT doses equivalent to the lowest photosensitizer quartile and the highest photosensitizer quartile, each multiplied by the light fluence of 75 J/cm^2 . This was achieved by each animal being given a light dose which was compensated to achieve the same total PDT dose (light dose multiplied by drug dose). These formulas used the following definitions below. In these definitions, the photosensitizer concentration distribution in the entire control group was used to calculate the mean, $[PS]_C$, the mean of the upper quartile $[PS_{UQ}]_C$ and the mean of the lower quartile $[PS_{LQ}]_C$. In the same way, for each individual animals in the compensated groups they were used to calculate the mean photosensitizer concentration, $[PS]_i$, or the lower quartile $[PS_{LQ}]_i$, or the upper quartile $[PS_{UQ}]_i$. Once calculated for each animal, the compensated dose was estimated and the animals were treated in one of the three groups according to the formulas:

(c) Compensation-to-Median PS value treatment group (CM-PDT): 17 animals. Total light dose for each subject was calculated from the dose calculation formula:

$$\text{Total light dose} = (75J/cm^2) \times ([PS]_c)/([PS]_i)$$

(d) Compensation-to-Lower PS quartile PDT treatment group (CL-PDT): 11 animals received photosensitizer dosimetry 3 hours after verteporfin injection. The total light dose for each subject was estimated from the formula:

$$\text{Total light dose} = (75J/cm^2) \times ([PS_{LQ}]_c)/([PS_{LQ}]_i)$$

(e) Compensation-to-Upper PS quartile, PDT treatment group (CU-PDT): 19 animals. The total light dose for each subject was calculated from the formula:

$$\text{Total light dose} = (75J/cm^2) \times ([PS_{UQ}]_c)/([PS_{UQ}]_i)$$

9.2.5 Tumor Regrowth Assay and Model Based Interpretation

Tumor regrowth assay was used to quantify the treatment effects of photodynamic therapy. Width (a), length (b) and height (c) were measured with slide calipers to determine the tumor volume, and calculations were performed using the formula $V = \frac{\pi}{6} \times a \times b \times c$. The longitudinal tumor volume data, as a function of time (in days) after treatment, are displayed on a semi-logarithmic scale. The advantage of the semi-logarithmic versus regular scale is that exponentially growing tumors follow a straight line so that the effects of the tumor growth delay are clearly seen. Moreover, expressing observations as $v_t = \ln(V_t)$,

where V_t is the tumor volume at time t , facilitates modeling of tumor growth and regrowth in treatment groups and their statistical comparison [316]. The following tumor regrowth model [316] has been applied to mathematically describe the dynamics of treated tumors: $v_t = \alpha + \beta t - \ln(SF\%)(e^{-\delta t} - 1)$, where α is the log tumor volume before the treatment, β is the growth rate of unaffected tumor cells, δ is cell loss constant at which the treated cells die, and $SF\%$ is survival fraction. This model allowed computing other treatment endpoints such as tumor growth delay (TGD) computed as and doubling time (DT) as the solution to the equation . Tumor growth delay (TGD), doubling time (DT) and survival fraction ($SF\%$) were used to determine variation of tumor response within and between groups.

9.3 Results

9.3.1 Inter-tumor and intra-tumor variation in photosensitizer uptake

Photosensitizer dosimetry measurements were performed on 40 animals (20 from CTRL group, 20 from NC-PDT group) at 3 hours post injection of verteporfin. Photosensitizer fluorescence intensity measured via PS dosimeter (Aurora Optics, Lebanon, NH) varied considerably between tumors and between locations on each tumor. Figure 9.1(a) demonstrates two tumors, one with small intra-tumor variation (coefficient of variation = 11.9%) and one with a large intra-tumor variation (coefficient of variation = 64.2%)(coefficient of

variation = standard deviation to mean ratio). This information illustrates how animals may have different photosensitizer uptake distributions, *e.g.* animal B has a higher percentage of low photosensitizer uptake area compared with animal A, possibly due to necrotic areas or damaged blood flow. The overall intra-tumor variation summarized from 40 animals is shown in Figure 9.1(b). Differences in data distribution for individual animals and a larger population are shown. Inter-tumor variation of photosensitizer uptake is shown in Figure 9.1(c). This graph summarizes the average photosensitizer uptake from 40 animals (coefficient of variation: 56.9%). Photosensitizer uptake is represented by the average of 100 data points measured from each tumor. In Figure 9.1(a), the mean and standard deviation are 0.291 and 0.082 for rat A (smaller variation), and 0.296 and 0.190 for rat B (larger variation), which correspond to coefficient of variation values of 11.9% and 64%, respectively. The mean and standard deviation in Figure 9.1(b) were 0.50 and 0.33, and coefficient of variation was 66.0%. In Figure 9.1(c), the mean and standard deviation values are 0.51 and 0.29, corresponding to a coefficient of variation of 57%.

9.3.2 Inter-tumor variation in treatment response

To assess the tumor response to PDT treatment, the tumor volume was measured daily immediately following PDT treatment. The animals in the photosensitizer only control group showed faster and less variable growth dynamics (Figure 9.2). The mean \pm standard variation of tumor volume on day one and day six were $213 \pm 71 \text{ mm}^3$ and $2224 \pm 735 \text{ mm}^3$.

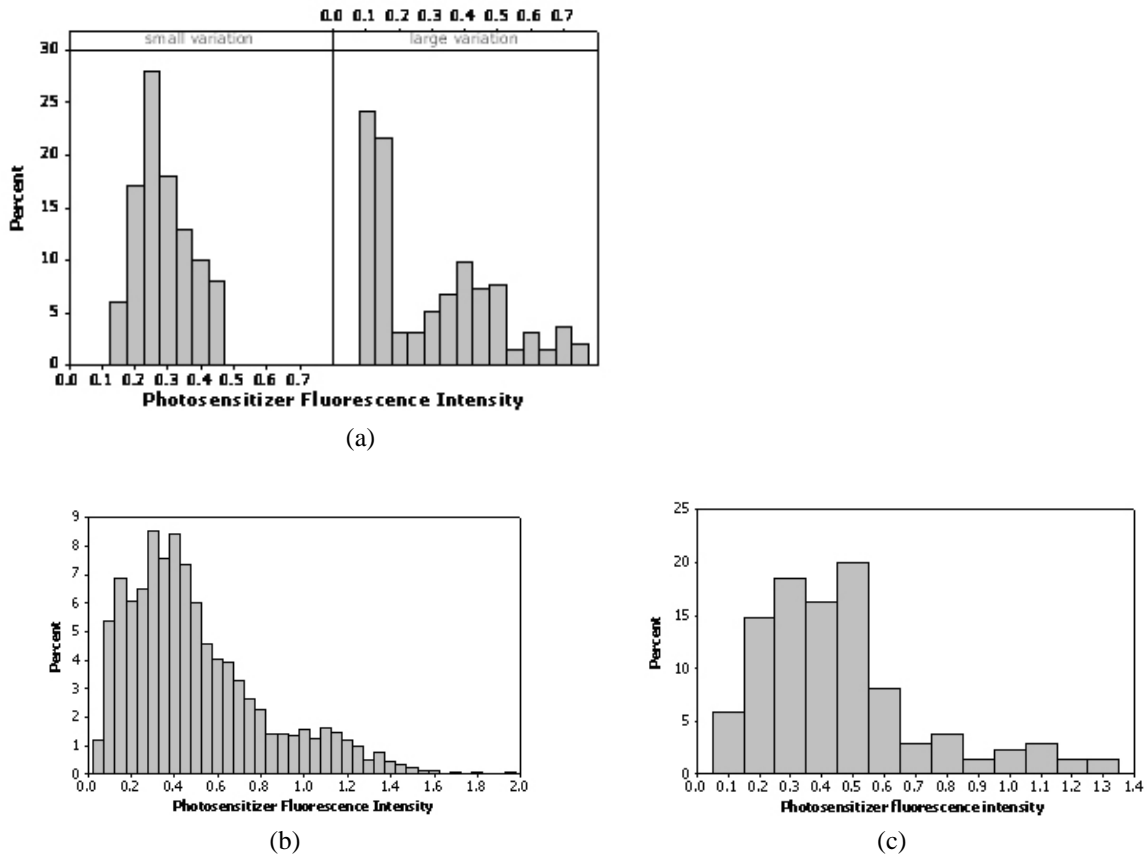


Figure 9.1: (a) Fluorescence intensity histogram for two individual animals. Coefficients of variation for the fluorescence intensity measurement are 11.9% and 64.2% for the left and right panel respectively. (b) Overall intra-tumor variation from 40 animals. Coefficient of variation is 66.0%. (c) Overall inter-tumor variation in photosensitizer uptake, the mean and standard deviation are 0.51 and 0.29, corresponding to a coefficient of variation of 57%.

The coefficients of variation were 33.4% and 33.1% respectively. The animals in the Non-Compensated PDT treatment group showed considerably more variation in growth dynamics after treatment. On day 1, the mean tumor volume was 204 mm^3 with a standard deviation of 55 mm^3 , which corresponds to a coefficient of variation of 26.9%. On day 8, the mean tumor volume increased to $1753 \pm 1151 \text{ mm}^3$, corresponding to coefficient of variation of 65.7%. By fitting the tumor volume to a double-exponential regrowth model, the control tumors were found to grow at an exponential rate of $e^{0.467 \times \text{days}}$, with a doubling time of 1.48 days. Non-compensated PDT treated tumors showed an average growth delay of 3.54 days (standard deviation: 0.41, coefficient of variation: 15.0%), tumor doubling time 3.42 ± 0.41 days (coefficient of variation: 12.0%) and surviving fraction of $19.7 \pm 4.9\%$ (coefficient of variation 24.9%) See Table 9.1 for these details.

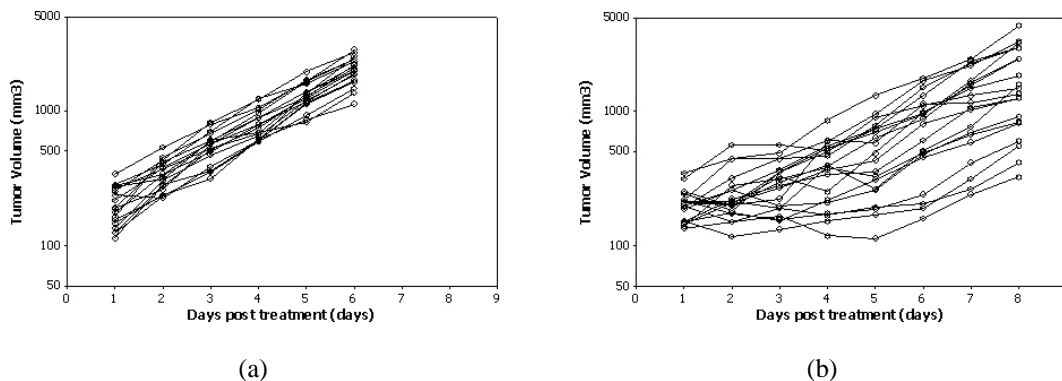


Figure 9.2: Tumor growth dynamics of animals in CTRL group (a) and NC-PDT group (b). Coefficients of variation for tumor volumes are 33.4% and 33.1% at day one and day six for CTRL animals, and 26.9% and 65.7% at day one and day eight for NC-PDT animals.

Tx. Group	DT	TGD	SF%
NC-PDT	3.42 ± 0.41 (12.0%)	3.54 ± 0.53 (15.0%)	19.68 ± 4.94 (24.9%)
CL-PDT	2.75 ± 0.28 (10.1%)	2.22 ± 0.33 (14.9%)	35.75 ± 5.72 (16.0%)
CM-PDT	3.39 ± 0.26 (7.5%)	2.84 ± 0.28 (9.9%)	27.12 ± 3.78 (14.0%)
CU-PDT	3.72 ± 0.30 (8.1%)	3.29 ± 0.32 (9.7%)	21.77 ± 3.47 (15.9%)

Table 9.1: Summary of tumor doubling time, tumor growth delay and surviving fraction for all treatment groups.

9.3.3 Compensated PDT reduces the inter-tumor variation in treatment response

Compensated PDT dose calculations were based on the photosensitizer dosimetry histogram values. All measurements were performed 3 hours after intravenous verteporfin injection. Inter-tumor (macroscopic) variation in the mean photosensitizer uptake are illustrated in Figure 9.3(b)9.3(d)9.3(f) for CU-PDT, CM-PDT and CL-PDT groups respectively. The mean and standard deviation for macroscopic photosensitizer uptake are 0.49 and 0.16 for CL-PDT (coefficient of variation = 33%), and 0.44 and 0.13 for CM-PDT (coefficient of variation = 30%) and 0.50 and 0.17 for CU-PDT (coefficient of variation = 34%). Overall intra-tumor (microscopic) variation in BPD uptake are shown in Figure 9.3(a)9.3(c)9.3(e) for three compensated PDT groups. The mean and standard deviation are 0.49 and 0.19 for CL-PDT (coefficient of variation = 39%), and 0.44 and 0.18 for CM-PDT (coefficient of variation = 41%) and 0.51 and 0.21 for CU-PDT (coefficient of variation = 41%). Compensated PDT treatments were performed 8 days following MAT-LyLu tumor implantation. The averaged volumes of the tumors being treated were 220.7±54.0 mm³ (24% variation),

220.1±46.2 mm³ (21%), and 190.9±54.6 mm³ (29%) for CL-PDT, CM-PDT and CU-PDT. Tumor volumes were recorded everyday after treatments (Figure 9.4(a)9.4(b)9.4(c)). Variations of tumor volume on day 8 were 35%, 31% and 42% for CL-PDT, CM-PDT and CU-PDT. These values are significantly less than the variation in tumor volume on day 8 of Non-Compensated PDT treatment group ($p < 0.05$) (Figure 9.3.3). Coefficient of variation in doubling time (DT), tumor growth delay (TGD) and surviving fraction (SF%) were 11.1%, 14.9% 16.0% for CL-PDT, 7.5%, 9.9% and 14.0% for CM-PDT and 8.1%, 9.7% and 15.9% for CU-PDT. Variations in these characteristic parameters are significantly less than was observed in compensated PDT treatments ($p < 0.05$).

9.3.4 Comparison of treatment efficacy of PDT treatments

All treatments showed effective control of tumor growth, but CL-PDT had significantly less control of the tumor growth as compared with NC-PDT, CM-PDT and CU-PDT (Figure 9.3.4). Paired comparisons of doubling time, tumor growth delay and surviving fraction showed CL-PDT had significantly shorter doubling time, as well as significantly shorter tumor growth delay and larger surviving fraction (Table 9.1 and Table 9.2).

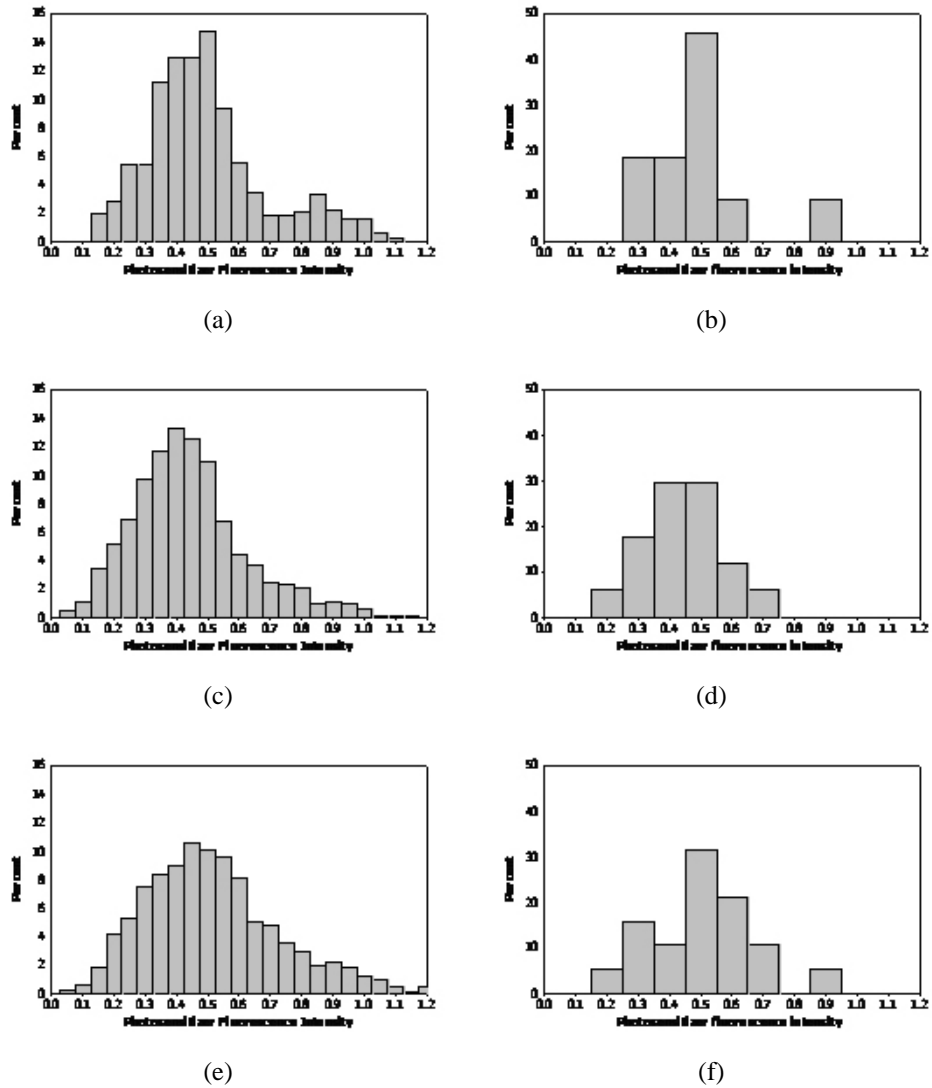


Figure 9.3: Distributions of intra-tumor (microscopic) variation (a, c, e) and inter-tumor (macroscopic) variation (b, d, f) in photosensitizer uptake for CU-PDT (a, b), CM-PDT (c, d) and CL-PDT (e, f) animals.

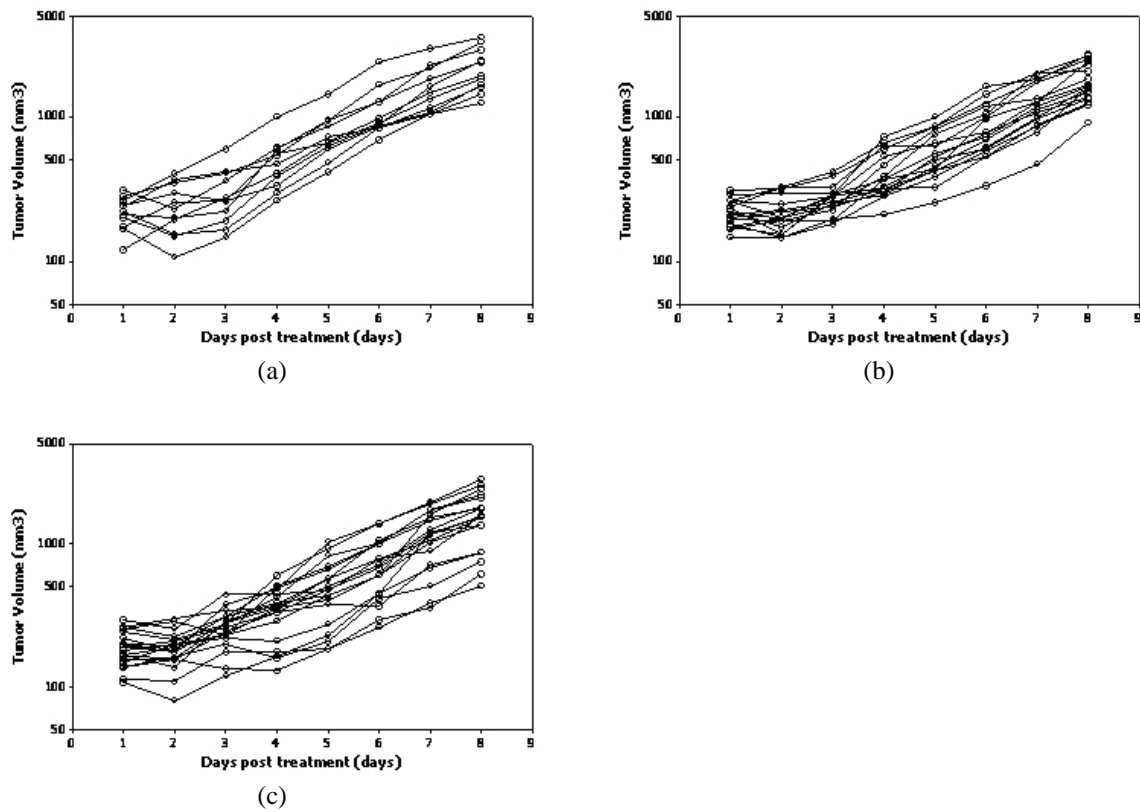


Figure 9.4: Tumor growth dynamics of animals in compensated PDT groups. Coefficients of variation for tumor volumes are 24% at day one and 35% at day eight for CL-PDT (a), 21% at day one and 31% at day eight for CM-PDT (b), and 29% at day one and 42% at day eight for CU-PDT (c).

Tx. Group	DT	TGD	SF%
CL-PDT <i>v.s.</i> NC-PDT	0.18	0.03 *	0.03 *
CM-PDT <i>v.s.</i> NC-PDT	0.94	0.24	0.23
CU-PDT <i>v.s.</i> NC-PDT	0.56	0.69	0.73
CM-PDT <i>v.s.</i> CL-PDT	0.09	0.16	0.21
CU-PDT <i>v.s.</i> CL-PDT	0.02 *	0.02 *	0.04 *
CU-PDT <i>v.s.</i> CM-PDT	0.4	0.29	0.3

Table 9.2: Paired comparisons of doubling time, tumor growth delay and surviving fraction for all treatment groups.

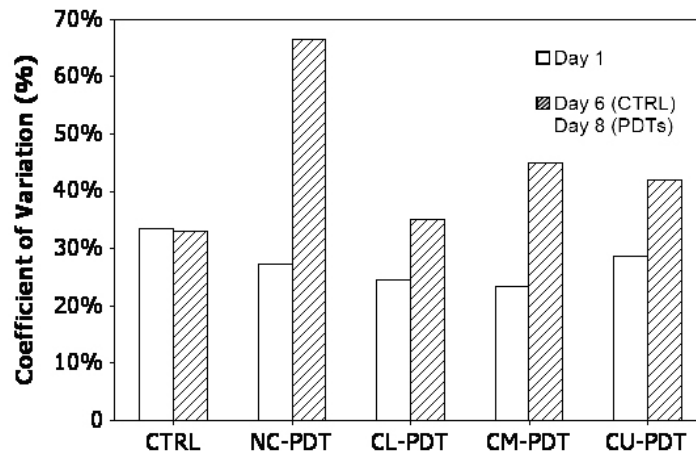


Figure 9.5: Coefficients of variation for tumor volumes. Data shown are CTRL group (day one and day six), and NC-PDT, CL-PDT, CM-PDT, CU-PDT groups (day one and day eight). CTRL = PS only control group; NC-PDT = Non-Compensated PDT; CL-PDT = Compensated-to-Lower PS quartile PDT treatment group; CM-PDT = Compensated-to-Median PS value PDT treatment group; CU-PDT = Compensated-to-Upper PS quartile PDT treatment group.

9.4 Discussion

Determining the best dosimetry technique for PDT has been an ongoing area of research for the past few decades. The path to correct and improve the accuracy of dosimetry can be envisioned somewhat by examining the parallel path that radiation therapy dosimetry has taken in that same time period. Clinical ionizing radiation therapy has developed from classical rectangular beams to intensity modulated radiation dose delivery where the total dose distribution can be controlled in three dimensions [338], and patient-specific dosimetry and treatment planning can be routinely realized to deliver dose distributions which are customized to the patients tissue and geometry [338]. Compared with the advanced treat-

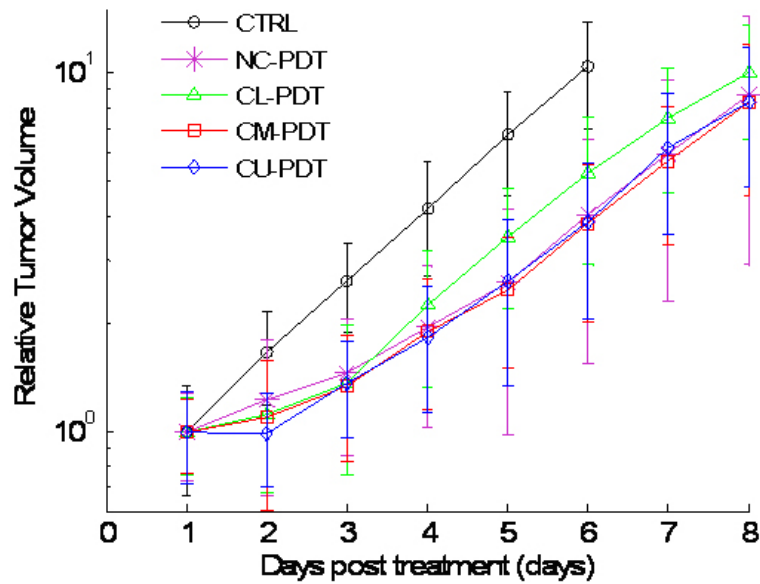


Figure 9.6: Averaged tumor volume on each day post treatment for all the groups. Error bars represent the standard deviation of measured tumor volumes. Open circle = CTRL; star = NC-PDT; open triangle = CL-PDT; open square = CM-PDT; open diamond = CU-PDT. Each point represents the mean \pm SD.

ment planning in radiation therapy, PDT dosimetry, dose distribution calculation and treatment planning are still in their infancy. During the last twenty years, many PDT dosimetry tools have been designed and tested. These include physical parameter dosimetry, *e.g.* light dosimetry [339, 340], PS dosimetry [256, 289, 291, 295, 300, 334, 335], oxygen dosimetry [264, 341–344], singlet oxygen generation [27, 345–347] and physiological parameter dosimetry, *e.g.* blood flow measurement [257], or NADH measurement [348]. Fluorescence dosimetry has been proposed for a long time and has had considerable discussion about it, as perhaps the most ideal and stable way to measure dose *in vivo*. Yet to this date, no clinical implementation of the concept has been used to tailor individual patient doses. This study was designed to demonstrate the variation in PS uptake, the variation in tumor biological response to PDT treatment, and do a preliminary examination of the advantage of PS-dosimetry controlled PDT treatment planning.

It was observed that there is considerable variation in PS uptake between tumors and within a tumor, with 57% coefficient of variation between animals and a factor of 14 in total variation of the mean value. After the PS is injected in the animal, PS molecules are distributed in the vasculature, transported across the vessel wall, and diffused in the tumor parenchyma [138]. The variation of PS concentration at different areas of tumor can be explained by the variation in these PS transport processes, *e.g.* different vasculature architecture, capillary permeability, and tumor interstitial diffusivity [138]. Figure 9.1(c) illustrates that different animals may have different PS microscopic distributions even when

they have the same mean PS uptake. For animal A, the PS concentration histogram can be fitted well with a normal distribution; while for animal B, there is a higher fraction of the lowest PS measurements, which probably indicates animal B has many poorly perfused vessels. The probe used in this study is designed to sample superficial regions of tissue in order to reduce the effect of photon scattering [289]. However, this is an artifact of the measurement technique which must be interpreted appropriately as the data are examined, and is a problem which is not readily solved. Probes which sample deeper in the tumor can be developed, but have the problem of sampling larger volumes of tissue, and so do not give a good measure of the tissue heterogeneity. Thus, an underlying hypothesis to this interpretation is that the measurements from the surface of the tumor can be used to represent overall PS uptake by the tumor, if sufficient sampling spots are taken. This may not be true, but presents an attempt to acquire multiple point data sets from a solid tumor *in vivo*, and has been examined by comparison with frozen section microscopy analysis in a previous paper, showing reasonable agreement [330]. The data in Figure 9.1(b) suggests there is considerable inter-tumor variation in PS uptake (as much as 14 fold increase in some animals). This large degree of variation is of course problematic, especially for the case as used in clinical implementation where no PS dosimetry is implemented, and every subject receives the same stipulated light irradiation. Subjects with lower PS uptake could be under-treated, resulting in partial response or even no response to the PDT treatment, or potentially even worse complications such as enhanced aggressiveness of the disease [240]. The origin of PS inter-tumor heterogeneity is not completely understood,

however it appears to be due to the chaotic patterns of vessels within tumors which lead to a highly heterogeneous and unpredictable environment at the microscopic level [138]. It is interesting to compare the inter-tumor variation and intra-tumor variation in PS delivery. First, individual tumors have significantly different PS microscopic distributions, as shown in Figure 9.1(a); second, the PS uptake variation at different points within one tumor is not easily predicted and bears no correlation to the variation between separate tumors; third, the overall relative intra-tumor variation estimated from a large group of tumors, is greater than the inter-tumor variation from the same population, indicating again that the micro-heterogeneity of each tumor dominates the variance observed.

Using a well accepted tumor regrowth assay [349] and a double exponential model [316], the growth characteristics were assessed for the MAT-LyLu Dunning prostate tumor model. Fitting the tumor growth dynamics to the double-exponential model for each subject indicates significant variation in the treatment response (Figure 9.2). Significant variation in the photodynamic dose delivered to individual animals must be present to cause these variation in response. Yet in this study, PDT treatments were carried out on the tumors with approximately same geometry, with similar light fluence. Thus, it appears that the variation in the delivered photons to tissue/tumor per unit time can be ignored, and the variance between animals is largely attributed to drug uptake variation. It is therefore reasonable to assume that adjusting the irradiation time is a reasonable method for compensating for the variation in PS uptake and for keeping the photodynamic dose constant. The three target

photodynamic doses studied represent lowest-quartile, median and upper quartile of the photodynamic doses in the Non-Compensated PDT group. It is not surprising to observe that the treatment efficacy of CL-PDT is significantly less than the other treatment groups, since a lower photodynamic dose is delivered to these animals. Other treatment groups did not show a treatment difference (Figure 9.3.4, Table 9.1 and Table 9.2). This indicates that increasing the irradiation time alone will result in a depletion of PS, and the tumor could be under-treated. Although the treatment efficacy are different, the variation in growth dynamics are significantly reduced for all three compensated PDT groups. However, there is still a 11-20% higher variation as compared with the control animals (Figure 9.3.3) This could be explained by variation in tumor oxygenation and/or variation in PS photobleaching dynamics.

There are still other factors besides photosensitizer concentration which will significantly affect the tumor treatment efficacy. For example, tumor oxygenation could be monitored non-invasively, yet this is challenging [58, 264, 341–343, 350–353]. Even with tumor oxygenation microscopic distributions, (percentage of hypoxia, *etc.*), adjusting the irradiation time alone is not a practically useful option for routine treatment monitoring, at this stage of the technology development. For a tumor with higher percentage of hypoxia fraction, and lower PS uptake, increasing the light irradiation time with a stipulated irradiance would still likely be insufficient as the lack of photosensitizer and oxygen is a multiplicative effect, requiring prohibitively long irradiation times for sufficient effect and

photobleaching of the PS may still take place from non-oxygen dependent mechanisms. Alternatively, different light irradiation schemes can be performed, *e.g.* decreasing the irradiance, while keep the total radiation dose same. This will also make the irradiation time longer, but will allow the oxygen and PS to re-perfuse in the tumor. Another option is to alter the tumor oxygenation itself, by the application of inflammatory mediators, *e.g.* histamine, bradykinin, substance P, or through oxygen or carbogen breathing. These agents may cause a rapid transient increase in endothelial permeability or plasma oxygenation and result in a plasma leakage [97, 318, 319, 328, 354–356]. Variation in photobleaching dynamics is another problem that needs to be solved. The observed bleaching rate can be heterogeneous, where different PS and different tumor environments can result in altered photobleaching rates. Each of these issues are complex and are themselves areas of intense research effort in PDT mechanisms. In this paper, the focus has remained on photosensitizer dosimetry, mainly because it is easily implemented, has high potential impact, and yet remains untested in clinical trials. The important observation of this study is that PS fluorescence can be a useful metric of treatment effect and can be used to correct for the total dose required for treatment on an individual subject basis. Follow up of this study will involve studying other treatment outcome metrics such as tumor cure rate, to determine if the effect holds for the conditions required for human tumor studies. For clinical and experimental work, several real-time PS dosimeters have been designed and tested for online, real-time measurement of PS concentration in the tumors. With dynamic PS concentration information, it should be possible to develop a real-time treatment planning methodology

which will improve the homogeneity of treatment outcome.

9.5 Conclusions

There are 57% inter-tumor and 66% intra-tumor variation in verteporfin PS concentration. The variation of PS between individual tumors leads to a variation in treatment response following PDT treatment. If a customized change to the prescribed light irradiance and irradiation time is used, based upon PS fluorescence dosimetry measurements, then the tumors regrowth rates become less variable between subjects in the same treatment group. For example, in this study, we have reduced the inter-individual variability in response to PDT from 25% in conventional PDT to average 15% in compensated-PDT treatments. In the future, PS-dosimetry and treatment planning of different light radiation doses should be examined as a real option for standard treatment in PDT. Further studies looking at the same model with the endpoint of tumor cure should be carried out to ensure that this effect is observed.

Part IV

Conclusions

Chapter 10

Conclusions

This thesis explored the relationship between photosensitizer microscopic transport processes, intra-tissue and inter-individual pharmacokinetic variability and inter-individual variability in response to PDT treatment. New strategies to reduce the inter-individual variation have been proposed.

The pharmacokinetics of the photosensitizer verteporfin (photoactive agent BPD-MA in a lipid formulation) has been studied in rat Dunning MAT-LyLu prostate tumor model inoculated in orthotopic and subcutaneous sites. It was shown that MAT-LyLu tumors grown at the orthotopic site exhibited 66% higher photosensitizer uptake early on after verteporfin i.v. injection, but this difference become less pronounced after several hours. The tumor microenvironment study showed that orthotopic tumors present with a 16.4% higher vessel density, 13.3% smaller vessel size and 100% lower VEGF expression level. Subcutaneous

tumors present 60.8% higher percentage of hypoxic fraction. Photosensitizer transport parameters, such as vascular permeability and interstitial diffusion coefficient were found to be 50% and 80% higher in orthotopic tumors. We concluded that the higher photosensitizer uptake in orthotopic tumors was due to these higher transport rates observed in these tumors, *i.e.*, higher vessel density, larger exchange area, higher permeability and higher interstitial diffusion rate. These values of transport parameters are increased partly due to the higher expression of VEGF in orthotopic tumors. Tumor necrosis areas were analyzed to assess tumor response to PDT treatment and a significantly one fold higher percentage of necrosis area was found in the orthotopic tumors in response to cellular targeting PDT treatment. This was explained by the higher hypoxia fractions observed in subcutaneous tumors, limiting the photodynamic damage.

This initial comparison between the two tumor types did not provide us with information about which transport parameter was dominant for photosensitizer tumor uptake, and how the inter-individual photosensitizer pharmacokinetic variability occurs. In Chapter 5, two mathematical models were presented to characterize the microscopic transport processes, transvascular transport and interstitial diffusion. The correlation between these microscopic transport parameters and photosensitizer tumor uptake was then analyzed. The inter-individual variability in plasma pharmacokinetics was demonstrated in Chapter 5, where it was found there was about 20-25% variation in parameter A , B , $\tau_{\alpha\frac{1}{2}}$ and $\tau_{\beta\frac{1}{2}}$ extracted from individual plasma concentration dynamics based on a two-compartment

model. Microscopic transvascular transport and interstitial transport model were developed based on the tumor microvasculature geometries obtained from histology images. Using a co-staining technique, photosensitizer fluorescence images of tumor tissues were partitioned into intravascular compartment and extravascular compartment. The mean fluorescence intensity in intravascular compartment were found highly heterogeneous at subcutaneous inoculation sites (CV% = 22%), possibly due to the heterogeneous blood flow in subcutaneous tumors. The extravascular compartment showed a significantly 38% lower mean fluorescence intensity as compared to the intravascular compartment at both tumor inoculation sites, 15 min after verteporfin injection. A 18% higher mean extravascular fluorescence intensity was found in orthotopic tumors, which can be explained by the higher transvascular permeability calculated in orthotopic tumors. Photosensitizer fluorescence intensity in the extravascular compartment was then plotted as a function of distance from the capillary wall. Significant variation were found among individual tumors and different regions within a tumor. This is because of the heterogeneous interstitial diffusion processes during the photosensitizer delivery to the tumor cells. Using a two-dimensional finite element model, effective interstitial diffusion coefficient was calculated for different tumors and multiple regions within a tumor. Subcutaneous tumors exhibit a lower and less variable diffusion coefficient as compared to orthotopic tumors. The effects of transport parameters such as, tumor vasculature architecture, transvascular permeability and interstitial diffusion coefficient on photosensitizer tumor uptake were studied once these transport parameters have been quantified. A strong correlation between total vascular volume and verteporfin

tumor uptake at 15 min was found in both tumor inoculation sites ($R^2 = 64.1\%$, $p < 0.001$ for subcutaneous tumors, and $R^2 = 63.6\%$, $p < 0.001$ for orthotopic tumors). Transvascular permeability and interstitial diffusion coefficient seemed to have less effect on the verteporfin tumor uptake at this time point ($p > 0.05$). However, for a longer drug-light interval *e.g.* 3 h, verteporfin tumor uptake is determined by the total photosensitizer molecules in extravascular compartment, which depends on the transvascular permeability.

Comparisons between different photosensitizer sampling techniques were discussed in Chapter 6. We have shown that the size of the region sampled affect the measurement histogram of the photosensitizer fluorescence intensity values, but does not affect the mean value. As the region sampled is increased to larger than the inter-vascular distance, the histogram tends to become narrower, and loses the lowest and highest values of the histogram, because of the averaging effect in a larger sampling area. A 100 μm periphery ring with average 2 fold higher fluorescence intensity was observed using a higher magnification objective microscope analyzing the frozen tissue samples. This mesoscopic variation is an important issue for non-invasive sampling of tumor tissue, since these measurements are taken from the surface of the tumor and this sampling region is biased towards higher values than the mean intensity of the whole tumor. The interpretation of the size scale of heterogeneity and validations of non-invasive quantification of photosensitizer fluorescence using the Aurora fluorometer were also discussed.

Once these microscopic transport models have been developed, and the correlation be-

tween these microscopic transport parameters and microscopic photosensitizer tumor uptake were established, our next objective was to understand the relationship between photosensitizer intra-tumor variability and inter-individual variability, as well as the relationship between individual pharmacokinetics and PDT treatment efficacy. In Chapter 7, it was shown that inter-individual variation in verteporfin tumor uptake at 3 h after i.v. injection is related to intra-tumor variation ($R^2 = 44.3\%$, $p < 0.05$). This implies that variation in microscopic transport processes may be related to the spatial heterogeneity of photosensitizer intra-tumor distribution, and possibly lead to inter-individual variation in verteporfin tumor uptake. The correlation study of verteporfin tumor uptake at 3 h and cellular PDT treatment response indicates the variation observed in response to treatment is caused by the inter-individual variation in photosensitizer tumor uptake ($R^2 = 44\%$, $p < 0.05$). Thus, a connection chain has been established from the microscopic transport to intra-, inter-individual photosensitizer uptake and to the effectiveness of cellular PDT treatment. On the other hand, inter-individual variation in verteporfin tumor uptake at 15 min after injection seems to not relate to the intra-tumor variation, and rather the effectiveness of vascular targeting PDT correlates to the verteporfin plasma concentration ($R^2 = 46\%$, $p < 0.05$). This implies that different photosensitizer monitoring techniques should be utilized in vascular and cellular targeting PDT, and should be applied in a manner where they sample the pertinent fraction of the tissue to be targeted.

Observations in Chapter 5 and 7 implies that inter-individual variability in observed in

cellular targeting PDT may be caused by the heterogeneity in drug transport process. Using mathematical models, we have concluded that the dominant transport parameter affecting the tumor uptake at 3 h post verteporfin administration is transvascular permeability. Thus it was hypothesized that modulating the microscopic transvascular transport process might enhance the verteporfin tumor uptake, thereby reducing the inter-individual variability and reducing the variation in response to cellular targeting PDT. Effects of a neurogenic inflammatory mediator, Substance P, on verteporfin transvascular transport, tumor uptake and PDT efficacy have been investigated. Verteporfin plasma pharmacokinetics were not affected by the intra-tumor application of Substance P. A 40% increase in microscopic vascular permeability was found after SP treatment. This is accompanied with an average 5-fold increase of blood flow in the tumor. This increase of blood flow is transient and it relaxes back to the normal level 5 min after SP application. Pre-treatment with SP reduced the inter-individual variation in verteporfin tumor uptake by 40% , and the variation in response to cellular targeting PDT by 50%.

Another strategy to reduce the inter-individual variability in response to cellular targeting PDT is through photosensitizer dosimetry controlled PDT treatment planning. The rationale of this comes from the classic photodynamic dose theory, that biological response to PDT is correlated to the number of photons absorbed by the photosensitizer molecules in the target tissue. The inter-individual variation in photosensitizer uptake can therefore be compensated by adjusting the delivered total light dose to the tumor controlled by the dose

calculation based on photosensitizer quantification in the targeting tissue. The photosensitizer tumor uptake was measured non-invasively using the Aurora fluorometer system, and based on these measurements, the light dose was adjusted. The tumor regrowth rates becomes less variable between subjects in the same treatment group with individualized PDT light treatment compared to the non-controlled PDT treatment. The inter-individual variation in response to PDT can be reduced from 25% in non-controlled PDT treatment compared to 15% in dosimetry-controlled PDT treatment.

This thesis address the inter-individual photosensitizer pharmacokinetic variability problems in PDT treatment, provided insightful information about verteporfin pharmacokinetics in a rat prostate tumor model. The origins of this pharmacokinetic variability and its effects on tumor response to PDT treatment have been presented. This thesis provided novel strategies to reduce the inter-individual pharmacokinetic variability and treatment effectiveness for the clinical PDT trials.

Bibliography

- [1] T. J. Dougherty. Photodynamic therapy. *Photochem Photobiol*, 58(6):895–900, Dec 1993.
- [2] T. J. Dougherty, C. J. Gomer, B. W. Henderson, G. Jori, D. Kessel, M. Korbelik, J. Moan, and Q. Peng. Photodynamic therapy. *J Natl Cancer Inst*, 90(12):889–905, 1998.
- [3] J. S. McCaughan. Photodynamic therapy: a review. *Drugs Aging*, 15(1):49–68, Jul 1999.
- [4] T. J. Dougherty. A brief history of clinical photodynamic therapy development at Roswell Park Cancer Institute. *J Clin Laser Med Surg*, 14(5):219–221, Oct 1996.
- [5] T. J. Dougherty. Hematoporphyrin as a photosensitizer of tumors. *Photochem Photobiol*, 38(3):377–379, Sep 1983.
- [6] T. J. Dougherty, W. R. Potter, and K. R. Weishaupt. The structure of the active component of hematoporphyrin derivative. *Prog Clin Biol Res*, 170:301–314, 1984.

- [7] D. A. Bellnier and T. J. Dougherty. A preliminary pharmacokinetic study of intravenous Photofrin in patients. *J Clin Laser Med Surg*, 14(5):311–314, Oct 1996.
- [8] K. Berg, P. K. Selbo, A. Weyergang, A. Dietze, L. Prasmickaite, A. Bonsted, B. . Engesaeter, E. Angell-Petersen, T. Warloe, N. Frandsen, and A. Hgset. Porphyrin-related photosensitizers for cancer imaging and therapeutic applications. *J Microsc*, 218(Pt 2):133–147, May 2005.
- [9] Q. Peng, K. Berg, J. Moan, M. Kongshaug, and J. M. Nesland. 5-Aminolevulinic acid-based photodynamic therapy: principles and experimental research. *Photochem Photobiol*, 65(2):235–251, Feb 1997.
- [10] J. C. Kennedy, R. H. Pottier, and D. C. Pross. Photodynamic therapy with endogenous protoporphyrin IX: basic principles and present clinical experience. *J Photochem Photobiol B*, 6(1-2):143–148, Jun 1990.
- [11] M. R. Detty, S. L. Gibson, and S. J. Wagner. Current clinical and preclinical photosensitizers for use in photodynamic therapy. *J Med Chem*, 47(16):3897–915, 2004.
- [12] V. C. Colussi, D. K. Feyes, J. W. Mulvihill, Y. S. Li, M. E. Kenney, C. A. Elmets, N. L. Oleinick, and H. Mukhtar. Phthalocyanine 4 (Pc 4) photodynamic therapy of human OVCAR-3 tumor xenografts. *Photochem Photobiol*, 69(2):236–241, Feb 1999.
- [13] G. A. Kostenich, I. N. Zhuravkin, and E. A. Zhavrid. Experimental grounds for

- using chlorin e6 in the photodynamic therapy of malignant tumors. *J Photochem Photobiol B*, 22(3):211–217, Mar 1994.
- [14] Ehud Rechtman, Thomas A Ciulla, Mark H Criswell, Ayala Pollack, and Alon Harris. An update on photodynamic therapy in age-related macular degeneration. *Expert Opin Pharmacother*, 3(7):931–938, Jul 2002.
- [15] Susan J Keam, Lesley J Scott, and Monique P Curran. Verteporfin : a review of its use in the management of subfoveal choroidal neovascularisation. *Drugs*, 63(22):2521–2554, 2003.
- [16] V. A. Miller, P. Ruukonen, M. Schellenbeck, C. Hartmann, and M. Tetz. Treatment of rubeosis iridis with photodynamic therapy with verteporfin—A new therapeutic and prophylactic option for patients with the risk of neovascular glaucoma? *Ophthalmic Res*, 35(1):60–64, 2003.
- [17] Robert A Weersink, Jason Forbes, Stuart Bisland, John Trachtenberg, Mostafa Elhiali, Pierre H Brun, and Brian C Wilson. Assessment of cutaneous photosensitivity of TOOKAD (WST09) in preclinical animal models and in patients. *Photochem Photobiol*, 81(1):106–113, 2005.
- [18] Zheng Huang, Qun Chen, Nadira Trncic, Susan M LaRue, Pierre-Herv Brun, Brian C Wilson, Howard Shapiro, and Fred W Hetzel. Effects of Pd-

- bacteriopheophorbide (TOOKAD)-mediated photodynamic therapy on canine prostate pretreated with ionizing radiation. *Radiat Res*, 161(6):723–731, Jun 2004.
- [19] Shimon Gross, Assaf Gilead, Avigdor Scherz, Michal Neeman, and Yoram Salomon. Monitoring photodynamic therapy of solid tumors online by BOLD-contrast MRI. *Nat Med*, 9(10):1327–1331, Oct 2003.
- [20] Vicki Plaks, Natalia Koudinova, Uri Nevo, Jehonathan H Pinthus, Hannah Kanety, Zelig Eshhar, Jacob Ramon, Avigdor Scherz, Michal Neeman, and Yoram Salomon. Photodynamic therapy of established prostatic adenocarcinoma with TOOKAD: a biphasic apparent diffusion coefficient change as potential early MRI response marker. *Neoplasia*, 6(3):224–233, 2004.
- [21] Natalia V Koudinova, Jehonathan H Pinthus, Alexander Brandis, Ori Brenner, Peter Bendel, Jacob Ramon, Zelig Eshhar, Avigdor Scherz, and Yoram Salomon. Photodynamic therapy with Pd-Bacteriopheophorbide (TOOKAD): successful in vivo treatment of human prostatic small cell carcinoma xenografts. *Int J Cancer*, 104(6):782–789, May 2003.
- [22] Josephine H Woodhams, Alexander J MacRobert, Marco Novelli, and Stephen G Bown. Photodynamic therapy with WST09 (Tookad): quantitative studies in normal colon and transplanted tumours. *Int J Cancer*, 118(2):477–482, Jan 2006.
- [23] Qun Chen, Zheng Huang, David Luck, Jill Beckers, Pierre-Herve Brun, Brian C

- Wilson, Avigdor Scherz, Yoram Salomon, and Fred W Hetzel. Preclinical studies in normal canine prostate of a novel palladium-bacteriopheophorbide (WST09) photosensitizer for photodynamic therapy of prostate cancers. *Photochem Photobiol*, 76(4):438–445, Oct 2002.
- [24] J. S. Dysart, G. Singh, and M. S. Patterson. Calculation of singlet oxygen dose from photosensitizer fluorescence and photobleaching during mTHPC photodynamic therapy of MLL cells. *Photochem Photobiol*, 81(1):196–205, 2005.
- [25] I. P. van Geel, H. Oppelaar, J. P. Marijnissen, and F. A. Stewart. Influence of fractionation and fluence rate in photodynamic therapy with Photofrin or mTHPC. *Radiat Res*, 145(5):602–9, 1996.
- [26] K. F. Fan, C. Hopper, P. M. Speight, G. A. Buonaccorsi, and S. G. Bown. Photodynamic therapy using mTHPC for malignant disease in the oral cavity. *Int J Cancer*, 73(1):25–32, Sep 1997.
- [27] J. S. Dysart, M. S. Patterson, T. J. Farrell, and G. Singh. Relationship between mTHPC fluorescence photobleaching and cell viability during in vitro photodynamic treatment of DP16 cells. *Photochem Photobiol*, 75(3):289–95, 2002.
- [28] S. A. Blant, T. M. Glanzmann, J. P. Ballini, G. Wagnieres, H. van den Bergh, and P. Monnier. Uptake and localisation of mTHPC (Foscan) and its ¹⁴C-labelled form

- in normal and tumour tissues of the hamster squamous cell carcinoma model: a comparative study. *Br J Cancer*, 87(12):1470–8, 2002.
- [29] Bin Chen, Brian W Pogue, and Tayyaba Hasan. Liposomal delivery of photosensitising agents. *Expert Opin Drug Deliv*, 2(3):477–487, May 2005.
- [30] Guolin Li, Adam Slansky, Mahabeer P Dobhal, Lalit N Goswami, Andrew Graham, Yihui Chen, Peter Kanter, Ronald A Alberico, Joseph Spornyak, Janet Morgan, Richard Mazurchuk, Allan Oseroff, Zachary Grossman, and Ravindra K Pandey. Chlorophyll-a analogues conjugated with aminobenzyl-DTPA as potential bifunctional agents for magnetic resonance imaging and photodynamic therapy. *Bioconjug Chem*, 16(1):32–42, 2005.
- [31] D. A. Bellnier, B. W. Henderson, R. K. Pandey, W. R. Potter, and T. J. Dougherty. Murine pharmacokinetics and antitumor efficacy of the photodynamic sensitizer 2-[1-hexyloxyethyl]-2-devinyl pyropheophorbide-a. *J Photochem Photobiol B*, 20(1):55–61, Sep 1993.
- [32] D. L. McCaw, E. R. Pope, J. T. Payne, M. K. West, R. V. Tompson, and D. Tate. Treatment of canine oral squamous cell carcinomas with photodynamic therapy. *Br J Cancer*, 82(7):1297–1299, Apr 2000.
- [33] Mukund Seshadri, Joseph A Spornyak, Richard Mazurchuk, Susan H Camacho, Allan R Oseroff, Richard T Cheney, and David A Bellnier. Tumor vascular response to

- photodynamic therapy and the antivascular agent 5,6-dimethylxanthenone-4-acetic acid: implications for combination therapy. *Clin Cancer Res*, 11(11):4241–4250, Jun 2005.
- [34] Timothy C Zhu, Jarod C Finlay, and Stephen M Hahn. Determination of the distribution of light, optical properties, drug concentration, and tissue oxygenation in-vivo in human prostate during motexafin lutetium-mediated photodynamic therapy. *J Photochem Photobiol B*, 79(3):231–241, Jun 2005.
- [35] M. Zellweger, A. Radu, P. Monnier, H. van den Bergh, and G. Wagnires. Fluorescence pharmacokinetics of Lutetium Texaphyrin (PCI-0123, Lu-TeX) in the skin and in healthy and tumoral hamster cheek-pouch mucosa. *J Photochem Photobiol B*, 55(1):56–62, Mar 2000.
- [36] A. Dimofte, T. C. Zhu, S. M. Hahn, and R. A. Lustig. In vivo light dosimetry for motexafin lutetium-mediated PDT of recurrent breast cancer. *Lasers Surg Med*, 31(5):305–12, 2002.
- [37] Timothy C Zhu, Stephen M Hahn, Amy S Kapatkin, Andreea Dimofte, Carmen E Rodriguez, Teodor G Vulcan, Eli Glatstein, and R. Alex Hsi. In vivo optical properties of normal canine prostate at 732 nm using motexafin lutetium-mediated photodynamic therapy. *Photochem Photobiol*, 77(1):81–88, Jan 2003.
- [38] Michael Solonenko, Rex Cheung, Theresa M Busch, Alex Kachur, Gregory M Grif-

- fin, Theodore Vulcan, Timothy C Zhu, Hsing-Wen Wang, Stephen M Hahn, and A. G. Yodh. In vivo reflectance measurement of optical properties, blood oxygenation and motexafin lutetium uptake in canine large bowels, kidneys and prostates. *Phys Med Biol*, 47(6):857–873, Mar 2002.
- [39] S. W. Young, K. W. Woodburn, M. Wright, T. D. Mody, Q. Fan, J. L. Sessler, W. C. Dow, and R. A. Miller. Lutetium texaphyrin (PCI-0123): a near-infrared, water-soluble photosensitizer. *Photochem Photobiol*, 63(6):892–897, Jun 1996.
- [40] M. J. Hammer-Wilson, M. Ghahramanlou, and M. W. Berns. Photodynamic activity of lutetium-texaphyrin in a mouse tumor system. *Lasers Surg Med*, 24(4):276–284, 1999.
- [41] R. A. Hsi, A. Kapatkin, J. Strandberg, T. Zhu, T. Vulcan, M. Solonenko, C. Rodriguez, J. Chang, M. Saunders, N. Mason, and S. Hahn. Photodynamic therapy in the canine prostate using motexafin lutetium. *Clin Cancer Res*, 7(3):651–660, Mar 2001.
- [42] K. W. Woodburn, Q. Fan, D. Kessel, Y. Luo, and S. W. Young. Photodynamic therapy of B16F10 murine melanoma with lutetium texaphyrin. *J Invest Dermatol*, 110(5):746–751, May 1998.
- [43] G. M. Griffin, T. Zhu, M. Solonenko, F. Del Piero, A. Kapakin, T. M. Busch, A. Yodh, G. Polin, T. Bauer, D. Fraker, and S. M. Hahn. Preclinical evaluation

- of motexafin lutetium-mediated intraperitoneal photodynamic therapy in a canine model. *Clin Cancer Res*, 7(2):374–381, Feb 2001.
- [44] J. L. Sessler and R. A. Miller. Texaphyrins: new drugs with diverse clinical applications in radiation and photodynamic therapy. *Biochem Pharmacol*, 59(7):733–739, Apr 2000.
- [45] W. M. Sharman, C. M. Allen, and J. E. van Lier. Photodynamic therapeutics: basic principles and clinical applications. *Drug Discov Today*, 4(11):507–517, 1999.
- [46] A. M. Fisher, A. L. Murphree, and C. J. Gomer. Clinical and preclinical photodynamic therapy. *Lasers Surg Med*, 17(1):2–31, 1995.
- [47] M. Gze, P. Morlire, J. C. Mazire, K. M. Smith, and R. Santus. Lysosomes, a key target of hydrophobic photosensitizers proposed for photochemotherapeutic applications. *J Photochem Photobiol B*, 20(1):23–35, Sep 1993.
- [48] K. Berg and J. Moan. Lysosomes as photochemical targets. *Int J Cancer*, 59(6):814–822, Dec 1994.
- [49] K. Berg and J. Moan. Lysosomes and microtubules as targets for photochemotherapy of cancer. *Photochem Photobiol*, 65(3):403–409, Mar 1997.
- [50] J. Moan, K. Berg, H. Anholt, and K. Madslie. Sulfonated aluminium phthalocyanines as sensitizers for photochemotherapy. Effects of small light doses on localiza-

- tion, dye fluorescence and photosensitivity in v79 cells. *Int J Cancer*, 58(6):865–70, 1994.
- [51] D. H. Ausprunk and J. Folkman. Migration and proliferation of endothelial cells in preformed and newly formed blood vessels during tumor angiogenesis. *Microvasc Res*, 14(1):53–65, Jul 1977.
- [52] J. Folkman. How is blood vessel growth regulated in normal and neoplastic tissue? G.H.A. Clowes memorial Award lecture. *Cancer Res*, 46(2):467–473, Feb 1986.
- [53] P. Hahnfeldt, D. Panigrahy, J. Folkman, and L. Hlatky. Tumor development under angiogenic signaling: a dynamical theory of tumor growth, treatment response, and postvascular dormancy. *Cancer Res*, 59(19):4770–4775, Oct 1999.
- [54] W. M. Star, H. P. Marijnissen, A. E. van den Berg-Blok, J. A. Versteeg, K. A. Franken, and H. S. Reinhold. Destruction of rat mammary tumor and normal tissue microcirculation by hematoporphyrin derivative photoradiation observed in vivo in sandwich observation chambers. *Cancer Res*, 46(5):2532–2540, May 1986.
- [55] V. H. Fingar, T. J. Wieman, and P. S. Haydon. The effects of thrombocytopenia on vessel stasis and macromolecular leakage after photodynamic therapy using photofrin. *Photochem Photobiol*, 66(4):513–517, Oct 1997.
- [56] V. H. Fingar, P. K. Kik, P. S. Haydon, P. B. Cerrito, M. Tseng, E. Abang, and T. J.

- Wieman. Analysis of acute vascular damage after photodynamic therapy using benzoporphyrin derivative (BPD). *Br J Cancer*, 79(11-12):1702–1708, Apr 1999.
- [57] B. W. Henderson and V. H. Fingar. Relationship of tumor hypoxia and response to photodynamic treatment in an experimental mouse tumor. *Cancer Res*, 47(12):3110–3114, Jun 1987.
- [58] Q. Chen, H. Chen, and F. W. Hetzel. Tumor oxygenation changes post-photodynamic therapy. *Photochem Photobiol*, 63(1):128–31, 1996.
- [59] Theresa M Busch, E. Paul Wileyto, Micheal J Emanuele, Fabio Del Piero, Laura Marconato, Eli Glatstein, and Cameron J Koch. Photodynamic therapy creates fluence rate-dependent gradients in the intratumoral spatial distribution of oxygen. *Cancer Res*, 62(24):7273–7279, Dec 2002.
- [60] B. W. Henderson and V. H. Fingar. Oxygen limitation of direct tumor cell kill during photodynamic treatment of a murine tumor model. *Photochem Photobiol*, 49(3):299–304, 1989.
- [61] V. H. Fingar, T. J. Wieman, S. A. Wiehle, and P. B. Cerrito. The role of microvascular damage in photodynamic therapy: the effect of treatment on vessel constriction, permeability, and leukocyte adhesion. *Cancer Res*, 52(18):4914–21, 1992.
- [62] D. E. Dolmans, A. Kadambi, J. S. Hill, C. A. Waters, B. C. Robinson, J. P. Walker, D. Fukumura, and R. K. Jain. Vascular accumulation of a novel photosensitizer,

- MV6401, causes selective thrombosis in tumor vessels after photodynamic therapy. *Cancer Res*, 62(7):2151–6, 2002.
- [63] M. Korbelik. Induction of tumor immunity by photodynamic therapy. *J Clin Laser Med Surg*, 14(5):329–334, Oct 1996.
- [64] Y. Merhi, R. Guidoin, P. Provost, T. K. Leung, and J. Y. Lam. Increase of neutrophil adhesion and vasoconstriction with platelet deposition after deep arterial injury by angioplasty. *Am Heart J*, 129(3):445–451, Mar 1995.
- [65] K. Chaudhuri, R. W. Keck, and S. H. Selman. Morphological changes of tumor microvasculature following hematoporphyrin derivative sensitized photodynamic therapy. *Photochem Photobiol*, 46(5):823–827, Nov 1987.
- [66] P. M. Steele, J. H. Chesebro, A. W. Stanson, D. R. Holmes, M. K. Dewanjee, L. Badimon, and V. Fuster. Balloon angioplasty. Natural history of the pathophysiological response to injury in a pig model. *Circ Res*, 57(1):105–112, Jul 1985.
- [67] V. H. Fingar, K. A. Siegel, T. J. Wieman, and K. W. Doak. The effects of thromboxane inhibitors on the microvascular and tumor response to photodynamic therapy. *Photochem Photobiol*, 58(3):393–399, Sep 1993.
- [68] V. H. Fingar, T. J. Wieman, P. S. Karavolos, K. W. Doak, R. Ouellet, and J. E. van Lier. The effects of photodynamic therapy using differently substituted zinc ph-

- thiocyanines on vessel constriction, vessel leakage and tumor response. *Photochem Photobiol*, 58(2):251–258, Aug 1993.
- [69] K. S. McMahon, T. J. Wieman, P. H. Moore, and V. H. Fingar. Effects of photodynamic therapy using mono-L-aspartyl chlorin e6 on vessel constriction, vessel leakage, and tumor response. *Cancer Res*, 54(20):5374–5379, Oct 1994.
- [70] C. J. Gomer, M. Luna, A. Ferrario, S. Wong, A. M. Fisher, and N. Rucker. Cellular targets and molecular responses associated with photodynamic therapy. *J Clin Laser Med Surg*, 14(5):315–321, Oct 1996.
- [71] M. Ochsner. Photophysical and photobiological processes in the photodynamic therapy of tumours. *J Photochem Photobiol B*, 39(1):1–18, 1997.
- [72] V. H. Fingar. Vascular effects of photodynamic therapy. *J Clin Laser Med Surg*, 14(5):323–8, 1996.
- [73] S. O. Gollnick, X. Liu, B. Owczarczak, D. A. Musser, and B. W. Henderson. Altered expression of interleukin 6 and interleukin 10 as a result of photodynamic therapy in vivo. *Cancer Res*, 57(18):3904–3909, Sep 1997.
- [74] G. Krosli, M. Korbelik, and G. J. Dougherty. Induction of immune cell infiltration into murine SCCVII tumour by photofrin-based photodynamic therapy. *Br J Cancer*, 71(3):549–555, Mar 1995.

- [75] S. Evans, W. Matthews, R. Perry, D. Fraker, J. Norton, and H. I. Pass. Effect of photodynamic therapy on tumor necrosis factor production by murine macrophages. *J Natl Cancer Inst*, 82(1):34–39, Jan 1990.
- [76] M. Korbelik, G. Krosi, J. Krosi, and G. J. Dougherty. The role of host lymphoid populations in the response of mouse EMT6 tumor to photodynamic therapy. *Cancer Res*, 56(24):5647–5652, Dec 1996.
- [77] C. Hopper. Photodynamic therapy: a clinical reality in the treatment of cancer. *Lancet Oncol*, 1:212–9, 2000.
- [78] B. F. Overholt, M. Panjehpour, and J. M. Haydek. Photodynamic therapy for Barrett’s esophagus: follow-up in 100 patients. *Gastrointest Endosc*, 49(1):1–7, Jan 1999.
- [79] U. O. Nseyo, B. Shumaker, E. A. Klein, and K. Sutherland. Photodynamic therapy using porfimer sodium as an alternative to cystectomy in patients with refractory transitional cell carcinoma in situ of the bladder. Bladder Photofrin Study Group. *J Urol*, 160(1):39–44, Jul 1998.
- [80] T. Uchibayashi, K. Koshida, K. Kunimi, and H. Hisazumi. Whole bladder wall photodynamic therapy for refractory carcinoma in situ of the bladder. *Br J Cancer*, 71(3):625–628, Mar 1995.
- [81] B. D. Wilson, T. S. Mang, H. Stoll, C. Jones, M. Cooper, and T. J. Dougherty.

- Photodynamic therapy for the treatment of basal cell carcinoma. *Arch Dermatol*, 128(12):1597–1601, Dec 1992.
- [82] F. Cairnduff, M. R. Stringer, E. J. Hudson, D. V. Ash, and S. B. Brown. Superficial photodynamic therapy with topical 5-aminolaevulinic acid for superficial primary and secondary skin cancer. *Br J Cancer*, 69(3):605–608, Mar 1994.
- [83] P. W. Sperduto, T. F. DeLaney, G. Thomas, P. Smith, L. J. Dachowski, A. Russo, R. Bonner, and E. Glatstein. Photodynamic therapy for chest wall recurrence in breast cancer. *Int J Radiat Oncol Biol Phys*, 21(2):441–446, Jul 1991.
- [84] J. L. Gluckman. Hematoporphyrin photodynamic therapy: is there truly a future in head and neck oncology? Reflections on a 5-year experience. *Laryngoscope*, 101(1 Pt 1):36–42, Jan 1991.
- [85] H. Takita and T. J. Dougherty. Intracavitary photodynamic therapy for malignant pleural mesothelioma. *Semin Surg Oncol*, 11(5):368–371, 1995.
- [86] C. P. Lowdell, D. V. Ash, I. Driver, and S. B. Brown. Interstitial photodynamic therapy. Clinical experience with diffusing fibres in the treatment of cutaneous and subcutaneous tumours. *Br J Cancer*, 67(6):1398–1403, Jun 1993.
- [87] J. A. Carruth. Clinical applications of photodynamic therapy. *Int J Clin Pract*, 52(1):39–42, 1998.

- [88] T. M. Busch, S. M. Hahn, E. P. Wileyto, C. J. Koch, D. L. Fraker, P. Zhang, M. Putt, K. Gleason, D. B. Shin, M. J. Emanuele, K. Jenkins, E. Glatstein, and S. M. Evans. Hypoxia and Photofrin uptake in the intraperitoneal carcinomatosis and sarcomatosis of photodynamic therapy patients. *Clin Cancer Res*, 10(14):4630–8, 2004.
- [89] F. Stewart, P. Baas, and W. Star. What does photodynamic therapy have to offer radiation oncologists (or their cancer patients)? *Radiother Oncol*, 48(3):233–48, 1998.
- [90] D. E. Dolmans, D. Fukumura, and R. K. Jain. Photodynamic therapy for cancer. *Nat Rev Cancer*, 3(5):380–7, 2003.
- [91] A. S. Derycke and P. A. de Witte. Liposomes for photodynamic therapy. *Adv Drug Deliv Rev*, 56(1):17–30, 2004.
- [92] E. Reddi. Role of delivery vehicles for photosensitizers in the photodynamic therapy of tumours. *J Photochem Photobiol B*, 37(3):189–95, 1997.
- [93] D. C. Drummond, O. Meyer, K. Hong, D. B. Kirpotin, and D. Papahadjopoulos. Optimizing liposomes for delivery of chemotherapeutic agents to solid tumors. *Pharmacol Rev*, 51(4):691–743, 1999.
- [94] Vladimir P Torchilin. Recent advances with liposomes as pharmaceutical carriers. *Nat Rev Drug Discov*, 4(2):145–160, Feb 2005.
- [95] V. P. Torchilin. Drug targeting. *Eur J Pharm Sci*, 11 Suppl 2:S81–S91, Oct 2000.

- [96] H. Maeda. The enhanced permeability and retention (EPR) effect in tumor vasculature: the key role of tumor-selective macromolecular drug targeting. *Adv Enzyme Regul*, 41:189–207, 2001.
- [97] H. Maeda, J. Fang, T. Inutsuka, and Y. Kitamoto. Vascular permeability enhancement in solid tumor: various factors, mechanisms involved and its implications. *Int Immunopharmacol*, 3(3):319–28, 2003.
- [98] T. Tanaka, S. Shiramoto, M. Miyashita, Y. Fujishima, and Y. Kaneo. Tumor targeting based on the effect of enhanced permeability and retention (EPR) and the mechanism of receptor-mediated endocytosis (RME). *Int J Pharm*, 277(1-2):39–61, 2004.
- [99] H. M. Patel. Serum opsonins and liposomes: their interaction and opsonophagocytosis. *Crit Rev Ther Drug Carrier Syst*, 9(1):39–90, 1992.
- [100] A. Nagayasu, K. Uchiyama, and H. Kiwada. The size of liposomes: a factor which affects their targeting efficiency to tumors and therapeutic activity of liposomal anti-tumor drugs. *Adv Drug Deliv Rev*, 40(1-2):75–87, 1999.
- [101] D. D. Lasic, F. J. Martin, A. Gabizon, S. K. Huang, and D. Papahadjopoulos. Sterically stabilized liposomes: a hypothesis on the molecular origin of the extended circulation times. *Biochim Biophys Acta*, 1070(1):187–192, Nov 1991.
- [102] D. Needham, T. J. McIntosh, and D. D. Lasic. Repulsive interactions and mechanical

- stability of polymer-grafted lipid membranes. *Biochim Biophys Acta*, 1108(1):40–48, Jul 1992.
- [103] Antoon Gijssens, Annelies Derycke, Ludwig Missiaen, Dirk De Vos, Jrg Huwyler, Alex Eberle, and Peter de Witte. Targeting of the photocytotoxic compound AlPcS4 to Hela cells by transferrin conjugated PEG-liposomes. *Int J Cancer*, 101(1):78–85, Sep 2002.
- [104] N. Oku, N. Saito, Y. Namba, H. Tsukada, D. Dolphin, and S. Okada. Application of long-circulating liposomes to cancer photodynamic therapy. *Biol Pharm Bull*, 20(6):670–673, Jun 1997.
- [105] W. M. Sharman, J. E. van Lier, and C. M. Allen. Targeted photodynamic therapy via receptor mediated delivery systems. *Adv Drug Deliv Rev*, 56(1):53–76, 2004.
- [106] M. S. Foley, A. Beeby, A. W. Parker, S. M. Bishop, and D. Phillips. Excited triplet state photophysics of the sulphonated aluminium phthalocyanines bound to human serum albumin. *J Photochem Photobiol B*, 38(1):10–7, 1997.
- [107] U. Kragh-Hansen. Structure and ligand binding properties of human serum albumin. *Dan Med Bull*, 37(1):57–84, 1990.
- [108] J. C. Maziere, P. Morliere, and R. Santus. The role of the low density lipoprotein receptor pathway in the delivery of lipophilic photosensitizers in the photodynamic therapy of tumours. *J Photochem Photobiol B*, 8(4):351–60, 1991.

- [109] N. Mantel. Evaluation of survival data and two new rank order statistics arising in its consideration. *Cancer Chemother Rep*, 50(3):163–70, 1966.
- [110] D. Kessel. In vitro photosensitization with a benzoporphyrin derivative. *Photochem Photobiol*, 49(5):579–82., 1989.
- [111] A. M. Richter, S. Cerruti-Sola, E. D. Sternberg, D. Dolphin, and J. G. Levy. Biodistribution of tritiated benzoporphyrin derivative (3H-BPD-MA), a new potent photosensitizer, in normal and tumor-bearing mice. *J Photochem Photobiol B*, 5(2):231–44, 1990.
- [112] A. M. Richter, B. Kelly, J. Chow, D. J. Liu, G. H. Towers, D. Dolphin, and J. G. Levy. Preliminary studies on a more effective phototoxic agent than hematoporphyrin. *J Natl Cancer Inst*, 79(6):1327–32, 1987.
- [113] A. M. Richter, E. Waterfield, A. K. Jain, B. Allison, E. D. Sternberg, D. Dolphin, and J. G. Levy. Photosensitising potency of structural analogues of benzoporphyrin derivative (BPD) in a mouse tumour model. *Br J Cancer*, 63(1):87–93, 1991.
- [114] A. M. Richter, E. Waterfield, A. K. Jain, A. J. Canaan, B. A. Allison, and J. G. Levy. Liposomal delivery of a photosensitizer, benzoporphyrin derivative monoacid ring A (BPD), to tumor tissue in a mouse tumor model. *Photochem Photobiol*, 57(6):1000–6., 1993.
- [115] B. M. Aveline, T. Hasan, and R. W. Redmond. The effects of aggregation, pro-

- tein binding and cellular incorporation on the photophysical properties of benzoporphyrin derivative monoacid ring a (BPDMA). *J Photochem Photobiol B*, 30(2-3):161–9, 1995.
- [116] B. A. Allison, P. H. Pritchard, and J. G. Levy. Evidence for low-density lipoprotein receptor-mediated uptake of benzoporphyrin derivative. *Br J Cancer*, 69(5):833–9., 1994.
- [117] B. A. Allison, P. H. Pritchard, A. M. Richter, and J. G. Levy. The plasma distribution of benzoporphyrin derivative and the effects of plasma lipoproteins on its biodistribution. *Photochem Photobiol*, 52(3):501–7., 1990.
- [118] B. A. Allison, E. Waterfield, A. M. Richter, and J. G. Levy. The effects of plasma lipoproteins on in vitro tumor cell killing and in vivo tumor photosensitization with benzoporphyrin derivative. *Photochem Photobiol*, 54(5):709–15, 1991.
- [119] M. Korbely and G. Krosi. Accumulation of benzoporphyrin derivative in malignant and host cell populations of the murine RIF tumor. *Cancer Lett*, 97(2):249–254, Nov 1995.
- [120] S. B. Brown and K. J. Mellish. Verteporfin: a milestone in ophthalmology and photodynamic therapy. *Expert Opin Pharmacother*, 2(2):351–61, 2001.
- [121] S. Gluck, A. Chadderton, and A. D. Ho. The selective uptake of benzoporphyrin

- derivative mono-acid ring A results in differential cell kill of multiple myeloma cells in vitro. *Photochem Photobiol*, 63(6):846–53., 1996.
- [122] M. Panjehpour, R. C. DeNovo, M. G. Petersen, B. F. Overholt, R. Bower, V. Rubinchik, and B. Kelly. Photodynamic therapy using verteporfin (benzoporphyrin derivative monoacid ring A, BPD-MA) and 630 nm laser light in canine esophagus. *Lasers Surg Med*, 30(1):26–30, 2002.
- [123] U. Schmidt-Erfurth, T. J. Flotte, E. S. Gragoudas, K. Schomacker, R. Birngruber, and T. Hasan. Benzoporphyrin-lipoprotein-mediated photodestruction of intraocular tumors. *Exp Eye Res*, 62(1):1–10, Jan 1996.
- [124] L. J. Scott and K. L. Goa. Verteporfin. *Drugs Aging*, 16(2):139–46; discussion 147–8, 2000.
- [125] M. R. Hamblin and E. L. Newman. Photosensitizer targeting in photodynamic therapy. II. conjugates of haematoporphyrin with serum lipoproteins. *J Photochem Photobiol B*, 26(2):147–57, 1994.
- [126] M. R. Hamblin and E. L. Newman. Photosensitizer targeting in photodynamic therapy. I. conjugates of haematoporphyrin with albumin and transferrin. *J Photochem Photobiol B*, 26(1):45–56, 1994.
- [127] C. Larroque, A. Pelegrin, and J. E. Van Lier. Serum albumin as a vehicle for zinc

- phthalocyanine: photodynamic activities in solid tumour models. *Br J Cancer*, 74(12):1886–1890, Dec 1996.
- [128] T. Nagae, A. Y. Louie, K. Aizawa, S. Ishimaru, and S. E. Wilson. Selective targeting and photodynamic destruction of intimal hyperplasia by scavenger-receptor mediated protein-chlorin e6 conjugates. *J Cardiovasc Surg (Torino)*, 39(6):709–715, Dec 1998.
- [129] N. Brasseur, R. Langlois, C. La Madeleine, R. Ouellet, and J. E. van Lier. Receptor-mediated targeting of phthalocyanines to macrophages via covalent coupling to native or maleylated bovine serum albumin. *Photochem Photobiol*, 69(3):345–352, Mar 1999.
- [130] E. Reddi, C. Zhou, R. Biolo, E. Menegaldo, and G. Jori. Liposome- or LDL-administered Zn (II)-phthalocyanine as a photodynamic agent for tumours. I. Pharmacokinetic properties and phototherapeutic efficiency. *Br J Cancer*, 61(3):407–411, Mar 1990.
- [131] Laura Polo, Giuliana Valduga, Giulio Jori, and Elena Reddi. Low-density lipoprotein receptors in the uptake of tumour photosensitizers by human and rat transformed fibroblasts. *Int J Biochem Cell Biol*, 34(1):10–23, Jan 2002.
- [132] U. Schmidt-Erfurth, W. Bauman, E. Gragoudas, T. J. Flotte, N. A. Michaud, R. Birngruber, and T. Hasan. Photodynamic therapy of experimental choroidal melanoma

- using lipoprotein-delivered benzoporphyrin. *Ophthalmology*, 101(1):89–99, Jan 1994.
- [133] U. Schmidt-Erfurth, H. Diddens, R. Birngruber, and T. Hasan. Photodynamic targeting of human retinoblastoma cells using covalent low-density lipoprotein conjugates. *Br J Cancer*, 75(1):54–61, 1997.
- [134] M. R. Hamblin and E. L. Newman. On the mechanism of the tumour-localising effect in photodynamic therapy. *J Photochem Photobiol B*, 23(1):3–8, 1994.
- [135] P. C. de Smidt, A. J. Versluis, and T. J. van Berkel. Transport of sulfonated tetraphenylporphine by lipoproteins in the hamster. *Biochem Pharmacol*, 43(12):2567–2573, Jun 1992.
- [136] H. E. de Vries, A. C. Moor, T. M. Dubbelman, T. J. van Berkel, and J. Kuiper. Oxidized low-density lipoprotein as a delivery system for photosensitizers: implications for photodynamic therapy of atherosclerosis. *J Pharmacol Exp Ther*, 289(1):528–534, Apr 1999.
- [137] Philip G Cavanaugh. Synthesis of chlorin e6-transferrin and demonstration of its light-dependent in vitro breast cancer cell killing ability. *Breast Cancer Res Treat*, 72(2):117–130, Mar 2002.
- [138] R. K. Jain. Delivery of molecular and cellular medicine to solid tumors. *Adv Drug Deliv Rev*, 46(1-3):149–68, 2001.

- [139] R. K. Jain. Transport of molecules, particles, and cells in solid tumors. *Annu Rev Biomed Eng*, 1:241–63, 1999.
- [140] R. K. Jain. Delivery of molecular and cellular medicine to solid tumors. *J Control Release*, 53(1-3):49–67, 1998.
- [141] R. K. Jain. Delivery of molecular and cellular medicine to solid tumors. *Adv Drug Deliv Rev*, 26(2-3):71–90, 1997.
- [142] R. K. Jain. The Eugene M. Landis Award Lecture 1996. Delivery of molecular and cellular medicine to solid tumors. *Microcirculation*, 4(1):1–23, 1997.
- [143] R. K. Jain. Delivery of molecular medicine to solid tumors. *Science*, 271(5252):1079–80, 1996.
- [144] R. K. Jain. 1995 Whitaker Lecture: delivery of molecules, particles, and cells to solid tumors. *Ann Biomed Eng*, 24(4):457–73, 1996.
- [145] R. K. Jain. Barriers to drug delivery in solid tumors. *Sci Am*, 271(1):58–65, 1994.
- [146] R. K. Jain. Physiological barriers to delivery of monoclonal antibodies and other macromolecules in tumors. *Cancer Res*, 50(3 Suppl):814s–819s, 1990.
- [147] R. K. Jain. Vascular and interstitial barriers to delivery of therapeutic agents in tumors. *Cancer Metastasis Rev*, 9(3):253–66, 1990.

- [148] R. K. Jain. Delivery of novel therapeutic agents in tumors: physiological barriers and strategies. *J Natl Cancer Inst*, 81(8):570–6, 1989.
- [149] R. K. Jain, K. D. Janda, and W. M. Saltzman. Drug discovery and delivery. *Mol Med Today*, 1(1):4, 1995.
- [150] R. K. Jain, J. M. Weissbrod, and J. Wei. Mass transport in tumors: characterization and applications to chemotherapy. *Adv Cancer Res*, 33:251–310, 1980.
- [151] O. Arosarena, C. Guerin, H. Brem, and J. Laterra. Endothelial differentiation in intracerebral and subcutaneous experimental gliomas. *Brain Res*, 640(1-2):98–104, 1994.
- [152] D. Fukumura, F. Yuan, W. L. Monsky, Y. Chen, and R. K. Jain. Effect of host microenvironment on the microcirculation of human colon adenocarcinoma. *Am J Pathol*, 151(3):679–88, 1997.
- [153] P. Guo, L. Xu, S. Pan, R. A. Brekken, S. T. Yang, G. B. Whitaker, M. Nagane, P. E. Thorpe, J. S. Rosenbaum, H. J. Su Huang, W. K. Cavenee, and S. Y. Cheng. Vascular endothelial growth factor isoforms display distinct activities in promoting tumor angiogenesis at different anatomic sites. *Cancer Res*, 61(23):8569–77, 2001.
- [154] S. K. Hobbs, W. L. Monsky, F. Yuan, W. G. Roberts, L. Griffith, V. P. Torchilin, and R. K. Jain. Regulation of transport pathways in tumor vessels: role of tumor type and microenvironment. *Proc Natl Acad Sci U S A*, 95(8):4607–12, 1998.

- [155] W. L. Monsky, C. Mouta Carreira, Y. Tsuzuki, T. Gohongi, D. Fukumura, and R. K. Jain. Role of host microenvironment in angiogenesis and microvascular functions in human breast cancer xenografts: mammary fat pad versus cranial tumors. *Clin Cancer Res*, 8(4):1008–13, 2002.
- [156] A. Pluen, Y. Boucher, S. Ramanujan, T. D. McKee, T. Gohongi, E. di Tomaso, E. B. Brown, Y. Izumi, R. B. Campbell, D. A. Berk, and R. K. Jain. Role of tumor-host interactions in interstitial diffusion of macromolecules: cranial vs. subcutaneous tumors. *Proc Natl Acad Sci U S A*, 98(8):4628–33, 2001.
- [157] W. G. Roberts, J. Delaat, M. Nagane, S. Huang, W. K. Cavenee, and G. E. Palade. Host microvasculature influence on tumor vascular morphology and endothelial gene expression. *Am J Pathol*, 153(4):1239–48, 1998.
- [158] Y. Tsuzuki, C. Mouta Carreira, M. Bockhorn, L. Xu, R. K. Jain, and D. Fukumura. Pancreas microenvironment promotes VEGF expression and tumor growth: novel window models for pancreatic tumor angiogenesis and microcirculation. *Lab Invest*, 81(10):1439–51, 2001.
- [159] P. Carmeliet. Mechanisms of angiogenesis and arteriogenesis. *Nat Med*, 6(4):389–95, 2000.
- [160] P. Carmeliet and R. K. Jain. Angiogenesis in cancer and other diseases. *Nature*, 407(6801):249–57, 2000.

- [161] N. Ferrara. VEGF and the quest for tumour angiogenesis factors. *Nat Rev Cancer*, 2(10):795–803, 2002.
- [162] J. Rossant and L. Howard. Signaling pathways in vascular development. *Annu Rev Cell Dev Biol*, 18:541–73, 2002.
- [163] G. D. Yancopoulos, S. Davis, N. W. Gale, J. S. Rudge, S. J. Wiegand, and J. Holash. Vascular-specific growth factors and blood vessel formation. *Nature*, 407(6801):242–8, 2000.
- [164] R. K. Jain. Molecular regulation of vessel maturation. *Nat Med*, 9(6):685–93, 2003.
- [165] J. R. Less, M. C. Posner, T. C. Skalak, N. Wolmark, and R. K. Jain. Geometric resistance and microvascular network architecture of human colorectal carcinoma. *Microcirculation*, 4(1):25–33, 1997.
- [166] J. R. Less, T. C. Skalak, E. M. Sevick, and R. K. Jain. Microvascular network architecture in a mammary carcinoma. *Exs*, 61:74–80, 1992.
- [167] J. R. Less, T. C. Skalak, E. M. Sevick, and R. K. Jain. Microvascular architecture in a mammary carcinoma: branching patterns and vessel dimensions. *Cancer Res*, 51(1):265–73, 1991.
- [168] H. Hashizume, P. Baluk, S. Morikawa, J. W. McLean, G. Thurston, S. Roberge, R. K. Jain, and D. M. McDonald. Openings between defective endothelial cells explain tumor vessel leakiness. *Am J Pathol*, 156(4):1363–80, 2000.

- [169] F. Steinberg, M. A. Konerding, and C. Streffer. The vascular architecture of human xenotransplanted tumors: histological, morphometrical, and ultrastructural studies. *J Cancer Res Clin Oncol*, 116(5):517–24, 1990.
- [170] B. Endrich, H. S. Reinhold, J. F. Gross, and M. Intaglietta. Tissue perfusion inhomogeneity during early tumor growth in rats. *J Natl Cancer Inst*, 62(2):387–395, Feb 1979.
- [171] R. K. Jain. Determinants of tumor blood flow: a review. *Cancer Res*, 48(10):2641–58, 1988.
- [172] D. J. Chaplin, P. L. Olive, and R. E. Durand. Intermittent blood flow in a murine tumor: radiobiological effects. *Cancer Res*, 47(2):597–601, 1987.
- [173] M. J. Trotter, D. J. Chaplin, R. E. Durand, and P. L. Olive. The use of fluorescent probes to identify regions of transient perfusion in murine tumors. *Int J Radiat Oncol Biol Phys*, 16(4):931–4, 1989.
- [174] R. E. Durand. Intermittent blood flow in solid tumours—an under-appreciated source of 'drug resistance'. *Cancer Metastasis Rev*, 20(1-2):57–61, 2001.
- [175] R. E. Durand and C. Aquino-Parsons. Clinical relevance of intermittent tumour blood flow. *Acta Oncol*, 40(8):929–36, 2001.
- [176] R. E. Durand and C. Aquino-Parsons. Non-constant tumour blood flow—implications for therapy. *Acta Oncol*, 40(7):862–9, 2001.

- [177] R. E. Durand and N. E. LePard. Tumour blood flow influences combined radiation and doxorubicin treatments. *Radiother Oncol*, 42(2):171–9, 1997.
- [178] R. E. Durand and N. E. LePard. Contribution of transient blood flow to tumour hypoxia in mice. *Acta Oncol*, 34(3):317–23, 1995.
- [179] R. K. Jain. Transport of molecules across tumor vasculature. *Cancer Metastasis Rev*, 6(4):559–93, 1987.
- [180] O. Kedem and A. Katchalsky. Thermodynamic analysis of the permeability of biological membranes to non-electrolytes. *Biochim Biophys Acta*, 27(2):229–46, 1958.
- [181] O. Kedem and A. Katchalsky. A physical interpretation of the phenomenological coefficients of membrane permeability. *J Gen Physiol*, 45:143–179, Sep 1961.
- [182] A Katchalsky and O Kedem. Thermodynamics of flow processes in biological systems. *Biophys J*, 2(2)Pt2:53–78, Mar 1962.
- [183] C. S. Patlak, D. A. Goldstein, and J. F. Hoffman. The flow of solute and solvent across a two-membrane system. *J Theor Biol*, 5(3):426–442, Nov 1963.
- [184] N. B. Ackerman and P. A. Hechmer. Studies on the capillary permeability of experimental liver metastases. *Surg Gynecol Obstet*, 146(6):884–8, 1978.
- [185] W. C. Dewey. Vascular-extravascular exchange of I131 plasma proteins in the rat. *Am J Physiol*, 197:423–31, 1959.

- [186] N. Z. Wu, B. Klitzman, G. Rosner, D. Needham, and M. W. Dewhirst. Measurement of material extravasation in microvascular networks using fluorescence video-microscopy. *Microvasc Res*, 46(2):231–253, Sep 1993.
- [187] F. Yuan, M. Leunig, D. A. Berk, and R. K. Jain. Microvascular permeability of albumin, vascular surface area, and vascular volume measured in human adenocarcinoma LS174T using dorsal chamber in SCID mice. *Microvasc Res*, 45(3):269–89, 1993.
- [188] J. R. Pappenheimer, E. M. Renkin, and L. M. Borrero. Filtration, diffusion and molecular sieving through peripheral capillary membranes; a contribution to the pore theory of capillary permeability. *Am J Physiol*, 167(1):13–46, 1951.
- [189] B. Rippe and B. Haraldsson. Transport of macromolecules across microvascular walls: the two-pore theory. *Physiol Rev*, 74(1):163–219, 1994.
- [190] G. Grotte. Passage of dextran molecules across the blood-lymph barrier. *Acta Chir Scand*, (Suppl 211):1–84, 1956.
- [191] P. Baluk, A. Hirata, G. Thurston, T. Fujiwara, C. R. Neal, C. C. Michel, and D. M. McDonald. Endothelial gaps: time course of formation and closure in inflamed venules of rats. *Am J Physiol*, 272(1 Pt 1):L155–70, 1997.
- [192] F. Yuan, Y. Chen, M. Dellian, N. Safabakhsh, N. Ferrara, and R. K. Jain. Time-dependent vascular regression and permeability changes in established human tumor

- xenografts induced by an anti-vascular endothelial growth factor/vascular permeability factor antibody. *Proc Natl Acad Sci U S A*, 93(25):14765–70, 1996.
- [193] L. T. Baxter and R. K. Jain. Transport of fluid and macromolecules in tumors. I. Role of interstitial pressure and convection. *Microvasc Res*, 37(1):77–104, 1989.
- [194] L. T. Baxter and R. K. Jain. Transport of fluid and macromolecules in tumors. II. Role of heterogeneous perfusion and lymphatics. *Microvasc Res*, 40(2):246–63, 1990.
- [195] P. L. Debbage, S. Seidl, A. Kreczy, P. Hutzler, M. Pavelka, and P. Lukas. Vascular permeability and hyperpermeability in a murine adenocarcinoma after fractionated radiotherapy: an ultrastructural tracer study. *Histochem Cell Biol*, 114(4):259–75, 2000.
- [196] C. Li, S. Ke, Q. P. Wu, W. Tansey, N. Hunter, L. M. Buchmiller, L. Milas, C. Charnsangavej, and S. Wallace. Tumor irradiation enhances the tumor-specific distribution of poly(l-glutamic acid)-conjugated paclitaxel and its antitumor efficacy. *Clin Cancer Res*, 6(7):2829–34, 2000.
- [197] P. Nejdfor, M. Ekelund, B. R. Westrom, R. Willen, and B. Jeppsson. Intestinal permeability in humans is increased after radiation therapy. *Dis Colon Rectum*, 43(11):1582–1587; discussion 1587–8, 2000.
- [198] J. W. Snyder, W. R. Greco, D. A. Bellnier, L. Vaughan, and B. W. Henderson. Pho-

- odynamic therapy: a means to enhanced drug delivery to tumors. *Cancer Res*, 63(23):8126–31, 2003.
- [199] D. Fukumura, F. Yuan, M. Endo, and R. K. Jain. Role of nitric oxide in tumor microcirculation. Blood flow, vascular permeability, and leukocyte-endothelial interactions. *Am J Pathol*, 150(2):713–25, 1997.
- [200] W. L. Monsky, D. Fukumura, T. Gohongi, M. Ancukiewicz, H. A. Weich, V. P. Torchilin, F. Yuan, and R. K. Jain. Augmentation of transvascular transport of macromolecules and nanoparticles in tumors using vascular endothelial growth factor. *Cancer Res*, 59(16):4129–35, 1999.
- [201] P. A. Netti, L. M. Hamberg, J. W. Babich, D. Kierstead, W. Graham, G. J. Hunter, G. L. Wolf, A. Fischman, Y. Boucher, and R. K. Jain. Enhancement of fluid filtration across tumor vessels: implication for delivery of macromolecules. *Proc Natl Acad Sci U S A*, 96(6):3137–42, 1999.
- [202] R. K. Jain. Transport of molecules in the tumor interstitium: a review. *Cancer Res*, 47(12):3039–51, 1987.
- [203] L. T. Baxter and R. K. Jain. Transport of fluid and macromolecules in tumors. IV. A microscopic model of the perivascular distribution. *Microvasc Res*, 41(2):252–72, 1991.

- [204] L. T. Baxter and R. K. Jain. Transport of fluid and macromolecules in tumors. III. Role of binding and metabolism. *Microvasc Res*, 41(1):5–23, 1991.
- [205] E.L. Cussler. Diffusion: mass transfer in fluid systems. In *Diffusion: mass transfer in fluid systems*. Cambridge University Press, Cambridge, United Kingdom, 1984. Cussler:1984.
- [206] M. A. Clauss and R. K. Jain. Interstitial transport of rabbit and sheep antibodies in normal and neoplastic tissues. *Cancer Res*, 50(12):3487–92, 1990.
- [207] J. R. Fox and H. Wayland. Interstitial diffusion of macromolecules in the rat mesentery. *Microvasc Res*, 18(2):255–76, 1979.
- [208] L. J. Nugent and R. K. Jain. Extravascular diffusion in normal and neoplastic tissues. *Cancer Res*, 44(1):238–44, 1984.
- [209] S. R. Chary and R. K. Jain. Direct measurement of interstitial convection and diffusion of albumin in normal and neoplastic tissues by fluorescence photobleaching. *Proc Natl Acad Sci U S A*, 86(14):5385–9, 1989.
- [210] K. Aukland and R. K. Reed. Interstitial-lymphatic mechanisms in the control of extracellular fluid volume. *Physiol Rev*, 73(1):1–78, 1993.
- [211] K. Aukland and G. Nicolaysen. Interstitial fluid volume: local regulatory mechanisms. *Physiol Rev*, 61(3):556–643, 1981.

- [212] E. A. Swabb, J. Wei, and P. M. Gullino. Diffusion and convection in normal and neoplastic tissues. *Cancer Res*, 34(10):2814–22, 1974.
- [213] W. D. Comper and T. C. Laurent. Physiological function of connective tissue polysaccharides. *Physiol Rev*, 58(1):255–315, 1978.
- [214] V. C. Mow, A. F. Mak, W. M. Lai, L. C. Rosenberg, and L. H. Tang. Viscoelastic properties of proteoglycan subunits and aggregates in varying solution concentrations. *J Biomech*, 17(5):325–38, 1984.
- [215] A. G. Ogston and T. F. Sherman. Effects of hyaluronic acid upon diffusion of solutes and flow of solvent. *J Physiol*, 156:67–74, 1961.
- [216] A. Pluen, P. A. Netti, R. K. Jain, and D. A. Berk. Diffusion of macromolecules in agarose gels: comparison of linear and globular configurations. *Biophys J*, 77(1):542–52, 1999.
- [217] L. Eikenes, O. S. Bruland, C. Brekken, and L. Davies Cde. Collagenase increases the transcapillary pressure gradient and improves the uptake and distribution of monoclonal antibodies in human osteosarcoma xenografts. *Cancer Res*, 64(14):4768–73, 2004.
- [218] D. G. Boyle and W. R. Potter. Photobleaching of photofrin ii as a means of eliminating skin photosensitivity. *Photochem Photobiol*, 46(6):997–1001, 1987.

- [219] G. J. Fowler and R. Devonshire. Photobleaching of 1,3-diphenylisobenzofuran by novel phthalocyanine dye derivatives. *J Photochem Photobiol B*, 14(3):177–85, 1992.
- [220] T. S. Mang, T. J. Dougherty, W. R. Potter, D. G. Boyle, S. Somer, and J. Moan. Photobleaching of porphyrins used in photodynamic therapy and implications for therapy. *Photochem Photobiol*, 45(4):501–6, 1987.
- [221] T. S. Mang and T. J. Wieman. Photodynamic therapy in the treatment of pancreatic carcinoma: dihematoporphyrin ether uptake and photobleaching kinetics. *Photochem Photobiol*, 46(5):853–8, 1987.
- [222] J. Moan, C. Rimington, and Z. Malik. Photoinduced degradation and modification of Photofrin II in cells in vitro. *Photochem Photobiol*, 47(3):363–7, 1988.
- [223] W. R. Potter, T. S. Mang, and T. J. Dougherty. The theory of photodynamic therapy dosimetry: consequences of photo-destruction of sensitizer. *Photochem Photobiol*, 46(1):97–101, 1987.
- [224] I. A. Boere, D. J. Robinson, H. S. de Bruijn, J. van den Boogert, H. W. Tilanus, H. J. Sterenborg, and R. W. de Bruin. Monitoring in situ dosimetry and protoporphyrin ix fluorescence photobleaching in the normal rat esophagus during 5-aminolevulinic acid photodynamic therapy. *Photochem Photobiol*, 78(3):271–7, 2003.

- [225] J. Moan and K. Berg. The photodegradation of porphyrins in cells can be used to estimate the lifetime of singlet oxygen. *Photochem Photobiol*, 53(4):549–53, 1991.
- [226] I. Georgakoudi and T. H. Foster. Singlet oxygen- versus nonsinglet oxygen-mediated mechanisms of sensitizer photobleaching and their effects on photodynamic dosimetry. *Photochem Photobiol*, 67(6):612–25, 1998.
- [227] I. Georgakoudi, M. G. Nichols, and T. H. Foster. The mechanism of photofrin photobleaching and its consequences for photodynamic dosimetry. *Photochem Photobiol*, 65(1):135–44, 1997.
- [228] B. Y. Kogan. Nonlinear photodynamic therapy. saturation of a photochemical dose by photosensitizer bleaching. *Photochem Photobiol Sci*, 2(6):673–6, 2003.
- [229] N. Van der Veen, H. S. De Bruijn, and W. M. Star. Photobleaching during and re-appearance after photodynamic therapy of topical ALA-induced fluorescence in UVB-treated mouse skin. *Int J Cancer*, 72(1):110–8, 1997.
- [230] I. Georgakoudi and T. H. Foster. Effects of the subcellular redistribution of two Nile blue derivatives on photodynamic oxygen consumption. *Photochem Photobiol*, 68(1):115–22, 1998.
- [231] C. W. Lin, J. R. Shulok, S. D. Kirley, C. M. Bachelder, T. J. Flotte, M. E. Sherwood, L. Cincotta, and J. W. Foley. Photodynamic destruction of lysosomes mediated by Nile blue photosensitizers. *Photochem Photobiol*, 58(1):81–91, 1993.

- [232] S. R. Wood, J. A. Holroyd, and S. B. Brown. The subcellular localization of Zn(ii) phthalocyanines and their redistribution on exposure to light. *Photochem Photobiol*, 65(3):397–402, 1997.
- [233] R. Muschter. Photodynamic therapy: a new approach to prostate cancer. *Curr Urol Rep*, 4(3):221–8, 2003.
- [234] M. R. Arnfield, J. D. Chapman, J. Tulip, M. C. Fenning, and M. S. McPhee. Optical properties of experimental prostate tumors in vivo. *Photochem Photobiol*, 57(2):306–11, 1993.
- [235] Q. Chen and F. W. Hetzel. Laser dosimetry studies in the prostate. *J Clin Laser Med Surg*, 16(1):9–12, 1998.
- [236] L. K. Lee, C. Whitehurst, M. L. Pantelides, and J. V. Moore. An interstitial light assembly for photodynamic therapy in prostatic carcinoma. *BJU Int*, 84(7):821–6, 1999.
- [237] L. K. Lee, C. Whitehurst, M. L. Pantelides, and J. V. Moore. In situ comparison of 665 nm and 633 nm wavelength light penetration in the human prostate gland. *Photochem Photobiol*, 62(5):882–6, 1995.
- [238] C. Whitehurst, M. L. Pantelides, J. V. Moore, P. J. Brooman, and N. J. Blacklock. In vivo laser light distribution in human prostatic carcinoma. *J Urol*, 151(5):1411–5, 1994.

- [239] A. M. Ballangrud, O. Barajas, A. Georgousis, G. G. Miller, R. B. Moore, M. S. McPhee, and J. Tulip. In vivo light transmission spectra in EMT6/Ed murine tumors and Dunning R3327 rat prostate tumors during photodynamic therapy. *Lasers Surg Med*, 21(2):124–33, 1997.
- [240] T. Momma, M. R. Hamblin, H. C. Wu, and T. Hasan. Photodynamic therapy of orthotopic prostate cancer with benzoporphyrin derivative: local control and distant metastasis. *Cancer Res*, 58(23):5425–31, 1998.
- [241] R. B. Moore, J. D. Chapman, J. R. Mercer, R. H. Mannan, L. I. Wiebe, A. J. McEwan, and M. S. McPhee. Measurement of PDT-induced hypoxia in Dunning prostate tumors by iodine-123-iodoazomycin arabinoside. *J Nucl Med*, 34(3):405–11, 1993.
- [242] Z. Xiao, Y. Tamimi, K. Brown, J. Tulip, and R. Moore. Interstitial photodynamic therapy in subcutaneously implanted urologic tumors in rats after intravenous administration of 5-aminolevulinic acid. *Urol Oncol*, 7(3):125–32, 2002.
- [243] X. Xie, J. B. Hudson, and E. S. Guns. Tumor-specific and photodependent cytotoxicity of hypericin in the human Incap prostate tumor model. *Photochem Photobiol*, 74(2):221–5, 2001.
- [244] G. F. Greene, Y. Kitadai, C. A. Pettaway, A. C. von Eschenbach, C. D. Bucana, and I. J. Fidler. Correlation of metastasis-related gene expression with metastatic

- potential in human prostate carcinoma cells implanted in nude mice using an in situ messenger rna hybridization technique. *Am J Pathol*, 150(5):1571–82, 1997.
- [245] P. Molnar, I. Fekete, K. E. Schlageter, G. D. Lapin, and D. R. Groothuis. Absence of host-site influence on angiogenesis, blood flow, and permeability in transplanted RG-2 gliomas. *Drug Metab Dispos*, 27(9):1085–91, 1999.
- [246] D. J. Waters, E. B. Janovitz, and T. C. Chan. Spontaneous metastasis of PC-3 cells in athymic mice after implantation in orthotopic or ectopic microenvironments. *Prostate*, 26(5):227–34, 1995.
- [247] M. Lein, F. Koenig, J. Misdraji, W. S. McDougal, K. Jung, S. A. Loening, T. Hasan, and B. Ortel. Laser-induced hyperthermia in rat prostate cancer: role of site of tumor implantation. *Urology*, 56(1):167–72, 2000.
- [248] T. Gohongi, D. Fukumura, Y. Boucher, C. O. Yun, G. A. Soff, C. Compton, T. Todoroki, and R. K. Jain. Tumor-host interactions in the gallbladder suppress distal angiogenesis and tumor growth: involvement of transforming growth factor beta1. *Nat Med*, 5(10):1203–8, 1999.
- [249] M. Dellian, B. P. Witwer, H. A. Salehi, F. Yuan, and R. K. Jain. Quantitation and physiological characterization of angiogenic vessels in mice: effect of basic fibroblast growth factor, vascular endothelial growth factor/vascular permeability factor, and host microenvironment. *Am J Pathol*, 149(1):59–71, 1996.

- [250] F. Yuan, M. Dellian, D. Fukumura, M. Leunig, D. A. Berk, V. P. Torchilin, and R. K. Jain. Vascular permeability in a human tumor xenograft: molecular size dependence and cutoff size. *Cancer Res*, 55(17):3752–6, 1995.
- [251] E. M. Bindels, M. Vermey, N. J. De Both, and T. H. van der Kwast. Influence of the microenvironment on invasiveness of human bladder carcinoma cell lines. *Virchows Arch*, 439(4):552–9, 2001.
- [252] M. J. Trotter, D. J. Chaplin, and P. L. Olive. Use of a carbocyanine dye as a marker of functional vasculature in murine tumours. *Br J Cancer*, 59(5):706–9, 1989.
- [253] T. R. Tennant, H. Kim, M. Sokoloff, and C. W. Rinker-Schaeffer. The Dunning model. *Prostate*, 43(4):295–302, 2000.
- [254] P. Vaupel, K. Schlenger, C. Knoop, and M. Hockel. Oxygenation of human tumors: evaluation of tissue oxygen distribution in breast cancers by computerized O₂ tension measurements. *Cancer Res*, 51(12):3316–22, 1991.
- [255] P. M. Loadman, M. C. Bibby, J. A. Double, W. M. Al-Shakhaa, and R. Duncan. Pharmacokinetics of PK1 and doxorubicin in experimental colon tumor models with differing responses to PK1. *Clin Cancer Res*, 5(11):3682–8, 1999.
- [256] C. Sheng, B. W. Pogue, E. Wang, J. E. Hutchins, and P. J. Hoopes. Assessment of photosensitizer dosimetry and tissue damage assay for photodynamic therapy in advanced-stage tumors. *Photochem Photobiol*, 79(6):520–5, 2004.

- [257] B. Chen, B. W. Pogue, I. A. Goodwin, J. A. O'Hara, C. M. Wilmot, J. E. Hutchins, P. J. Hoopes, and T. Hasan. Blood flow dynamics after photodynamic therapy with verteporfin in the RIF-1 tumor. *Radiat Res*, 160(4):452–9, 2003.
- [258] J. Vieweg, W. D. Heston, E. Gilboa, and W. R. Fair. An experimental model simulating local recurrence and pelvic lymph node metastasis following orthotopic induction of prostate cancer. *Prostate*, 24(6):291–8, 1994.
- [259] M. W. Dewhirst. Concepts of oxygen transport at the microcirculatory level. *Semin Radiat Oncol*, 8(3):143–50, 1998.
- [260] M. Leunig, F. Yuan, M. D. Menger, Y. Boucher, A. E. Goetz, K. Messmer, and R. K. Jain. Angiogenesis, microvascular architecture, microhemodynamics, and interstitial fluid pressure during early growth of human adenocarcinoma ls174t in scid mice. *Cancer Res*, 52(23):6553–60, 1992.
- [261] R. A. Stephenson, C. P. Dinney, K. Gohji, N. G. Ordonez, J. J. Killion, and I. J. Fidler. Metastatic model for human prostate cancer using orthotopic implantation in nude mice. *J Natl Cancer Inst*, 84(12):951–7, 1992.
- [262] B. W. Pogue, J. A. O'Hara, E. Demidenko, C. M. Wilmot, I. A. Goodwin, B. Chen, H. M. Swartz, and T. Hasan. Photodynamic therapy with verteporfin in the radiation-induced fibrosarcoma-1 tumor causes enhanced radiation sensitivity. *Cancer Res*, 63(5):1025–33, 2003.

- [263] D. Preise, O. Mazor, N. Koudinova, M. Liscovitch, A. Scherz, and Y. Salomon. Bypass of tumor drug resistance by antivasular therapy. *Neoplasia*, 5(6):475–80, 2003.
- [264] T. H. Foster and L. Gao. Dosimetry in photodynamic therapy: oxygen and the critical importance of capillary density. *Radiat Res*, 130(3):379–83., 1992.
- [265] T. H. Foster, R. S. Murant, R. G. Bryant, R. S. Knox, S. L. Gibson, and R. Hilf. Oxygen consumption and diffusion effects in photodynamic therapy. *Radiat Res*, 126(3):296–303., 1991.
- [266] M. A. Konerding, A. J. Miodonski, and A. Lametschwandtner. Microvascular corrosion casting in the study of tumor vascularity: a review. *Scanning Microsc*, 9(4):1233–43; discussion 1243–4, 1995.
- [267] R. E. Hewitt, D. G. Powe, K. Morrell, E. Balley, I. H. Leach, I. O. Ellis, and D. R. Turner. Laminin and collagen iv subunit distribution in normal and neoplastic tissues of colorectum and breast. *Br J Cancer*, 75(2):221–9, 1997.
- [268] J. M. Papadimitrou and A. E. Woods. Structural and functional characteristics of the microcirculation in neoplasms. *J Pathol*, 116(2):65–72, 1975.
- [269] P. B. Vermeulen, D. Verhoeven, H. Fierens, G. Hubens, G. Goovaerts, E. Van Marck, E. A. De Bruijn, A. T. Van Oosterom, and L. Y. Dirix. Microvessel quantifica-

- tion in primary colorectal carcinoma: an immunohistochemical study. *Br J Cancer*, 71(2):340–3, 1995.
- [270] H. F. Dvorak, J. A. Nagy, J. T. Dvorak, and A. M. Dvorak. Identification and characterization of the blood vessels of solid tumors that are leaky to circulating macromolecules. *Am J Pathol*, 133(1):95–109, 1988.
- [271] L. E. Gerlowski and R. K. Jain. Microvascular permeability of normal and neoplastic tissues. *Microvasc Res*, 31(3):288–305, 1986.
- [272] L. Davies Cde, D. A. Berk, A. Pluen, and R. K. Jain. Comparison of IgG diffusion and extracellular matrix composition in rhabdomyosarcomas grown in mice versus in vitro as spheroids reveals the role of host stromal cells. *Br J Cancer*, 86(10):1639–44, 2002.
- [273] R. D. Blumenthal, R. M. Sharkey, R. Kashi, A. M. Natale, and D. M. Goldenberg. Influence of animal host and tumor implantation site on radio-antibody uptake in the GW-39 human colonic cancer xenograft. *Int J Cancer*, 44(6):1041–7, 1989.
- [274] C. Brekken, O. S. Bruland, and C. de Lange Davies. Interstitial fluid pressure in human osteosarcoma xenografts: significance of implantation site and the response to intratumoral injection of hyaluronidase. *Anticancer Res*, 20(5B):3503–12, 2000.
- [275] H. I. Pass. Photodynamic therapy in oncology: mechanisms and clinical use. *J Natl Cancer Inst*, 85(6):443–56, 1993.

- [276] A. Krogh. The number and distribution of capillaries in muscels with calculations of the oxygen pressurehead necessary for supplying the tissue. *J Physiol*, 52:409–415, 1919.
- [277] A. S. Popel. Theory of oxygen transport to tissue. *Crit Rev Biomed Eng*, 17(3):257–321, 1989.
- [278] L. Lapidus and G. F. Pinder. *Numerical Solution of Partial Differential Equations in Science and Engineering*. Wiley, New York, 1999.
- [279] J Crank. *The Mathematics of Diffusion*. Oxford University Press, New York, second edition, 1975.
- [280] R. J. Collins. Bandwidth reduction by automatic renumbering. *Int J Numer Meth Eng*, 6(3):345–356, 1973.
- [281] David A Bellnier, William R Greco, Gregory M Loewen, Hector Nava, Allan R Os-eroff, Ravindra K Pandey, Takaaki Tsuchida, and Thomas J Dougherty. Population pharmacokinetics of the photodynamic therapy agent 2-[1-hexyloxyethyl]-2-devinyl pyropheophorbide-a in cancer patients. *Cancer Res*, 63(8):1806–1813, Apr 2003.
- [282] D. A. Berk, F. Yuan, M. Leunig, and R. K. Jain. Fluorescence photobleaching with spatial Fourier analysis: measurement of diffusion in light-scattering media. *Biophys J*, 65(6):2428–36, 1993.

- [283] G. Clough, C. C. Michel, and M. E. Phillips. Inflammatory changes in permeability and ultrastructure of single vessels in the frog mesenteric microcirculation. *J Physiol*, 395:99–114, 1988.
- [284] M. Panjehpour, R. E. Sneed, D. L. Frazier, M. A. Barnhill, S. F. O'Brien, W. Harb, and B. F. Overholt. Quantification of phthalocyanine concentration in rat tissue using laser-induced fluorescence spectroscopy. *Lasers Surg Med*, 13(1):23–30, 1993.
- [285] A. E. Profio and J Sarnaik. Fluorescence of HpD for tumor detection and dosimetry in photoradiation therapy. In J. Gomer D. Doiron, editor, *Porphyrin localization and treatment of tumors*, pages 301–314. Alan R. Liss, New York, 1984.
- [286] C. Menon, S. N. Kutney, S. C. Lehr, S. K. Hendren, T. M. Busch, S. M. Hahn, and D. L. Fraker. Vascularity and uptake of photosensitizer in small human tumor nodules: implications for intraperitoneal photodynamic therapy. *Clin Cancer Res*, 7(12):3904–3911, Dec 2001.
- [287] R. A. Weersink, J. E. Hayward, K. R. Diamond, and M. S. Patterson. Accuracy of noninvasive in vivo measurements of photosensitizer uptake based on a diffusion model of reflectance spectroscopy. *Photochem Photobiol*, 66(3):326–335, Sep 1997.
- [288] J. R. Mourant, T. M. Johnson, G. Los, and I. J. Bigio. Non-invasive measurement of chemotherapy drug concentrations in tissue: preliminary demonstrations of in vivo measurements. *Phys Med Biol*, 44(5):1397–1417, May 1999.

- [289] B. W. Pogue and G. Burke. Fiber-optic bundle design for quantitative fluorescence measurement from tissue. *Applied Optics*, 37(31):7429–7436, 1998.
- [290] C. C. Lee, B. W. Pogue, R. R. Strawbridge, K. L. Moodie, L. R. Bartholomew, G. C. Burke, and P. J. Hoopes. Comparison of photosensitizer (AIPcS2) quantification techniques: in situ fluorescence microsampling versus tissue chemical extraction. *Photochem Photobiol*, 74(3):453–60, 2001.
- [291] R. Cubeddu, A. Pifferi, P. Taroni, A. Torricelli, G. Valentini, D. Comelli, C. D’Andrea, V. Angelini, and G. Canti. Fluorescence imaging during photodynamic therapy of experimental tumors in mice sensitized with disulfonated aluminum phthalocyanine. *Photochem Photobiol*, 72(5):690–5, 2000.
- [292] S. Andersson-Engels, C. Klinteberg, K. Svanberg, and S. Svanberg. In vivo fluorescence imaging for tissue diagnostics. *Phys Med Biol*, 42(5):815–24, 1997.
- [293] C. M. Gardner, S. L. Jacques, and A. J. Welch. Fluorescence spectroscopy of tissue: recovery of intrinsic fluorescence from measured fluorescence. *Appl. Opt.*, 35(10):1780–1792, 1996.
- [294] B. W. Pogue, S. L. Gibbs, B. Chen, and M. Savellano. Fluorescence imaging in vivo: raster scanned point-source imaging provides more accurate quantification than broad beam geometries. *Technol Cancer Res Treat*, 3(1):15–21, 2004.
- [295] C. C. Lee, B. W. Pogue, J. A. O’Hara, C. M. Wilmot, R. R. Strawbridge, G. C. Burke,

- and P. J. Hoopes. Spatial heterogeneity and temporal kinetics of photosensitizer (AlPcS2) concentration in murine tumors RIF-1 and MTG-B. *Photochem Photobiol Sci*, 2(2):145–50, 2003.
- [296] S. Iinuma, K. T. Schomacker, G. Wagnieres, M. Rajadhyaksha, M. Bamberg, T. Momma, and T. Hasan. In vivo fluence rate and fractionation effects on tumor response and photobleaching: photodynamic therapy with two photosensitizers in an orthotopic rat tumor model. *Cancer Res*, 59(24):6164–70, 1999.
- [297] Q. Peng, J. Moan, G. Farrants, H. E. Danielsen, and C. Rimington. Localization of potent photosensitizers in human tumor LOX by means of laser scanning microscopy. *Cancer Lett*, 58(1-2):17–27, 1991.
- [298] N. S. Trivedi, H. W. Wang, A. L. Nieminen, N. L. Oleinick, and J. A. Izatt. Quantitative analysis of Pc 4 localization in mouse lymphoma (LY-R) cells via double-label confocal fluorescence microscopy. *Photochem Photobiol*, 71(5):634–9, 2000.
- [299] L. Lilge, C. O’Carroll, and B. C. Wilson. A solubilization technique for photosensitizer quantification in ex vivo tissue samples. *J Photochem Photobiol B*, 39(3):229–35, 1997.
- [300] G. A. Wagnieres, W. M. Star, and B. C. Wilson. In vivo fluorescence spectroscopy and imaging for oncological applications. *Photochem Photobiol*, 68(5):603–32, 1998.

- [301] B. Aveline, T. Hasan, and R. W. Redmond. Photophysical and photosensitizing properties of benzoporphyrin derivative monoacid ring A (BPD-MA). *Photochem Photobiol*, 59(3):328–35, 1994.
- [302] J. Moan, H. Anholt, and Q. Peng. A transient reduction of the fluorescence of aluminium phthalocyanine tetrasulphonate in tumours during photodynamic therapy. *J Photochem Photobiol B*, 5(1):115–9, 1990.
- [303] B. M. Aveline and R. W. Redmond. Can cellular phototoxicity be accurately predicted on the basis of sensitizer photophysics? *Photochem Photobiol*, 69(3):306–16, 1999.
- [304] B. M. Aveline, R. M. Sattler, and R. W. Redmond. Environmental effects on cellular photosensitization: correlation of phototoxicity mechanism with transient absorption spectroscopy measurements. *Photochem Photobiol*, 68(1):51–62, 1998.
- [305] B. C. Wilson, M. S. Patterson, and L. Lilge. Implicit and explicit dosimetry in photodynamic therapy: a new paradigm. *Lasers in Medical Science*, 12(3):182–199, 1997.
- [306] B. W. Pogue and T. Hasan. Fluorophore quantitation in tissue-simulating media with confocal detection. *Ieee Journal of Selected Topics in Quantum Electronics*, 2(4):959–964, 1996.
- [307] X. Zhou, B. W. Pogue, B. Chen, and T. Hasan. Analysis of effective molecular

- diffusion rates for verteporfin in subcutaneous versus orthotopic Dunning prostate tumors. *Photochem Photobiol*, 79(4):323–31, 2004.
- [308] G. Helmlinger, F. Yuan, M. Dellian, and R. K. Jain. Interstitial pH and pO₂ gradients in solid tumors in vivo: high-resolution measurements reveal a lack of correlation. *Nat Med*, 3(2):177–82, 1997.
- [309] M. R. Horsman, A. A. Khalil, D. W. Siemann, C. Grau, S. A. Hill, E. M. Lynch, D. J. Chaplin, and J. Overgaard. Relationship between radiobiological hypoxia in tumors and electrode measurements of tumor oxygenation. *Int J Radiat Oncol Biol Phys*, 29(3):439–42, 1994.
- [310] M. S. Patterson, B. C. Wilson, and R. Graff. In vivo tests of the concept of photodynamic threshold dose in normal rat liver photosensitized by aluminum chloro-sulphonated phthalocyanine. *Photochem Photobiol*, 51(3):343–9, 1990.
- [311] C. J. Tralau, A. J. MacRobert, P. D. Coleridge-Smith, H. Barr, and S. G. Bown. Photodynamic therapy with phthalocyanine sensitisation: quantitative studies in a transplantable rat fibrosarcoma. *Br J Cancer*, 55(4):389–95, 1987.
- [312] B. W. Pogue, K. D. Paulsen, J. A. O’Hara, C. M. Wilmot, and H. M. Swartz. Estimation of oxygen distribution in rif-1 tumors by diffusion model-based interpretation of pimonidazole hypoxia and eppendorf measurements. *Radiat Res*, 155(1 Pt 1):15–25, 2001.

- [313] V. H. Fingar, T. J. Wieman, Y. J. Park, and B. W. Henderson. Implications of a pre-existing tumor hypoxic fraction on photodynamic therapy. *J Surg Res*, 53(5):524–8, 1992.
- [314] M. Hockel, C. Knoop, K. Schlenger, B. Vorndran, E. Bausmann, M. Mitze, P. G. Knapstein, and P. Vaupel. Intratumoral pO₂ predicts survival in advanced cancer of the uterine cervix. *Radiother Oncol*, 26(1):45–50, 1993.
- [315] M. Hockel, K. Schlenger, B. Aral, M. Mitze, U. Schaffer, and P. Vaupel. Association between tumor hypoxia and malignant progression in advanced cancer of the uterine cervix. *Cancer Res*, 56(19):4509–15, 1996.
- [316] E. Demidenko. *Mixed Models: Theory and Applications*. New Jersey, 1st ed. edition, 2004.
- [317] G. Soubrane, E. Souied, W. Haddad, S. Razavi, W. Roquet, and G. Coscas. [Alternative therapies for choroidal neovessels resulting from age-related macular degeneration]. *J Fr Ophthalmol*, 26(8):876–878, Oct 2003.
- [318] G. Majno and G. E. Palade. Studies on inflammation. I. The effect of histamine and serotonin on vascular permeability: an electron microscopic study. *J Biophys Biochem Cytol*, 11:571–605, 1961.
- [319] G. Majno, G. E. Palade, and G. I. Schoefl. Studies on inflammation. II. The site of

- action of histamine and serotonin along the vascular tree: a topographic study. *J Biophys Biochem Cytol*, 11:607–26, 1961.
- [320] I. Joris, G. Majno, and G. B. Ryan. Endothelial contraction in vivo: a study of the rat mesentery. *Virchows Arch B Cell Pathol*, 12(1):73–83, 1972.
- [321] G. Majno, S. M. Shea, and M. Leventhal. Endothelial contraction induced by histamine-type mediators: an electron microscopic study. *J Cell Biol*, 42(3):647–672, Sep 1969.
- [322] J. Fox, F. Galey, and H. Wayland. Action of histamine on the mesenteric microvasculature. *Microvasc Res*, 19(1):108–26, 1980.
- [323] C. Weidner, M. Klede, R. Rukwied, G. Lischetzki, U. Neisius, P. S. Skov, L. J. Petersen, and M. Schmelz. Acute effects of substance P and calcitonin gene-related peptide in human skin—a microdialysis study. *J Invest Dermatol*, 115(6):1015–1020, Dec 2000.
- [324] K. Bohlin and I. A. Cotgreave. Pro-inflammatory cytokines increase the permeability of paracetamol across a human endothelial-smooth muscle cell bilayer model. *Scand J Clin Lab Invest*, 59(4):259–66, 1999.
- [325] D. J. Brooks, R. P. Beaney, A. A. Lammertsma, D. R. Turton, J. Marshall, D. G. Thomas, and T. Jones. Studies on regional cerebral haematocrit and blood flow in

- patients with cerebral tumours using positron emission tomography. *Microvasc Res*, 31(3):267–76, 1986.
- [326] T. Hkfelt, J. O. Kellerth, G. Nilsson, and B. Pernow. Experimental immunohistochemical studies on the localization and distribution of substance P in cat primary sensory neurons. *Brain Res*, 100(2):235–252, Dec 1975.
- [327] J. W. Brock and I. G. Joshua. Substance P mechanisms in the regulation of striated muscle microcirculation. *Microvasc Res*, 41(1):24–28, Jan 1991.
- [328] N. Z. Wu and A. L. Baldwin. Transient venular permeability increase and endothelial gap formation induced by histamine. *Am J Physiol*, 262(4 Pt 2):H1238–47, 1992.
- [329] R. van Hillegersberg, W. J. Kort, and J. H. Wilson. Current status of photodynamic therapy in oncology. *Drugs*, 48(4):510–27, 1994.
- [330] B. W. Pogue, B. Chen, X. Zhou, and P. J. Hoopes. Analysis of sampling volume and tissue heterogeneity on the in vivo detection of fluorescence. *J Biomed Opt*, 10(4):41206, 2005.
- [331] S. G. Bown, C. J. Tralau, P. D. Smith, D. Akdemir, and T. J. Wieman. Photodynamic therapy with porphyrin and phthalocyanine sensitisation: quantitative studies in normal rat liver. *Br J Cancer*, 54(1):43–52, 1986.
- [332] T. J. Farrell, B. C. Wilson, M. S. Patterson, and M. C. Olivo. Comparison of the in vivo photodynamic threshold dose for photofrin, mono- and tetrasulfonated alu-

- minum phthalocyanine using a rat liver model. *Photochem Photobiol*, 68(3):394–9, 1998.
- [333] K. T. Moesta, W. R. Greco, S. O. Nurse-Finlay, J. C. Parsons, and T. S. Mang. Lack of reciprocity in drug and light dose dependence of photodynamic therapy of pancreatic adenocarcinoma in vitro. *Cancer Res*, 55(14):3078–84, 1995.
- [334] A. J. Pope, A. J. MacRobert, D. Phillips, and S. G. Bown. The detection of phthalocyanine fluorescence in normal rat bladder wall using sensitive digital imaging microscopy. *Br J Cancer*, 64(5):875–9, 1991.
- [335] V. X. Yang, P. J. Muller, P. Herman, and B. C. Wilson. A multispectral fluorescence imaging system: design and initial clinical tests in intra-operative photofrin-photodynamic therapy of brain tumors. *Lasers Surg Med*, 32(3):224–32, 2003.
- [336] V. H. Fingar, W. R. Potter, and B. W. Henderson. Drug and light dose dependence of photodynamic therapy: a study of tumor cell clonogenicity and histologic changes. *Photochem Photobiol*, 45(5):643–50, 1987.
- [337] J. C. van Gemert, M. C. Berenbaum, and G. H. Gijsbers. Wavelength and light-dose dependence in tumour phototherapy with haematoporphyrin derivative. *Br J Cancer*, 52(1):43–9, 1985.
- [338] W.R. Hendee, G.S. Ibbott, and E.G. Hendee. *Radiation Therapy Physics*. John Wiley & Sons, Inc., New Jersey, 3rd ed. edition, 2005.

- [339] L. I. Grossweiner. PDT light dosimetry revisited. *J Photochem Photobiol B*, 38(2-3):258–68., 1997.
- [340] L. I. Grossweiner. Optical dosimetry in photodynamic therapy. *Lasers Surg Med*, 6(5):462–6, 1986.
- [341] T. M. Busch, S. M. Hahn, S. M. Evans, and C. J. Koch. Depletion of tumor oxygenation during photodynamic therapy: detection by the hypoxia marker EF3 [2-(2-nitroimidazol-1[h]-yl)-n-(3,3,3- trifluoropropyl)acetamide]. *Cancer Res*, 60(10):2636–42., 2000.
- [342] I. P. Torres Filho, M. Leunig, F. Yuan, M. Intaglietta, and R. K. Jain. Noninvasive measurement of microvascular and interstitial oxygen profiles in a human tumor in SCID mice. *Proc Natl Acad Sci U S A*, 91(6):2081–5, 1994.
- [343] B. J. Tromberg, A. Orenstein, S. Kimel, S. J. Barker, J. Hyatt, J. S. Nelson, and M. W. Berns. In vivo tumor oxygen tension measurements for the evaluation of the efficiency of photodynamic therapy. *Photochem Photobiol*, 52(2):375–85, 1990.
- [344] J. M. Vanderkooi, G. Maniara, T. J. Green, and D. F. Wilson. An optical method for measurement of dioxygen concentration based upon quenching of phosphorescence. *J Biol Chem*, 262(12):5476–82, 1987.
- [345] S. C. Chang, G. Buonaccorsi, A. MacRobert, and S. G. Bown. Interstitial and

- transurethral photodynamic therapy of the canine prostate using meso-tetra-(m-hydroxyphenyl) chlorin. *Int J Cancer*, 67(4):555–62, 1996.
- [346] M. Niedre, M. S. Patterson, and B. C. Wilson. Direct near-infrared luminescence detection of singlet oxygen generated by photodynamic therapy in cells in vitro and tissues in vivo. *Photochem Photobiol*, 75(4):382–91, 2002.
- [347] M. J. Niedre, C. S. Yu, M. S. Patterson, and B. C. Wilson. Singlet oxygen luminescence as an in vivo photodynamic therapy dose metric: validation in normal mouse skin with topical amino-levulinic acid. *Br J Cancer*, 92(2):298–304, 2005.
- [348] B. W. Pogue, J. D. Pitts, M. A. Mycek, R. D. Sloboda, C. M. Wilmot, J. F. Brandsema, and J. A. O’Hara. In vivo NADH fluorescence monitoring as an assay for cellular damage in photodynamic therapy. *Photochem Photobiol*, 74(6):817–24, 2001.
- [349] G. W. Barendsen. [experimental data concerning cellular recovery and repopulation of tumors following fractionated irradiation]. *Ned Tijdschr Geneesk*, 113(48):2170–1, 1969.
- [350] M. Shibata, S. Ichioka, J. Ando, and A. Kamiya. Microvascular and interstitial pO₂ measurements in rat skeletal muscle by phosphorescence quenching. *J Appl Physiol*, 91(1):321–7, 2001.
- [351] H. M. Swartz, S. Boyer, P. Gast, J. F. Glockner, H. Hu, K. J. Liu, M. Moussavi, S. W.

- Norby, N. Vahidi, T. Walczak, and et al. Measurements of pertinent concentrations of oxygen in vivo. *Magn Reson Med*, 20(2):333–9, 1991.
- [352] I. P. Torres Filho and M. Intaglietta. Microvessel po₂ measurements by phosphorescence decay method. *Am J Physiol*, 265(4 Pt 2):H1434–8, 1993.
- [353] L. Zheng, A. S. Golub, and R. N. Pittman. Determination of pO₂ and its heterogeneity in single capillaries. *Am J Physiol*, 271(1 Pt 2):H365–72, 1996.
- [354] K. E. Arfors, G. Rutili, and E. Svensjo. Microvascular transport of macromolecules in normal and inflammatory conditions. *Acta Physiol Scand Suppl*, 463:93–103, 1979.
- [355] T. W. Hennigan, R. H. Begent, and T. G. Allen-Mersh. Histamine, leukotriene C₄ and interleukin-2 increase antibody uptake into a human carcinoma xenograft model. *Br J Cancer*, 64(5):872–4, 1991.
- [356] D. M. McDonald. Endothelial gaps and permeability of venules in rat tracheas exposed to inflammatory stimuli. *Am J Physiol*, 266(1 Pt 1):L61–83, 1994.